Theoretical and Electrochemical Investigation on Controlling Metal (carbon steel/ruthenium) Dissolution in Corrosive Environments

A THESIS

Submitted in Partial Fulfilment of the Requirements for the Degree of

DOCTOR OF PHILOSOPHY

Nikhil Rahul Dhongde

DEPARTMENT OF CHEMICAL ENGINEERING

INDIAN INSTITUTE OF TECHNOLOGY GUWAHATI,

GUWAHATI – 781039, ASSAM, INDIA

January, 2025

DEDICATION

To my parental grandmother ***Smt. Gangubai Arjun Dhongde***, maternal grandmother ***Smt. Nanda Bhanudas Jamgade***.

Without your endless love, support, and encouragement, it would not have been possible.

To my supervisor, ***Dr. R. Prasanna Venkatesh***,

For your patience, support, and unwavering faith in me. Thank you for always guiding me and showing me the right path.

My family ***Mrs. Kirti Dhongde, Mr. Rahul Dhongde*** and ***Dr. Vicky Dhongde.***

And

To the Almighty.

For giving me the power and strength to go through the right way.

STATEMENT ON ACADEMIC INTEGRITY

I hereby declare that the work contained herein is exclusively the result of investigations accomplished by me in the Department of Chemical Engineering, Indian Institute of Technology Guwahati, Guwahati, Assam, India under the supervision of **Dr. Prasanna Venkatesh Rajaraman**.

In keeping with the general practice of reporting scientific observations, the thesis has been prepared without resorting to plagiarism and due acknowledgement and citation has been made wherever the work described is based on the findings of other investigations.

Place: IIT Guwahati, India **Mr. Nikhil Rahul Dhongde**

Date: **Roll no. 196107013**

Dr. Prasanna Venkatesh Rajaraman

Associate Professor

Department of Chemical Engineering Indian Institute of Technology Guwahati-781039, Assam, India

CERTIFICATE

It is certified that the work contained in the thesis entitled, Theoretical and Electrochemical Investigation on Controlling Metal (carbon steel/ruthenium) Dissolution in Corrosive Environments, by **Mr**. **Nikhil Rahul Dhongde (Roll No. 196107013)**, has been carried out by him in the Department of Chemical Engineering, Indian Institute of Technology Guwahati, Guwahati, Assam, India under my supervision and that this work has not been submitted elsewhere for a degree.

Date:

Dr. Prasanna Venkatesh Rajaraman

(Thesis Supervisor)

ACKNOWLEDGEMENT

This wonderful Ph.D. journey of mine has become a reality due to the support and presence of many individuals. At this moment of accomplishment, I would like to thank everyone and expresses my deepest gratitude for helping me in making this thesis possible and accomplishing this dream of mine.

First and foremost, I would like to express my sincere gratitude and warmest regards to my supervisor ***Dr. Prasanna Venkatesh Rajaraman***, for imparting the knowledge and guiding me in every possible way. His kindness, politeness, patience, professionalism, cooperativeness and enthusiasm have motivated me towards the completion of my research work and making this thesis possible. I could not have imagined having a better mentor and supervisor for my Ph.D. journey. It was a great honour to work under him and I will be forever indebted to him for his immense support. I would also to express my gratefulness to my Doctoral Committee members, ***Prof. Chandan Das*** (Department of Chemical Engineering), ***Prof. Prabu Vairakannu*** (Department of Chemical Engineering) and ***Dr. G. Indu Siva Ranjani*** (Department of Civil Engineering) for their priceless time, valuable suggestions and relevant insights throughout my research period.

I express my gratitude to ***Prof. Kaustubha Mohanty***, Head of the Department of Chemical Engineering for his benevolent support. I am also thankful to the faculty members of the Department of Chemical Engineering along with other departments of Indian Institute of Technology Guwahati, for their generousness and assistance. I am also grateful to all the technical staff members of Department of Chemical Engineering along with other departments for helping me in using the analytical research facilities. I am also thankful to the non-teaching staff of all the departments for their immense help.

I would also like to express my gratitude to ***Prof. Jin-Goo Park***, Department of Materials Science and Chemical Engineering, Hanyang University, Ansan, Republic of Korea for providing the Biovia Material Studio (Accelyrl company, USA) software and supporting me in my research work (Monte Carlo simulation). I am also grateful to ***Dr. Jenasree Hazarika***, Department of Materials Science and Chemical Engineering, Hanyang University, Ansan, Republic of Korea for performing the Monte Carlo simulations in Biovia Material Studio (Accelyrl company, USA) software. In addition, I would like to acknowledge the Department of Materials Science and Chemical Engineering, Hanyang University, Ansan, Republic of Korea for supporting me in my theoretical/simulation research work.

I would like to acknowledge the Aries Engineer, Maharashtra, India for metal fabrication, Subodh Technologists Metallurgical & Corrosion Testing Laboratory, Maharashtra, India for their assistance in salt spray test and Caltech Engineering Services, Maharashtra, India for the pull-off adhesion test. Also, acknowledge ***Dr. Partho Sarathi Gooh Pattader*** (Department of Chemical Engineering) for providing goniometer to perform contact angle measurements.

I sincerely acknowledge Central Workshop, Analytical Lab-Department of Chemical Engineering, Department of Nano Technology and Central Instruments Facility, IIT Guwahati for providing me with the fabrication and analytical facilities required for my research work.

My heartful thanks and respect to my research family ***Dr. Apeksha Gupta, Dr. Anusuya Talukdar, Dr. Prince Baranwal, Dr. Shravan Kumar, Sayani Adhikari, Rushabh Kale, Shaimpu Babu, Vinay Kumar, Rohan Kumar, Mansi Singh, Naveen Kumar, Kunal Gurjar, Murrupurna Anand Kumar***. My deepest gratitude to ***Dr. Barnali Bhui, Dr. Pradeep Sahu, Shekhar Jyoti Pathak, Dr. Roni Mallick, Koushik Jena, Dr. Vinod Vanarse, Dr. Anil Kumar, Dr. Nagendra Prasad, Dr. Deepak Kanumuri, Dr. Imran Hussain, Dr. Arindam Dutta, Dr. Jiwajyoti Mahanta, Dr. Nipu Kumar Das, Dr. Titikshya Mohapatra, Dr. Yumnam Gyani***

Devi, Dr. Mihul Gabhane, Radhesham Verma, Aniket Masram, Suraj Junghare for all the care and support. The joyful, friendly and supportive nature that you all showered in the lab has always helped me in carrying out my research work smoothly and made my stay worth memorable.

Thank You

Nikhil Rahul Dhongde

ABSTRCAT

Carbon steel (CS), one of the most important and valuable materials is widely used in a variety of applications including pipelines, shipping, biomedical implants, rail transportation, and infrastructure construction due to its outstanding processability, high tensile strength, recyclability, and low cost. However, chemical substances like water, oxygen, halides, etc. can corrode them under a variety of circumstances. Hence, it is very necessary to use epoxy-based coating to protect the CS in corrosive environment. In the present study (objective 1 and 2), epoxy-based coating with carbon-based fillers were used to protect the carbon steel substrate in 3.5 wt% NaCl solution.

Ruthenium (Ru) as barrier/interconnect material is of great interest among microelectronics fabrication industries. Chemical mechanical planarization (CMP) is a crucial process for achieving effective planarization of metal surfaces at both the local and global levels using a chemical slurry consists of various additives. Protecting the metal in CMP process from corrosion is regarded as a highly critical component. Hence, it is very necessary to introduces appropriate corrosion inhibitor for the protection of Ru metal and analyse the interaction mechanism between inhibitor and Ru metal at macroscale level. The primary objective 3 of the present work is to get insight on physicochemical interaction between azoles and Ru at the microscale level using quantum chemistry calculations and Monte Carlo simulation.

In the first part of the present study, ionic liquid functionalization graphene oxide (FGO) filler used with epoxy coating to protect the carbon steel metal in 3.5 wt % NaCl solution. In the first part, an anticorrosive organic coating of epoxy on carbon steel was modified with uniformly dispersed graphene oxide (GO) after functionalization with ionic liquid (FGO). The ionic liquid (IL) used was 1-butyl-3-methylimidazolium acetate which possess higher solubility and the graphene oxide was prepared by improved Hummer's method. The successful grafting of IL on

the GO was confirmed by various techniques including Fourier-transform infrared spectroscopy, Raman, XPS, XRD, thermogravimetric analysis, BET, field emission scanning electron microscope, and field emission transmission electron microscope. The surface characterization studies revealed that uniform dispersion of FGO is achieved in the epoxy matrix. Further, electrochemical studies such as potentiodynamic polarization, and electrochemical impedance spectroscopy (EIS) showed higher corrosion protection efficiency (~99%) against corrosive fluid (3.5 wt% NaCl solution).

In the second part of the present study, carbon quantum dots filler obtained from biomass used with epoxy coating was investigated to protect the carbon steel metal in a 3.5 wt % NaCl solution. The corrosion resistance of carbon quantum dots was analysed through experimental and theoretical methods. Carbon quantum dots synthesized from waste biomass (rice husk quantum dots/RH-QDs) through a hydrothermal synthesis reaction was explored for the anti-corrosive applications. 0.1 and 0.5 wt% RH-QDs (with respect to epoxy) were integrated into the epoxy composite and applied to a carbon steel substrate. The anti-corrosive performance of coating was investigated using EIS, potentiodynamic polarization, and salt spray test. The outcomes showed that the use of RH-QDs significantly enhanced the corrosion protection performance of the epoxy coating in 3.5 wt% NaCl. In addition, the adhesion strength of epoxy on the carbon steel substrate was also enhanced (3.6 MPa) due to the bond interaction between RH-QDs and epoxy. The complementary analysis based on the density functional theory (DFT) reveals that the RH-QDs significantly influence the strengthening of the interface between this moiety and the epoxy-hardener, thereby retarding the electrochemical reaction.

In the third part of the present study, azoles were used as corrosion inhibitors in an alkaline environment to protect ruthenium metal in chemical mechanical planarization applications. The corrosion inhibition behaviour of azoles was analysed through experimental and theoretical methods. The adsorption performance and inhibition mechanism of azoles;

Imidazole (IMD), 1, 2, 4-Triazole (TAZ), and 1, 2, 3-Benzotriazole (BTAH) inhibitors on ruthenium (Ru) at 9 pH, were investigated in this study using electrochemical techniques and density functional theory (DFT) simulations. The electrochemical data demonstrate that the three azole compounds being investigated are mixed type corrosion inhibitors with anodic predominance, and the order of corrosion inhibition efficiency for Ru is BTAH > TAZ > IMD. The azole compounds suppress the metal dissolution reaction rate by adhering on to the Ru surface and nature of adsorption (combined physisorption and chemisorption) is explained via Langmuir adsorption isotherm model. The results of quantum chemical calculations showed that the BTAH provides higher inhibition efficiency, as evidenced by the ΔN value. However, the trend obtained for inhibition efficiency (i.e., BTAH>TAZ>IMD) could not be explained by quantum chemical descriptors. Furthermore, the experimental trend is well explained by the Mulliken charge density and Monte Carlo simulation. The higher adsorption of BTAH on the Ru surface attributed to the higher number of active cites (N13, N14, C4, C5, C7, and C8), planner/horizontal orientation of the BTAH molecule on the Ru surface during the adsorption process, and significantly lower adsorption energy. The research methods and findings presented in this third objective are beneficial for investigating the adsorption characteristics and inhibition mechanisms of inhibitors on metal surfaces at the microscale level.

KEYWORDS: carbon steel, graphene oxide, ionic liquid, epoxy coating, anticorrosive coating, rice husk, carbon quantum dots, chemical mechanical planarization, ruthenium, corrosion inhibitor, azoles, electrochemical impedance spectroscopy, potentiodynamic polarization, quantum chemical calculation, Monte Carlo simulation

NOMENCLATURE

English Symbols

C	Capacitance
C_{dl}	Double Layer Capacitance
d	Density
i_{corr}	Corrosion Current Density
E_{corr}	Corrosion Potential
R	Resistance
R_{ct}	Charge Transfer Resistance
R	Ideal Gas Constant
R_p	Polarization Resistance
R_{sol}	Solution Resistance
T	Temperature
t	Time
Z	Impedance
Z_0	Magnitude of Impedance
Z_F	Faradic Impedance
Z_{Re}	Real Component of Impedance
Z_{Im}	Imaginary Component of Impedance
Z_{total}	Total Impedance
Z	Impedance

Greek Symbols

α	Transfer Coefficient
β	Tafel Constant
βa	Anodic Tafel Constant
βc	Cathodic Tafel Constant

ABBREVIATION

PP	Potentiodynamic Polarization
EIS	Electrochemical impedance spectroscopy
RR	Removal Rate
Ru	Ruthenium
V	Volt
XPS	X-ray photoelectron spectroscopy
XRD	X-ray Diffraction
AFM	Atomic force microscopy
CPE	Constant phase element
EDX	Energy Dispersive X-ray
FESEM	Field Emission Scanning Electron Microscopy
HOMO	Highest occupied molecular orbital
LUMO	Lowest unoccupied molecular orbitals

TABLE OF CONTENT

LIST OF TABLES

LIST OF FIGURES

CHAPTER 1

INTRODUCTION

1.1 Corrosion

Corrosion, in the context of material science, can be described as the process by which materials undergo degradation, resulting in a decrease in their inherent properties (Dwivedi et al., 2017a; Esmaily et al., 2017; Ma et al., 2009a, 2009b; Sørensen et al., 2009a). This degradation occurs as a result of detrimental interactions between the materials and the surrounding environments to which they are exposed. Similar to natural disasters, corrosion is responsible for significant economic losses, poses environmental risks, and poses a threat to human life. According to a study carried out by the National Association of Corrosion Engineers (NACE), the estimated global cost attributed to corrosion amounts to a staggering US$2.5 trillion (Aljeaban et al., 2020; Alum and Eze, 2020; Ashwathareddy et al., 2024). This substantial figure is equivalent to approximately 3.4% of the world's gross domestic product (GDP) as of 2013. According to the NACE (2019), corrosion has a 2.4% impact on India's GDP. For developing economy like ours, it is huge burden. The discovery of potential savings of up to 35% in corrosion-related expenses through the implementation of existing corrosion control methodologies elicits a complex mix of emotions, encompassing both a sense of tragedy and a feeling of relief (Solovyeva et al., 2023). Corrosion control plays a pivotal role in safeguarding public safety and preserving the environment, while also yielding significant economic benefits (Prasad et al., 2020).

Aqueous corrosion is a process that involves two half-reactions, namely oxidation and reduction, as well as the flow of charge in the form of electrons. The process in which electrons are released is referred to as an anodic reaction, which is an oxidation process as shown below.

$$M \rightarrow M^{n+} + n^{e-} \qquad \textbf{(1.1)}$$

Similarly, the process in which electrons are released is known as a cathodic reaction, which is a reduction process. The cathodic reactions are contingent upon the characteristics of the surrounding environment while the oxidation process is contingent upon the oxidation state. During the process of iron corrosion, iron ions that have already undergone oxidation can undergo further oxidation, as demonstrated by the following example:

$Fe \rightarrow Fe^{2+} + 2e^-$ **(1.2)**

$Fe^{2+} \rightarrow Fe^{3+} + 1e^-$ **(1.3)**

1.1.1 Types of corrosion and factors affecting corrosion

Based on the nature of the material and the surrounding environmental conditions, corrosion can occur in various forms when a material is in use. The schematic various types of corrosion are presented in **Figure 1.1.** Here are some commonly observed and reported types of corrosion in industries.

(a) Uniform corrosion: It is commonly referred to as general corrosion. The most common type of corrosion, characterized by a uniform attack over the entire exposed surface of a material. It occurs when the material reacts with a corrosive environment, such as air, water, or chemicals, leading to a consistent and predictable thinning or loss of material. This type of corrosion is typically slower and easier to monitor and manage compared to localized forms, as it does not create concentrated areas of damage. An example is the rusting of steel surfaces exposed to atmospheric moisture. The rate of uniform corrosion can be easily determined by measuring the mass loss. Uniform corrosion is exemplified by phenomena such as rust formation, silver tarnishing, nickel fogging, and high-temperature oxidation.

(b) Galvanic corrosion: Galvanic corrosion, also referred to as electrolytic corrosion, is a type of localized corrosion that can happen when two or more alloys come into contact with each other in an environment that facilitates the transfer of ions (Alum and Eze, 2020; Ghali et al.,

2004; Han et al., 2010). Galvanic corrosion can be electrically measured due to its electrochemical nature. Every alloy is assigned an electrical value or "potential", and materials that exhibit better corrosion resistance are commonly referred to as more "noble" or "passive". When two alloys are in contact in a corrosive environment, the less noble alloy experiences increased corrosion, while the more noble alloy benefits from enhanced protection. Galvanic corrosion is commonly observed in galvanized iron, which refers to a sheet of iron or steel that is coated with a layer of zinc. Even if the protective zinc coating is damaged, the underlying steel remains unaffected. On the contrary, the zinc corrodes due to its lower nobility. Rusting of the base metal can only occur after it has been consumed.

(c) Pitting corrosion: This form of corrosion is characterized by the formation of circular and irregular-shaped cavities on the surface of the metal. Their size and dimensions are determined by various factors associated with the metal, the environment, and the conditions of use. Pitting corrosion is exemplified by the deterioration of a metal due to inadequate maintenance and exposure to water droplets and dust particles. The region beneath the droplet lacks sufficient oxygenation, whereas the surrounding areas are adequately oxygenated. This leads to a phenomenon known as differential aeration corrosion, in which the surrounding areas exhibit cathodic behavior while the small area below the droplets and dust particles becomes anodic. Electrons traverse the metal and encounter water and oxygen. Carbon steel tanks or pipes in swimming pool environments or seawater suffer from pitting due to chloride ions breaking down the protective oxide layer.

(d) Crevice corrosion: Crevice corrosion is the term used to describe corrosion that happens in small, enclosed spaces where a stagnant solution is trapped and not replaced. These areas are commonly referred to as crevices. Crevices are commonly found in gaps and contact areas between parts, beneath gaskets or seals, within cracks and seams, in spaces filled with deposits,

and underneath sludge piles. Crevice corrosion can occur in all grades of stainless steel and aluminium alloys.

(e) Erosion corrosion: Erosion-induced corrosion can take place in fluid environments. The corrosion in question is influenced by the velocity at which the fluid is flowing. Local thinning of the metal causes the formation of scratches, gullies, and undulations that consistently align with the flow direction.

(f) Exfoliation corrosion: Exfoliation corrosion is a specific form of corrosion that occurs along multiple planes parallel to the direction of rolling or extrusion.

(g) Intergranular corrosion: The corrosion spreads in all directions, affecting all the metallurgical constituents equally. It does not selectively target specific areas, but rather propagates within the grains.

(h) Microbial induced corrosion: Microbial-induced corrosion is the result of bacteria causing chemical reactions at the anode and/or cathode of corrosion concentration cells, leading to metal deterioration. A proposed mechanism suggests that the bacteria trigger cathodic depolarization by removing hydrogen that has adhered to metal surfaces. Various strains of bacteria have the ability to cause corrosion in steel pipework. Sulphate-Reducing Bacteria (SRB) is a widely recognised bacteria species frequently present in chilled water closed loops. Microbial induced corrosion affects various industries, such as onshore and offshore oil and gas, water treatment, and nuclear power generation.

(a) Uniform corrosion

(b) Galvanic corrosion

(c) Pitting corrosion

(d) Crevice corrosion

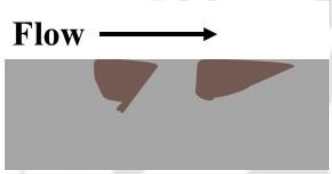

(e) Erosion corrosion

(f) Exfoliation corrosion

(g) Intergranular corrosion

(h) Microbial induced corrosion

Figure 1.1 Types of corrosion

1.2 Carbon steel

A wide variety of products are extracted and processed in the oil and gas industries to meet the global energy demand. However, in the current situation, a major challenge is to fulfil these demands while preserving environmental stability and simultaneously enhancing refining margins (Dwivedi et al., 2017b). On the flip side, industries must priorities infrastructure integrity, process safety, and personnel safety as crucial challenges that require attention. The material of construction used in oil industries and construction of ships is subjected to significant stress (Lee et al., 2004). Thus, it is crucial for industries to take into account all these issues when selecting metals for use.

Carbon steels are widely used in prioritize industrial applications, including the oil and gas industries and ship construction. Despite the wide range of metals and alloys available, such as stainless steel, aluminum, and copper, carbon steels are the preferred choice for engineering construction (Yin et al., 2009). Carbon steels are widely used in various industries due to their affordability and numerous benefits in terms of mechanical, electrical, and thermal properties (Clover et al., 2005a). They are considered to be the go-to material for construction purposes. For example, in industry, these materials are widely utilized in infrastructure fabrication for drilling, processing, and transportation. They are used in operating columns, reactors, tubes, sheets, pipelines, and more.

Carbon steel is an iron-carbon alloy that typically contains a maximum of 1.5 - 2% carbon (Prasad et al., 2020). When the carbon concentration is increased, the material strength is also enhanced, resulting in improved resistance against corrosion (Dwivedi et al., 2017a). The increase in carbon concentration contributes to enhanced material strength through mechanisms like carbide formation, solid solution strengthening, and grain structure refinement (Clover et al., 2005b; Dwivedi et al., 2017a; López et al., 2003; Ma et al., 2009a). These improvements in mechanical properties also indirectly boost corrosion resistance by limiting deformation and maintaining surface integrity. Additionally, in certain alloys, carbon improves the stability and protective nature of passive oxide layers, further enhancing resistance to corrosive environments (Clover et al., 2005b; J. Wang et al., 2018; Yan et al., 2021). However, the precise effects depend on the material composition, heat treatment, and intended application. Carbon is the main secondary component of this alloy, as the name suggests. It plays a role as an impurity within the body-centered cubic (BCC) crystalline structure of iron, resulting in an enhancement of the material's hardness. In addition, it slows down the movement of dislocations and enhances the physical and mechanical properties of carbon steel, resulting in excellent ductility, strength, and hardness (Ma et al., 2009c). This

enables the material to undergo multiple cold forming operations. Nevertheless, its corrosion resistance is somewhat limited, likely due to the unevenness of the surfaces. This makes it prone to corrosion, particularly in industries like oil and gas, or when stable protective films cannot form on the surfaces.

Carbon steel can be classified into four categories based on the carbon content in the alloy. Steels with lower carbon content have a softer and more malleable nature, while steels with higher carbon content are harder and stronger, but less flexible. Additionally, higher carbon steels pose challenges in terms of machining and welding. The following are the characteristics of carbon steel grades:

Low Carbon Steel: The composition consists of carbon ranging from 0.05% to 0.25% and manganese content of up to 0.4%. Commonly referred to as mild steel, this material is inexpensive and highly malleable. Although carburizing does not make the steel as hard as higher-carbon steels, it can enhance its surface hardness.

Medium Carbon Steel: The composition consists of carbon ranging from 0.25 % to 0.6 % and manganese up to 0.4%. Commonly referred to as mild steel, it is an inexpensive material that is highly malleable. Although not as difficult as higher-carbon steels, carburizing can enhance its surface hardness.

High Carbon Steel: The composition consists of carbon ranging from 0.55% to 0.95%, along with manganese ranging from 0.30% to 0.90%. It possesses high strength and exhibits excellent shape memory, rendering it well-suited for applications such as springs and wire.

Very High Carbon Steel: Consists of carbon ranging from 0.96% to 2.1%. The material's high carbon content contributes to its exceptional strength. Special precautions must be taken when handling this grade due to its brittleness.

1.3 Ruthenium

Ruthenium (Ru) as a barrier/interconnect material is of great interest among microelectronics fabrication industries. The role of barrier material is to prevent the diffusion of the interconnect metal (Cu) to dielectric material (SiO_2) (Hazarika et al., 2023a). In order to accommodate the shrinking feature size of integrated circuits (ICs) to 10 nm or below, there is a requirement for a novel barrier material that is ultra-thin, possesses lower resistivity, and exhibits superior performance compared to the conventional barrier layer, tantalum (Ta) (Du et al., 2017). Ru exhibits exceptional electrical characteristics, including superior conductivity, elevated breakdown voltage, and minimal leakage current. Ru metal has garnered a lot of interest and has been considered as the most ensuring barrier liner. In addition, the chemically stable transition metal Ru has a high melting point (2250 ºC) and lower electrical resistivity (7.1 μΩ cm) (Xu et al., 2022). Thus, employing Ru as an interconnect is also being explored in lower technology nodes as it eliminates the requirement for a barrier layer and reducing the device's line volume.

Chemical mechanical planarization (CMP) is a crucial process for achieving effective planarization of metal surfaces at both the local and global levels using a chemical slurry consists of various additives. Protecting the barrier metal in CMP process from corrosion is regarded as a highly critical component. The slurry, which plays a vital role in the CMP system, combines chemical corrosion and mechanical abrasion mechanisms in a synergistic manner to efficiently achieve material removal while also maintaining a desirable surface quality (Jiang et al., 2014a).

In this present study, we are focusing on controlling the corrosion of carbon steel and ruthenium metal.

1.4 Corrosion control strategies

Corrosion control strategies that are widely employed encompass the proper materials selection, the use of cathodic protection, coating, and corrosion inhibitors **(Figure 1.2)**. These techniques have proven to be effective in mitigating the detrimental effects of corrosion on these infrastructure components.

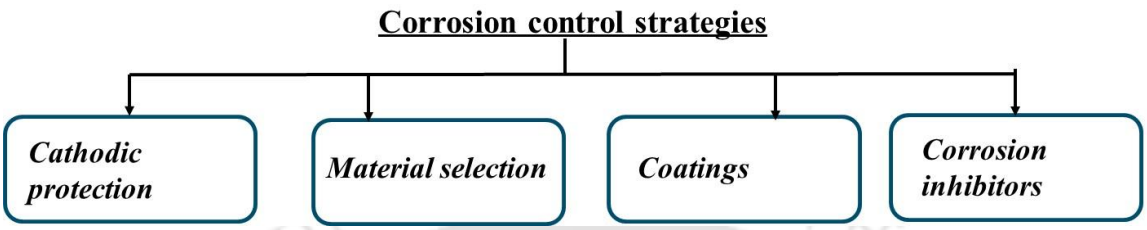

Figure 1.2 Corrosion control strategies

The following are the four most common methods for the prevention of corrosion:

Material selection: The objective of prevention through material selection and design is to eliminate the primary causes of corrosion. This can involve the utilization of metals that are less prone to chemical reactions compared to carbon steel, such as stainless steel or platinum. Alternatively, it can be achieved by strategically avoiding areas that are susceptible to corrosion during the initial design process. While no metal is entirely impervious to corrosion, certain metals possess a greater ability to withstand the process for an extended period of time. Furthermore, it is impractical for any developing country or industry to choose a metal with lower reactivity. Undoubtedly, price becomes a paramount consideration when evaluating this approach, alongside the mechanical properties of the chosen metals, which serve as a primary selection criterion.

Advantages:

1. Provide superior protection against rust and other forms of corrosion. This means that these materials can extend the life expectancy of any structure or object significantly, as it will be protected from the effects of corrosive environments such as saltwater or industrial pollutants.

Disadvantages:

1. It can be significantly more expensive than traditional metals. In some cases, this additional cost may outweigh the benefits provided by these materials; if you don't need superior protection against rust and corrosion, then it may not make sense to invest in more expensive options.

Cathodic protection: Cathodic protection is one of the methods used for preventing corrosion, which relies on the principles of anodic and cathodic behavior in galvanic systems. The identical electrochemical mechanisms observed in a galvanic cell are utilized to safeguard a particular metal substrate. Corrosion of the more reactive metal usually takes place when two different metals are in electrical contact with each other and are exposed to a conductive electrolyte. The process is analogous to that of a typical galvanic cell, where the more reactive metal undergoes corrosion, resulting in the release of metal ions and the generation of electrons, while the less reactive (more noble) metal is safeguarded as the cathode. For instance, when zinc and carbon steel are connected, zinc will undergo corrosion. Conversely, when carbon steel and copper are connected, the carbon steel will undergo corrosion. This behavior can be attributed to the position of carbon steel in the galvanic series relative to zinc and copper. Cathodic protection devices incur significant costs and impose financial burdens on a site's budgets when they require periodic replacement. Schematic illustration of a galvanic cathodic protection system depicted in the **Figure 1.3**.

Advantages:

1. No need for the frequent maintenance.

2. Convenient, simple and easy to install.

3. Effectively provide uniform current distribution.

Disadvantages:

1. It has short lifetime and limited capacity.

2. It has lower driving voltage/current.

3. It is more expensive and difficult to replace the spent anode.

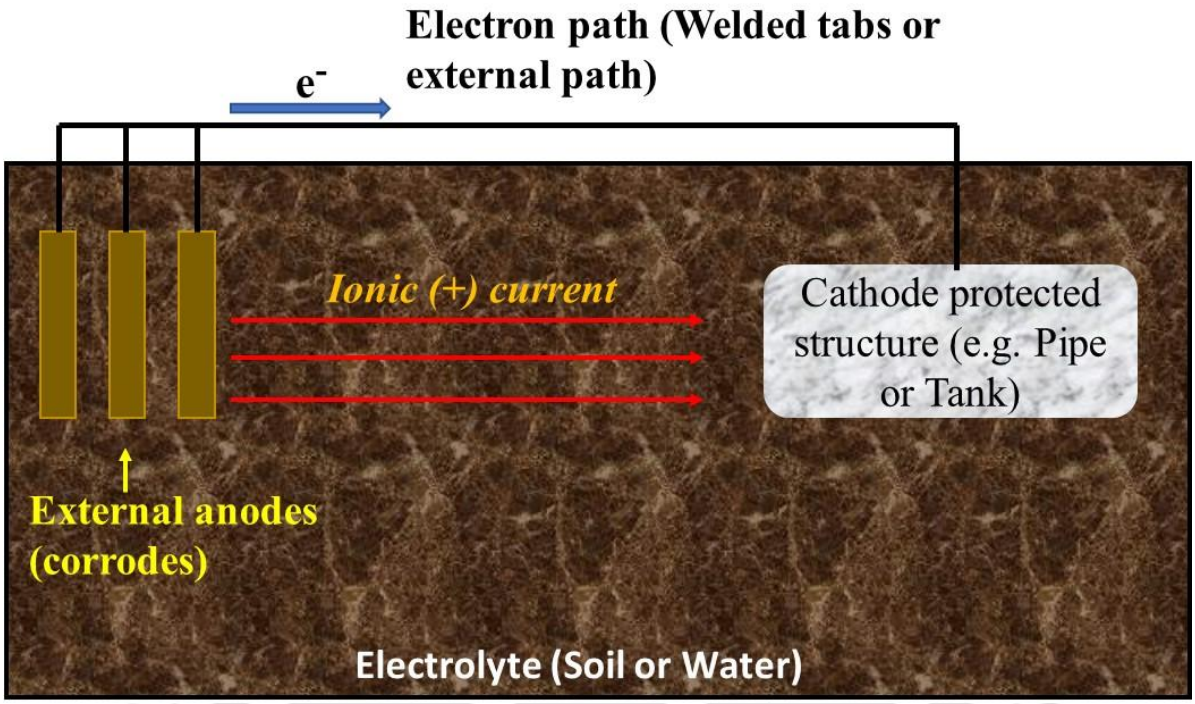

Figure 1.3 Schematic illustration of a galvanic cathodic protection system

Coatings: Coatings are frequently employed as a prevalent method to safeguard metals against corrosion. They create a barrier that separates the metal from its surrounding environment. Applying an organic coating to the outer layer of a reactive metal is an intelligent approach to prevent corrosion while simultaneously achieving additional surface properties without compromising mechanical attributes. They are the predominant method for safeguarding metal surfaces against corrosion, particularly in the fields of transportation, pipelines, marine industry, and infrastructure.

Advantages:

1. It is more cost-effective and non-hazardous.

2. Maintenance and replacement of the coating is not difficult.

3. It can protect all the metallic surface.

4. It can work at very low temperature also.

Disadvantages:

1. The most common cause for premature anti-corrosion coating failure is insufficient care during the mixing, application and curing processes.

2. Inadequate surface preparation results in poor adhesion to the substrate. This includes blistering, peeling and inter-coat delamination.

3. At very high temperature coatings are not working.

Corrosion inhibitors: Corrosion inhibitors are chemical compounds that, in small amounts, improve the ability of an electrochemical system to withstand corrosion or decrease the corrosive nature of the surrounding environment. Inhibitors are an economical strategy for mitigating corrosion, widely employed in various industrial applications such as refining and crude oil extraction, water treatment, and manufacturing processes involving solution baths and transport.

Disadvantages:

1. Negative impact on the taste and odor of water.

2. It can be harmful to aquatic life.

Advantages:

1. Provide corrosion inhibition in many types of closed recirculation systems.

2. Protect against cavitation and erosion.

3. Cost-effective, easy application and use.

The use of corrosion inhibiter techniques has been widely regarded by the industry as a cost-effective and efficient approach to address the issue of internal corrosion (Q.H. Zhang et al., 2020). The commercial market for corrosion inhibitors, which was valued at approximately $2.5 billion in 2017 solely in the United States, has fostered a competitive environment that encourages the exploration and development of novel and enhanced formulations with improved efficiency.

Among the various control strategies available, in this work the focuses will primarily on explor anti-corrosive coatings and corrosion inhibiter techniques for corrosion control.

1.4.1 Anti-corrosive coating

Anticorrosive coatings have been widely recognized as an effective and commonly employed method for protecting the metal structures from the detrimental effects of corrosion. While significant advancements have been made in achieving exceptional performance in terms of adhesion, mechanical properties, and durability for these materials, it is important to acknowledge that the products are subjected to a range of mechanical, chemical, and thermal stresses during their service life. These external factors can result in the development of microcracks and ultimately lead to premature failure of the coating system. The maintenance and repair of damaged coatings on large steel structures, such as offshore oil rigs and sea ships, is widely recognized as a costly endeavor within the industrial sector (Chen et al., 2023). The costs associated with structural failures are significantly elevated, encompassing not only financial implications but also environmental contamination and, in certain instances, even human casualties (Sørensen et al., 2009b). Various anticorrosive coatings are commercially available for numerous applications. Different types of anticorrosive coatings as follows:

Self-healing organic coatings: The ability of coatings to undergo self-healing is a desirable characteristic of corrosion inhibitor compounds. These coatings are created by adding active inhibitory chemicals to polymer coatings using a technique that involves gradually releasing inhibitors from damaged coating. In order to maintain its mechanical properties and prevent corrosion, the polymer matrix undergoes an intelligent healing process when damage occurs. The functionality of the self-healing coatings is determined by their chemical composition.

Anti-fouling organic coatings: Marine biofouling incurs significant financial losses for the maritime industry and gives rise to numerous problems. Consequently, there is a significant demand for environmentally-friendly antifouling technology. Antifouling coating is a traditional technique used to prevent the attachment of marine biomass or organisms to surfaces. Antifouling occurs as a result of a chemical reaction between a fluid and the surface of a component. This coating is especially crucial for protecting alloys and metals from corrosion caused by microorganisms in water environments. It stimulates the growth of living organisms, leading to an increase in the amount of coating, a decrease in the efficiency of movement through water and machine usage, reduced speed and maneuverability, higher energy consumption, the spread of biological entities between different surfaces, and ultimately causing damage to ship coatings. To prevent the attachment or formation of a biofilm or fouling, an antifouling coating can be applied to the top surface.

Self-cleaning organic coatings: The three categories of self-cleaning coatings are hydrophilic, hydrophobic, and super hydrophobic. A hydrophilic coating induces water to disperse across the surfaces, effectively transporting dirt and other impurities away. The self-cleaning activity is determined by the surface contact angle between the liquid drop and the solid material. Water's surface behavior and the prevention of surface flaws or imperfections that could lead to coating peeling are crucial factors to consider when applying these coatings effectively. The

wettability and water contact angle of a solid coated surface are affected by its geometric structure, chemical composition, roughness, and energy. The process of producing self-cleaning coatings with biocidal properties involves the combination of nano-Ag and nano-TiO_2 within the paint layer.

Painting: For the initial step of painting, it is necessary to select an alkali-resistant primer. This primer can be made of various materials such as polyvinyl butyral, vinyl epoxy, acrylic, baked phenolic, or polyurethane. Pigments such as chromate and titanium dioxide have been employed to enhance the ability of materials to resist corrosion. Painting method is the most straightforward and adaptable approach to applying a coating. This technique is suitable for the application of solvent-free compounds, such as two-pack commodities, which can be mixed directly at the nozzle of the spray gun during the application process. To achieve optimal results, it is necessary to utilize expensive equipment and employ highly skilled labor.

Powder coating: Powder coating is a type of coating that consists of solid particles. It is applied in a dry powder form and then subjected to heat in order to create a solid film. The process involves the utilization of a solid binder and the application of pigment. Upon heating, the solid binder undergoes a phase change and liquefies, thereby establishing a chemical bond with the pigment. Subsequently, upon cooling, the binder solidifies, resulting in the formation of a protective coating around the pigment. In recent years, there has been a growing popularity of powder coatings, and the demand for functional powder coatings has also been steadily rising. The most prevalent techniques for powder coating are electrostatic powder spraying, flame spraying of thermoplastic powders, and fluidized bed spraying.

Sol–gel coating: The gelation of the colloidal suspension results in the formation of a solid phase. The substance can undergo a drying process to transform into a state of dry gel. This dry gel can be used to remove any unreacted organic byproducts, stabilize the gel, increase its

density, or introduce crystallinity. Here are several advantages of using sol-gel coatings: The processing temperature is maintained at a low level, typically close to ambient temperature. Utilizing liquid precursors enables the formation of coatings on intricate shapes and the production of thin films without the need for machining or melting. Nevertheless, mechanical deposition methods such as dipping, spin-coating, and spraying are constrained by a small maximum thickness, which represents a significant drawback of sol-gel technology.

Inhibitive coatings: In contrast to impermeable coatings, inhibitive coatings counteract corrosion by chemically reacting with the environment to create a protective layer on the metal surface. The study of the inhibitory efficacy of corrosion inhibitor coatings primarily focuses on the direct use of chemical substances as inhibitors, rather than simply adding them as paint additives. When the coating contains corrosion resistant pigments or chemical compounds that impede chemical or electrochemical metal corrosion, this mechanism is triggered. An active protection system utilizes a leaching mechanism. This process involves the release of the inhibitor from the coating and its movement towards areas where corrosion occurs, resulting in the protection of the substrate in the defective coating area. Most inhibitory pigments are water-soluble inorganic salts. Due to their limited solubility, pigments can only be gradually released if there are imperfections in the coating. These materials are primarily utilized in industrial sectors with a significant likelihood of atmospheric corrosion, and they are not intended for immersion in water or burial in soil. This coating is typically employed as a primer due to its effectiveness in preventing the reaction between soluble components and the metal.

1.4.2 Epoxy-based coating

Epoxy resins are classified as a distinct category of pre-polymers or polymers that exhibit a high reactivity due to the presence of epoxide groups within their molecular structures (Chen et al., 2023; Sørensen et al., 2009b). The term "epoxy" encompasses all final products, whether

in their basic or cured form, that are derived from epoxy resins. Epoxy resins possess the ability to engage in catalytic homo-polymerization, resulting in the formation of cross-linked macromolecular compounds. Alternatively, they can also participate in reactions with a diverse range of co-reactants. These co-reactants include polyfunctional aliphatic and aromatic amines, acid derivatives such as acid chlorides, amides, esters, and anhydrides, as well as aliphatic and aromatic alcohols and thiols, commonly referred to as mercaptans (Mestry and Mhaske, 2019a). The co-reactants referred to in this context are commonly known as *curatives or hardeners*. The chemical process of cross-linking, which occurs between these co-reactants, is frequently referred to as *curing*. The curing process of epoxides typically results in a significant increase in brittleness due to the formation of a highly interconnected network of cross-linked polymer chains. The curing process of epoxy resins leads to the creation of thermosetting polymers characterized by their remarkable mechanical strength and exceptional thermal and chemical stability (S. Wang et al., 2019a). The precise customization of epoxy resins for specific applications can be achieved through the meticulous selection of appropriate resin, cross-linking agent, and modifiers. Epoxy resins are known for their extensive range of applications, encompassing various fields such as surface coatings for metallic materials, electric insulation, fiber reinforced plastic materials, paintbrush manufacturing, electrical components and LEDs, as well as adhesive formulations (Saxena et al., 2011a).

Epoxy resins possess a multitude of intriguing properties, as outlined below:

(1) A diverse array of options can be achieved by carefully choosing the appropriate resin, curing agents, and modifying agents. This allows for the creation of a broad spectrum of epoxy resins, ranging from low viscosity liquids to high melting point solids.

(2) Epoxy resins can be cured over a broad temperature range of 0 °C to 180 °C by carefully selecting the appropriate curing agents.

(3) Epoxy resins exhibit strong adhesion capabilities to different substrates, particularly metallic surfaces, owing to their high surface functionalities, including the presence of peripheral hydroxyl (-OH) groups and ether (-O-) bonds.

(4) Epoxy-based polymers exhibit minimal shrinkage, which sets them apart from the majority of thermosetting polymers. Epoxy resins typically exhibit a shrinkage rate of less than 2%.

(5) The mechanical properties of cured epoxy resins, when combined with themselves and co-reactants, exhibit exceptional strength, rendering them highly suitable for a wide range of industrial applications.

(6) The cured epoxy resins exhibit exceptional electrical properties, serving as highly effective insulators with good resistance to arcs and surface leakage across a broad temperature range.

(7) The cured epoxy resins exhibit exceptional chemical stability in both acidic and basic environments. The exceptional chemical stability of epoxy resins is due to their cross-linking, which prevents the infiltration of solvent molecules or other reactive substances.

(8) Dimensional stability refers to the ability of cured epoxy resins to maintain their shape and size over time, demonstrating exceptional durability.

(9) The cured epoxy resins exhibit excellent microbial resistance, particularly in terms of protection against fungal attack.

In addition to the mentioned traits, epoxy resins are highly compressible substances with exceptional resistance to corrosion, high tensile strength, durability against physical damage, and superior fatigue resistance. Furthermore, to enhance the resistance to corrosion and prolong the lifespan of the epoxy-based coating, *multiple fillers* were employed. In this decade, researches are focusing to improve the effectiveness and services life of the epoxy coatings. Hence, numerous *carbon-based fillers* were used in the epoxy coating.

1.4.3 Fillers for epoxy coatings

There are various types of fillers, including carbon-based, metallic, polymer-based, ceramic, mineral silicates, and lubricant fillers. These fillers have the potential to strengthen the epoxy matrix when used alone or in various combinations. When multiple types of nano-fillers are combined, the resulting system is commonly known as a hybrid system. Hybrid systems have been found to possess the optimal characteristics of different fillers when combined in carefully determined compositions, as determined through a series of iterative experiments. Through the incorporation of various nano-fillers, there has been a notable enhancement in the tribological properties, specifically in reducing the coefficient of friction and minimizing wear between sliding interfaces (S. Wang et al., 2019a). This improvement can be observed whether the nano-fillers are used independently or in combination with other materials. In the following sections, we will explore how these reinforcements contribute to enhancing the properties of epoxy coating systems.

In the recent years, researchers are working on carbon-based fillers. *Graphene oxide (GO)* is one of the most popular fillers for the epoxy coating. The phenomenon of graphene oxidation has garnered significant attention in recent times, primarily driven by the potential utilization of *GO* as a means to achieve cost-effective synthesis of substantial quantities of *graphene* (Li et al., 2020) .

The predominant approach employed for the production of *GO* involves utilizing the Improved Hummers method (Marcano et al., 2010a). This method relies on subjecting natural graphite to oxidation treatment, resulting in the creation of an uneven distribution of oxygen functional groups on the graphene sheets (Li et al., 2020). The aforementioned intriguing groups offer a means to facilitate subsequent surface chemical functionalization through the utilization of well-established carbon chemistry techniques. The available empirical data indicates that *GO* sheets possess epoxy, hydroxyl, and carboxyl functional groups (Shen et al., 2022). The

dispersion and exfoliation of *GO* in epoxy matrices have been observed to occur effectively even at significantly low filler concentrations.

Nevertheless, it is worth noting that *GO* exhibits a notable inclination towards forming substantial aggregations when subjected to relatively high loading. This behavior can be attributed to factors such as its high surface area, Van der Waals' interaction, and the utilization of vacuum filtration during the preparation process (Das et al., 2020a). Consequently, it is observed that the anticipated properties of *GO* in polymer matrices may not be entirely realized. The aggregated *GO* sheets undergo a transformation, resulting in the manifestation of coating defects. These defects subsequently contribute to a deterioration in the overall anticorrosion performance. Consequently, a considerable amount of research has been dedicated to addressing the complex issue of dispersing *GO* in epoxy coatings. This predicament can be effectively tackled through two distinct approaches, namely covalent and non-covalent modifications of *GO* sheets (Mestry and Mhaske, 2019a). Furthermore, it is worth noting that mechanical damages to coatings commonly occur, resulting in the detrimental disruption of their passive barrier effect. However, the prospective applications of graphene are hindered by its poor dispersibility in solvents and epoxy matrices. Various methods have been developed throughout the years to improve graphene dispersibility and polymer compatibility.

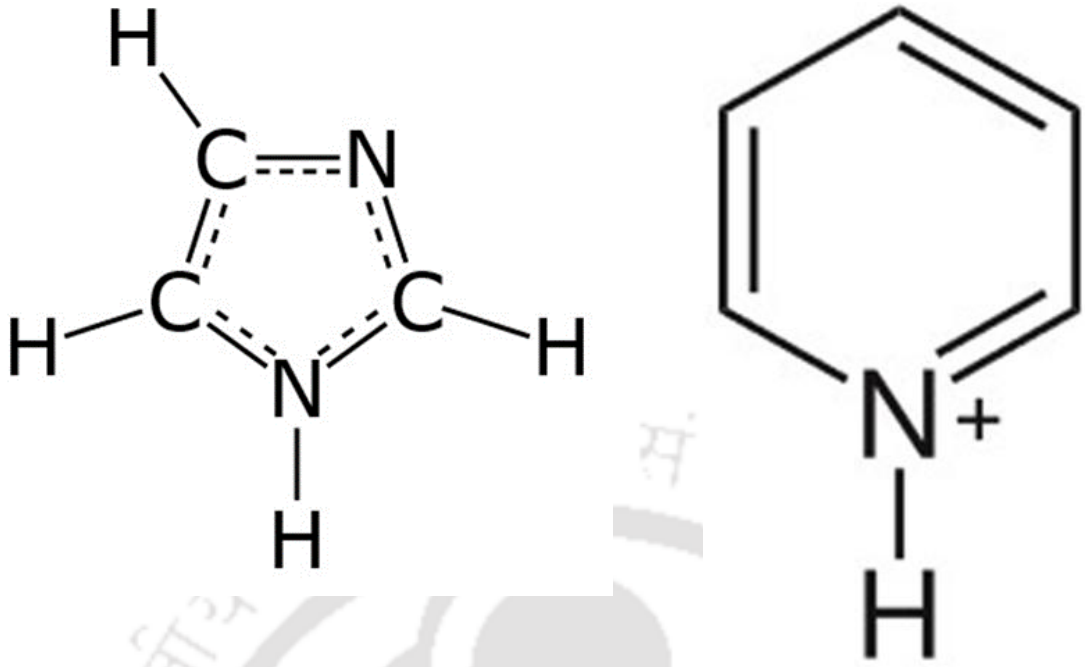

(a) **(b)**

Figure 1.4 Structure of (a) imidazolium [$C_3N_2H_4$] and (b) pyridinium [$C_5H_5NH]^+$

Over the past few decades, there has been a strong focus on advancing research in ionic liquids (ILs) with an emphasis on promoting environmentally friendly and sustainable chemistry. ILs is an organic salt based on imidazolium, pyridinium, ammonium, and phosphonium cations combined with organic or inorganic anions(Singh and Savoy, 2020). The structure of imidazolium and pyridinium are presented in **Figure 1.4**. They have low volatility, toxicity, and high thermal stability, which enhance their utility as green materials used for different environmentally friendly applications (Udunwa et al., 2022). Due to their outstanding solubility, the use of IL to develop functional hybrid nanomaterials has been a focus for researchers (Fallah et al., 2021). The field of research has seen significant growth, showcasing the immense value of ILs in various scientific disciplines such as chemistry, biology, and physics. In recent years, ILs have gained recognition as an environmentally friendly option for solvents and catalysts, offering a viable alternative to traditional volatile organic solvents (Wu et al., 2020a). In addition, ILs are showing great potential in various fields such as synthesis,

catalysis, cell biology, material science, physical chemistry, electrochemistry, genetics heredity, nuclear physics, medicinal chemistry, engineering, and more, both in industrial and laboratory settings (Kaur and Kumar, 2022). Considering their ongoing growth, it would be advantageous to explore ILs' physico-chemical properties and other significant characteristics (Singh and Savoy, 2020). The ionic liquid functionalized GO was evaluated for various other applications (supercapacitors, sensors, etc.,). In the present study, the IL modified GO is considered as a filler in the epoxy coating.

Carbon quantum dots (CQDs) are a fascinating type of carbon nanoparticles that were first discovered in 2004 while extracting single walled carbon nanotubes (Gong et al., 2017). These nanoparticles have a size range of less than 10 nm and exhibit distinct properties, including high biocompatibility, low toxicity, high solubility in water, and unique fluorescence. *CQDs* exhibit properties similar to those of graphene nanomaterials, with an amorphous structure (Zainal Abidin et al., 2020a). The unique properties of *CQDs* make them a suitable choice for various applications, including biosensing, bioimaging, and photocatalysis. The *CQDs* particles have adjustable fluorescence emission, excellent dispersibility and solubility in water, and are chemically inert. These carbon nanoparticles are composed of carbon atoms that are hybridized in both -sp2 and -sp3 configurations, enabling researchers to explore their adjustable properties (Wongso et al., 2021). Recently, a range of resources have been used as precursors to prepare CQDs, including glucose, citric acid, and chitosan (Astuti et al., 2022).

In the present work, CQDs were evaluated for the coating applications.

1.4.4 Corrosion inhibitors for chemical mechanical planarization (CMP)

A corrosion inhibitor refers to a combination of compounds that bestows protection to a metallic material when it is subjected to an environment that promotes corrosion. The use of corrosion inhibitors has been widely recognized by the industry as a highly cost-effective and efficient approach to combat corrosion (Ferraa et al., 2023). Despite notable advancements in

technology pertaining to corrosion inhibitors over the last few decades, the majority of inhibitors continue to be developed through empirical experimentation. This is primarily attributed to a limited comprehension of the underlying scientific principles that govern inhibition mechanisms. The inhibitory mechanisms of the subject under investigation have been broadly categorized as follows:

A) The inhibitor attaches to the metal surface through chemical or physical adsorption and creates a protective film that hinders the occurrence of anodic and cathodic reactions.

B) The inhibitor functions as an oxidizing agent and creates a defensive oxide layer on the underlying metal. This is applicable to metals that exhibit active-passive transitions.

C) The inhibitor functions as a ligand that binds to metal cations, resulting in the formation of insoluble chemical complexes on the surface of the metal.

In the present work, we were focus on the azoles-based inhibitor for the Ru chemical mechanical planarization application.

1.5 Analysis of corrosion

Corrosion is a process that involves electrochemical reactions involving oxidation and reduction. Electrochemical techniques such as open circuit potential (OCP), potentiodynamic polarization (PP), and electrochemical impedance spectroscopy (EIS) are used in order to observe and comprehend the electrochemical phenomena and corrosion mechanisms occurring in a metal immersed in a solution. Further, Quantum chemical (QC) calculation and Molecular dynamics (MD) simulation are also used to analyze the anticorrosion behavior. Finally, salt spray and pull-off adhesion are employed to check the effectiveness of coatings.

1.5.1 Open Circuit Potential

The open circuit potential (OCP), also known as the corrosion potential, equilibrium potential, or rest potential, serves as the primary starting point for a majority of electrochemical experiments. The OCP refers to the equilibrium state of the electrochemical potential that arises at the surface of the working electrode when exposed to a corrosive environment. This potential is measured relative to the reference electrode, providing valuable insights into the corrosion behavior of the system under investigation. OCP is observed when the cathodic reaction rates reach a state of equilibrium with the anodic reaction rates in the absence of any externally applied current or potential. This implies that the electron flow rate within the system is effectively zero. When the OCP demonstrates stability, it indicates that the material under investigation has achieved a state of equilibrium with the surrounding electrolyte. This milestone allows for the continuation of experiments on the specific system in question. **Figure 1.5** depicts a conventional OCP curve as a function of time. Carbon steel was used as the working electrode, while a 3.5 wt% NaCl solution served as the electrolyte to obtain the OCP plot at 25°C.

In order to comprehend the corrosion behavior of metals in a given solution, it is imperative to consider two fundamental parameters: the corrosion potential *(E_{corr})* and the corrosion current *(i_{corr})*. These parameters play a pivotal role in elucidating the mechanisms underlying the corrosion process. E_{corr} is the inherent ability of a metal or non-metal surface to release electrons when exposed to an electrolyte solution. i_{corr} is a corrosion current produced in an electrochemical cell while corrosion occurs. Electrochemical corrosion involves the transfer of electrons from the anode to the cathode. The concept of E_{corr} offers valuable insights into the corrosion condition of a metal, enabling researchers to evaluate its state. However, i_{corr} provides researchers with real-time data on the corrosion rate, allowing them to gain a more comprehensive understanding of the ongoing corrosion processes. At the OCP, the summation of the oxidation current *(I_{ox})* and reduction current *(I_{red})* (as described by equation 1.3) is found

to be zero. Consequently, it is not feasible to directly measure the corrosion current *(i_{corr})* under these circumstances. In order to obtain a comprehensive understanding of the corrosion rate, researchers commonly employ the measurement of the i_{corr} value through the technique of potentiodynamic polarization.

$$I_{summation} = I_{corr} = I_{ox} + I_{red} = 0 \qquad \textbf{1.3}$$

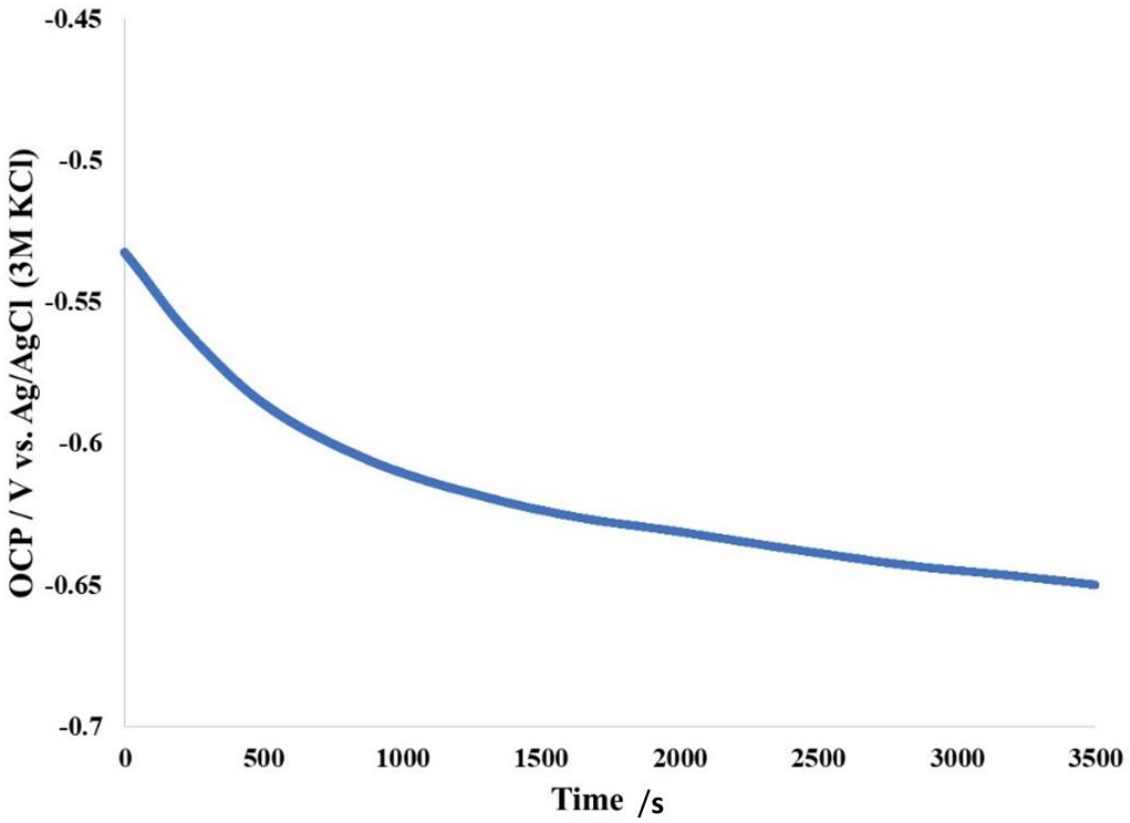

Figure 1.5 An OCP vs time representative curve

1.5.2 Potentiodynamic polarization

The utilization of the Potentiodynamic polarization (PP) technique proves to be highly advantageous in the estimation of corrosion rates and the examination of materials' susceptibility to corrosion. The PP technique is a method that entails the gradual alteration of the potential of a metal sample, specifically the working electrode, either in a positive or negative direction relative to the OCP. The polarization curve depicted in **Figure 1.6** illustrates the relationship between potential (V) and the logarithm of the absolute current (A/cm^2) with

respect to the exposed surface area of the electrode. This plot is obtained under steady state conditions. In order to facilitate the visualization of current density magnitudes, logarithmic values of the absolute current are utilized during the plotting process. The curved line depicted in **Figure 1.6** represents the cumulative sum of both cathodic and anodic currents at various potentials applied to the working electrode.

The designated point denoted as 'A' within the depicted diagram represents the corrosion potential, also known as the OCP. The portion of the curve relative to the OCP that exhibits a decrease in current is referred to as the cathodic polarization curve, indicating a prevalence of cathodic current. Conversely, the section of the curve relative to the OCP that demonstrates an increase in current is known as the anodic polarization curve, indicating a prevalence of anodic current. The determination of the E_{corr} and i_{corr} values of the system is achieved by identifying the point of intersection resulting from the extrapolation of the linear section of the cathodic and anodic curve, as depicted in **Figure 1.6**. The i_{corr} values are indicative of a corrosion rate. It is important to acknowledge that the measurement of current is typically carried out when PP is employed, while the measurement of voltage is conducted when galvanostatic polarization (PP) is performed.

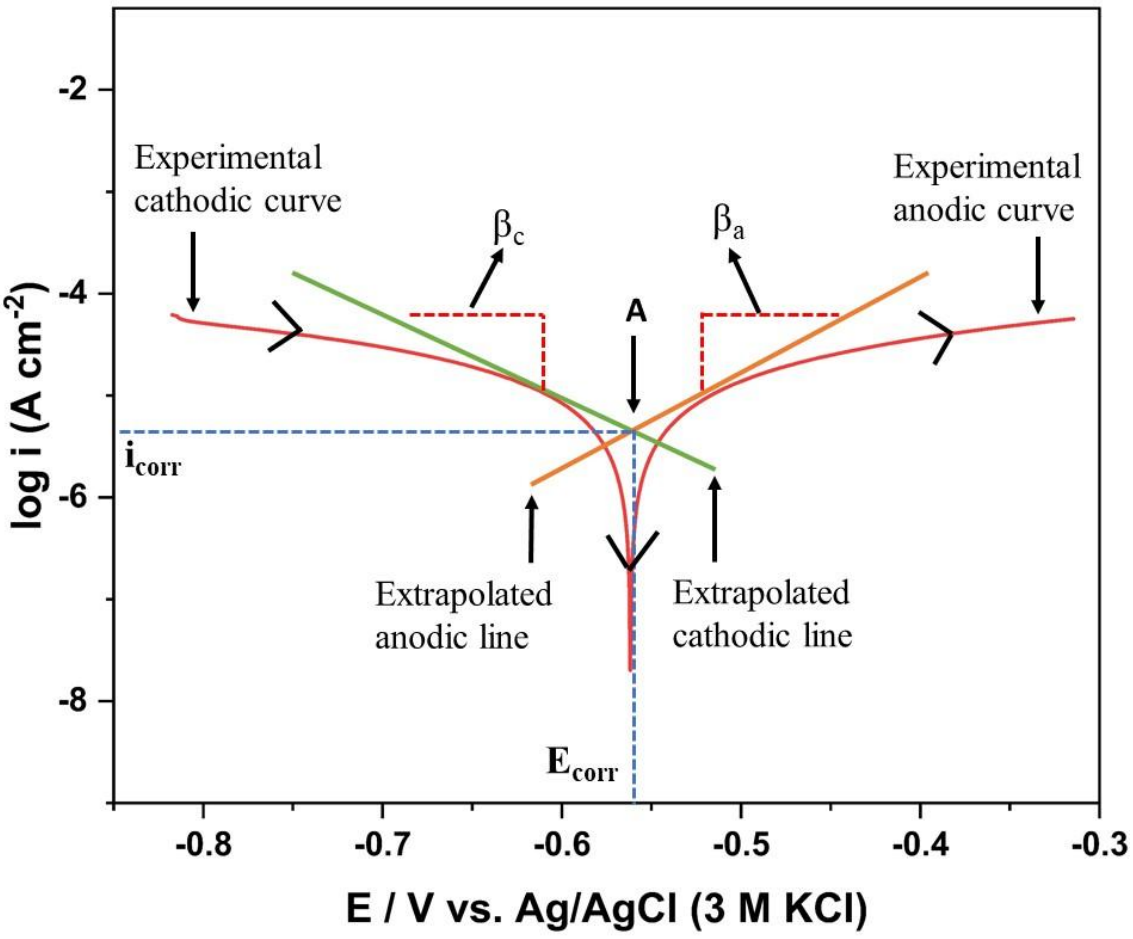

Figure 1.6 A polarization curve obtained from potentiodynamic polarization measurements

When the working electrode functions as an anode, anodic reactions (equation 1.4) take place as electrons are released and the potential shifts towards the positive direction. In this context, the anodic current is regarded as positive. Conversely, cathodic reactions take place when electrons adhere to the surface of the working electrode (equation 1.5). In this case, the overvoltage, defined as the discrepancy between the final potential and the equilibrium potential, is negative. In this case, the rate at which metal ions are formed is lower than the rate at which they are deposited.

$$\text{Metal} - ne^- \rightarrow \text{Metal}^{n+} \quad \textbf{(1.4)}$$

$$\text{Metal}^{n+} + ne^- \rightarrow \text{Metal} \quad \textbf{(1.5)}$$

In order to gain a more comprehensive conception of the oxidation and reduction processes, two models were proposed the Butler-Volmer equation and the Stern-Geary equation. These models assume that the anodic and cathodic reactions are regulated by the kinetics of electron transfer at the metal's surface.

Butler-Volmer equation:

Some of the approximations of Butler-Volmer equations are as follows: (a) potential deviates ± 10-25 mV w.r.t. E_{corr} or OCP, with the resulting curve being a straight line whose slope has a unit of resistance; (b) $\left(e^{\frac{2.303(E-E^0)}{\beta}} \right)$ of the Taylor equation is expanded neglecting second and higher order terms.

For anodic overpotential, the cathodic component becomes negligible and the Butler-Volmer equation reduction to the Tafel equation for anodic reaction as

$$I = I^0 \left(e^{\frac{2.303(E-E^0)}{\beta_a}} \right) \quad \textbf{(1.6)}$$

Similarly, for the high cathodic overpotential, Tafel equation for cathodic reaction is given by

$$I = I^0 \left(e^{\frac{2.303(E-E^0)}{\beta_c}} \right) \quad \textbf{(1.7)}$$

Where, i_{corr} (A) stands for corrosion current and β_a (V/decade of current) and β_c (V/decade of current) are the respective anodic and cathodic Tafel constant. ΔE which almost nears to E_{corr} is the applied potential difference whereas ΔI is its associated polarization current.

Stern-Geary equation:

Simplifying and rearranging the Butler-Volmer equations, the Stern-Geary equation (equations 1.8) is obtained.

$$I_{corr} = \frac{1}{R_p}\left(\frac{\beta_a \beta_c}{2.303(\beta_a + \beta_c)}\right) \quad \textbf{(1.8)}$$

Here,

$$R_p = \left(\frac{\Delta E}{\Delta I}\right)_{\Delta E \to 0} \quad \textbf{(1.9)}$$

Here, Polarization resistance, R_p (Ω) signifies the resistance against oxidation of the corroding species when a potential is applied. Lowers the corrosion rate, higher will be the R_p values and vice versa.

1.5.3 Electrochemical Impedance Spectroscopy (EIS)

At the interface between the working electrode and the electrolyte, various types of reactions take place, including electrochemical, diffusion, and adsorption-desorption processes. These reactions also occur within the bulk solution. EIS is a powerful technique that enables precise measurement of impedance, even at extremely low frequencies such as 1 mHz. This capability makes EIS a valuable tool for investigating various mechanisms. The data that can be derived from EIS encompasses various phenomena, including the adsorption, desorption, and diffusion of compounds, the formation of passive layers, the occurrence of faradic and non-faradic reactions, as well as the formation of electrical double layers. The technique known as impedance spectroscopy involves the application of a low-intensity, oscillating voltage signal disturbance in order to measure the reaction of the electrochemical system in term of resulting alternating current. The utilization of a perturbation in the form of a small amplitude AC signal is implemented in order to obtain a linear or pseudo-linear output response from the system (Lvovich and Smiechowski, 2006; Srinivasan and Fasmin, 2021). According to Ohm's Law, which is represented by the equation $E=IR$, it is understood that resistance refers to the inherent

ability of an element to withstand the passage of electric current. Nevertheless, it is important to note that impedance pertains to circuit elements that exhibit a higher degree of complexity and present a greater challenge in terms of comprehension when compared to resistance. Hence, in more concise terms, impedance can be defined as the frequency-dependent opposition to the flow of electric current in a complex circuit component, encompassing not only resistors but also capacitors, inductors, and other elements. It is worth noting that, in contrast to resistors, inductors and capacitors possess an imaginary component and exhibit frequency dependence. According to the works of Brett, and Faulkner (Brett, 1993; Faulkner, 2000), it is evident that these researchers have made significant contributions to the field of electrochemistry. Their studies have shed light on various aspects of this discipline, providing valuable insights and advancing our understanding of electrochemical processes. In EIS technique various circuit elements like capacitance (C) resistance (R) inductance (L) are measured by applying AC voltage in an electrochemical cell. When a DC voltage is applied, in any system, the voltage (V), resistance (R), and current (I) satisfy Ohm's law. Similarly, when an AC voltage is applied to an electrochemical cell, the impedance interrupts the current flow. This impedance ($\omega = 2\pi f$ is the angular frequency of the applied AC voltage) can be expressed as $Z(\omega) = V(\omega)/I(\omega)$, which is the equation for Ohm's law for an AC circuit. The disruptions are depicted by different components in a circuit, like resistors, inductors, and conductors, which make up the total impedance. In a real system, the electrochemical cell is comprised of a variety of circuit elements with different combinations. Therefore, it is more precise to utilize the notion of impedance rather than a resistance to depict an electrochemical system. When potential is applied with angular frequency *(ω)*, the response of current (I) shows a phase shift (ϕ).

The EIS data is represented either by Nyquist plot (real part of impedance data vs imaginary part of impedance data) or Bode plot {Bode modulus (impedance vs log of frequency) and

bode phase plot (phase shift vs log of frequency)}. It is to be noted that, although both plots give similar information, unlike Bode plot, Nyquist plot don't display the frequency at which the impedance data are being noted. Typical EIS plots {(a) Nyquist (b) Bode modulus (c) Bode phase plot} are illustrated in **Figure 1.7**.

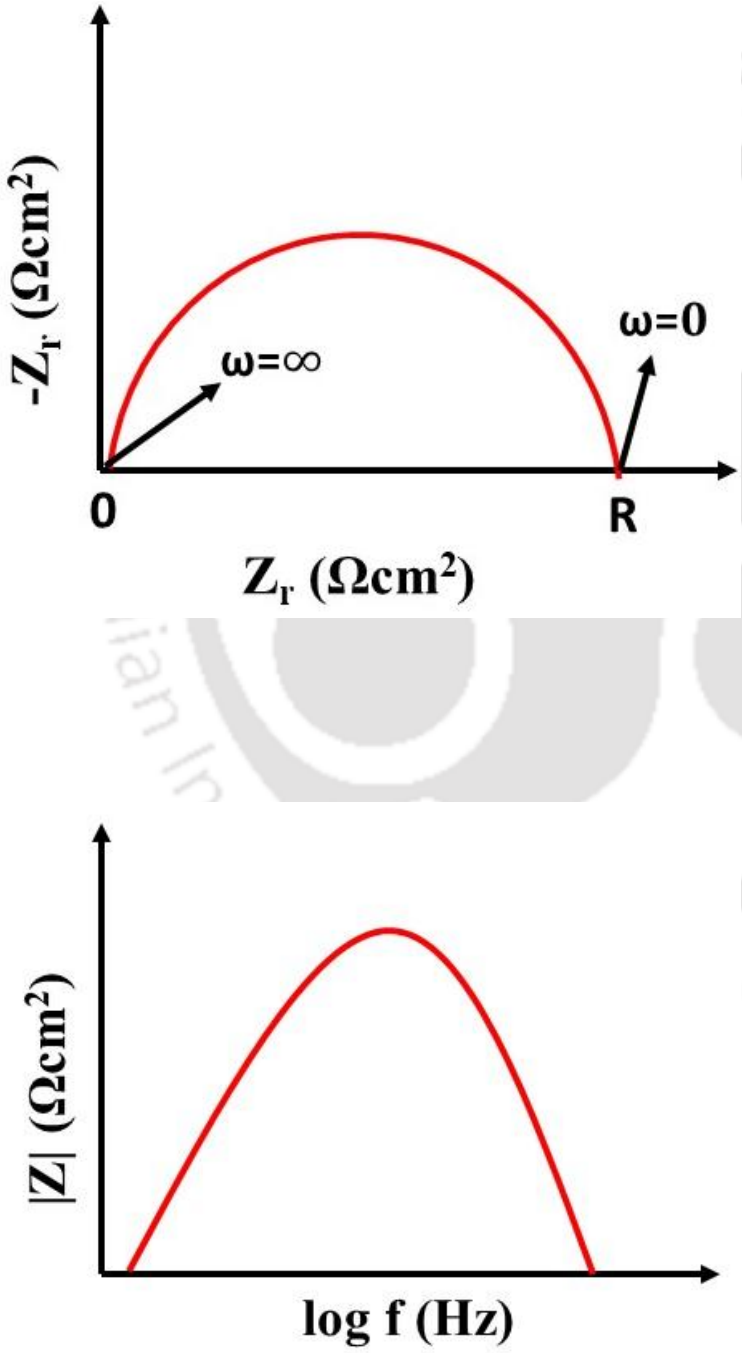

(c)

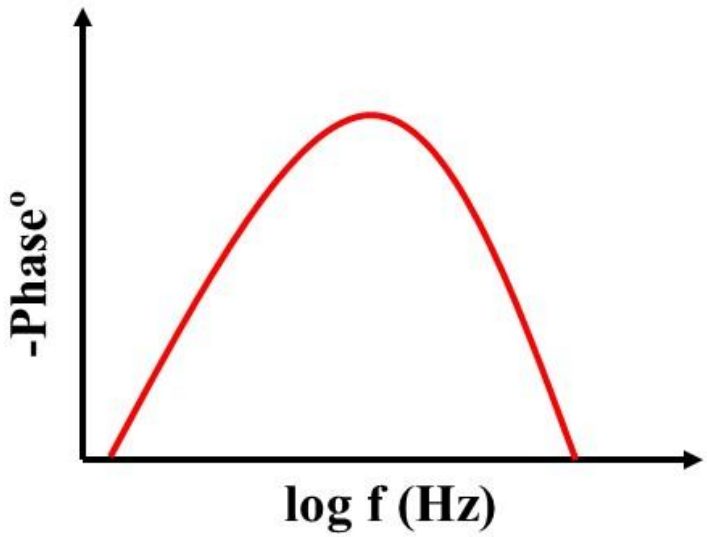

Figure 1.7 A standard EIS plot (a) Nyquist (b) Bode modulus (c) Bode phase

The constant phase element (CPE) is used instead of ideal capacitance *(C)* to account for non-ideal behaviour and its impedance is calculated as follows.

$$Z = \frac{(j\omega)^{-n}}{Y_0} \qquad \textbf{(1.10)}$$

$$C = Y_0(\omega_{max})^{n-1} \qquad \textbf{(1.11)}$$

Where ω_{max}, Y_0, *a*nd *j* denote the maximum angular frequency corresponds to the Z_{im}, CPE parameter, and imaginary root, respectively. When n = 1, the constant phase element (CPE) is treated as a pure capacitor while n = 0 is treated as a resistor. The non-ideal capacitance is characterized by 0<n<1 which arises due to the heterogeneities of the electrode surface (Meng Cheng et al 2021). Polarisation resistance *(Rp)* refers to the resistance encountered during a reaction when the frequency is reduced to zero and the perturbation amplitude is also reduced to zero. This resistance is observed at the lower end of the frequency spectrum and with small perturbations. The R_p is calculated using following equation.

$$Rp = R_1 + R_2 \qquad \textbf{(1.12)}$$

Where, R_1 and R_2 are the resistances associated with passive film formed by inhibitors on the metal/working electrode surface respectively

The inhibition efficiency *(IE %)* is estimated using the following equation.

$$\text{IE}\ (\%) = \frac{R_p - R_po}{R_p} \times 100 \qquad \textbf{(1.13)}$$

Where R_p and R_po refer to the polarization resistance in the presence and absence of an inhibitor.

1.5.4 Electrical Equivalent Circuit (EEC)

The physio chemical process occurring at the bulk solution and solution metal interface are evaluated from the impedance data using the EEC model. A typical circuit known as Randles circuit is displayed in **Figure 1.8**. For a given impedance data, the circuit elements of fitted EEC circuit could be in both series and parallel connection. Elements in series signifies, that similar current passes through all the elements whereas elements in parallel signifies that the current through each element sums up to the total current.

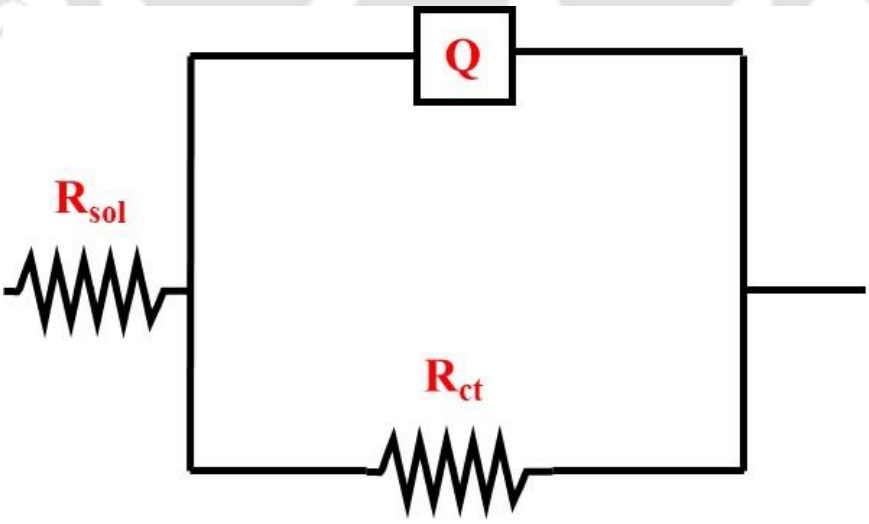

Figure 1.8 The Randles circuit

Here, R_{sol} signifies solution resistance, R_{ct} is the charge transfer resistance, and Q represents the capacitance. R_{ct} refers to the reaction resistance under conditions of infinite frequency and

zero amplitude AC perturbation, excluding the effects of double layer capacitance and solution resistance. In practical terms, it refers to a disturbance that occurs frequently and has a small magnitude. The presence of a small Q arc in the high-frequency region was observed to be unaffected by potential and is considered to represent the resistive/capacitive behavior associated with charge-transfer processes.

1.5.5 Adsorption isotherm

Understanding the basic principle of the adsorption process and the type of adsorption requires knowledge of the adsorption isotherms parameters. In order to understand the underlying interaction between the adsorbate (inhibitor) and the adsorbent (metallic surface), several adsorption isotherms as employed. Adsorption isotherms were inferred by fitting the surface coverage, which is estimated from the polarization curves, as a function of inhibitor concentration to understand the adsorption process.

The Langmuir isotherm is founded on the assumptions of a homogenous surface with identical adsorption sites, monolayer coverage, and no lateral interactions between adsorbed molecules.

The Langmuir isotherm, as computed in Eq. **1.14**, was found to have the best fit in all the concentrations, with linear regression coefficients (R^2) being close to 1(W. Li et al., 2022a; Xu et al., 2020).

$$\frac{C_{inh}}{\theta} = \frac{1}{K_{ads}} + C_{inh} \qquad (\mathbf{1.14})$$

Herein, θ is the surface coverage which is estimated from Eq. 1.14, C_{inh} is the concentration of inhibitor, and K_{ads} is the equilibrium constant of the adsorption process.

$$\theta = 1 - \frac{i_{corr}o}{i_{corr}} \qquad (\mathbf{1.15})$$

The plots of C versus C/θ that yield straight lines with an intercept of $1/K_{ads}$. The standard adsorption free energy (ΔG_{ads}) can be calculated as follows(Sun et al., 2021a).

$$K_{ads} = \frac{1}{55.5} \exp\left(-\frac{\Delta G_{ads}}{RT}\right) \qquad \textbf{(1.16)}$$

Where R (kJ/mol) and T (K) denote the molar gas constant and the absolute temperature respectively. A high value of K_{ads} and a low value of ΔG_{ads} (kJ/mol) often point to a stronger potential for the inhibitor to be adsorbed on the metal surface, demonstrating a higher level of inhibitive ability.

The Temkin isotherm introduces a correction for adsorbate-adsorbate interactions and assumes that the adsorption heat decreases linearly with increasing surface coverage due to these interactions.

$$\theta = f^{-1} \ln(K_{ads}) + f^{-1} \ln(C_{inh}) \qquad \textbf{(1.17)}$$

This model is more applicable to systems where the adsorbate exhibits moderate interactions, providing a realistic representation of heterogeneous adsorption behavior.

The Frumkin isotherm extends the Langmuir approach by incorporating the effects of lateral interactions between adsorbed molecules, either attractive or repulsive. It modifies the adsorption expression by introducing an exponential factor to account for these interactions.

$$\log[\theta/((1-\theta)C_{inh})] = \log(K_{ads}) + g\theta \qquad \textbf{(1.18)}$$

This model is particularly suitable for analyzing systems with significant adsorbate interactions or deviations from ideal monolayer adsorption. These isotherms provide distinct yet complementary insights into adsorption mechanisms, enabling a tailored understanding of the specific physicochemical characteristics of adsorption systems.

1.5.6 Theoretical studies for metal corrosion inhibition analysis

Quantum chemical (QC) calculation and Molecular dynamics (MD) simulation are highly effective in exploring the molecular-level mechanisms of corrosion inhibitors in reducing corrosion. Experimental approaches can provide values that reflect average properties, but they have limitations when it comes to obtaining detailed structural and dynamic information at atomic and molecular scales. Thanks to advancements in computer technology, researchers can now use computational techniques to study the mechanisms of corrosion inhibition. This allows them to explore the relationship between molecular structure and inhibition efficiency, and discover new types of corrosion inhibitors, all without relying on harmful chemicals or expensive lab equipment.

Adsorption energies and Fukui functions have been used to identify reactive sites within inhibitor molecules, predicting where interactions with the metal surface are likely to occur. By integrating QC calculations and MD simulations, comprehensive insights into corrosion inhibition can be achieved. For instance, QC can predict the electronic properties of a molecule, which can be further validated by MD to study its dynamic behavior on a metal surface. A combined study on amino acid-based inhibitors showed that the QC-predicted active sites of molecules formed strong bonds with iron atoms, which was corroborated by MD simulations demonstrating stable adsorption. Such studies enable the rational design of new, environmentally friendly, and efficient corrosion inhibitors.

1.5.7 Density functional calculation theory

Density functional calculation theory (DFT) is a highly effective quantum mechanical method for obtaining precise information about the structural and electronic properties of compounds. Several reactivity descriptors, both global and local, defined within the DFT framework, can be utilized to predict the potential mechanism and corrosion inhibition properties of an inhibitor (Kumar et al., 2024, 2018a). According to frontier molecular orbital (FMO) theory, the

chelation process of chemisorption can be analyzed by focusing on the Highest Occupied Molecular Orbital (HOMO) and Lowest Unoccupied Molecular Orbital (LUMO). These two molecular orbitals play a crucial role in determining the chemical reactivity descriptors of most chemical reactions (Kumar et al., 2024, 2018a). By examining the interaction between the inhibitor's *HOMO* and/or *LUMO* and the metal surface, we can calculate these descriptors. The most used DFT-based quantum mechanical molecular descriptors include the highest occupied molecular orbital energy *(E_{HOMO})*, lowest unoccupied molecular orbital energy *(E_{LUMO})*, energy band gap *($\Delta E = E_{LUMO} - E_{HOMO}$)*, ionization potential *(I)*, electron affinity *(A)*, global hardness (η), global softness (σ), absolute electrophilicity index (ω), global electronegativity (χ), and the number of electrons transferred (ΔN) (John and Joseph, 2013; Singh et al., 2018).

The E_{HOMO} value represents the ability of inhibitor molecules to donate electrons, while the E_{LUMO} value represents their ability to accept electrons. The higher the E_{HOMO} value, the stronger will be the electron-donating capability of the inhibitor, and therefore, better inhibition efficiency will be observed (Punathil Meethal et al., 2023a; Saha and Banerjee, 2015). Lower the value of E_{LUMO}, more it will be prone towards accepting electrons. The difference in energy between the *LUMO* and *HOMO* is a crucial factor that indicates the effectiveness of inhibitor molecules in preventing corrosion reactions (Mamand et al., 2023; Sujatha and Lavanya, 2023). Typically, when ΔE is smaller, the energy required to remove an electron from the last occupied orbit is lower, resulting in higher inhibition efficiency. In addition, *ΔE* serves as a measure of molecular stability, with a lower *ΔE* value indicating enhanced stability of the complex formed on the metal surface(Kokalj, 2021; Mamand et al., 2023).

According to Koopman's theorem, the inhibitor molecule's orbital energies for the *HOMO* and *LUMO* are connected to ionization potential *(I)* and electron affinity (*A)*. Likewise, the letter *I* and *A* are used to represent the molecule's electron donation and acceptance capabilities. *A* higher value indicates a greater ease for the corresponding process to take place. Increased

values of global softness *(σ)*, electronegativity *(χ),* and electrophilicity index *(ω)* or decreased values of global hardness *(η)* are indicative of stronger corrosion inhibition (Kumar et al., 2018b; Qadr and Mamand, 2021). These findings primarily rely on the behavior of inhibitor molecules in accepting and donating electrons, as well as Pearson's hard/soft acid/base principle. The ΔN value obtained through Pearson's calculation method indicates the capacity of electron donation. If *ΔN* is greater than 0, the inhibitor molecule transfers electrons to the metal. Conversely, if *ΔN* is less than 0, it retrieves electrons. In previous research conducted by Lukovit et al., (Gajalakshmi and Tamilmani, 2020), it was found that the effectiveness of corrosion inhibition increases as the value of *ΔN* increases, specifically when *ΔN* is less than 3.6. This correlation is attributed to the enhanced electron-donating capability of the metal surface (John and Joseph, 2013).

The identification of active sites for inhibitor molecules is crucial in understanding the mechanisms of corrosion inhibition. The Mulliken charge distribution is commonly employed to analyse the charge density distribution and to identify potential binding sites. The Mulliken charge distribution is a useful tool for identifying the active sites involved in the reaction between an inhibitor molecule and a metal surface (Oyeneyin et al., 2022). Typically, when the atomic charge of the adsorption sites is more negative, it becomes easier to donate electrons to nearby unoccupied orbitals. The Mulliken charge distribution is frequently used in conjunction with the *HOMO* energy density distribution to make predictions about the active site of the inhibitor molecule. In other words, a higher *HOMO* energy density and a more negative atomic charge indicate a greater likelihood of the adsorption site (Boughoues et al., 2020).

1.5.8 Adsorption energy calculation method

The use of computational methods for studies of metal corrosion inhibition has seen a steady increase. Additionally, conventional methods have proven to be inadequate in providing

significant insight into the interaction between metal surfaces and inhibitors. The effectiveness of corrosion inhibitors in preventing metallic corrosion is typically assessed through various experimental techniques, including the weight loss method, electrochemical impedance spectroscopy, and potentiodynamic polarization. These methods are effective for obtaining physical and electrochemical properties of the corrosion inhibitor, but they do involve the use of chemicals and can be time-consuming. Computational studies on metal corrosion inhibition using molecular dynamic (MD) simulation offer valuable insights into the mechanism and interaction between a metal surface and inhibitor molecules at a minimal cost. MD simulation was initially introduced in 1956 by Berni Alder. However, it wasn't until 2003 that Bartley et al. (Bartley et al., 2003) reported the use of MD simulation for metal corrosion inhibition application. In their study, they focused on copper corrosion inhibition using alkyl ester compounds (Bartley et al., 2003). Since then, the use of MD for simulating metal surface-inhibitor interaction has garnered significant attention from scientists and researchers worldwide and has made great strides in the field of corrosion science. MD simulations offer valuable insights into the adsorption behavior and orientation of corrosion inhibitors on metal–electrolyte interfaces. MD simulations involve using computer models to describe the movement of molecules over time, based on classical Newtonian mechanics (Haris et al., 2020a).

Monte Carlo (MC) simulations are a powerful tool for predicting condensed-phase and gas-phase properties across a wide range of chemical systems. They offer efficient and accurate predictions, making them invaluable for rapid simulations. In the simulations, the interaction between the inhibitor and metal surface is carried out in a specially designed simulation box, where the inhibitor directly contacts the metal surface. The simulation results include the arrangement of multiple layers of iron atoms and the optimized structures of the inhibitor. Moreover, there are many factors to be considered during the simulations, such as the

description of van der Waals interactions, the handling of electrostatic interactions, the selection of a temperature control system, the settings of the time step and total simulation time for implementation and the settings of the cut-off distance, spline width, and buffer width (Madkour et al., 2018; Verma et al., 2018a).

The adsorption of inhibitor molecules on metallic surfaces is an exothermic process that results in the evolution of energy in the form of heat. In MC simulations, the total energy (E_{total}) is defined as the sum of the energies of inhibitor molecules $(E_{inhibitor})$, rigid adsorption energy (E_{rigid}), and deformation energy (E_{def}). The adsorption energy is a crucial energy parameter when it comes to adsorption. It consists of two components: the energy of sorbate adsorption onto the surface in its initial conformation (referred to as rigid adsorption energy), and a slight energy change (known as deformation energy) caused by the sorbate's relaxation in the presence of the surface (Guo et al., 2021; Haris et al., 2020a). The adsorption energy refers to the energy that is released or required when the unrelaxed adsorbate components are adsorbed on the metal, before any geometry optimization is performed. The deformation energy refers to the energy that is released when the adsorbed adsorbate components undergo relaxation on the metal surface. The total energy encompasses both the adsorption energy and the internal energy of the sorbate. Under these conditions, the substrate energy (iron surface) is considered to be zero. The differential adsorption energy, also known as dE_{ad}/dN_i, refers to the energy required to remove a sorbate from a specific component (Gajalakshmi and Tamilmani, 2020).

1.5.9 Salt spray analysis

The salt spray (fog) test is widely used to analyse the anticorrosion properties of different coatings. This practice involves creating a controlled corrosive environment to gather information on the corrosion resistance of metal specimens and coated metals exposed in a specific test chamber. The edge of the coated steel plates was sealed using tape, and the samples

were then subjected to a salt spray test in a chamber at a temperature of 35 °C. The test involved continuous spraying of a 5 wt% NaCl solution. A salt spray test was conducted on the coating samples, which had varying filler loadings. To validate the impact, the resistance of different coatings against salt spray was tested and documented using digital images. The test is conducted in accordance with ASTM B117 standards.

1.5.10 Pull off adhesion test

The strength of the bond between the coating and the substrate plays a crucial role in assessing the effectiveness of corrosion protection provided by the coating. In addition, coatings that possess exceptional barrier properties are typically associated with strong adhesion. The pull-off tests involved applying a force at a 90° angle to a bonded substrate, while the sample remained securely in place, as shown in **Figure 1.9**. The tensile stress was measured by tracking the displacement of the stud. The force required to remove the coating from the substrate was then used to determine the adhesion force. The glued studs were left to dry for 48 hours at room temperature. Prior to conducting the pull-off test, the excess glue near the studs was carefully removed to prevent any potential impact on the adhesive behaviour of the samples. The reference point for zero displacement was established at the location where the recorded tensile stress measured 1 N. The stud was then moved upwards at a steady speed of 1 mm per minute until it was released. The pull-off adhesion test made in accordance with ASTM D4541 standard is used to assess the adhesion of various coatings applied to metal sample.

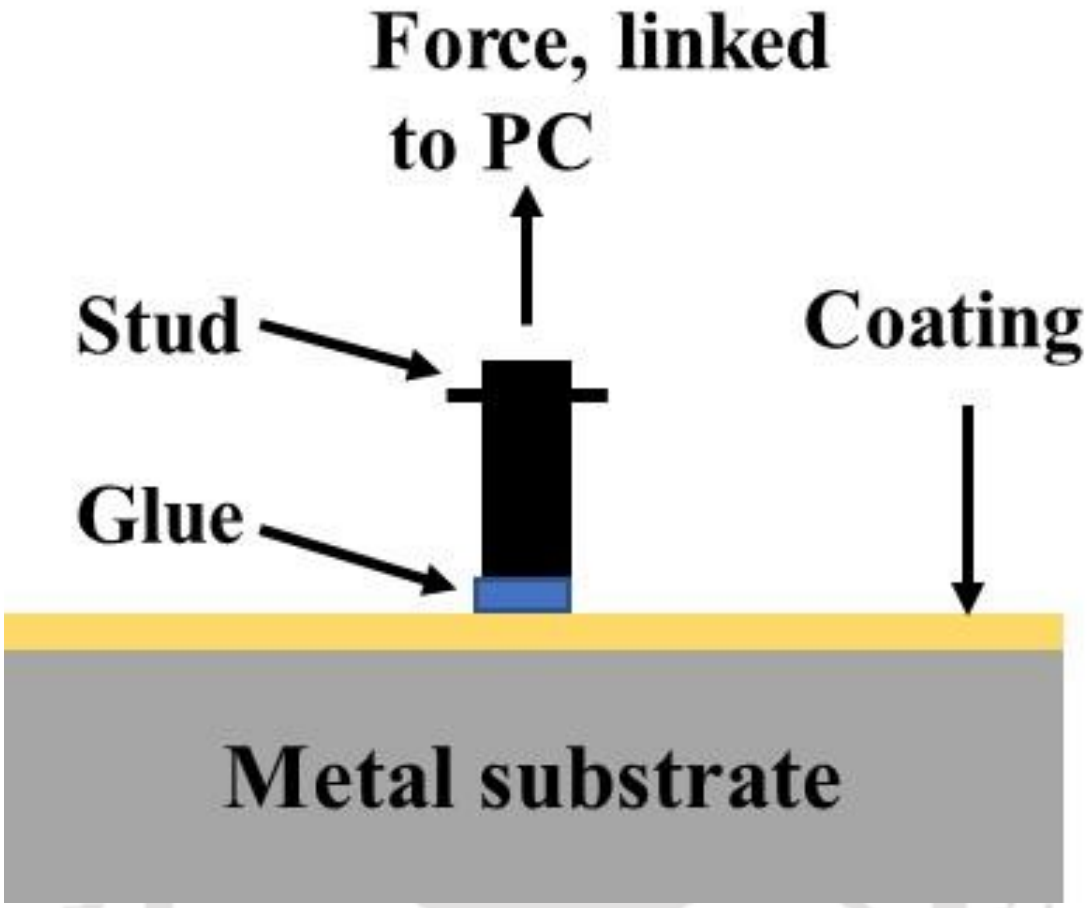

Figure 1.9 Schematic representation of the pull-off test

Among the different corrosion controlling strategies, we are focusing on anticorrosive coatings and corrosion inhibition techniques for the protection of carbon steel and Ru metal in the present study. In ***Chapter 2****, a substantial literature study is given.*

CHAPTER 2

LITERATURE REVIEW

In this section, the literature survey was carried out for the anti-corrosive coating for carbon steel and corrosion inhibitors to control the Ru dissolution.

2.1 Anticorrosive coating for carbon steel

The first commercial attempts to prepare resins from epichlorohydrin were made in 1927 in the United States. Credit for the first synthesis of bisphenol-A-based epoxy resins is shared by Dr. Pierre Castan of Switzerland and Dr. S.O. Greenlee of the United States in 1936. In the recent year, commercially bisphenol-A-based epoxy resins, polyurethanes, and waterborne resins are using for the protection of metal from corrosion. Bahram Ramezanzadeh et al (Ramezanzadeh et al., 2016), used bisphenol A diglycidyl ether (BADE) epoxy to protect the mild steel substrates in the 3.5 wt% NaCl solution. O. Dagdag et al (Dagdag et al., 2020), used BADE epoxy to protect the aluminium Alloy AA2024-T3. Rachid Hsissou et al 2021, used BADE epoxy to protect the carbon steel in 3.5% NaCl solution. The outcomes of the study suggested that the pure BADE epoxy coating is not effectively protect the metal in harsh corrosive environment. Hence, fillers are introducing to reinforce the epoxy matrix. The fillers are broadly classified into, carbon-based, metallic, polymer based, ceramic, mineral silicates and lubricant fillers. In the present study we are focusing on the carbon-based filler.

2.2 Graphene oxide

The Hummers method, modified Hummers method, and improved Hummers method are the three commonly used method for the synthesis of *GO*. Daniela C. Marcano et al (Marcano et al., 2010a) compared all the three methods for the synthesis of *GO* and reported that the improved Hummers method for generating *GO* offers notable benefits compared to Hummers'

method and modified Hummers method (Zaaba et al., 2017). The representation of the procedures followed starting with graphite flakes for the synthesis of *GO* is presented in **Figure 2.1**. The reaction protocol does not entail a significant exothermic reaction and does not generate any hazardous gas. Furthermore, the improved Hummers method produces a greater proportion of thoroughly oxidised hydrophilic carbon material (Marcano et al., 2010a). This implies that the improved Hummers method may cause less disturbance to the basal plane of the graphite compared to Hummers' method (Chen et al., 2022). Collectively, these data indicate that the improved Hummers method could be beneficial for the extensive manufacturing of GO (Marcano et al., 2010a).

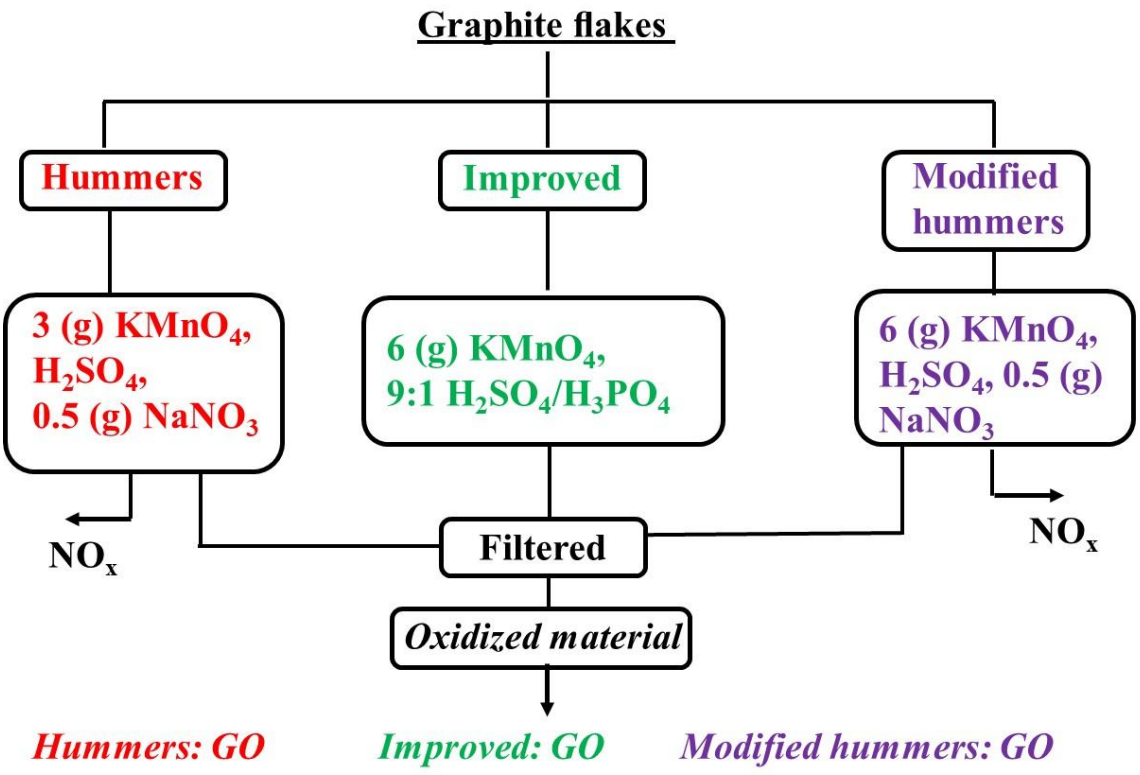

Figure 2.1 Representation of the procedures followed starting with graphite flakes for the synthesis of GO

The *GO* offers low production cost, easy processing, and large-scale production as its key benefits (G. Li et al., 2022). It is commonly utilised as a precursor for creating reduced graphene oxide (RGO). Lately, through more research on *GO*, scientists have discovered its

outstanding properties due to the presence of abundant active oxygen-containing functional groups (Das et al., 2020a). These oxygen-containing groups or reduced doping elements can serve as catalytic active centres for covalent/non-covalent modification design based on the needs of particular application areas (Chen et al., 2013a). Moreover, the existence of oxygen-containing groups further widens the interlayer gap of GO (H. Yu et al., 2016). Functionalization can be achieved through small molecules or polymer intercalations. Currently, significant advancements have been made in the functionalization of graphene oxide (Shen et al., 2022, 2021b). It has been utilised in various fields such as desalination, drug delivery, oil-water separation, catalysis, solar cells, energy storage, healthcare, and more (Keshmiri et al., 2022). Nevertheless, it is important to acknowledge that the single component graphene material exhibits certain limitations, including diminished electrochemical activity, propensity for agglomeration, and challenges in processing (G. Li et al., 2022). These limitations significantly restrict the potential applications of graphene (S. Wang et al., 2019a)**.** Hence, it is imperative to facilitate the functional modification of graphene and GO in order to broaden their range of applications. The process of functionalizing *GO* involves modifying their inherent structure (G. Li et al., 2022).

In the present study, we have employed the improved Hummers method for the synthesis of GO.

2.3 Study on graphene-based epoxy coating

Graphene materials are being broadly considered for anti-corrosive coating applications owing to its numerous distinguishing properties including thermal and chemical stability, excellent impermeability against aggressive oxidizing and corrosive species, outstanding mechanical properties, and high specific surface area. However, the prospective applications of graphene are hindered by its poor dispersibility in solvents and epoxy matrices (Cheng Zhang et al., 2022). Various methods have been developed throughout the years to improve graphene

dispersibility and polymer compatibility. B. Ramezanzadeh et al (Ramezanzadeh et al., 2016) studied the effect of covalent functionalization of a diamine compound on the *GO* surface on the barrier and corrosion protection properties of an epoxy coating was studied (Shen et al., 2022). The outcomes of the suggested the without functionalization of the GO material shows poor anticorrosion property compare the modified *GO*. Hence, researchers are focusing on the modification of *GO* to improve the dispersibility in the epoxy and achieve the higher anticorrosion property. The summary of few studies on modified *GO* for an anticorrosive coating application is depicted in **Table 2.1**.

Table 2.1 Summary of few studies on modified GO for an anticorrosive application in 3.5 wt% NaCl solution

Metal	**Epoxy: Hardener**	**Fillers**	**Reference**
2024-T3 aluminium alloy	Green Epoxy Primer	3-amino-propyl-tri-ethoxy-silane functionalized GO	Ahmed Najm Obaid et al., 2023
Q235 carbon steel	water-based epoxy curing agent-BANCO901	phytic acid functionalize GO	Xingnan Zhou et al., 2020
Aluminum alloy sheets (AA6061)	Epoxy (E51) curing agent-BANCO 916	Dimethyloctadecyl[3-(trimethoxysilyl) propyl]ammonium chloride/GO	Yuqin Tian et al., 2022
Carbon steel	epoxy resin Epikote 828 and amine-type hardener	Molybdate intercalated hydrotalcite/graphene oxide composite	Thuy Duong Nguyen et al 2020

Low carbon steel Q235	Epoxy resin (E-44) curing agent polyamide (650)	Benzotriazole-GO/covalent organic framework	Chenyang Zhang et al., 2021
steel	WEP coatings, CTW-6064	Maleic acid-GO	Lisheng Zhou et al., 2022
mild steel	Araldite epoxy resin and hardener	GO functionalized with 2-Aminothiazole (AT) and 2-amino-4-(1-Naphthyl)Thiazole (ANT)	Kamalon Rajitha et al., 2020
Q235 steel	Curing agent (CU-600) and waterborne epoxy emulsion (MU-618)	cerium organic network modified graphene oxide	Hao Li et al., 2023
Q235 carbon steel	epoxy (WSR6101 E-44) and epoxy AB glue	CeO2-Modified Graphene Oxide	Kai Lyu et al., 2022

2.4 Limitations associated with the pure graphene coating

Pure graphene can block the corrosive media from entering the anti-corrosion coating. But it has not provided the long-term effective protection of the underlying metal substrate. Yuhua Dong (Dong et al., 2019) reported that with increasing soaking time, the graphene coating peeled off, resulting in more serious corrosion than bare *Cu* in corrosive environment. Maria Schriver (Schriver et al., 2013) studied the short-term and long-term performance of graphene-coated copper. In a short period of time (a few minutes or a few hours), the graphene coating provided effective protection in high temperature environments. For a longer duration, graphene led to the severe galvanic corrosion of *Cu* at ambient temperature, and even the corrosion resistance was not as good as that of bare *Cu*.

2.5 Ionic liquids

The term "ionic liquids" (ILs) typically refers to compounds that consist entirely of ions and possess a melting point lower than 100 °C. The initial documentation of ethylammonium nitrate (IL) was documented by Paul Walden in 1914 (Paul Walden et al., 1914). However, it was not anticipated by Walden at that time that ILs would eventually emerge as a significant field of study after nearly a century. ILs are the organic salts that are liquids at or close to room temperature with melting point below 100 °C (Shen et al., 2022, 2021b). The ILs are gaining extensive interest because of their high thermal and chemical stability, low volatility, very high ability to dissolve a wide range of compounds and environmental-friendly behaviours (Udunwa et al., 2022). They are widely used as catalysts and reactions media for chemical transformations, electrolytes for batteries, fuel and solar cells, heat transfer fluids, lubricants, corrosion inhibitors, protein stabilizers, in chromatography as stationary phase, and nanoscience (Cabaço et al., 2012a).

In recent times, there has been a significant increase in the utilisation of ILs for the purpose of functionalizing carbon-based materials, including carbon nanotubes, activated carbon, and *GO*. This trend can be attributed to the robust interactions that exist between ionic liquids and carbon-based materials. Previous studies have documented the interactions between *GO* and ILs through a combination of experimental and computational methodologies(Ravula et al., 2015). A comprehensive comprehension of physiochemical properties, including viscosity, solubility, heat capacity, and density, facilitates the cost-effective, environmentally sustainable, and dependable development of pure and chemically blended ILs for industrial purposes (Shiflett and Yokozeki, 2010). The potential industrial applications of ILs can be further investigated once a comprehensive understanding of their significant physiochemical properties and their interactions with other compounds has been obtained(Wu et al., 2016). The physiochemical characteristics of ionic liquids are believed to be influenced by the specific

characteristics of anions and cations present. The liquidus range of ILs is primarily determined by their melting and decomposition temperatures, making these properties of utmost importance. The majority of ionic liquids that are currently recognised exhibit a temperature range of 200–300 °C, rendering them suitable for utilisation as solvents in chemical reactions necessitating elevated temperatures(Fallah et al., 2021). The utilisation of ILs as thermal storage fluids in diverse sectors, such as solar thermal electric power plants, is prevalent due to their elevated decomposition temperature. The melting point of ILs is primarily influenced by the symmetry of anions and cations, the length of the carbon chain, and the extent of charge accessibility. It is evident that the melting point of ILs decreases as the length of the carbon chain increases (Bogolitsyn et al., 2009a).

2.6 ILs-based functionalization

A comprehensive review of the literature indicates that *GOs* have been extensively functionalized through the use of ILs. ILs engage in non-covalent interactions with the graphene sheet (Saxena et al., 2011a). The cations and anions in the ionic liquids arrange themselves in a layered manner at the interfaces, with the cations being closer to the graphene than the anions (Zambare et al., 2022a). Nevertheless, it was also noted that both cations and anions exhibit simultaneous adsorption without any preference. However, the formations associated with the interactions between *GO* and cations are characterised by higher adsorption energy compared to the conformations associated with the interactions between *GO* and anions. By manipulating the pressure, the intermolecular interactions of *GO-ILs* can be adjusted without impacting the temperature and chemical composition of the reacting substances. The study revealed that under normal pressure conditions, the interactions between alkyl-substituted imidazolium ILs primarily occur between *GO* and their cationic moiety. However, under high pressure conditions, the interactions between graphene and the alkyl chain become more predominant. Experimental techniques such as X-ray spectroscopy (XRD), atomic force

microscopy (AFM), and scanning tunnelling microscopy (STM) are commonly employed to investigate the interactions between *GO-ILs*. On the other hand, computational methods like density functional theory (DFT), molecular dynamics (MD) and Monte Carlo (MC) simulations are also frequently utilised (Udunwa et al., 2022). The experimental determination of the interactions between GO and ILs relies on the observation that ILs create layers of cations and anions (with a thickness ranging from 1.5 to 3.0 nm) on the *GO* (or other solid substrate) (Chenyang Zhang et al., 2022a). These layers become denser and stronger as they approach the surface of the *GO*.

Chengbao et al. (Liu et al., 2018a) investigated the amino-terminated IL grafted with *GO* waterborne epoxy coating for the anti-corrosive application. The *GO* was prepared by modified Hummer's method and the results suggested that increasing *FGO* concentration to 1 wt.% leading to aggregation of graphene. Shen et al. confirmed synergistic combination of barrier and cathodic protection properties using bilayer structure of amino terminated ionic liquid (1-aminoethyl-3-methyl-imidazolium bromide) assisted *GO* (prepared via modified Hummer's method) and zinc-rich epoxy resin coatings. Y Wu et al.(Wu et al., 2020a) synthesised fluorinated reduced graphene oxide (prepared via modified Hummer's method) and then functionalized with IL (Acrizidinium) for anticorrosive applications. The summary of few studies on *IL-GO* composites used for an anticorrosive application is presented in **Table 2.2**.

Table 2.2 Summary of recent studies on IL-GO composites used for an anticorrosive application in 3.5 wt% NaCl solution

Metal	Epoxy: Hardener	Fillers	Reference
Q235 steel	Waterborne epoxy resin (E51): polyamide-8538	N-(3-Aminopropyl)-imidazole ionic liquid/graphene oxide	Chengbao L et al., 2018
Mild steel	waterborne epoxy resin: CU-600	Acridizinium ionic liquid (IL)/graphene oxide	Yangmin Wu et al., 2020
Mild steel	Epoxy resin (MU-601) : curing agent (CU-600)	1-aminoethyl-3-methyl-imidazolium bromide/graphene oxide.	Lu Shen et al., 2021

However, to the best of author's knowledge, alkyl imidazolium ionic liquids has not been explored with GO for carbon steel corrosion in saline water. Thus 1 butyl – 3 methylimidazolium acetate ionic liquid, which is prominent IL among other ILs was employed, as it has greater solubility and electrochemical window. Bogolistyn and co-workers (Bogolitsyn et al., 2009a) reported the physiochemical properties of 1 butyl – 3 methylimidazolium acetate ionic liquid.

Thus, in the present study, we employed the 1 butyl – 3 methylimidazolium acetate ionic liquid for the modification of GO materials.

2.7 Carbon quantum dots (QDs)

The initial acquisition of carbon quantum dots *(CQDs)* occurred in 2004 through the use of preparative electrophoresis to purify single-walled carbon nanotubes. Subsequently, in 2006, *CQDs* were obtained by laser ablation of graphite powder and cement. Carbon-based quantum

dots, known for their intriguing characteristics, have emerged as a promising addition to the field of nanocarbons (A. Abbas 2018). This is primarily due to their benign, abundant, and cost-effective nature. Carbon is typically a dark substance and was previously believed to have limited ability to dissolve in water and exhibit low levels of fluorescence. Carbon-based quantum dots have garnered significant attention due to their favourable solubility and robust luminescent properties, leading to their designation as carbon nano lights (Wang and Wang, 2019).

Over the past decade, numerous techniques have been suggested for the synthesis of *CQDs*, which can be broadly categorised as either "Top-down" or "Bottom-up" methods. The synthesis of *CQDs* could be done in several ways, including liquid peeling, hydrothermal, electrochemical, microwave-assisted, soft template metal-catalysed methods, and green synthesis (X. Yang et al., 2021). Three issues pertaining to the preparation of *CQDs* must be acknowledged: (i) The occurrence of carbonaceous aggregation during the process of carbonisation can be mitigated through the utilisation of electrochemical synthesis, confined pyrolysis, or solution chemistry techniques. (ii) The attainment of size control and uniformity is crucial for achieving consistent properties and conducting mechanistic investigations. This can be enhanced through post-treatment methods such as gel electrophoresis, centrifugation, and dialysis. (iii) The surface properties, which play a vital role in solubility and specific applications, can be adjusted either during the preparation process or after processing (W. Liu et al., 2021). Various biomass is used for the synthesis of *QDs* for various application (X. Yang et al., 2021). Few studies on *QDs* synthesis from biomass for various applications are presented in **Table 2.3**.

Table 2.3 Summary of few studies on QDs synthesis from biomass for various applications

Raw biomass for synthesis of QDs	**Product**	**Application**	**References**
Neem leaves	Amine-terminated graphene quantum dots GQDs (Am-GQDs)	Photoluminescence on–off–on probe for Ag+ ions	Anil Suryawanshi et al., 2014
Rice grains	Graphene quantum dots (GQDs)	Cellular imaging of GQDs using HeLa cells	Hemen Kalita et al., 2016
Neem and Fenugreek leaf	Graphene quantum dots (GQDs)	White LEDs	Prathik Roy et al., 2014
Coffee grounds	Graphene quantum dots (GQDs) and poly (ethylene imine)-GQDs	Bioimaging and sensing	Liang Wang et al., 2016
Spent black tea bags	Graphene quantum dots (GQDs)	fluorescence sensor to detect the traces of Fe3+	A. Abbas et al., 2023
bamboo leaves	Carbon quantum dots (CQDs)	Copper(II) ion detection	Yingshuai Liu et al., 2014
Sweet potato	Carbon quantum dots (CQDs)	Fe3 + sensing and cell imaging	Jie Shen et al., 2017
Grape seeds	Carbon quantum dots (CQDs)	on–off–on fluorescence probe for the detection of trace Cu(II) and ascorbic acid (AA)	Jiawei Li et al., 2021

Mulberry Leaves	Carbon quantum dots (CQDs)	Ratiometric Detection of Dopamine	Varsha Lisa John et al., 2023

2.8 Carbon quantum dots synthesis from rice husk

For the creation of *CQDs*, a variety of natural raw materials can be used. In order to create *CQDs*, several researchers have found the best way to use biomass as a versatile synthetic material. When compared to other carbonaceous precursors for the synthesis of *CQDs*, biomass is an environmentally friendly natural carbon source that offers a number of benefits. Fruits, fruit peels and juice, animal products (such as silkworm and chicken eggs), spices, vegetables, leftover kitchen scraps (like paper), and plant leaves and their derivatives are examples of biomass materials (Jing et al., 2019). One important characteristic *f-CQDs* derived from biomass is their ability to transform low-value biowaste into valuable and functional materials (Singh et al., 2023).

Rice, scientifically referred to as Oryza sativa, serves as a fundamental dietary component for a global population of approximately 3.8 billion individuals (Bhandari et al., 2020). According to Childs et al (Childs et al., 2020), the annual rice production is projected to reach 550 million tonnes by 2030 and 590 million tonnes by 2040, based on a total harvested area of 162.9 million hectares in 2020. According to Muthayya et al (Muthayya et al., 2014) , the composition of threshed paddy rice consists of 65% white rice, 25% husk, and 10% bran and germ. Annually, 150 million tonnes of husk are disposed of as solid waste during the rice milling process. RH, specifically rice hull, is frequently incinerated on-site or disposed of in landfills as a lignocellulosic bio residue. Currently, there is a significant emphasis on the "waste-to-wealth" strategy, wherein rice husk is either directly combusted as a biofuel or transformed into

bioenergy through thermochemical or biochemical processes (Chieng and Kuan, 2022). Usually, huge quantity of this material is burned outside which causes serious atmospheric difficulties (Tan et al., 2024). So, the utilization of RH in various applications is really preferred as it offers advantage in terms of low-cost feed material and further helps in achieving environmental sustainability. RH is rich in carbon, green, abundant, and easily available. Thus, it could be an ideal precursor for the synthesis of *QDs*. The *QDs* have been synthesised from various precursors including RH. Aayushi Kundu et al (Kundu et al., 2022a) prepared quantum dots from rice husk and employed in dual-mode nanosensors that can identify metal ions and fluoroquinolones. The potential of rice husk derive *QDs* is also being explored for Fe^{3+} sensing and cadmium adsorption (X. Wang et al., 2019). Although carbon quantum dots derived from rice husk have been explored for various applications such as supercapacitors, sensors etc., their effectiveness as anti-corrosive coatings have not been evaluated. Also, to the best of author's knowledge, the anti-corrosive properties of epoxy coating with biomass-derived carbon quantum dots as filler have not been reported in the literature yet. Hence, the primary objective of this study is to assess the corrosion-resistant characteristics of carbon quantum dots obtained from rice husk in the harsh corrosive environment.

2.9 Study on carbon quantum dots (QDs)/epoxy coating

Table 2.4 Summary of few studies on CQDs for an anticorrosive coating application in 3.5 wt% NaCl

Metal	**Epoxy: Hardener**	**Fillers *(Carbon Quantum dots)***	Reference
Q235 carbon steel	Epoxy resin (E-51): waterborne curing agents	Nitrogen-doped carbon dots (N-CDs)	Juan Wang et al., 2019
Mild steel	Epiran 01 EP resin: polyamide polymer	Cerium oxide (CeO) quantum dots/ graphene oxide	M.H. Shahini et al., 2021
Q235 carbon steel	Epoxy resin (E44):Hardener (T31)	silane-modified graphene quantum dots-TiO2 nanotube	Xiaohong Ji et al., 2022
Q235 steel	MU-618 waterborne epoxy:CU-600	Graphene quantum dots and metal-organic framework	Ziyang Zhou et al., 2023

Xiaohong Ji (X. Ji et al., 2022a) and co-authors studied the anticorrosion effect of silane-modified graphene quantum dots-TiO2 nanotube *(GQD@TNT)* on steel substrate in 3.5 wt% NaCl solution. They emphasised the benefits of modified *GQD@TNT* nanohybrids in epoxy coatings to attain durable protection against corrosion over an extended period. Ziyang Zhou et al (Zhou et al., 2023a), experimentally and theoretically showed the higher corrosion protection properties of graphene quantum dots and metal-organic framework *(F-GQDs@MOF)* hybrid material-based coating on *Q235* steel structures. Furthermore, they demonstrated that graphene quantum dots can also be employed for their anti-fouling characteristics. Juan Wang (2019a) and co-workers investigated the bond interaction between nitrogen-doped carbon dots *(N-CDs)* and waterborne epoxy during anticorrosion operation in

harsh environments and based on the results, an anti-corrosive mechanism is suggested. M. H. Shahini et al (Shahini et al., 2021), synthesised cerium oxide (CeO) quantum dots using an in-situ technique decorated with graphene oxide (CeO-QDs-GO) to enhance the anti-corrosive property of epoxy. All these studies clearly demonstrate that addition of quantum dots to the epoxy matrix significantly improve the anti-corrosive properties. Even though, *QDs* shows promising results in anticorrosive application, *QDs* were synthesized using conventional chemical route. In recent years, green synthesis of carbon quantum dots from biomass is of great interest. The summary of few studies on *CQDs* for an anticorrosive coating application in 3.5 wt% NaCl presented in **Table 2.4**. However, the application of carbon quantum dots derived from biomass in anti-corrosive coating application has not been explored yet.

Hence, in the present study we will focus on the carbon quantum dots derived from biomass.

2.10 Study on chemical mechanical planarization of Ru

Chemical mechanical polishing (CMP) which was first employed for BEOL metallization in the early 1990s, has emerged out as an enabling technology for planarizing materials in the semiconductor industry. CMP is extensively used in microelectronic chip fabrication industries to polish the surfaces of various materials such as copper, ruthenium, tantalum, and tungsten. In addition, the polishing slurry containing various additives among these corrosion inhibitors play vital role. Hence, we are focusing on the corrosion inhibitor for CMP of metals at microscale level.

Ruthenium (Ru), a noble metal can be used as a barrier metal for lower node devices due its various properties such as low resistivity (~7 μΩ cm), high melting point (2334 °C) and negligible solid solubility with copper (Sagi et al., 2017). The planarization of Ru is very challenging because of its chemical resistance and mechanical hardness.

Thus, it has been proposed that altering the chemical composition could potentially improve the rate at which Ru is removed. Iron (Ru) exhibits solubility in an aqueous solution when it exists as RuO_4. Therefore, the formulation of the slurry should be designed in a manner that facilitates the oxidation of the Ru surface to either RuO_4 or $RuO_2.2H_2O$ (Chenwei Wang et al., 2021). The incorporation of solely abrasives, namely silica, alumina, and ceria, into the slurry resulted in a minimal polish rate of less than 1nm per minute (Peethala et al., 2011). Hence, the inclusion of multiple oxidising agents and additives was proposed for Ru CMP. Several recommended oxidizers include ceric ammonium nitrate (CAN), hydrogen peroxide (H_2O_2), percarbonate-based slurries, potassium bromate (Victoria et al., 2010a**)**, Oxone (Victoria et al., 2012), sodium hypochlorite (Victoria et al., 2010), and sodium periodate ($NaIO_4$) (Cheng et al., 2016), among others.

The observed reactions on the surface of Ru are as follows.

$$4RuO_4^- + 4H^+ \leftrightarrow RuO_2.2H_2O + 3RuO_4 \quad \textbf{(2.1)}$$

$$IO_4^- + 2(RuO_2.2H_2O) \leftrightarrow 4H_2O + RuO_4 + I^- \quad \textbf{(2.2)}$$

$$RuO_4 + H_2O \leftrightarrow H_2RuO_5 \quad \textbf{(2.3)}$$

2.11 Corrosion inhibitor in CMP Application

In order to avoid the formation of defects caused by corrosion during the metal post-CMP cleaning process, corrosion inhibitors are introduced into the CMP slurry as well as in post CMP cleaning solutions, particularly for advanced node devices. Typically, organic chemicals with electron-dense functional groups are employed as corrosion inhibitors in the CMP /post CMP cleaning process (Ryu et al., 2021). There is a consensus in the corrosion literature that inhibitor compounds provide protection to metals against corrosion by adsorbing them onto the metal surface through chemical or physical processes. This adsorption process results in the

formation of a protective film on the surface. Subsequently, the thickened film serves as a safeguarding shield for metal, shielding it from harmful substances present in the surrounding environment (Li et al., 2023). Chemical adsorption occurs when electrons are shared between inhibitor molecules and the atoms of the metal surface, resulting in the formation of coordination bonds(Tang et al., 2018). On the other hand, physical bonding involves the electrostatic and/or van der Waals interactions between the inhibitor molecules and the metal surface (Ma et al., 2020). Organic inhibitors are the predominant corrosion inhibitors utilised in industrial settings, particularly in acidic environments for acid pickling, acid descaling, and acid cleaning procedures of metallic materials. These organic compounds possess lone pair electrons of heteroatoms (such as O, N, P, and S), functional groups (such as alcohols, acids, and amines), and/or multiple bonds on their molecular structures (Lee et al., 2021). These elements serve as favourable sites for adsorption during inhibitor-metal interactions. The adsorption process of inhibitors, and consequently their ability to protect, is influenced by various factors such as the chemical composition and charge characteristics of the metal surface, the electronic and molecular structures of the inhibitor, the pH and temperature of the solution, the duration of contact between the inhibitory solution and the metal, and the hydrodynamic conditions (Ryu et al., 2021).

2.12 Azole-based corrosion inhibitor in CMP Application

Numerous organic heterocyclic molecules have been employed as anti-corrosion agents in various metal/medium systems, with the investigation of additional compounds ongoing by numerous researchers globally (Ryu et al., 2021). Heterocyclic molecules that include nitrogen, oxygen, and/or sulphur atoms, such as azole, oxazole, and thiazole compounds or their derivatives, have demonstrated exceptional efficacy in protecting against metallic corrosion in various aggressive environments (Zhang et al., 2020). These compounds are aromatic ring molecules consisting of five atoms, with a nitrogen atom and at least one additional nitrogen,

oxygen, or sulphur atom incorporated into the ring structure. There are three primary classes of azole-based compounds: N-, N&O-, and N&S-containing azole sets. Azole-based compounds possess appealing molecular structures, including heteroatoms, double bonds, and a planar arrangement (Li et al., 2023). Furthermore, they exhibit solubility in a wide range of polar and aggressive environments, especially in acidic media. The summary of few studies on azole-based corrosion inhibitor used for corrosion protection for Ru metal in CMP applications presented in **Table 2.5**.

Table 2.5 Azole based corrosion inhibitor used for corrosion protection for metal in CMP applications

Metal	Electrolyte solution	Corrosion inhibitor	Reference
Ru	Titania (1 wt%), and sodium hypochlorite (0.5 wt%) at pH 9	1, 2, 3-Benzotriazole (5 mM)	K. Yadav et al., 2017
Ru	Potassium iodate (0.2 M) at pH value of 9	1, 2, 3-Benzotriazole (5 mM)	J. Hazarika et al., 2023
Ru	Hydrogen peroxide (0.3 wt%), glycine (2 wt%), and isooctyl alcohol polyoxyethylene ether	1,2,4-triazole and phytic acid	F. Luo et al., 2023
Cu	Deionized water at pH value of 9	1, 2, 3-Benzotriazole and 5 - Methyl (1 H) benzotriazole	D. Yin et al., 2021
Co	Deionized water at pH value of 9	1,2,4-triazole and 1, 2, 3-Benzotriazole	D. Yin et al., 2020

The corrosion literature extensively examines and reports on the corrosion inhibitory properties of nitrogen-azole derivatives (N-azoles) in comparison to thiazole (N&S-azoles) and oxazole (N&O-azoles) (Tang et al., 2018). In recent times, there has been a significant focus on the synthesis of novel derivatives containing azole, thiazole, and oxazole substituents. These derivatives exhibit enhanced prevention capabilities and stability across various metal/medium combinations.

Azoles and azole derivatives are frequently used as corrosion inhibitors for metal CMP and post-CMP cleaning operation. Especially for Ru CMP, Fu Luo and co-authors (Luo et al., 2023a)compared the corrosion inhibition performance of phytic acid and 1, 2, 4-Triazole on the Ru surface in polishing slurry containing hydrogen peroxide (0.3 wt%), glycine (2 wt%), and isooctyl alcohol polyoxyethylene ether (3 ml/L), indicating that the inhibition performance of 1, 2, 4-Triazole is better. Jenasree Hazarika et al (Hazarika et al., 2023c) reported that with the addition of BTA (5mM) in potassium iodate (0.2 M) based polishing slurry, the inhibition efficiency of 68.42 % was achieved for Ru at pH value of 9. Kavita Yadav et al (Yadav et al., 2017) demonstrated that BTA (5 mM) is crucial to the corrosion inhibition of Ru in a slurry composed of titania (1 wt%), and sodium hypochlorite (0.5 wt%) at pH 9.

As various inhibitors are available, it is imperative to compare their performance for CMP applications. Theoretical chemistry has recently advanced quickly and aids in the research of inhibition effectiveness. Quantum chemistry computations have been extensively employed to examine the chemical reactivity characteristics and adsorption mechanism of inhibitors. This approach can also be used to study reaction mechanisms at the molecular level and their associated electronic structure level. Calculations based on Density Functional Theory (DFT) are performed to investigate the predictive properties. Da Yin et al (D. Yin et al., 2020a) employed DFT and Monte Carlo simulation methods to evaluate the inhibition effect of BTAH and M-BTAH (5 - Methyl (1 H) benzotriazole) on copper at the molecular level. Da Yin and

co-workers (Yin et al., 2021a) proposed that the adsorption mechanism of BTAH and 1,2,4-triazole inhibitors on the cobalt surface using DFT and Monte Carlo simulation. However, the effects of various inhibitors on the Ru dissolution are not investigated for CMP and post CMP applications, and the interaction of corrosion inhibitor on Ru surface on molecular scale level is also not explored yet.

Based on the above literature survey three following gaps have been identified and the objectives of this thesis were formulated.

Research gap

- Alkyl imidazolium ionic liquids with GO (synthesized from improved Hummer's method) have very limited work reported for carbon steel corrosion protection in 3.5 wt% NaCl solution.
- Carbon quantum dots derived from biomass, specifically rice husk, have not been explored for their anticorrosive properties in 3.5 wt% NaCl solution.
- The interaction of corrosion inhibitor (Azole based) on Ru surface on microscale level is also not explored yet

Objectives

1. To synthesise the functionalization of graphene oxide with an ionic liquid (1 butyl - 3 methylimidazolium acetate): Preparation of epoxy-based coating on carbon steel for anticorrosive applications in a 3.5 wt% NaCl solution.
2. To investigate the anti-corrosive properties of the synthesis of carbon quantum dots (derived from rice husk) in a 3.5 wt% NaCl solution for anti-corrosive coating applications: Electrochemical and Theoretical analysis.
3. To investigate the corrosion inhibitory effects of azoles in alkaline medium for ruthenium chemical mechanical planarization applications: Electrochemical and theoretical analysis.

CHAPTER 3

MATERIALS AND METHODOLOGY

In this chapter, the materials used in the experimental and the experimental methodology employed in the present research work is explained in detail.

3.1 Materials

Graphite powder (particle size ≥ 100 mesh), 1 butyl – 3 methylimidazolium acetate, bisphenol A diglycidyl ether (BADE), and 4-4'-diaminodiphenyl sulfone (DDS) were procured from Sigma-Aldrich. Other chemical reagents such as hydrogen peroxide (H_2O_2), potassium hydroxide (KOH), potassium permanganate ($KMnO_4$), sodium chloride (NaCl), sodium hydroxide (NaOH), hydrochloric acid (35%), sulfuric acid (98%), ortho-phosphoric acid (88%), sodium hydroxide (NaOH), sulfuric acid (98%), and nitric acid (96%). Imidazole (HiMedia, India), 1, 2, 4-Trizole (Otto chemie Private Limited, India), and 1, 2, 3-Benzotriazole (Loba Chemicals Private Limited, India) chemicals were used without further purification. The chemicals used in this study are all of analytical grade. Raw RH was obtained from Khurana Trading Co., MP, India. The carbon steel (13 × 3 mm) was fabricated and received from Aries Engineers Pvt. Ltd., Mumbai, India. The ruthenium metal (99.9% purity) with dimensions of 10 mm × 2 mm was received from Tecnisco, Ltd. All the electrolyte solutions were prepared using deionized water from Milli-Q Synthesis unit (Model: Elix 3, Millipore®, USA). Potassium hydroxide (HiMedia, India) was used to adjust the pH value.

The carbon steel/Ru samples underwent a comprehensive cleaning process involving polishing by use of emery sheets (600, 800, 1000, and 1200 grits) and abrasive alumina (1.0 and 0.3 μm) powder to eliminate any oxides or contaminants. After polishing, the sample was rinsed in Millipore water and subjected to ultrasonication for 2 minutes and then air dried. Subsequently, Ru samples were submerged in the desired solution for a predetermined period of time.

Subsequently they were rinsed with deionized water, and then dried at room temperature with nitrogen gas.

The chemical compositions of the carbon steel are given in **Table 3.1.**

Table 3.1 Chemical composition (wt.%) of the carbon steel

Element	Ti	S	V	P	Si	Mn	Nb	V	C	Fe
Wt.%	0.005	0.007	0.004	0.009	0.23	0.82	0.003	0.004	0.13	Bal.

3.2 Electrochemical study setup

The corrosion cell manufactured by Metrohm, India, with a capacity of 400 ml was utilised for coating experiments and with a capacity of 100 ml was utilised for corrosion inhibition experiments. Both the electrochemical setup presented in the **Figure 3.1 and 3.2.** All electrochemical experiments, including OCP, Potentiodynamic polarisation, and EIS, were conducted using the same corrosion cell. The exposed surface area of working electrode to the electrolyte solution was 0.78 cm^2. All the electrolyte solutions were prepared using deionized (DI) water from Milli-Q Synthesis unit (Model: Elix 3, Millipore®, USA). The electrolyte solutions were prepared by introducing the stoichiometric quantity of inhibitor (IMD/TAZ/BTAH) into DI water. The electrolyte solution was subjected to magnetic stirring (Tarsons, India) for a duration of 1 min. in order to achieve appropriate dilution. A concentration of 0, 5, 10, and 15 (mM) was used to prepare the electrolyte solution of IMD, TAZ, and BTAH. The electrolyte solution is regarded as a blank electrolyte solution in the absence of an inhibitor at pH 9.

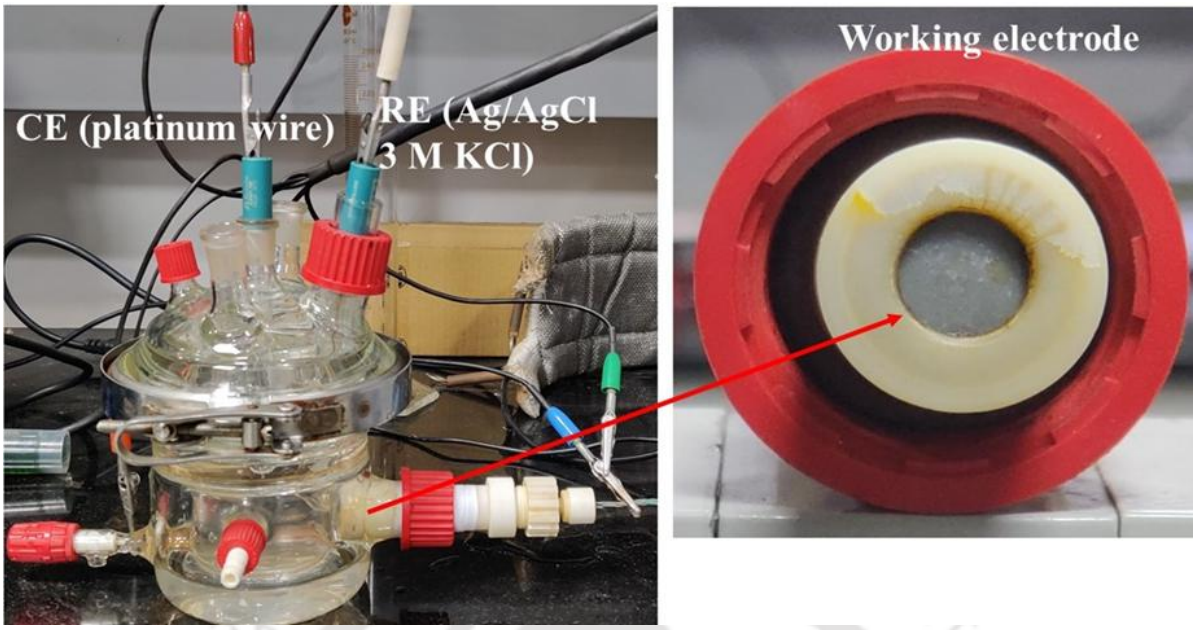

Figure 3.1 Electrochemical setup for the coating experiments

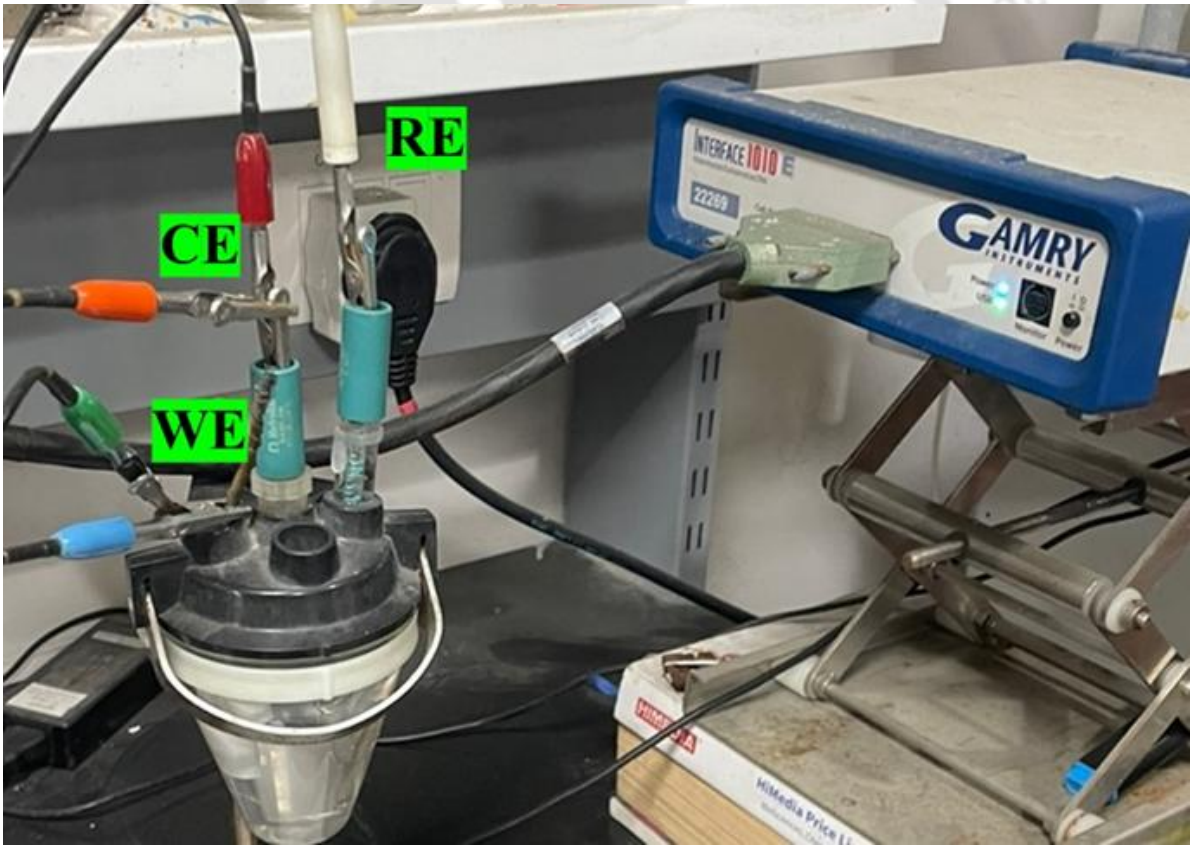

Figure 3.2 Electrochemical setup for the corrosion inhibition experiments

3.3 Electrochemical experiments

The electrochemical test was executed by employing three-electrode system using electrochemical workstation (Gamry Interface 1010E). Coated carbon steel/Ru as the working electrode. A platinum wire and Ag/AgCl (3 M KCl) were used as counter electrode and reference electrode, respectively. The electrode was then extensively cleaned with DI water after being sonicated in ethanol. Prior to any electrochemical experiment, open circuit potential (OCP) measurement was conducted in order to ensure the stability of the system. Thus, OCP of carbon steel electrode was measured against Ag/AgCl (3 M KCl) for a certain time-period, until it reached a stable value. The Potentiodynamic polarisation experiments were carried out at a scan rate of 1 mV/s from -250 to 250 mV w.r.t OCP. The electrochemical corrosion characteristics, such as corrosion potential (E_{corr}), corrosion current density (i_{corr}), anodic Tafel anodic (βa), and cathodic Tafel slopes (βc) were extracted from these polarisation curves using the Gamry Echem Analyst software. The protection efficiency (PE) was calculated using the follow equation (3.1).

$$PE(\%) = \frac{i_{corr,o} - i_{corr,i}}{i_{corr.o}} \times 100 \qquad \textbf{(3.1)}$$

Here, $i_{corr,o}$ and $i_{corr,i}$ represent corrosion current density (A/cm^2) retrieved in the absence and presence of inhibitor respectively. The electrochemical impedance spectroscopy (EIS) test was conducted at OCP in the frequency range of 10 kHz to 10 mHz and with sinusoidal perturbation of ±10 mV amplitude, ZSimpWin software was used to fit the acquired data with the appropriate electrical equivalent circuit.

3.4 Theoretical analysis

The initial structure of molecules was generated and optimized using $DMol^3$ module-based DFT calculation in Biovia Material Studio (MS) software (Accelyrl company, USA). The generalised gradient approximation (GGA) was used to perform DFT calculation using Becke-

Lee-Yang-Parr (BLYP) with double numeric polarization (DNP) basis set including d as well as p orbital polarization functionals. All the DFT calculations were performed with the implicit COSMO solvent (Water) model. Compared to conventional DFT methods such as BLYP, this method is adapted adequately for calculating non-covalent interactions, making it appealing for the calculation of all three inhibitors and Ru (0 0 1) surface.

The chemical stability and reactivity of the system can be evaluated through the energy gap (ΔE) between HOMO (Highest Occupied Molecular Orbital) and LUMO (Lowest Unoccupied Molecular Orbital). The DFT was used to calculate the frontier molecular orbital, E_{HOMO} and E_{LUMO}. Besides the energy gap (ΔE), the quantum chemical parameters including ionization potential (*I*), electron affinity (*A*), electronegativity (χ), global hardness (η) were calculated using Eq. 3.2, Eq. 3.3, Eq. 3.4 and Eq. 3.5, respectively.

$$\Delta E = E_{LUMO} - E_{HOMO} \quad \textbf{(3.2)}$$

$$I = -E_{HOMO} \quad \textbf{(3.3)}$$

$$A = -E_{LUMO} \quad \textbf{(3.4)}$$

$$\chi = 0.5(I + A) \quad \textbf{(3.5)}$$

$$\eta = 0.5(I - A) \quad \textbf{(3.6)}$$

Further, global softness (σ) and absolute electrophilicity index (ω) can be calculated from the Eq. 3.6 and 3.7 respectively.

$$\sigma = \frac{1}{\eta} \quad \textbf{(3.7)}$$

$$\omega = \frac{\chi^2}{2\eta} \quad \textbf{(3.8)}$$

In addition, with the help of quantum chemical calculations, the number of electrons transferred between inhibitor and metal (ΔN) can be calculated as per the following equation

$$\Delta N = \frac{\phi_{Ru} - \chi_{Ru}}{2(\eta_{Ru} + \eta_{inhi})} \quad \textbf{(3.9)}$$

The η_{Ru} values of 0 (eV/mol) was chosen for the calculation of ΔN. The value ϕ_{Ru}, work function of Ru (001) was taken as 4.71 (eV).

3.5 Adsorption energy calculation method

The adsorption energy calculations were performed with the help of an adsorption locator module in Biovia Material Studio (MS) (Accelyrl company, USA). A 12 layer optimal Ru surface (001) was chosen to simulate the system. Additionally, the system was simulated using a super cell (6×6) of Ru (0 0 1) and a vacuum slab with 15 Å along the C-axis in a simulation box with dimensions of 13.529 Å×13.529 Å×38 Å. Then, molecular dynamic simulations were conducted using cubic spline truncation method with a time step of 1 fs and a temperature of 298 K for 500 ps. The electrostatic forces and van der Waals forces were calculated using the atom-based summation method. The cut off distance of 12.5 Å were considered for this calculation. Finally, computational simulations were conducted to assess the adsorption energy associated with the inhibitor in the presence of the Ru metal. To accurately replicate the corrosion environment in the aqueous phase, ten water molecules along with inhibitor molecule were considered in the simulations. The simulation methodology employs the Universal force field in order to optimize the structural configuration of the complete corrosion system. Adsorption energy calculations were carried out to identify sites with low energy adsorption. The inhibitor molecule's orientation is adjusted to achieve the minimum free energy of adsorption. Consequently, the investigation of inhibitors' preferential adsorption characteristic can be studied (Heinz et al., 2009).The energy released by the corrosion inhibitor molecule

adsorbed on the metal surface is referred to as "adsorption energy," (Guo et al., 2020; Punathil Meethal et al., 2023b)and it is explained as

$$E_{ads} = E_{total} - \left(E_{surface+water} + E_{inhibitor+water}\right) + E_{water} \quad \textbf{(3.10)}$$

Where E_{total} is the overall energy of the whole investigated system containing Ru (0 0 1) with an inhibitor, $E_{surface+water}$ denoted the total energy total energy of Ru (0 0 1) surface and solution without the inhibitor, $E_{inhibitor+water}$ indicate the cumulative energy of both the inhibitor and the solution, and E_{water} is the total energy of the water.

3.6 Characterization techniques

To get a clear picture of the surface morphology and various properties od sample characterization studies were being performed. The different studies done along with the sample preparation are as follows:

X-ray diffraction (XRD) measurements

To characterize the crystal phase and lattice constant of the sample XRD measurements were employed. The measurements were conducted with SmartLab9KW diffractometer (Rigaku Corporation, Japan) that emits Cu radiation of 1.5406 Å wavelength.

Fourier transform infrared spectroscopy (FTIR)

Fourier Transform Infrared Spectroscopy (FTIR) was performed by scanning the sample in the wavenumber range of 4000-400 cm^{-1} on Spectrum series (Perkin Elmer, USA) unit. Using an Attenuated Total Reflectance (ATR) accessory with a diamond crystal, FTIR allows for direct analysis of solid and liquid samples with minimal preparation, as the diamond crystal enhances sensitivity and depth of analysis. The sample absorbs infrared radiation at specific frequencies based on its molecular vibrations, and the resulting data is processed using a Fourier transform to produce a spectrum that reveals characteristic peaks, providing information about the

functional groups and molecular structure of the sample. The compounds of sample formed at the mentioned chemical treatments were confirmed by detecting the functional groups from the peaks.

Field emission scanning electron microscopy (FESEM) and energy dispersive X-Ray spectroscopy (EDS) measurements

FESEM analysis of sample was conducted on field emission scanning electron microscope (FESEM) (Zeiss, Sigma). Before every analysis the metal samples were polished using emery sheets and cleaned properly to remove the impurities or oxides. The samples are then washed again, dried and taken for analysis. The surface morphology and microstructure of the sample were analysed from the FESEM images. In order to obtain a fracture surface, the samples were subjected to immersion in liquid nitrogen to induce brittleness in the epoxy coating, after which they were promptly broken for observation. The gold (Au) sputter coating was applied with a thickness ranging from 0.5 to 1 (nm) prior to performing FESEM analysis using the Rotary Pumped Coater (Quorum Q150R ES plus). The elemental composition of the samples was determined using EDS, with FESEM (Zeiss, Sigma, Germany) being used for analysis.

Field emission transmission electron microscopy (FESEM)

FETEM is another useful technique of characterization of nanomaterials. It's a quantitative method to determine the particle size, shape and distribution. TEM is also an electronic spectroscopic imaging technique but having a higher resolution than SEM. Drop casting method were employed for the analysis and 300 mesh grids was used. ImageJ (1.46r) software was used to calculate particle size from FETEM pictures

Contact angle analysis

The traditional sessile drop technique was employed to determine contact angle between the droplet and treated sample surface. The contact angle was determined using a goniometer

(Holmarc Opto-Mechatronics, model: HO-IAD-CAM-01B) with a water droplet volume of 2 µL at room temperature and 71% relative humidity. The contact angle of the settled droplet was measured with the help of the camera present along with the inbuilt Holmarc software. The analysis was evaluated in a Goniometer (Holmarc opto-mechatronics). Contact angle analysis sample preparation is similar to that of FESEM analysis. It is to be mentioned that a minimum of 4 droplets were deposited separately and angle was measured to ensure repeatability. A contact angle difference of less than 20 was observed on the both the sides of the droplet ensuring reproducibility.

X-ray photoelectron spectroscopy (XPS)

The chemical composition of samples was analysed using X-ray photoelectron spectroscopy (PHI5000VersaProbe III Scanning XPS Microprobe, ULVAC-PHI, INC.) with a monochromatic Al K-α source at a take-off angle of 45º. The XPS spectra were acquired using the SmartSoft-XPS v2.0 (PHI) software.

Thermogravimetric analysis (TGA)

TGA was employed to observe the thermal stability of sample in the Thermogravimetric analyzer (STA449F3A00) (Netzch, India). The analysis was done in a nitrogen environment while rising the temperature from 20℃ to 900℃ at a rate of 10℃/min.

Atomic force microscopy

The thickness of the samples was analysed using atomic force microscopy (AFM, OxfordInstruments, Model: Cypher S). Dried sample were deposited on the carbon tape used for the analysis. The height profile of the sample calculated using Gwyddion software.

Raman spectroscopy seasurements

The samples were analyzed using Micro-Raman spectroscope (Horiba Jobin Vyon, LabRam HR, Japan) in order to chemical state. Before the analysis samples were dried in the vacuum oven over night. The Raman spectra of the sample were recorded over a range of 100 cm^{-1} to 2000 cm^{-1} with an excitation wavelength of 633 nm.

3.7 Coating analysis

Using a salt spray test, the coating's anticorrosion capabilities were tested. The coating was applied to a carbon steel plate ($9 \times 9 \times 5$ cm^3) with an average coating thickness of 50 ± 2 µm. According to ASTM B117 standard, an artificial scratch was created on the samples and kept in a salt spray chamber. The adhesion strength of various coatings was also evaluated using a pull-off adhesion tester (Digital Hydraulic Adherence tester Biuged-CHINA) according to ASTM D4541 standard.

CHAPTER 4

RESULTS AND DISCUSSION

4.1 To synthesise the functionalization of graphene oxide with an ionic liquid (1 butyl - 3 methylimidazolium acetate): Preparation of epoxy-based coating on carbon steel for anticorrosive applications in a 3.5 wt% NaCl solution

4.1.1 Motivation

Carbon steel corrosion is of great concern in many industries (Deyab and Mele, 2020; Talukdar and Rajaraman, 2020) One of the industrial practices to mitigate corrosion is to apply coating on the carbon steel substrate. Various epoxy-based coating materials have been explored for easy and effective corrosion mitigation of carbon steel in corrosive environment. Ionic liquid functionalized graphene oxide (ILGO) materials are using for various application such as energy storages, sensors, bio-sensors etc. IL functionalized *GO* has been the subject of extensive research in academia, government laboratories, and commercial sectors. However, only very limited literatures are available on the IL functionalized *GO* materials used in organic coating for the anticorrosive applications as summarized herein.

Hence, in this study an anticorrosive organic coating of epoxy on carbon steel (CS) was modified with uniformly dispersed graphene oxide (GO) after functionalization with ionic liquid (FGO). The ionic liquid (IL) used was 1-butyl-3-methylimidazolium acetate which possess higher solubility and the graphene oxide was prepared by improved Hummer's method. The successful grafting of IL on the GO was confirmed by various techniques including Fourier-transform infrared spectroscopy, Raman, XPS, X-ray diffraction, thermogravimetric analysis, BET, field emission scanning electron microscope, and field emission transmission electron microscope. The surface characterization studies revealed that uniform dispersion of FGO is achieved in the epoxy matrix. Further, electrochemical studies such as

potentiodynamic polarization, and electrochemical impedance spectroscopy showed higher corrosion protection efficiency (~99%) against corrosive fluid (3.5 wt% NaCl solution). This approach may offer an easy, ecologically benign way to create a new candidate coating for the protection of CS.

4.1.2 Experimental Procedure

4.1.2.1 Materials

Graphite powder (particle size ≥ 100 mesh), 1 butyl – 3 methylimidazolium acetate, bisphenol A diglycidyl ether (BADE), and 4-4'-diaminodiphenyl sulfone (DDS) were procured from Sigma-Aldrich. Other chemical reagents such as hydrogen peroxide (H_2O_2), potassium hydroxide (KOH), potassium permanganate ($KMnO_4$), sodium chloride (NaCl), sodium hydroxide (NaOH), hydrochloric acid (35%), sulfuric acid (98%), and ortho-phosphoric acid (88%) used in this study are all of analytical grade. The carbon steel (13 × 3 mm) was fabricated and received from Aries Engineers Pvt. Ltd., Mumbai, India.

4.1.2.2 Preparation of GO via Improved Hummers method

A 90 ml of sulfuric acid (H_2SO_4) and 10 ml of phosphoric acid (H_3PO_4) in a ratio of 9:1 were mixed thoroughly in a circular bottom flask using a magnetic stirrer for 15 minutes at 700 rpm. Thereafter, 2 g of graphite powder was added gradually to the swirling mixture, and in very minute amounts. The mixture was agitated for a further 10 min, then 6 g of $KMnO_4$ was added and mixed for approximately an hour. During this step, the temperature was maintained between 0-3 °C. Then the mixture was blended for 13 h at room temperature. Following that, 100 mL of deionized water were added in a dropwise manner. Lastly, the oxidation process was terminated by introducing 20 mL of H_2O_2 (30%). GO nanosheets were created by centrifuging the suspension, washing the GO three times with a 1 M hydrochloric acid (HCl)

solution, and four times with deionised water. The graphite oxide solution finally obtained was kept for drying in the hot-air oven at below 50 °C to attain GO in powder form.

4.1.2.3 Preparation of IL functionalized graphene oxide (FGO)

0.103 g of IL was mixed with 50 mg of GO dispersion in 10 mL water (0.5 mg/mL). 0.1 g of KOH was introduced to the solution, then ultrasonically processed for 45 min. The homogenous solution was then aggressively agitated at 90±2 ºC for 24 h to produce ionic liquid functionalized graphene oxide. The resulting FGO solution was then dried in a hot-air oven at temperatures below 50 °C after being centrifuged numerous times with deionized water and ethanol. **Figure 4.1.1(a** and **b)** show the chemical structure of IL and IL grafting on the GO, respectively.

4.1.2.4 Preparation of FGO coatings on carbon steel

Initially, 5 mg of FGO was mixed with 10 mL deionized water for 10 min on a magnetic stirrer, and sonicated for 1 h room temperature. FGO suspension was incorporated into DDS (hardener), and sonicated for 1 h. Subsequently, for the preparation of 2 wt% FGO to the above-sonicated mixture, a stochiometric amount of epoxy resin (BADE) (the weight ratio of BADE and DDS was 1:1.5) was added and placed on a magnetic stirrer for 1.5 h to ensure proper mixing. The evenly mixed epoxy resin was then moved to the vacuum drying oven and left there for 15 minutes in order to prevent the production of bubbles during the coating process. Before coating, the carbon steel was thoroughly cleaned using ethanol and acetone. Finally, coatings with a required thickness 50±2 µm were accomplished on carbon steel (pretreated by abrading with emery sheets of 600, 800, 1000, and 1200 grits) using four sides thin film applicator. Then curing time of 96 h was provided. Epoxy and epoxy/GO composite coatings were also applied on the CS substrate using similar processes.

4.1.2.5 Characterization

The functional group, chemical state, and chemical structure of GO and FGO were determined through a Fourier-transform infrared spectrum (FTIR, Shimadzu IR affinity-1), X-ray diffraction (9 kW powder XRD, Rigaku Technologies, Samrt lab), Raman sprectra (Horiba JobinYvon, LabRam HR) and X-ray photoelectron spectroscopy (PHI5000VersaProbe III Sacnning XPS Microprobe, ULVAC-PHI, INC.) measurements. Brunauer-Emmett-Teller (Tristar II; Micrometrics) was used to determine the specific area and pore size distribution. Thermogravimetric analysis (TGA, temperature was increased 20-900 ºC with a heating rate of 10 ºC/min) was performed to evaluate the loading of IL in GO nanosheet. The goniometer (Holmarc Opto-Mechatronics, model: HO-IAD-CAM-01B) was used to measure the contact angle using the water droplet size of 2 µL. The morphologies of GO and IL-GO were studied using field emission scanning electron microscope (FESEM, Zesis, Sigma 300) and field emission transmission electron microscope (FETEM, JEOL 2100). Energy Dispersive X-rays spectrometer (EDX) analysis was also performed for elemental mapping (Gemini 500 FE-SEM).

4.1.2.6. Corrosion tests

An electrochemical workstation (Gamry Interface 1010E) was used to examine the coating's electrochemical activity in simulated saltwater (3.5 wt% NaCl solution) and a three-electrode system composed of a working electrode (coated carbon steel electrode with an exposed area of 0.78 cm^2), the counter electrode (platinum wire) and, the reference electrode (Ag/AgCl 3 M KCl). The open circuit potential (OCP) was maintained until it reached a stable state prior to all electrochemical measurements. At OCP, the electrochemical impedance spectroscopy (EIS) test with a frequency range of 10 kHz to 10 mHz and sinusoidal perturbation of ± 10 mV amplitude were carried out and ZSimpWin software was employed to fit the collected data

using an electrical equivalent circuit technique. The potentiodynamic polarisation experiments were performed from -250 to 250 mV w.r.t OCP at a scan rate of 1 mV/s.

The coating's anticorrosion potential was evaluated using salt spray test. A carbon steel plate of the size of 9 × 9 × 5 cm was coated, with an average coating thickness of about 50±2 µm. Thereafter, the coated samples with fake scratches were put in the salt spray chamber and continually sprayed with a 5% NaCl solution in accordance with ASTM B117. A pull-off adhesion tester made in accordance with ASTM D4541 standard (Digital Hydraulic Adherence tester Biuged-CHINA) was also used to assess the adhesion of various coatings applied to carbon steel.

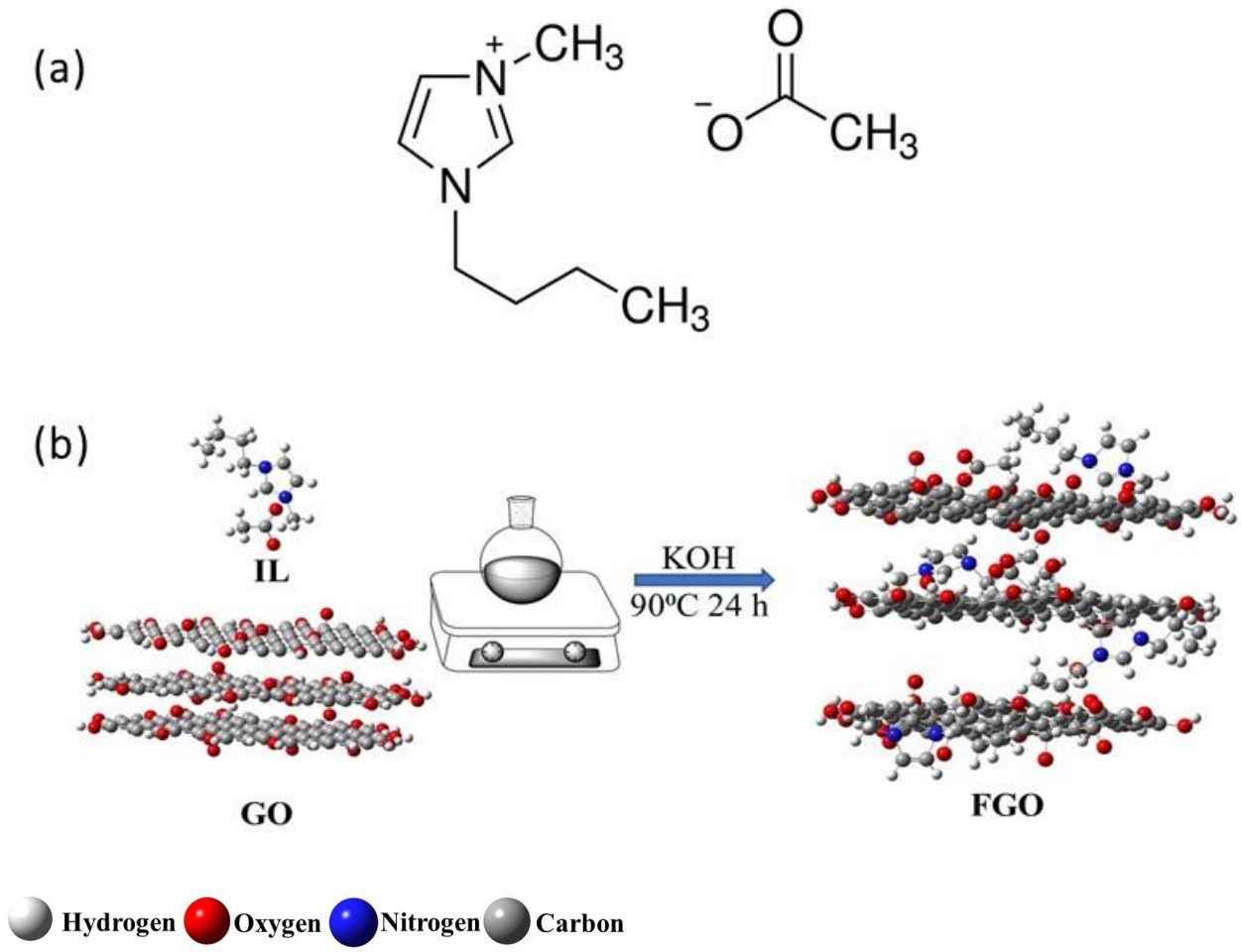

Figure 4.1.1 (a) Structure of 1 butyl – 3 methylimidazolium acetate ionic liquid and (b) schematic of the preparation of FGO

4.1.3 Results and discussion

4.1.3.1 Characterization of the GO and FGO nanomaterials

The covalent binding of IL with the GO basal plane was examined using FT-IR spectroscopy. The distinctive peaks of GO are seen in **Figure 4.1.2a** at 1070 cm^{-1} (C-O stretching), 1227 cm^{-1} (C-O vibration), 1620 cm^{-1} (C=C aromatic ring), and 1723 cm^{-1} (C=O stretching vibration) (Wang et al., 2012). Additionally, a broad peak at 3390 cm^{-1} was noticed, which can be ascribed to the hydroxyl group (Marcano et al., 2010b). After functionalization, the broad peak was moved and appeared at 3219 cm^{-1} (Ramezanzadeh et al., 2017; Shen et al., 2021a). The new peaks correspond to the stretching of C-N and N-H were detected at 1153 cm^{-1} and 1570 cm^{-1}. These peaks indicated an amide interaction between IL and the carboxyl groups in GO, indicating that the IL was effectively grafted onto GO (Liu et al., 2018b; Shen et al., 2021a).

Raman spectra for the GO and FGO are shown in **Figure 4.1.2b.** The disorder band (D band) of GO is seen at 1336 cm^{-1} and G band of GO is visible at 1601 cm^{-1} in the Raman spectra of GO. They represent, respectively, the in-plane vibration of sp^2 and sp^3 carbon atoms from the functional groups (Kudin et al., 2008). The ratio of the D and G bands' relative intensity, which also serves to indicate the degree of disorder in graphene, was frequently used to indicate the normal size of C sp^2 domain (Stankovich et al., 2007). In comparison to GO, the functionalized GO's equivalent I(D)/I(G) ratio was substantially larger (1.12), indicating that the FGO's level of disorder was more severe. The enhanced intensity ratio of the FGO is believed to be the result of attachment of IL (which has a huge imidazole ring) on the GO nanosheets. The Raman spectroscopy spectra data indicated that the IL was chemically bonded to the nanosheet of GO's edge (Liu et al., 2018b).

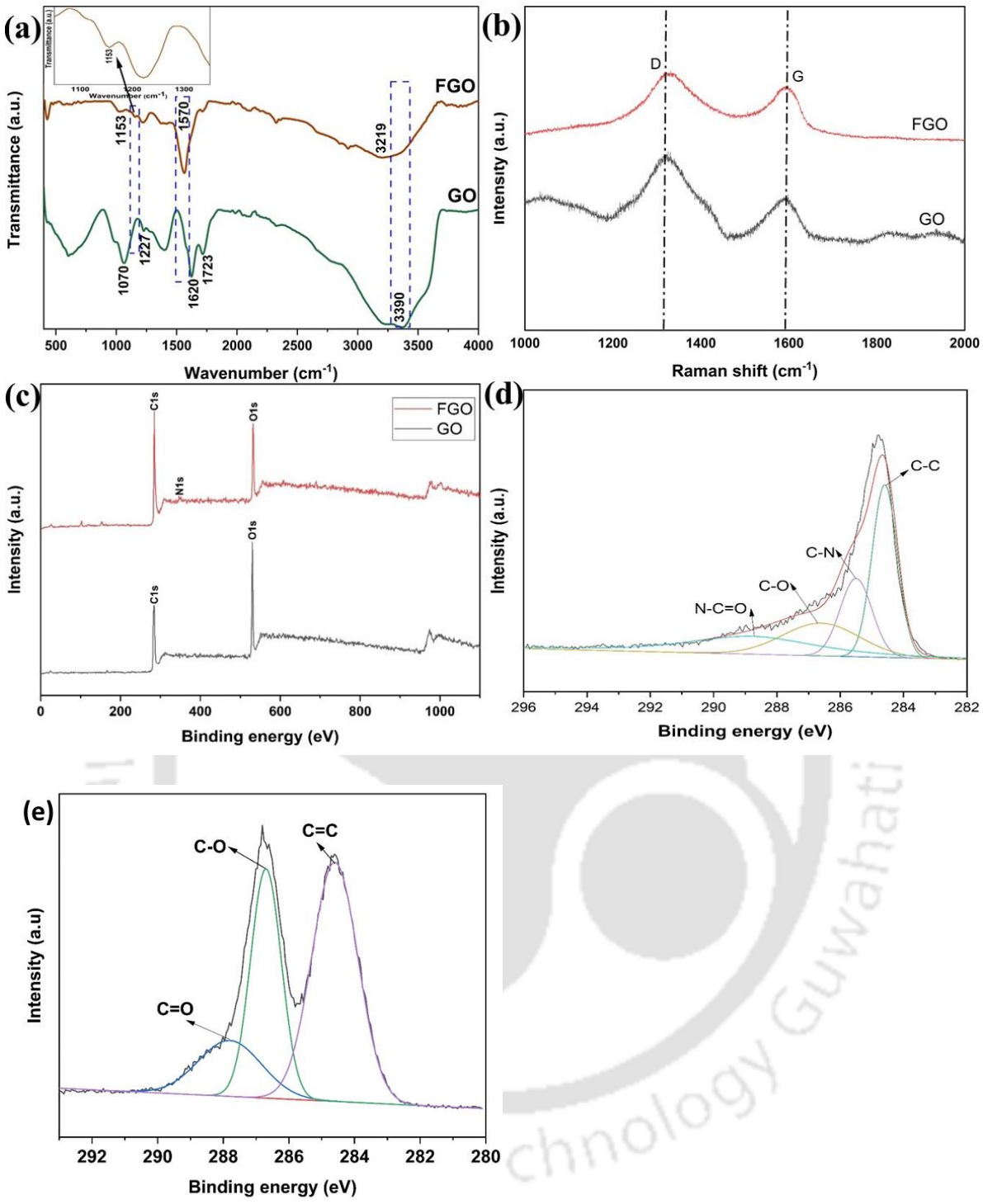

Figure 4.1.2 (a) FTIR spectra for GO and FGO and (b) Raman spectra for GO and FGO (c) Survey XPS scan of GO and FGO (d-e) High-resolution XPS spectra deconvolution C 1s profile of GO and FGO

Table 4.1.1 The deconvolution peaks C 1S of high-resolution XPS spectra for the GO and FGO

Sample	Binding energy (eV)	Phase/Groups
GO	284.6	C=C
	286.7	C-O
	287.8	C=O
FGO	284.5	C-C
	285.5	C-N
	286.7	C-O
	288.8	N-C=O

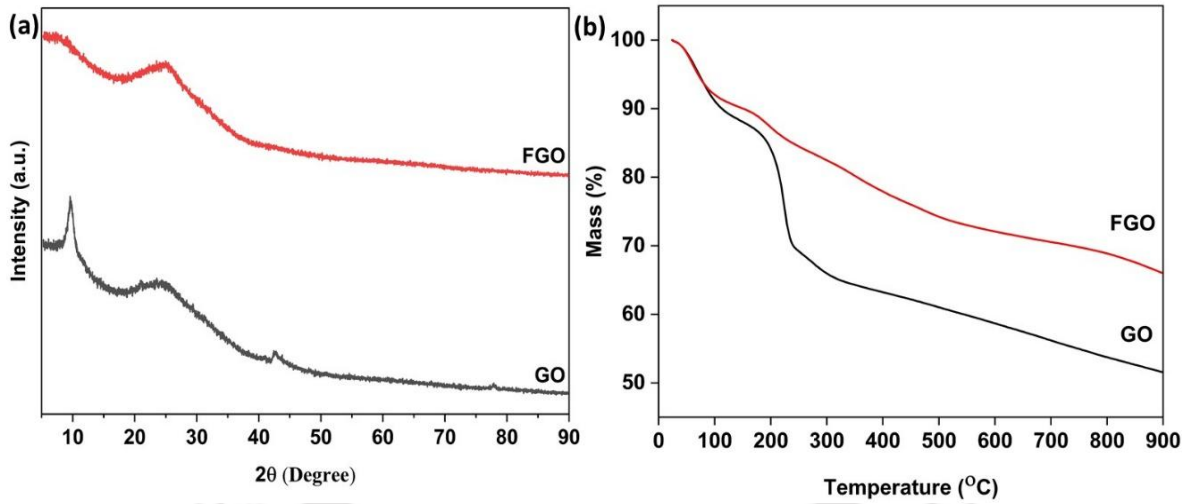

Figure 4.1.3 (a) XRD and (b) TGA in a nitrogen atmosphere of GO and FGO

The composition analysis and valence states of GO and FGO were evaluated using XPS measurements. The two separate peaks C 1s and O 1s, were found for GO depicted in **Figure 4.1.2c**. The nitrogen peak at 401 eV binding energy was clearly seen in the FGO, which showed the covalent grafting of GO with the amino group of IL. In **Figure 4.1.2d**, The C 1s XPS spectra of FGO revealed carbon components C-C, C-N, C-O and N-C=O at 284.5, 285.5, 286.7, and 288.8 eV respectively(Liu et al., 2018b; Zambare et al., 2017). Specifically, the existence of the N-C=O bond corresponding to the amide nitrogen suggested that amide bonds has

established between carboxylic acid groups of GO and the amino group of IL (Shen et al., 2020; Zambare et al., 2022b). The presence of C-N bond illustrates the grafting of ionic liquid with graphene sheets via ring opening reaction (Wu et al., 2020b; Chenyang Zhang et al., 2022b). Additionally, the C/O intensity ratio **(Figure 4.1.2e)** was used to represent the reduction degree of GO. It is clear that the FGO has a greater intensity ratio (3.26) than the GO (2.26), which denotes the reduction reaction-induced removal of oxygen-containing groups (Al-Gaashani et al., 2019). The deconvolution peaks C 1s of high-resolution XPS spectra for the GO and FGO presented in the **Table 4.1.1.** These conclusions are consistent with the outcomes of the FTIR and Raman examinations. All of the aforementioned findings suggested that the FGO material was successfully prepared by grafting together the carboxyl and epoxide groups of GO.

Crystallinity of synthesized GO and FGO was investigated using XRD measurements. **Figure 4.1.3a** depicts the XRD pattern of GO and FGO. The diffraction peak of GO corresponding to the (001) plane appears at $2\theta = 9.62^{o}$, showing the existence of functional groups containing oxygen following the oxidation process(Pham et al., 2010). This reveals the highly ordered structure of GO with interlayer spacing(Zhang et al., 2019). A small broad peak at 26.10^{o} of GO is attributed to the presence of natural graphite or unconverted graphite in the GO(Rao et al., 2018; Surekha et al., 2020). In addition, a narrow (100) peak at 42.78^{o} was identified for GO. As for FGO, the characteristic peaks of GO disappeared, leaving only a diffraction peak at 26.10^{o}. It demonstrates the successful grafting of the IL onto the GO sheets and the removal of the majority of oxygen groups as a result of the reduction event(Liu et al., 2018b).

The surface area and pore size of the synthesized GO and FGO powders were analysed by nitrogen adsorption/desorption studies. The surface area and pore size distribution found from the adsorption isotherms are reported in **Table 4.1.2**. The BET surface area of FGO is greater than that of GO, demonstrating the development of holes or fissures at the junction of graphite

layers (Das et al., 2020b). In addition, a 25.66 % increment was observed after the functionalization of GO, indicating IL was successfully loaded on the GO nanosheet. Zhihang L et al.(Liu et al., 2022) previously reported a similar increment following IL modification of the GO.

Table 4.1.2 Structural characteristics calculated from N_2 adsorption

	GO	**FGO**
BET Surface Area (m^2/g)	13.9	18.7
t-Plot micropore volume (cm^3/g) × 10^3	15.17	18.65
Pore Size (nm)	4.37	3.98

TGA was employed to observe the thermal stability of GO and FGO. In the **Figure 4.1.3b**, it is seen that GO and FGO were nearly lost throughout the heating procedure. Mass loss of 8 % and 9 % were noticed at around 100 ºC as a result of the water absorbed in GO, and FGO, respectively, and for GO, a loss of around 24 % was noticed between 200-300 ºC. This could be attributed to the breakdown of mainly non-stable molecules containing oxygen-based functionalized groups and their conversion to CO_2 or other vapors (Sheng et al., 2016). At 200-300 ºC, FGO only lost around 5% of its weight, indicating that it was significantly more thermally stable. It is possible to deduce that functionalizing GO with IL reduces the number of oxygen-containing groups, hence improving thermal stability. FGO was an excellent barrier filler in the epoxy coating to withstand antagonistic corrosives or water because of the decreased number of oxygen-containing groups.

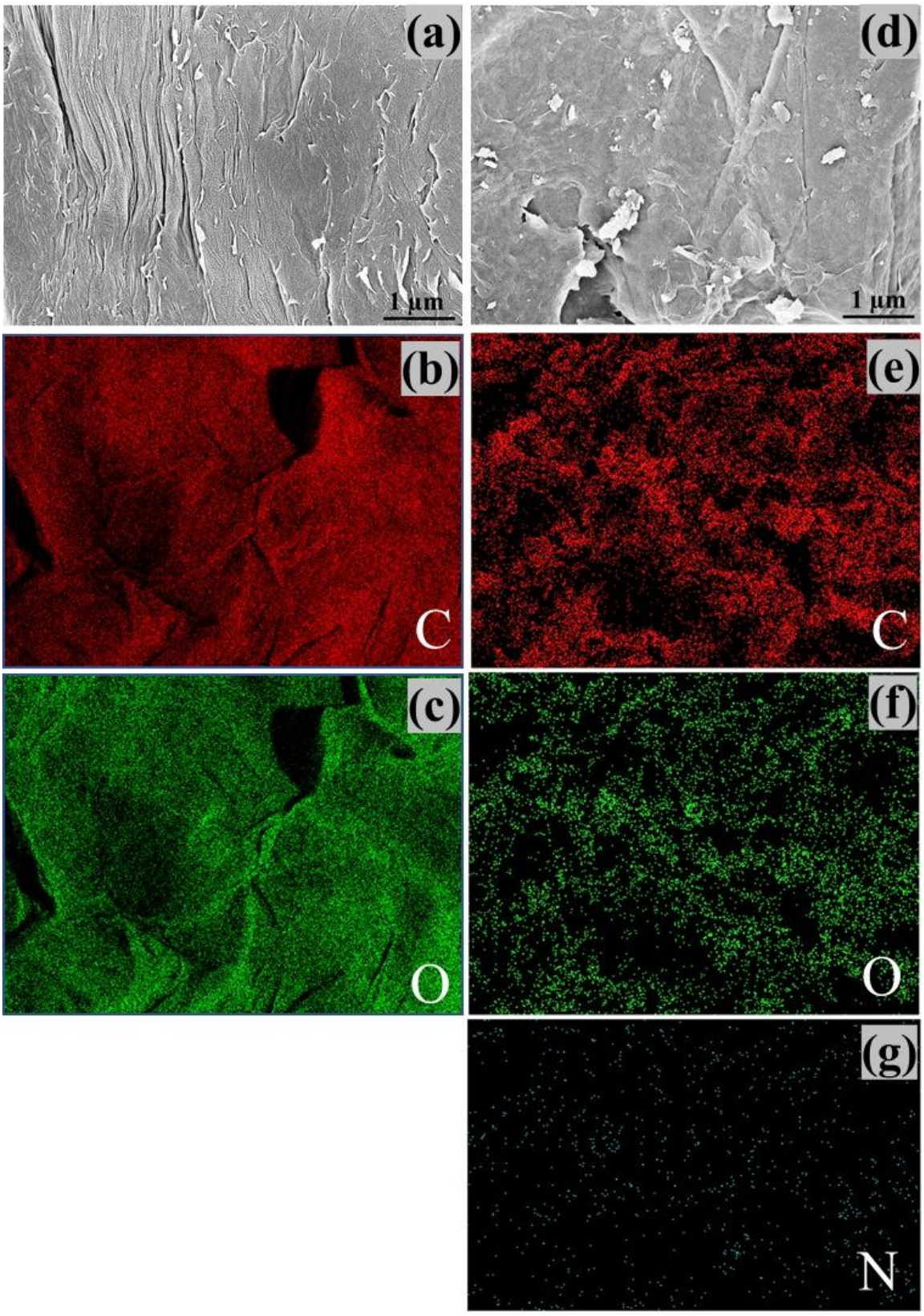

Figure 4.1.4 FESEM image of (a) GO, (e) FGO. EDS mapping images of GO and FGO; (b and f) C, (c and g) O, (h) N

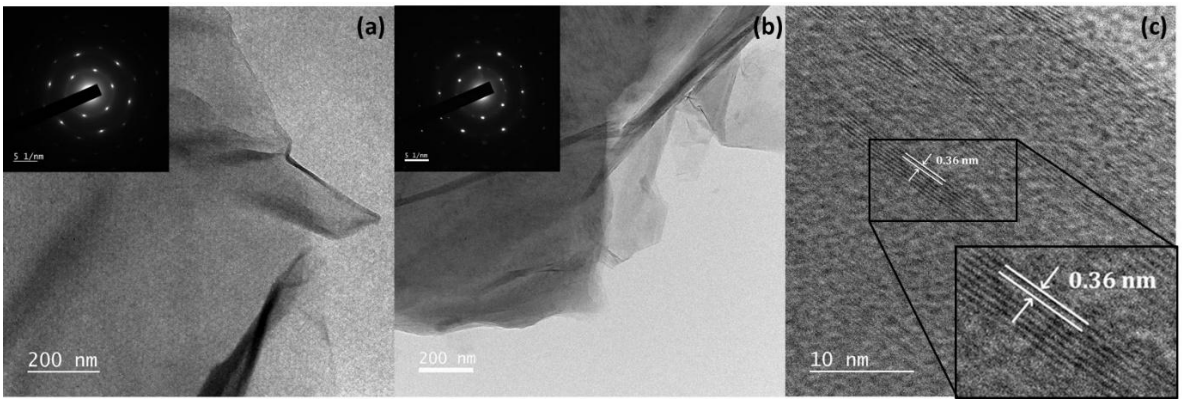

Figure 4.1.5 (a and b) FETEM micrograph of GO, and FGO and its corresponding SAED pattern. (c) HRTEM image of FGO and its crystal lattice was mentioned inside

FESEM was used to examine the microstructure and morphology of GO and FGO. **Figure 4.1.4a** illustrates the densely layered, big sheet structure with an apparent fold of GO. Small lamellae in the FGO **(Figure 4.1.4d)** revealed that the GO lamellae have been divided into many separate layers due to the van der Waals interaction (Sun et al., 2022). EDS was used to examine the GO and FGO's composition. EDS mapping pictures of GO revealed that C and O only (**Figure 4.1.4b-c)**, and FGO revealed that C, O, and N elements were evenly distributed across the surfaces of both FGO as shown in **Figure 4.1.4(e, f and g)**. As presented in **Table 4.1.3**, the increased C elements and the decreased O element on FGO corroborates with FTIR, Raman, and XPS results. The 4.80 wt% N element were observed after functionalization of GO using IL. The results of the FESEM, EDS mapping and chemical composition from EDX analysis showed that the IL successfully functionalized with the GO sheet was distributed uniformly across GO.

FETEM: For GO, a significant state of aggregation was seen in **Figure 4.1.5a.** Previously, Zhang et al. observed a similar aggregation into thicker flakes(Zhang et al., 2014). FGO's translucent and thin layer structure is clearly evident from the existence of an imidazolium ring at the edge of the GO sheet (**Figure 4.1.5b**). Besides, the selected area electron diffraction (SAED) pattern of the GO and FGO were utilized to successfully comprehend them. In the

SEAD pattern of GO and FGO, a disordered, diffused diffraction ring shape was identified. Lattice fringes were seen in several places on the HRTEM picture of the FGO. **Figure 4.1.5c** also depicts the Fast Fourier Transform (FFT) of the FGO lattice fringe image. The structure's ordering can be seen in the magnified image of fringes, from which it can be inferred that the interplanar spacing is 0.36 nm. These fringes are observed as a result of overlap of graphene oxide nanosheets. As they are parallel in the current micrograph, fringes can be classified as translational (Saxena et al., 2011b). Here, the separation is boosted by the ionic liquid cations trapped between two nearby GO nanosheets.

Table 4.1.3 Chemical composition of GO and FGO from EDX analysis

	GO		**FGO**	
Element	Atomic (%)	Weight (%)	Atomic (%)	Weight (%)
C	58.27	51.18	61.9	68.0
O	41.73	48.82	33.0	27.2
N	-	-	5.1	4.8

4.1.3.2 Characterization of the epoxy, epoxy/GO, and epoxy/FGO coatings

The cross-sectional morphology of epoxy, epoxy/GO, and epoxy/FGO composite coatings on the CS substrate has been characterized using FESEM. As depicted in **Figure 4.1.6a,** the pure epoxy resin coating displays the characteristic brittle fractures. After adding of only graphene oxide to the epoxy matrix, the results, as seen in **Figure 4.1.6b**, demonstrate considerable stacking and agglomeration (S. Wang et al., 2019b). **Figure 4.1.6c** shows that a smooth surface was achieved after adding FGO to the epoxy matrix. Further discernible aggregation was not found, proving that evenly dispersed IL-GO gave the coating system greater integrity. Tight binding and strong embedding of FGO inside the epoxy matrix indicate highly positive

interfacial interaction of FGO with epoxy coating. The strong interaction between FGO and the epoxy matrix is established through a combination of covalent bonding, hydrogen bonding, and physical interlocking, enabled by the functional groups on FGO and the reactive epoxide groups in the matrix (Ropalekar et al., 2023; Vinod et al., 2018)**.** This results in highly positive interfacial interactions and improved overall properties of the epoxy coating. Additionally, hydrogen bonding and van der Waals forces further enhance the interaction(Cui et al., 2023; da S. Medeiros et al., 2022).

TGA curves of cured samples are revealed in **Figure 4.1.7**. The gases and absorbed moisture in all three coatings are the principal causes of the early weight loss up to 100 ºC. At temperatures between 100 and 300 ºC, weight loss of 5.06 %, 2.81%, and 2.70 % for epoxy, epoxy/GO, and epoxy/FGO, respectively, was noted. This weight loss was caused by the degradation and decomposition of the molecular networks of epoxy resins-GO and epoxy resins-FGO (X. Ji et al., 2022b; Mestry and Mhaske, 2019b). At temperatures ranging from 300 to 600 ºC, a significant weight loss was observed. This might be linked to the presence of FGO in the epoxy coating, which aids breakdown by producing char and preventing further degradation of the epoxy resin backbone. The FGO concentration improves the material's thermal stability as well as its capacity to produce char. The greater interfacial interaction between the two phases and uniform dispersion may provide an explanation for this (Bouibed and Doufnoune, 2019). It seems that while the uniform distribution of FGO does act as a protective barrier, its effect on postponing epoxy deterioration does not appear to result in a significant delay. The FGO may offer some initial resistance to degradation, but its influence on extending the overall stability of the epoxy seems limited. Further investigation might be necessary to fully understand the long-term impact of FGO on the epoxy's performance.

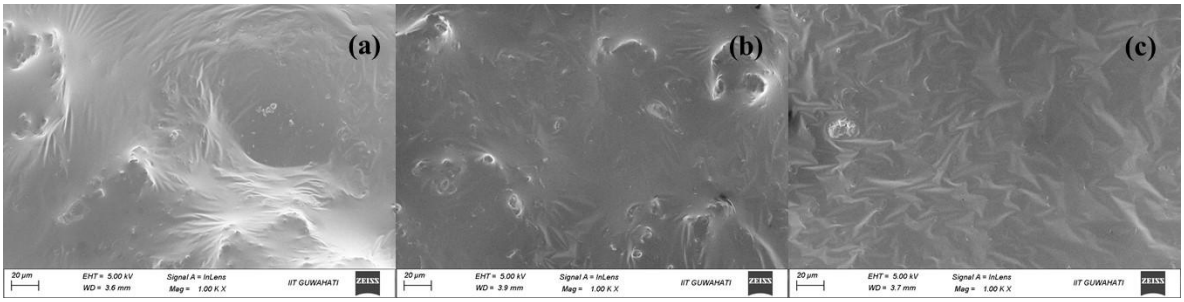

Figure 4.1.6 FESEM micrographs from a cross-section of (a) epoxy (b) epoxy/GO and, (c) epoxy/FGO coating on the CS substrate

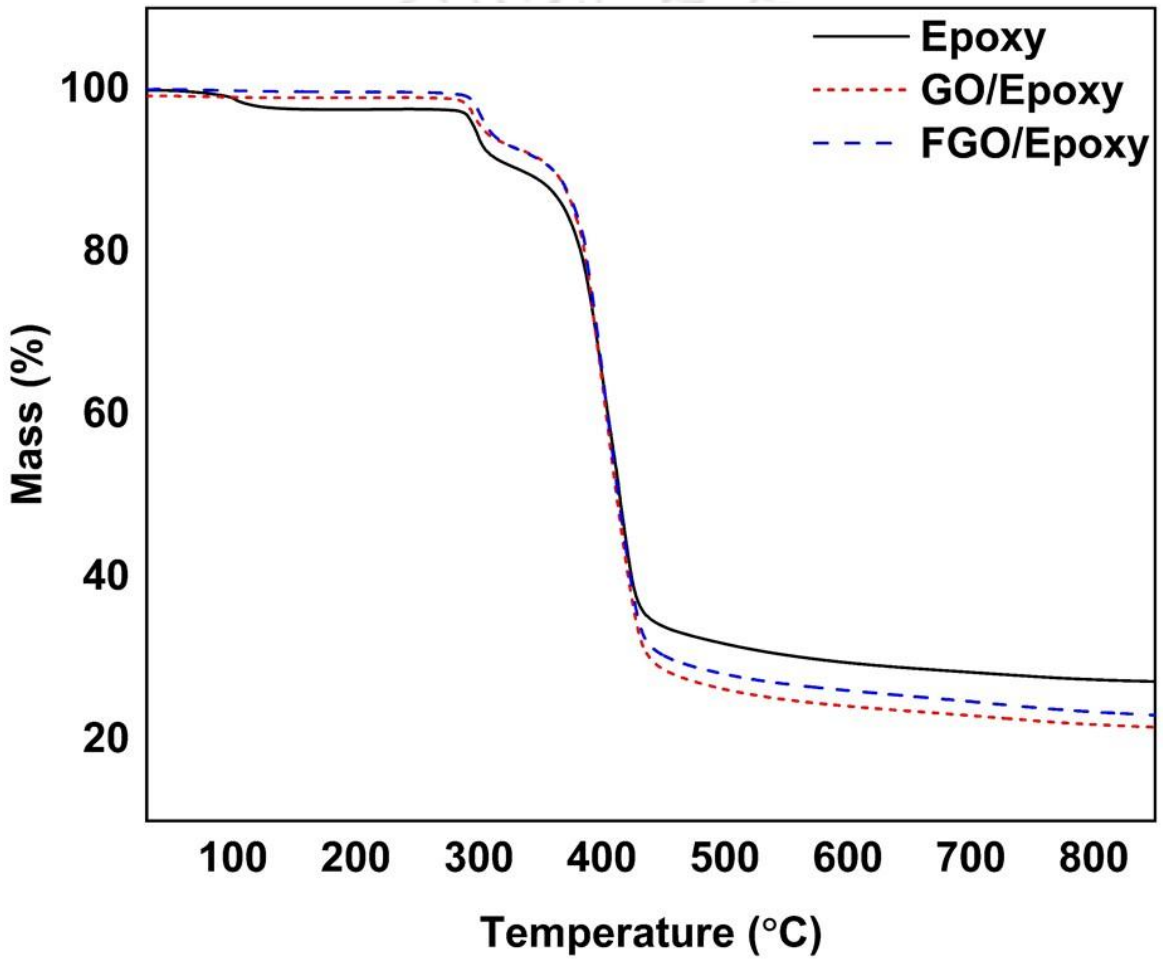

Figure 4.1.7 TG plot for epoxy, epoxy/GO, and epoxy/FGO coatings in a nitrogen atmosphere

By measuring contact angles, the composite coating's wettability was further investigated. The contact angles for over epoxy, epoxy/GO, and epoxy/FGO composite coatings were measured after submerging the composites for 1, 15, and 30 days in NaCl solution (3.5 wt%) to get an

insight into their water-repellent qualities (**Figure 4.1.8**). After 24 h of immersion, relative to the epoxy coating, the contact angle of the epoxy/GO coating is slightly lower (62.57 º). This was mainly because a significant percentage of the functional groups contained oxygen, and when the coated surface came into touch with water, those functional groups effortlessly formed hydrogen bonds with water molecules (Zhang et al., 2019; Chenyang Zhang et al., 2022b). As shown in **Figure 4.1.8**, the contact angle of epoxy/FGO is relatively higher and increases over the duration of immersion, reaching 90.76 º after 30 days. The hydrophobicity of FGO and its dispersion in epoxy resin were evident from the higher water contact angles (Zhang et al., 2019). This helped to improve the corrosion resistance capability of the epoxy/FGO coated CS substrate (Chenyang Zhang et al., 2022b).

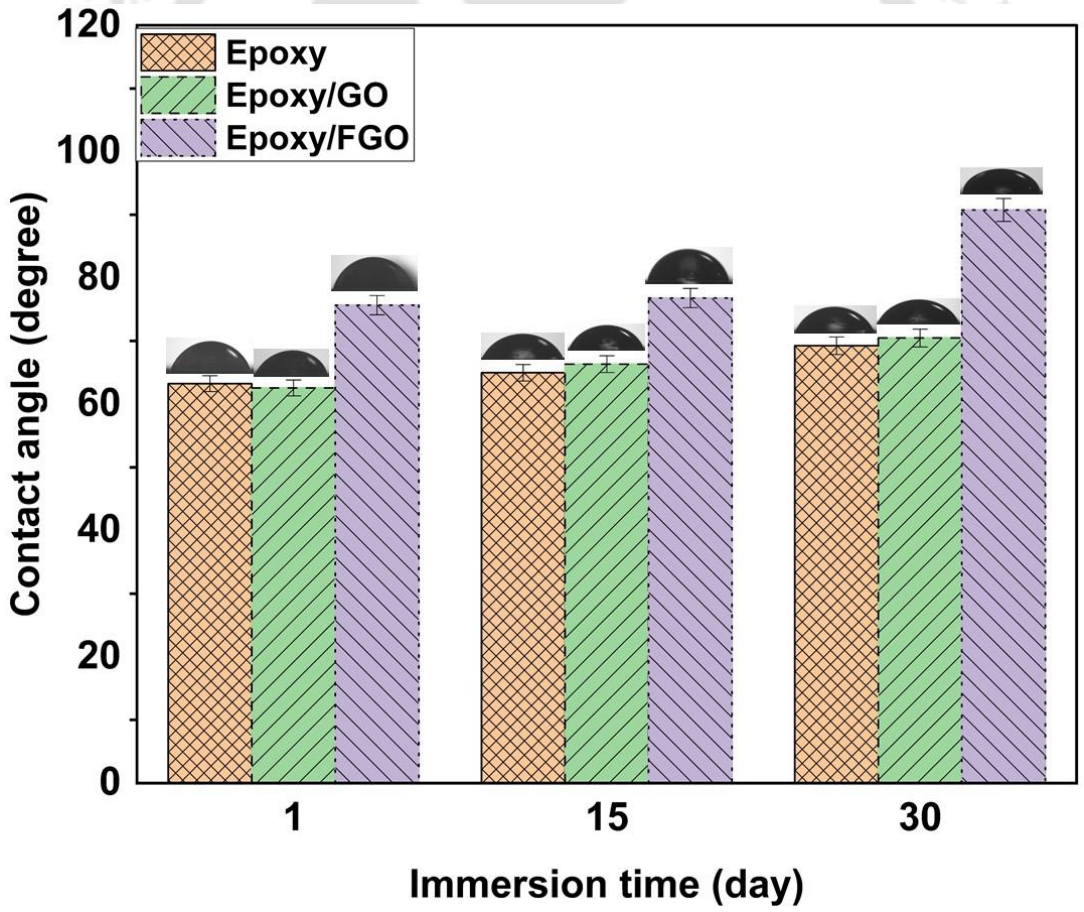

Figure 4.1.8 Contact angle of epoxy, epoxy/GO, and, epoxy/FGO coatings after 1, 15, and 30 days of immersion in 3.5 wt.% NaCl solution

4.1.3.3 Coating performance

Open circuit potential (OCP) measurement

Figure 4.1.9 showcases the fluctuation in open-circuit potential (OCP) for three different coatings: the as-fabricated epoxy, epoxy/GO, and epoxy/FGO coatings. These coatings were subjected to immersion in a 3.5 wt% NaCl environment for varying durations. The OCP testing over time offers valuable insight into the coating's resilience when subjected to a challenging environment. As time elapsed, a noticeable transformation occurred in the OCP values of all three samples, gradually veering towards increasingly negative potentials. This intriguing shift can be plausibly ascribed to the oxidation process taking place on the metal surface, coupled with the gradual degradation of the formed hydroxide/oxide film. The superior OCP value exhibited by the epoxy/FGO coated sample, in comparison to the pure epoxy and epoxy/GO coated carbon steels throughout the entire immersion period, unmistakably suggests the attainment of optimal anti-corrosion performance.

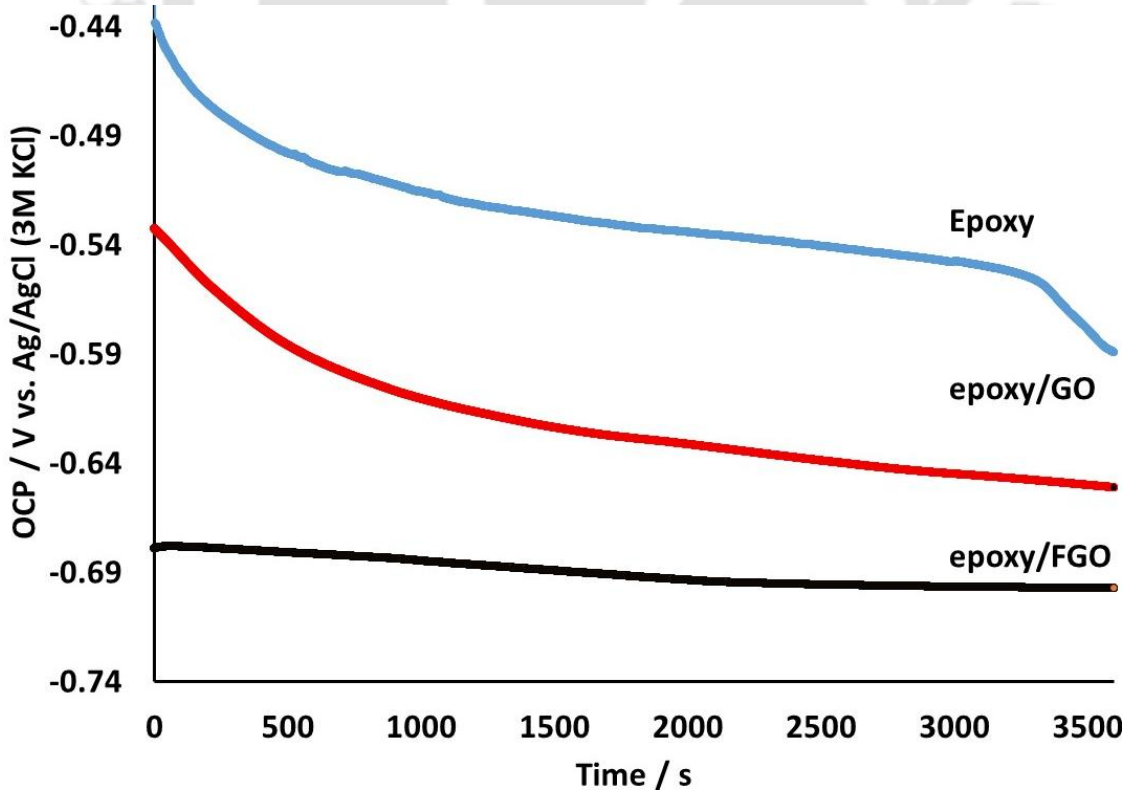

Figure 4.1.9: Time variance of the OCP of epoxy, epoxy/GO, and epoxy/FGO coatings in NaCl solution (3.5 wt.%)

Potentiodynamic polarization measurements

By using a potentiodynamic polarization test, the corrosion protection capabilities of a carbon steel substrate, epoxy, epoxy/GO, and epoxy/GO coatings were assessed in 3.5 wt% NaCl solution. **Figure 4.1.10** depicts the polarization behavior of carbon steel coated with various coatings. The corrosion potential (E_{corr}) and the corrosion current density (i_{corr}) values were estimated from these polarization curves along with anodic (β_a) and cathodic Tafel slopes (β_c) via Gamry Echem Software. The same is reported in **Table 4.1.3**. The polarization resistance (R_p), corrosion rate (CR) and coating protection efficiency (PE) were estimated from the following Stern-Geary equation [31,39].

$$R_p(\text{k}\Omega.\text{cm}^2) = \frac{\beta_a\beta_c}{2.303(\beta_a+\beta_c)i_{corr}} \qquad \textbf{(4.1.1)}$$

$$\text{CR}(\text{mm/year}) = \frac{kMi_{corr}}{D} \qquad \textbf{(4.1.2)}$$

$$\text{PE}(\%) = \frac{i_{corr,o}-i_{corr,i}}{i_{corr.o}} \times 100 \qquad \textbf{(4.1.3)}$$

Where *k* is a constant (3268.6 mol/A), M is the molecular weight of carbon steel (56 g/mol), D is the density of carbon steel (7.85 g/cm^3), $i_{corr,o}$ and $i_{corr,i}$ represent corrosion current density (A/cm^2) of blank CS and coated sample respectively. It is observed from **Figure 4.1.10** and **Table 4.1.3** that the E_{corr} values for carbon steel coated with epoxy, epoxy/GO, and epoxy/FGO coating shifts towards positive potential as compared to the blank CS substrate. The difference in E_{corr} values for epoxy, epoxy/GO, and epoxy/FGO coating is approximately calculated to be 63, 103, and 414 mV, respectively with respect to the blank CS. This considerable positive shift demonstrates the high anticorrosion property of the applied coatings, in particular that of the epoxy/FGO coating. Further, a substantial drop in the anodic current density regime is

observed for the coated CS substrates in the order epoxy<epoxy/GO<epoxy/FGO. According to the observed results, the corrosion current density (i_{corr}) of epoxy coating is nearly double that of untreated steel (Table 4). Epoxy coatings are believed to have a high resistance to diffusive ions, which makes the occurrence of reduced i_{corr} for these coatings particularly apparent. Subsequently, the CR values **(Table 4.1.4)** in the order blank CS< epoxy coating<epoxy/GO coating<epoxy/FGO coating. The epoxy/FGO coating exhibits satisfactory corrosion resistance performance with extremely high polarization resistance (2520 kΩ.cm^2), low CR (0.002 mm/year), and high corrosion protection efficiency of 99.90%. An improved anticorrosion performance was mainly attributed to the well-dispersed FGO in the epoxy coating matrix having reduced the porosity of the coating and enhanced the tortuosities of the diffusion pathways for aggressive species. Interestingly, the epoxy/GO coating, wherein GO was prepared via improved Hummers method, also demonstrates a high corrosion protection efficiency of 97.20%.

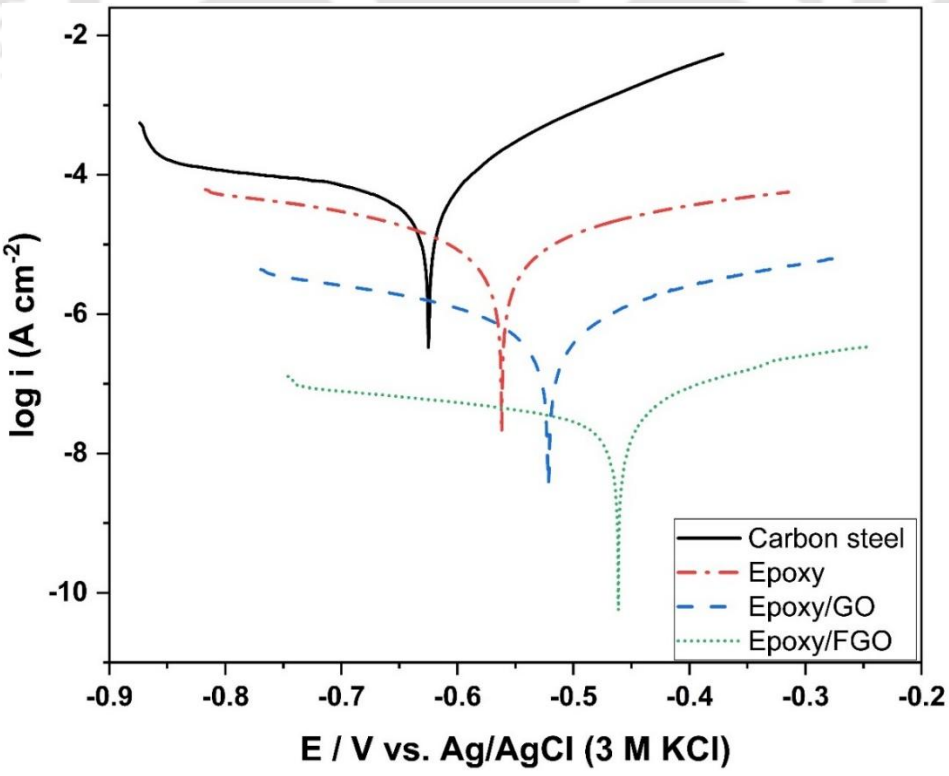

Figure 4.1.10 Polarization curves of carbon steel, epoxy, epoxy/GO, and epoxy/FGO coatings in NaCl solution (3.5 wt.%)

Table 4.1.4 Electrochemical corrosion measurement of anticorrosive coatings

	E_{corr} (mV)	i_{corr} (μA/cm^2)	βa (V/dec)	$-\beta c$ (V/dec)	R_p (kΩ.cm^2)	PE (%)	CR (mm/y)
CS	-625 ±5.1	109.23 ±0.9	0.12 ±0.005	1.128 ±0.88	0.457 ±0.002	-	2.546 ±0.25
Epoxy	-562 ±4.7	56.02 ±0.8	0.91 ±0.009	0.898 ±0.12	3.50 ±0.12	48.70 ±2.02	1.306 ±0.002
Epoxy/GO	-522 ±6.6	3.05 ±0.5	0.45 ±0.003	0.981 ±0.035	45.60 ±1.9	97.20 ±0.99	0.071 ±0.001
Epoxy/FGO	-211 ±3.1	0.10 ±0.6	1.66 ±0.04	0.988 ±0.005	2520 ±2.05	99.90 ±1.11	0.002 ±0.001

Electrochemical impedance spectroscopy (EIS) studies are employed to assess the coatings protection ability against corrosion while submerged in a corrosive environment. **Figure 4.1.11** displays the Nyquist and Bode plots of the epoxy, epoxy/GO, and epoxy/FGO coatings following various intervals of soaking in the NaCl solution (3.5 wt%). The solid continuous curve in these figures represents the outcomes of fitting the EIS data with the electrical equivalent circuits. The dotted curve in these figures represents the experimental findings that were recorded. Low frequency impedance modulus ($|Z|_{0.01\ Hz}$) might be utilised as a semi-quantitative measure of the coating's impermeability. Wider capacitive arcs frequently denote more effective protection of coating systems (Ding et al., 2022a; Zhao et al., 2019). After a day of immersion, the epoxy coating in **Figure 4.1.11(a-b)** exhibits a considerably lower $|Z|_{0.01Hz}$ value of 2.51×10^4 (Ω cm^2). The $|Z|_{0.01Hz}$ value dropped significantly to 4.45×10^3 (Ω cm^2)

after 45 days of immersion in NaCl solution (3.5 wt%), dropping by 82.27 %, representing that the epoxy coating has a poor barrier and protective efficacy. In this instance, aggressive species invasion pathways have been made available, and leading to the epoxy covering failed (Ding et al., 2022a; Jiang et al., 2019). **Figure 4.1.11(c-d)** shows the impedance findings for epoxy/GO coating at varied exposure times in 3.5 wt.% NaCl solution, which shows a similar pattern. The $|Z|_{0.01Hz}$ value after a day of immersion is 1.08×10^7 (Ω cm^2) and the $|Z|_{0.01Hz}$ value steadily decreased during the course of the immersion. After 45 days of immersion, the $|Z|_{0.01Hz}$ value dropped to 7.97×10^5 (Ω cm^2). The justification was the flaws in the coating would allow corrosive media to get through and corrode the carbon steel surface as the immersion period grew longer (Ye et al., 2021a). However, the composite coating containing FGO had the greatest impedance modulus throughout the immersion duration. For epoxy/FGO coatings **(Figure 4.1.11e-f)**, the $|Z|_{0.01Hz}$ values were much higher compared to epoxy coating and epoxy/GO coating. It indicates that the effect of IL modification on the GO strengthening corrosion resistance. Additionally, the epoxy/FGO coating displayed the greatest $|Z|_{0.01Hz}$ value, after 1 and, 10 days immersion the $|Z|_{0.01Hz}$ value was 5.5×10^7 (Ω cm^2) and 1.09×10^7 (Ω cm^2) respectively. Even after 45 days of immersion in 3.5 wt.% NaCl solution the $|Z|_{0.01Hz}$ value dropped to 2.21×10^6 (Ω cm^2). Furthermore, in the Bode modulus plots **(Figure 4.1.11b, d, and f)**, the coatings' increasing modulus at 0.01 Hz in the order epoxy < GO/epoxy < FGO/epoxy was proof that the coatings' capacity to endure corrosive environments improved with FGO loadings. Bode plot for FGO/epoxy coating, **Figure 4.1.11f** shows a higher $|Z|_{0.01Hz}$ value up to ~10^8 after 1 day of immersion and kept higher than ~10^6 after 45 days of immersion. This finding showed that the coating matrix's barrier properties were enhanced by the well-dispersed FGO.

In order to quantitatively analyze the anti-corrosive properties of the produced coatings, the corresponding electrical parameters were estimated using ZSimpWin software by fitting the

EIS data with equivalent electrical circuit $R_s(Q_c(R_{pore}(Q_{dl}R_{ct})))$ as illustrated in **Figure 4.1.12e**. The selected circuit has a good fit quality ($\chi^2 < 0.01$). Here, R_s represents solution resistance while Q_c and Q_{dl} represent coating capacitance and double layer capacitance respectively. Similarly, R_{pore} and R_{ct} correspond to pore resistance and charge transfer resistance respectively. To provide better fitting results, a constant phase element (CPE, Q) is proposed in the place of an ideal capacitor. The following equation defines the impedance of CPE.

$$Z = \frac{(j\omega)^{-n}}{Y_0} \qquad \textbf{(4.1.4)}$$

$$Q = Y_0(\omega_{max})^{n-1} \qquad \textbf{(4.1.5)}$$

where Y_0, j and ω_{max} attribute to the CPE parameter, imaginary root, and the angular frequency, respectively. ω_{max} is the frequency associated with the highest value of Z_{imag}. When n = 1, the CPE is pure capacitance, however n = 0 represent a resistor. In the range of 0 and 1, the CPE is attributed to the heterogeneities of the electrode surface (Cheng et al., 2021a). R_{pore} and Q_c were related to the interface between a corrosive solution and a coating, the charge transfer processes at the interface between a corrosive solution and a carbon steel substrate were attributed to R_{ct} and Q_{dl}, R_{pore} and R_{ct} represented the coating's resistance to electrolyte diffusion, and Q_c and Q_{dl} were viewed as parameters to measure the resistance to water penetration (Zhao et al., 2019). For all coatings, R_{pore} / R_{ct} values decreased for all coatings with increasing immersion time, indicating a decrease in the coatings' corrosive media barrier qualities. This was due to coating delamination induced by 3.5 wt% NaCl penetration, which touches the carbon steel substrate.

After 45 days of exposure to corrosive solution, it was evident that the epoxy/FGO composite coating presented the greatest values of R_{pore} and R_{ct}, 1.87 $\times 10^6$ (Ω cm^2) and 2.11 $\times$ 10^6 (Ω cm^2) respectively. when compared to epoxy (910 Ω cm^2 and 3.34 $\times$ 10^3 Ω cm^2) and epoxy/GO (2.28 $\times$ 10^5 Ω cm^2 and 8.66 $\times$ 10^5 Ω cm^2) coatings **(Figure 4.1.12a-b)**. However, after 10 days of

immersion, the Q_c values of epoxy and epoxy/GO coatings 2.70×10^{-7} and 4.97×10^{-11} (F cm^{-2} S^{n-1}) respectively, considerably increased, whilst the Q_c values of FGO remained at around 3.34×10^{-11} (F cm^{-2} S^{n-1}) **(Figure 4.1.12c)**. Additionally, similar patterns in the Q_{dl} values were also seen **(Figure 4.1.12d)**. The epoxy/FGO composite coating's higher R_{pore} / R_{ct} and lower Q_c / Q_{dl} values indicate that the right quantity of ILGO, evenly distributed throughout the coating, excellently prevents the entry of corrosive media and greatly boosts barrier the performance. Both charge transfer resistance and the polarization resistance estimated from EIS data acquired after one day immersion in corrosive solution show that the corrosion protection efficiency of FGO/epoxy coatings is increased to 99.9% as compared to pure epoxy coatings as observed in polarization measurements. Thus, electrochemical measurements clearly demonstrate the superior barrier property of prepared FGO/epoxy coatings.

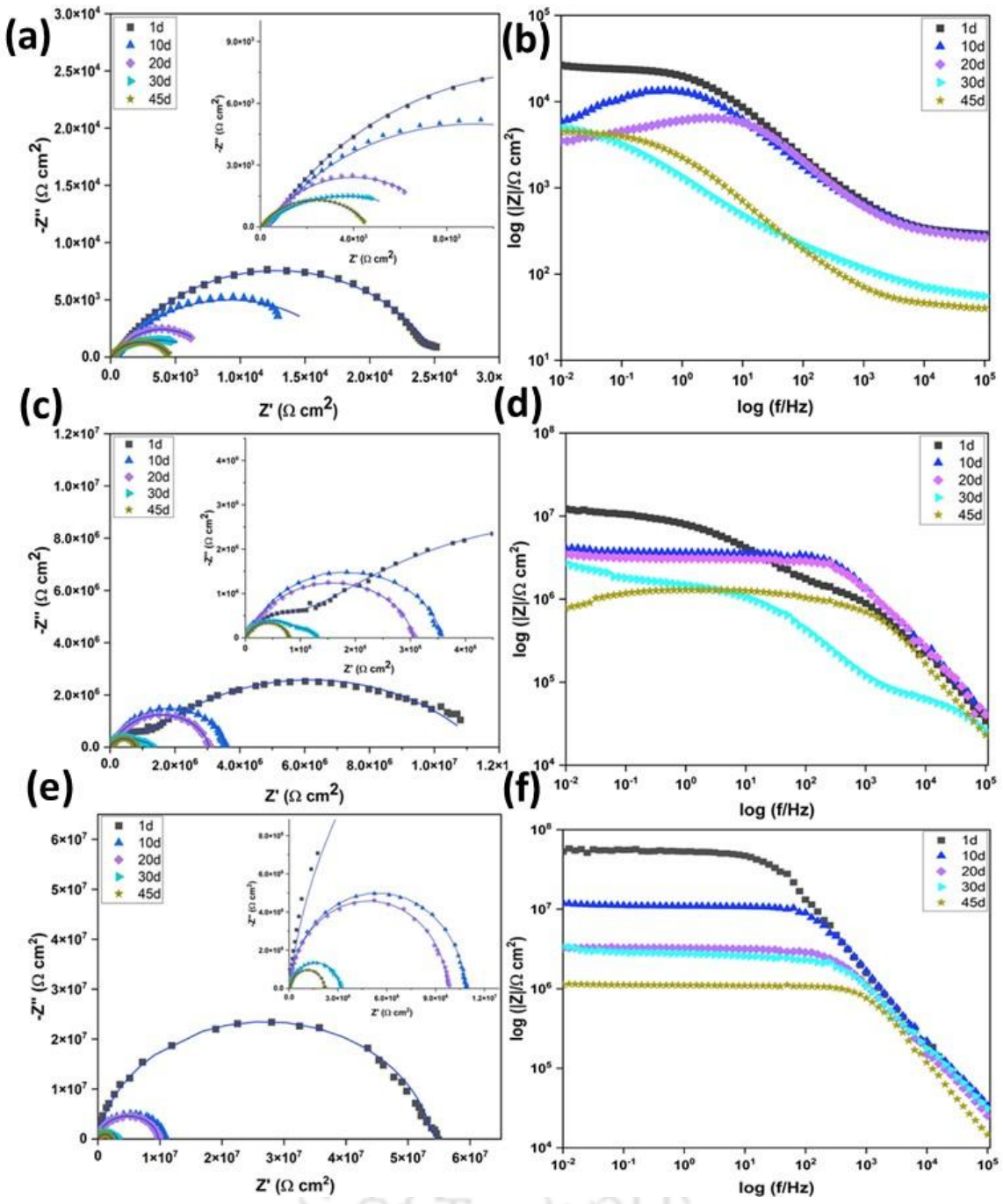

Figure 4.1.11 The Nyquist and Bode diagram of Epoxy (a, b), GO (c, d) and FGO (e, f) coatings applied on the carbon steels after immersion in 3.5 wt.% NaCl solution for 1, 10, 20, 30, and 45 days; solid lines and marker points represent the fitting and experimental data, respectively. Every test was performed at least three times

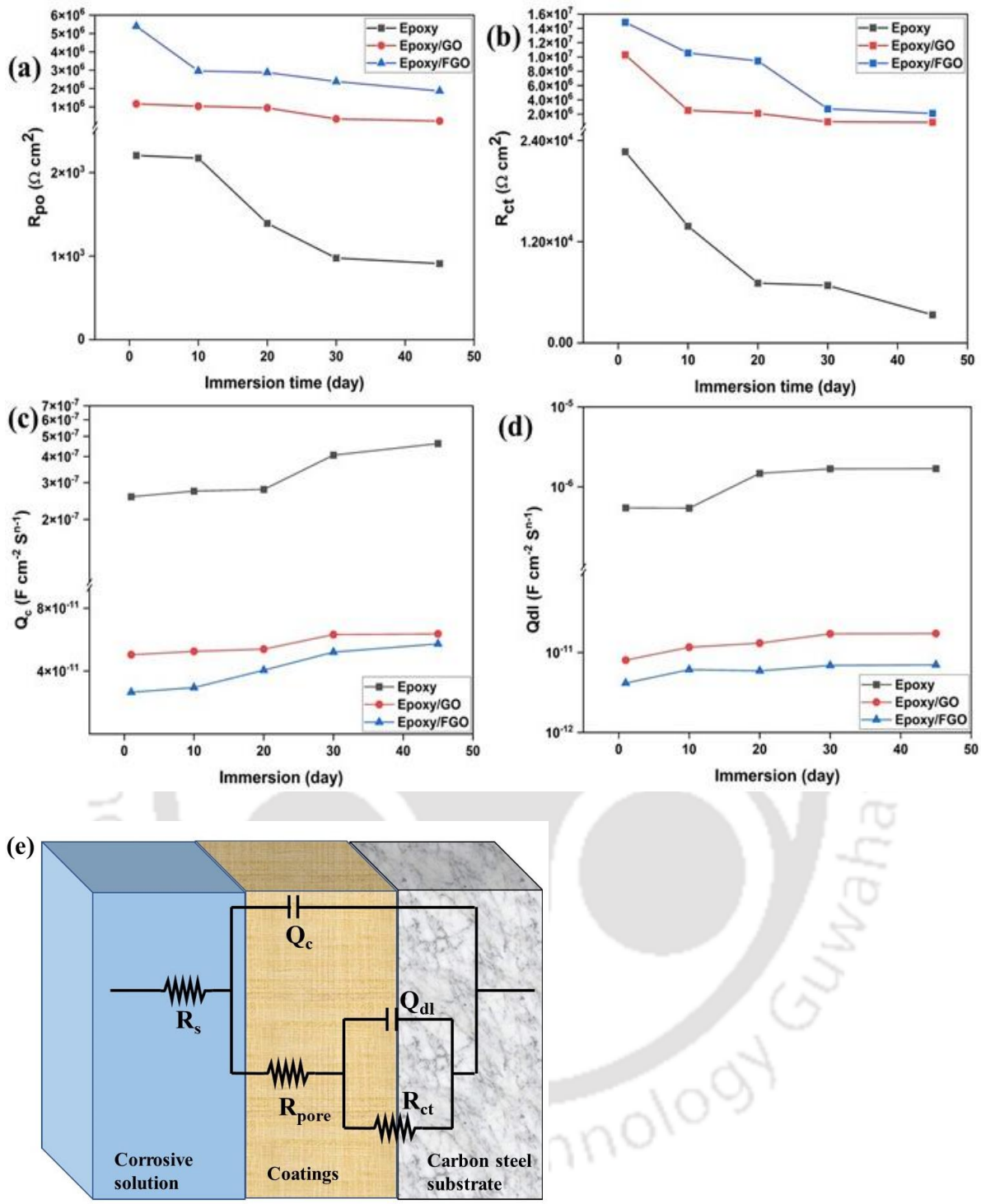

Figure 4.1.12 Fitting parameters of the coating during immersion in 3.5 wt.% NaCl: (a) R_{po}; (b) R_{ct}; (c) Q_c; (d) Q_{dl} (e) Equivalent electrical circuit model for the composite coatings

Salt spray test

A salt spray test was used to examine the sample-coated carbon steel's corrosion resistance, and optical photography was used to capture the corrosion morphologies at and around the

scratched coatings **(Figure 4.1.13)**. After 48 h of exposure, corrosion products and bubbles were seen to develop around the scratches in the epoxy coating on the CS substrate. In order to prove the dismal collapse of the epoxy and its low anticorrosion properties, the immersion duration was increased to 250 h. The enhanced corrosion of the epoxy sample was caused by the infiltration of the more corrosive media into the coating via the coating small pores. For epoxy/GO coating, compared to epoxy coating, the layer around the scratches peeled less easily. The corrosive rust increased in the scratched regions with an increase in exposure time (500 h), covering the sample surface, and exhibiting the epoxy/GO coating's insufficient barrier effectiveness on carbon steel. However, after a 500 h. exposure test, no overt corrosion products were found in the epoxy/FGO coating. The coatings' barrier properties were significantly enhanced by the evenly scattered graphene nanosheets. Furthermore, the ionic liquid corrosion inhibitor at the GO's edge prevented carbon steel oxidation in the scratches. These findings evidently demonstrated that the FGO considerably enhanced the epoxy coatings' ability to resist corrosion.

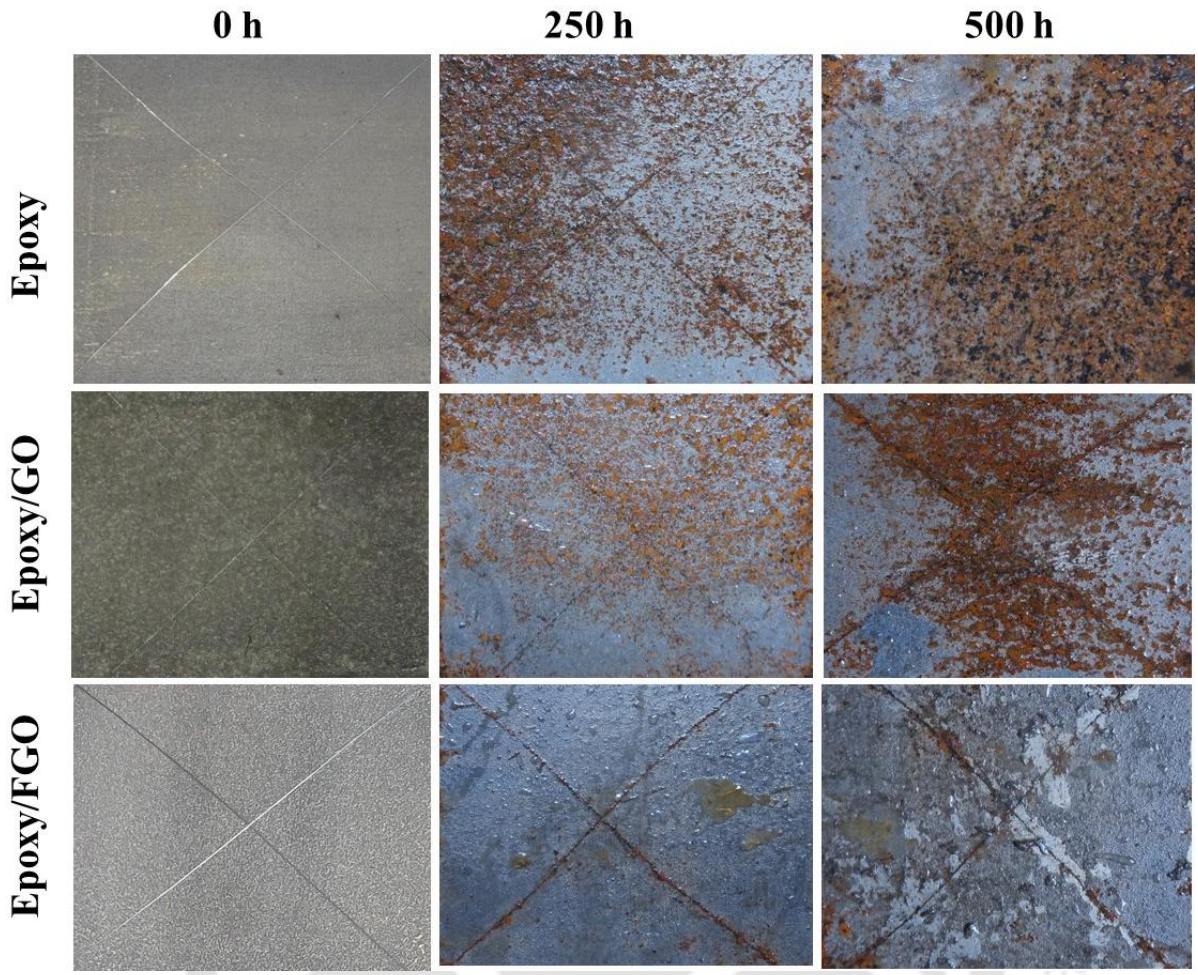

Figure 4.1.13 Optimal pictures of the salt spray tests of carbon steel substrates coated by epoxy, epoxy/GO, and epoxy/FGO after 0 h, 250 h, and 500 h. of immersion (the thickness of coating 50±1 µm and the 9 cm length of artificial)

Pull off adhesion analysis

The coating's adhesion strength to a substrate is a crucial aspect in determining the coating's anticorrosive efficacy. A coating system with outstanding protective capabilities is said to have strong adhesion strength. As a result, we used a pull-off adhesion test to determine the specimens' adhesion strength. The pull off adhesion properties of the coatings to the CS substrate is depicted in **Figure 4.1.14**. After pull off adhesion analysis, all of the three different coatings exhibit adhesive failure from a qualitative perspective, and they are entirely removed from the metallic substrate. From a quantitative perspective, epoxy coatings have the lowest

adhesion strength of 1 ± 0.10 MPa. The adhesion strengths to CS plates of epoxy coatings with GO and FGO have increased by 9.90 % and 44.44 %, respectively. Previously, a similar increment was reported by Zhou Ziyang et al. (Zhou et al., 2022a) (40.98 %) and Zhiheng Zhao et al. (Zhao et al., 2019) (31.48 %) for functionalized GO. As a result of the highly dispersed FGO, the void spacing in the epoxy/FGO coating matrix is decreased, increasing the coating density, and It is found that the IL functionalized GO effectively increases the coating's capacity to adhere to the CS substrate. These findings show that the epoxy/FGO significantly increases the adhesive force and prevents the coating from peeling away from the CS surface, which may have given the composite coating a higher level of protective performance. In fact, the epoxy/CS interface has a more robust and powerful interfacial adhesion because of the IL modification by graphene oxide molecules.

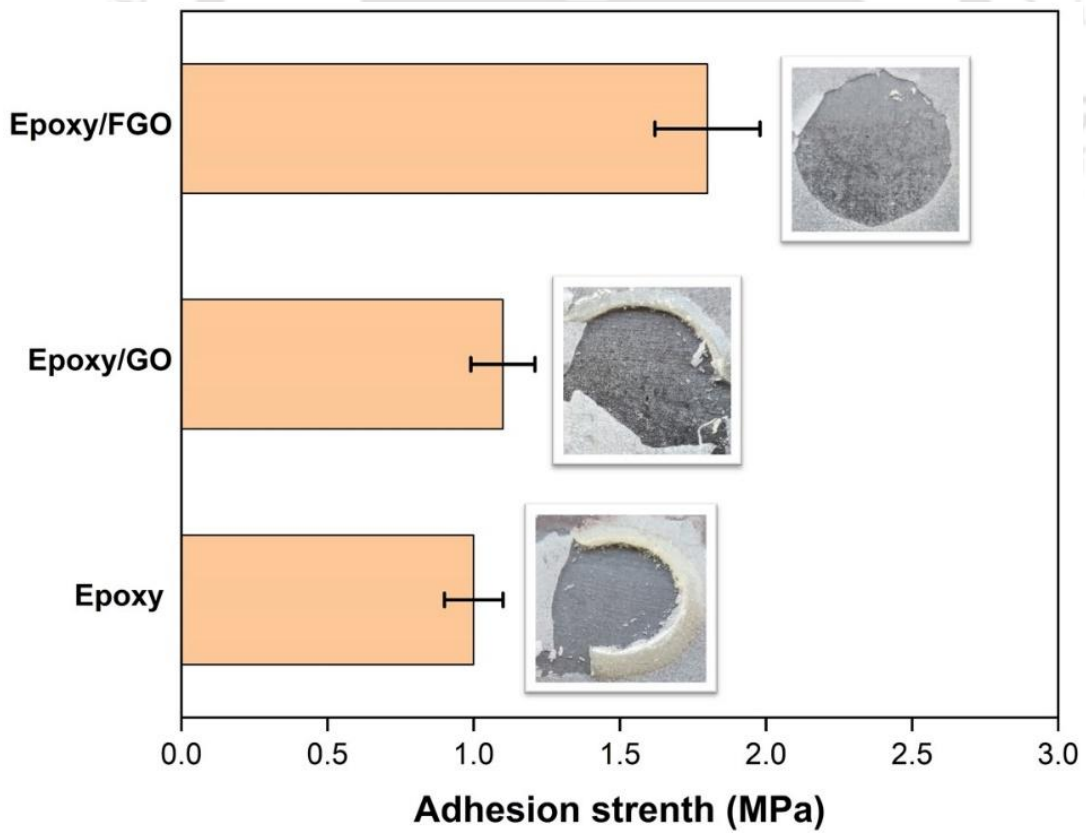

Figure 4.1.14 Adhesion strength and visual performances (inserted) of the specimens obtained from the pull-off test

4.1.4 Corrosion protection mechanism

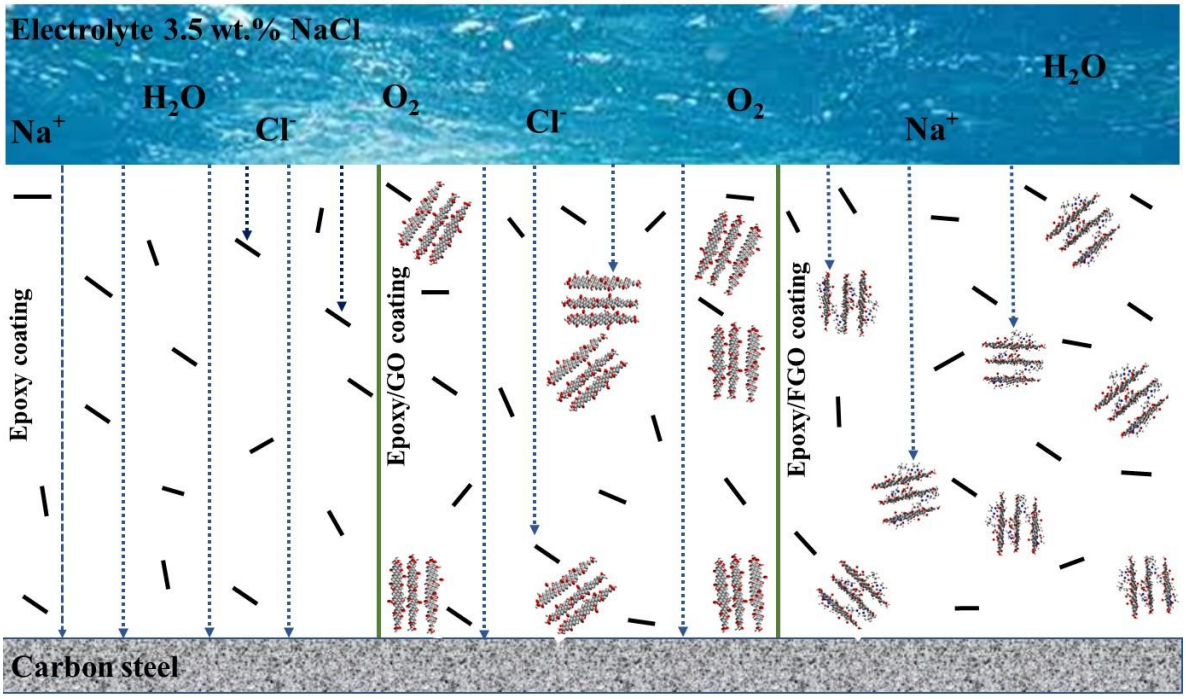

Figure 4.1.15 Schematic diagram of corrosion protection mechanism of epoxy, epoxy/GO and epoxy/FGO coatings

The schematic given in **Figure 4.1.15** is presented to illustrate the interaction of the corrosive media and various composite coatings. Corrosive fluids (such as H_2O, O_2, and Cl^-) diffuse through the coating and initiate the CS corrosion reactions (Qiu et al., 2017a). The typical CS corrosion reactions occurring in sea water are widely studied and reported in the literature (Xintong Wang et al., 2022; Y. Zeng et al., 2022). Micro-pores and fractures were generated in the coating during the film production and dissolution processes. Because of the epoxy coating's poor barrier effect and larger micropores, the corrosive fluids penetrate the CS coating rather quickly and leading to CS corrosion. With the addition of GO, the epoxy/GO composite coating's crosslinking density would increase, limiting the channel for corrosive medium penetration and lengthening the time for corrosive medium diffusion into the coating. As compared to GO, FGO has a greater specific surface area. Thus, when mixed with the epoxy coating, it acts as a barrier and blocks faults. Stronger chemical interactions between the GO

nanosheets and the epoxy matrix appear to be created when GO nanosheets are coated with IL, which appears to inhibit the agglomeration of the GO nanosheet in the coating. This could leads to uniform dispersion of GO sheets in the epoxy matrix and eventually restrict the generation of micropores and lengthen the path by which corrosive substances can permeate into the coating's contact with the CS substrate. In addition, epoxy/FGO coating have greater adhesion strength to the CS substrate, which further endowed a strong corrosion protection performance to the composite coating.

4.2 To investigate the anti-corrosive properties of the synthesis of carbon quantum dots (derived from rice husk) in a 3.5 wt% NaCl solution for anti-corrosive coating applications: Electrochemical and Theoretical analysis

4.2.1 Motivation

Carbon quantum dots (QDs), a novel class of carbon nanomaterial in a size range of less than 10 nm(Abbas et al., 2018), are gaining interest among researchers (Liu et al., 2021; Yang et al., 2021). The QDs are extremely soluble in water and they have a lot of oxygen-rich groups such as epoxy, hydroxyl and carbonyl on their edges that function as binding sites with metallic substrates and polymer coating materials (Zhou et al., 2023b). Due to its excellent properties, QDs are utilized in numerous applications like photocatalysis, sensing, photovoltaics, biomedical, photovoltaics, energy storage, supercapacitors, and batteries (Ma et al., 2022; Qiu et al., 2023). Besides, it is also being explored in anticorrosive coatings. The QDs shows promising results in anticorrosive application, QDs were synthesized using conventional chemical route. In recent years, green synthesis of carbon quantum dots from biomass is of great interest. However, the application of carbon quantum dots derived from biomass in anti-corrosive coating application has not been explored yet. Although carbon quantum dots derived from rice husk have been explored for various applications such as supercapacitors, sensors etc., their effectiveness as anti-corrosive coatings have not been evaluated. Also, to the best of author's knowledge, the anti-corrosive properties of epoxy coating with biomass-derived carbon quantum dots as filler have not been reported in the literature yet. Hence, the primary objective of this study is to assess the corrosion-resistant characteristics of carbon quantum dots obtained from rice husk in the harsh corrosive environment.

Hence, in this work, RH-QDs were synthesized from biomass (rice husk) by a cost - effective hydrothermal process and were characterized by using various techniques. Subsequently, 0.1

and 0.5 wt% of RH-QD were loaded into the epoxy matrix and applied as a coating on the carbon steel substrate. The morphological and hydrophobic behaviour of RH-QDs/epoxy coating were analyzed by FESEM and contact angle measurements. Electrochemical and salt spray studies were conducted to assess the corrosion inhibition capabilities of RH-QDs with epoxy coating on carbon steel substrates in severe marine conditions over different durations. Besides, the pull-off adhesion test is employed to assess the influence of RH-QDs on the adhesive properties of the composites. In addition, the key experimental findings are supported by quantum chemical calculations with the help of density functional theory (DFT), which provides a physical justification for the experimental observations. This work clearly demonstrates that the biomass-derived carbon quantum dots could be used as filler in epoxy matrix to enhance the anti-corrosive properties of the latter.

4.2.2 Experimental Section

4.2.2.1 Materials

Raw RH was obtained from Khurana Trading Co., MP, India. Bisphenol A diglycidyl ether (epoxy), and 4-4'-diaminodiphenyl sulfone (hardener) were produced from Sigma-Aldrich. Other analytical grade chemical reagents utilised in this study include sodium chloride (NaCl), sodium hydroxide (NaOH), sulfuric acid (98%), and nitric acid (96%). The carbon steel substrate (13 × 3 mm^2) was fabricated and obtained from Aries Engineers Pvt. Ltd., Maharashtra, India.

4.2.2.2 RH-QDs synthesis

The raw RH was first dried in an oven at 85 ± 3 °C after being properly cleaned two to three times with distilled water. The raw RH was ground to powder (100 mesh) and subsequently treated in a tube furnace (SoNaLiTe) in the N_2 atmosphere at 500 °C for 1 h. 50 ml NaOH (1 N) was introduced to the determined quantity of rice husk ash (RHA), which was then mixed

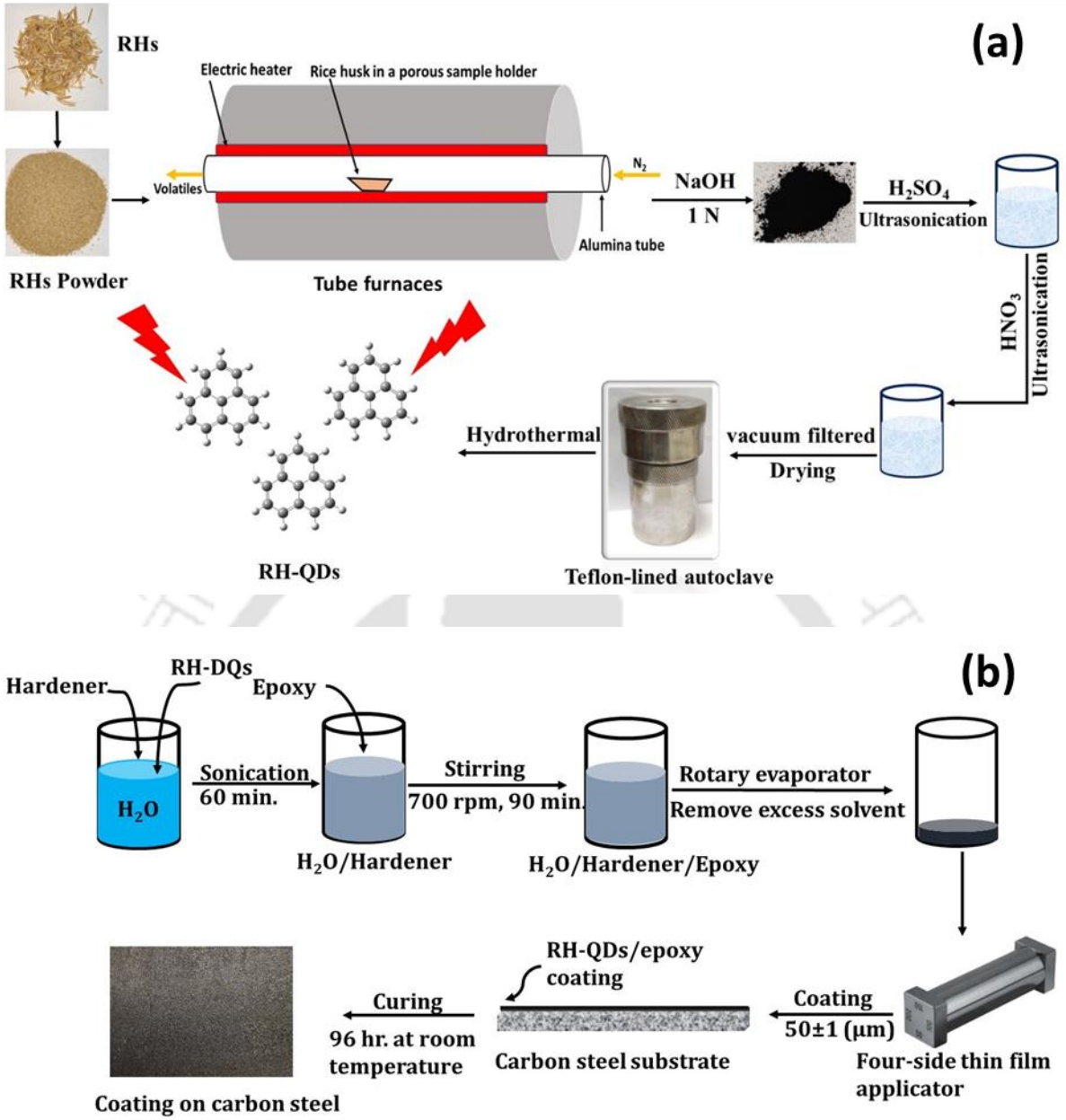

Figure 4.2.1 Schematic representation of (a) Synthesis of RH-QDs, and (b) RH-QDs/epoxy coating on the carbon steel

and heated at 100 °C for 3 h. In order to create rice husk carbon (RHC), the solution was completely rinsed with distilled water, vacuum filtered, and dried for 12 h at 90 ± 3 °C. 0.1 gm of RHC was dissolved in distilled water (6 mL) and H_2SO_4 (20 mL) and ultrasonicated for 8 h. HNO_3 (40 mL) was gradually added and ultrasonicated for 12 h. The resulting solution was vacuum filtered and centrifuged using a 0.22 µm microporous membrane. Moreover, the solution was re-dispersed in 60 mL of distilled water before reaching pH 7 by adding NaOH

(1.0 M). The dispersion was placed in a Teflon-lined autoclave and heated to 200 °C for 12 hours to undergo hydrothermal treatment. After being cooled to room temperature, the solution was centrifuged and filtered. The synthesis method is depicted in **Figure 4.2.1(a).**

4.2.2.3 Preparation of RH-QDs coatings on carbon steel

Firstly, 0.25 mg of RH-QDs and 150 mg of hardener was mixed with 10 mL distilled water for 30 minutes on a magnetic stirrer and at ambient temperature sonicated for 1.5 hours. After that, 100 mg of epoxy resin was added to the previously sonicated mixture in order to prepare 0.1 wt% RH-QDs/epoxy, and the mixture was then placed on a magnetic stirrer for 2 hours to guarantee proper mixing. In order to avoid the formation of air bubbles during the coating process, the epoxy resin was placed in the vacuum-drying oven for 20 minutes. The carbon steel substrate was ground using progressively increasing grades of silicon carbide (SiC) sheet (180, 320, 600, and 1000), after which it was polished using alumina powder with a particle size of 1.0 μm and 0.3 μm. After rinsing the carbon steel substrate with Millipore water, any particles that had adhered to the substrate were eliminated via ultrasonication. Finally, drying with the compressed air to remove moisture. The cleaned carbon steel substrate was coated with a requisite thickness of 50 ± 2 μm using a four-sided thin film applicator. Finally, 4 days of curing time was provided. **Figure 4.2.1(b)** depicts the coating technique. Pure epoxy and 0.5 wt% RH-QDs/epoxy was also coated on the carbon steel substrate using a similar method.

4.2.2.4 Characterization

The chemical state and functional group of RH-QDs were determined through Raman sprectra (Horiba JobinYvon, LabRam HR) and Fourier-transform infrared spectrum (FTIR, Shimadzu IR affinity-1). The chemical composition of RH-QDs was analysed using X-ray photoelectron spectroscopy (PHI5000VersaProbe III Scanning XPS Microprobe, ULVAC-PHI, INC.) with a monochromatic Al K-α source at a take-off angle of 45º. The XPS spectra were acquired using

the SmartSoft-XPS v2.0 (PHI) software. The morphology, microstructure, and size of RH-QDs were studied by field emission scanning electron microscope (FESEM, Zesis, Sigma 300) and field emission transmission electron microscope (FETEM, JEOL 2100), and ImageJ (1.46r) software was used to calculate particle size from TEM pictures. Further, the compatibility between the RH-QD and epoxy matrix was assessed by observing the fracture surfaces of coatings using FESEM. In order to obtain a fracture surface, the samples were subjected to immersion in liquid nitrogen to induce brittleness in the epoxy coating, after which they were promptly broken for observation. The gold (Au) sputter coating was applied with a thickness ranging from 0.5 to 1 (nm) prior to performing FESEM analysis using the Rotary Pumped Coater (Quorum Q150R ES plus). The thickness of RH-QDs was analysed using atomic force microscopy (AFM, OxfordInstruments, Model: Cypher S). The contact angle was determined using a goniometer (Holmarc Opto-Mechatronics, model: HO-IAD-CAM-01B) with a water droplet volume of 2 µL at room temperature and 71% relative humidity.

4.2.2.5 Corrosion tests

The electrochemical experiments were performed on Gamry Interface 1010E electrochemical workstation with a three-electrode system. The working electrode was coated carbon steel substrate with a 0.78 cm^2 exposed area. Platinum wire and Ag/AgCl 3 M KCl was used as a counter electrode and reference electrode, respectively. The electrolyte solution contains 3.5 wt% NaCl. Prior to all electrochemical tests, the open circuit potential (OCP) was kept up until it reached a stable state. The time taken for the OCP stabilization was 25 min. The Potentiodynamic polarisation experiments were carried out at a scan rate of 1 mV/s from -250 to 250 mV w.r.t OCP. i_{corr} and E_{corr} values were extracted from the polarization plot by extrapolating the linear section of anodic and cathodic curves using Gamry Echem Analyst Software. The electrochemical impedance spectroscopy (EIS) test was conducted at OCP with a sinusoidal perturbation of ± 10 mV amplitude and 10^5 to 10^{-2} Hz frequency range. ZSimpWin

software was used to fit the acquired data with the electrical equivalent circuit technique. Prior to each electrochemical experiment, we utilized a freshly applied coating on the carbon steel sample. Furthermore, each test was conducted a minimum of three times. Using a salt spray test, the coating's anticorrosion capabilities were tested. The coating was applied to a carbon steel plate ($9 \times 9 \times 5$ cm^3) with an average coating thickness of 50 ± 2 µm. According to ASTM B117 standard, an artificial scratch was created on the samples and kept in a salt spray chamber. The adhesion strength of various coatings was also evaluated using a pull-off adhesion tester (Digital Hydraulic Adherence tester Biuged-CHINA) according to ASTM D4541 standard.

4.2.2.6 Computational details

The initial structure of epoxy, hardener, and RH-QDs were built with the help of Gauss View 6.0 software followed by optimization using B3LYP/6-311G (d, p) level of theory (Becke, 1988; Fu and Singh, 2018; Schäfer et al., 1992). The particular basis set (6-311G) was used in DFT calculations as it is able to accurately estimate energy values compared to that of expensive MP2 approaches (Grimme, 2005). Also, it is well suited for computing non-covalent interactions (Das et al., 2023a), making it an attractive option for analysing the epoxy and hardener systems and interactions with RH-QDs. **Figure 4.2.2(a-c)** shows the optimized structure of Bisphenol A diglycidyl ether (epoxy), 4, 4-Diaminodiphenyl (hardener), and RH-QDs

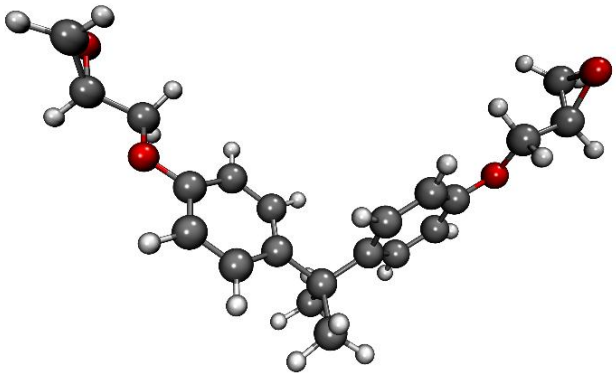

(a)

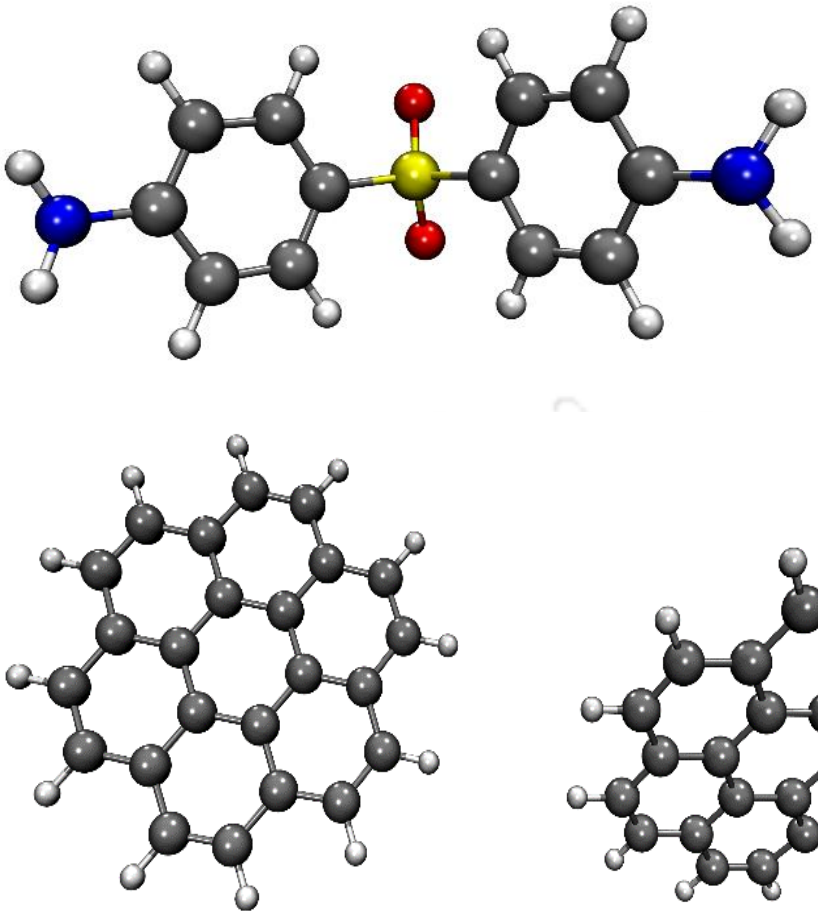

Atom legend: white = H, gray = C, yellow = S, red = O, and blue = N.

Figure 4.2.2 The optimized structure of (a) Bisphenol A diglycidyl ether (epoxy), (b) 4, 4-Diaminodiphenyl (hardener), and (c) RH-QDs using B3LYP/6-311G (d, p) level of theory in Gaussian 09W

In addition, multiple orientations and conformations of the RH-QDs were investigated for the epoxy and hardener system, with the aim of selecting the structure with the lowest energy value. Following geometry optimizations, the total adsorption energy (E_{ads}) calculations were carried out using same functional and basis set. The E_{ads} of the RH-QDs surface, epoxy and hardener system was computed using the supramolecular approach and corrected for basis set superposition error (BSSE) using the counterpoise (CP) method proposed by Boys and Bernardi, as given in equation 4.2.1.

$$E_{ads} = [E_{AB} - (E_A + E_B)] \quad \textbf{(4.2.1)}$$

Here E_{AB} is the total energy of RH-QDs surface and epoxy-hardener system while E_A and E_B are the total energy of the monomers i.e., RH-QDs and epoxy – hardener system respectively. If total adsorption energy of the system is less than zero, then the adsorption process is considered to be spontaneous (Zhou et al., 2023b). Further, more negative adsorption energy implies more stable system. The chemical stability and reactivity of the system can also be evaluated through the energy gap between HOMO (Highest Occupied Molecular Orbital) and LUMO (Lowest Unoccupied Molecular Orbital). The Koopmans's theorem was used to calculate the quantum chemical parameters such as chemical potential, chemical hardness and other chemical descriptors as follows.

Energy gap, $\boldsymbol{\Delta E = E_{LUMO} - E_{HUMO}}$ **(4.2.2)**

Electronegativity and chemical potential, $\boldsymbol{\chi = -\mu = -0.5(I + A)}$ **(4.2.3)**

Hardness, $\boldsymbol{\eta = 0.5\ (I - A)}$ **(4.2.4)**

Where, I and A corresponds to $-E_{HOMO}$ and $-E_{LUMO}$ respectively

Softness, $\boldsymbol{\sigma = \frac{1}{\eta}}$ **(4.2.5)**

Electrophilicity, $\boldsymbol{\omega = \frac{\mu^2}{2\eta}}$ **(4.2.6)**

Further, with the help of quantum chemical calculations, the number of electrons transferred (ΔN) was calculated by the following equation. ΔN is the difference of electronegativity between metal surface and coating.

$$\boldsymbol{\Delta N = \frac{\phi_{Fe} - \chi_{Fe}}{2(\eta_{Fe} + \eta_{inhi})}} \quad \textbf{(4.2.7)}$$

Here, η_{Fe} value of 0 eV/mol was chosen for the calculation of ΔN. The value ϕ_{Fe}, work function of Fe (110) is taken as 4.83 eV (Hsissou et al., 2020; Sastri and Perumareddi, 1997). It is to be noted that corrosion inhibition studies typically used Fe (110) plan (Cao et al., 2014; Kokalj, 2012).

4.2.3 Results and Discussion

4.2.3.1 Characterization of RH-QDs

The Raman spectroscopy measurements were performed to understand the structure and degree of carbonization of RH-QDs and the results are shown in **Figure 4.2.3(a).** The D band (1347 cm^{-1}) and G band (1587 cm^{-1}) in the Raman spectra of RH-QDs stand for the structural disorder of sp^2-domain and the presence of the crystalline phase, respectively(Ma et al., 2023; Wang et al., 2016). **Figure 4.2.3(a)** illustrates that the intensity ratio in the Raman spectra (I_D/I_G) is 0.84.

The FT-IR spectrum of the RH-QDs was measured in order to identify the components and displayed in **Figure 4.2.3(b)**. The stretching vibrations of hydroxyl (–OH) are represented by a large band in the spectrum at around ~3300 cm^{-1}. Likewise, the stretching vibrations of C=O in carbonyl groups and, the stretching vibrations of C-N in amine groups are associated with the peaks at 1585 and 1384 cm^{-1}. These functional groups give them a hydrophilic character and greatly increase their water dispersibility(Abbas et al., 2020). It was verified that synthetic RH-QDs do not contain any silica contaminants.

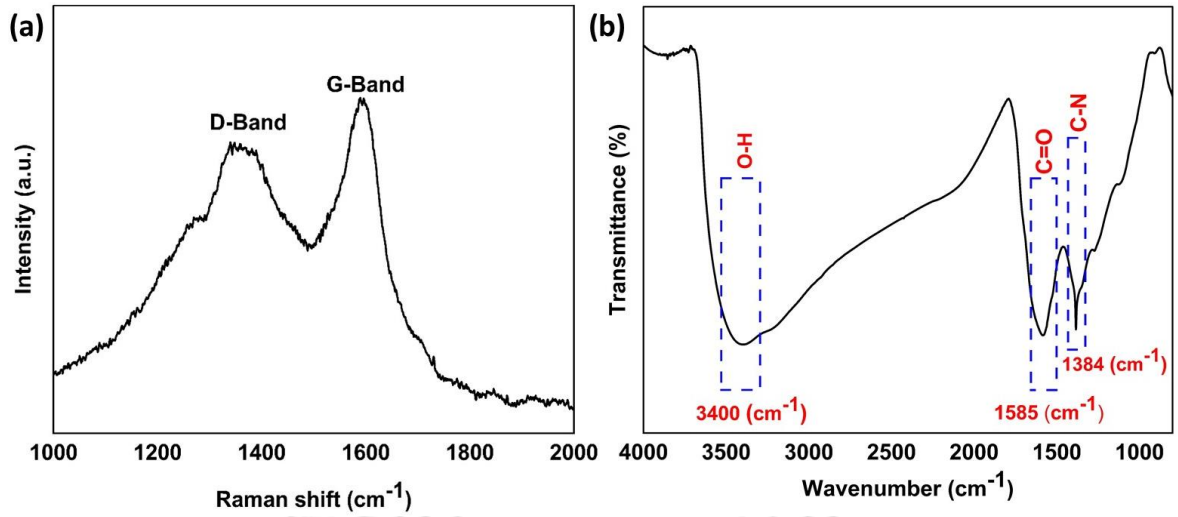

Figure 4.2.3 (a) Raman spectra, and (b) FTIR of RH-QDs

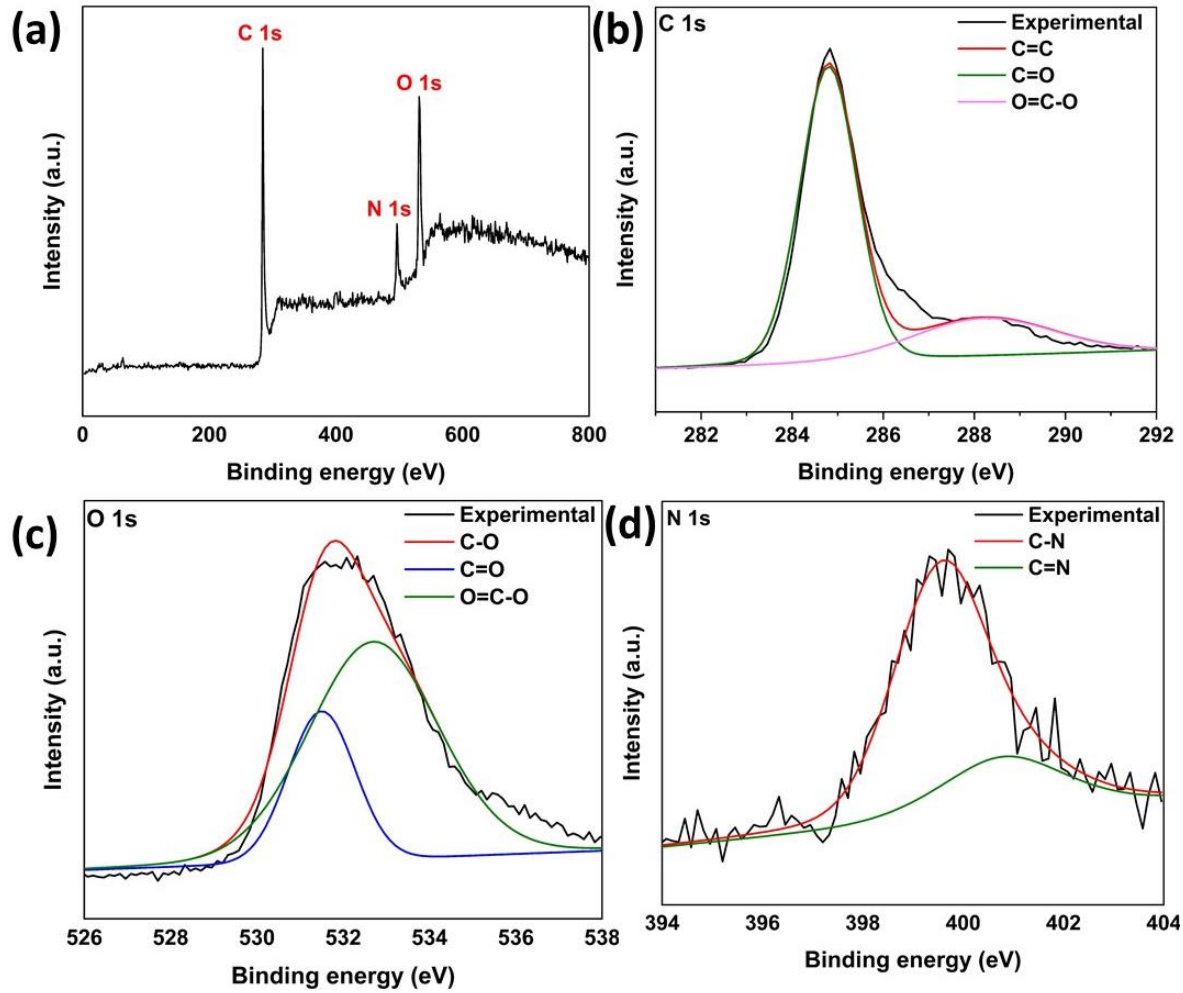

Figure 4.2.4 (a) XPS survey spectrum of RH-QDs, high resolution (b) C 1s, (b) O 1s, and (d) N 1s

The surface chemical properties of the RH-QDs were identified via XPS analysis. As shown in **Figure 4.2.4(a).** three peaks (i.e. C 1s, N 1s, and O 1s) were observed for RH-QDs. Previously, Zheyuan Ding et. al.(Ding et al., 2018) and Zicheng Liang et. al.(Liang et al., 2014) also reported similar peaks. The deconvolution of C 1s spectra leads to three peaks at 284.86, 287.36, and 289.01 eV corresponding to C=C, C=O, and O=CO, respectively(Kundu et al., 2022b) (**Figure 4.2.4b**). The O 1s spectrum **(Figure 4.2.4c)** shows peaks at 530.6 and 533.6 eV which is attributed to the presence of C-O, C=O, and O=C−O, respectively(Kundu et al., 2022b). The N 1s spectrum **(Figure 4.2.4d)** shows peaks at 531.6 and 532.1 eV corresponding to C-N, and C=N, respectively(Abbas et al., 2020). The elemental composition of RH-QDs samples is shown in **Table 4.2.1** and the C/O ratio of RH-QDs is found to be 2.65.

Table 4.2.1 Atomic concentration data of RH-QDs from XPS analysis

Sample	C atomic (%)	N atomic (%)	O atomic (%)	C/O ratio
RH-QD	67.58	6.92	25.50	2.65

FESEM was used to capture the surface morphology of RH-QDs. **Figure 4.2.5(a)** illustrates the spherical structure of the particle. The TEM findings supported the fabrication of highly distributed, uniformly shaped, nanosized RH-QDs (**Figure 4.2.5b).** Significantly, the selected area electron diffraction (SEAD) pattern confirms the amorphous nature of RH-QDs. The particle size RH-QDs is in the range of 1-14 nm with the average particle size of 6.3 ± 0.8 nm (**Figure 4.2.5c). Figure 4.2.5(e)** shows an HRTEM image of RH-QDs with a lattice space of 0.21 nm. which corresponds to (1120) lattice fringes of graphene(Wang et al., 2016). AFM measurements were used to determine the thickness of RH-QDs. The AFM picture and height profiles **(Figure 4.2.6)** demonstrate that the RH-QDs have a thickness of around 2.9 – 3.0 nm, equivalent to 2-3 layers of graphene(W. Wang et al., 2018a).

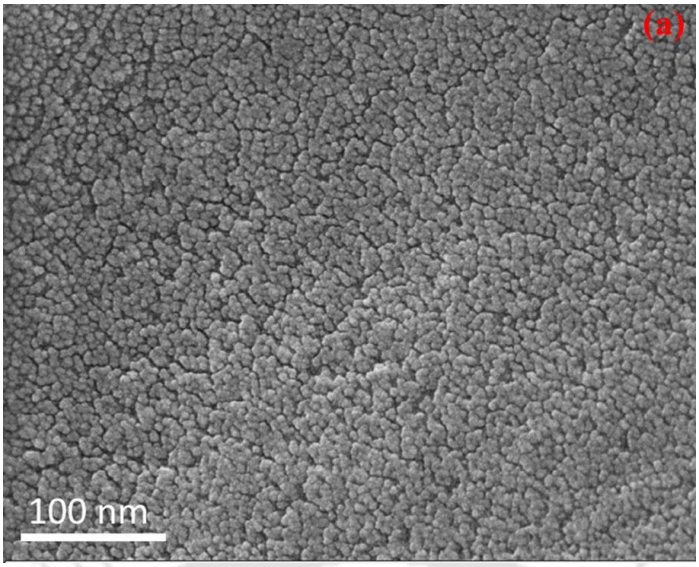

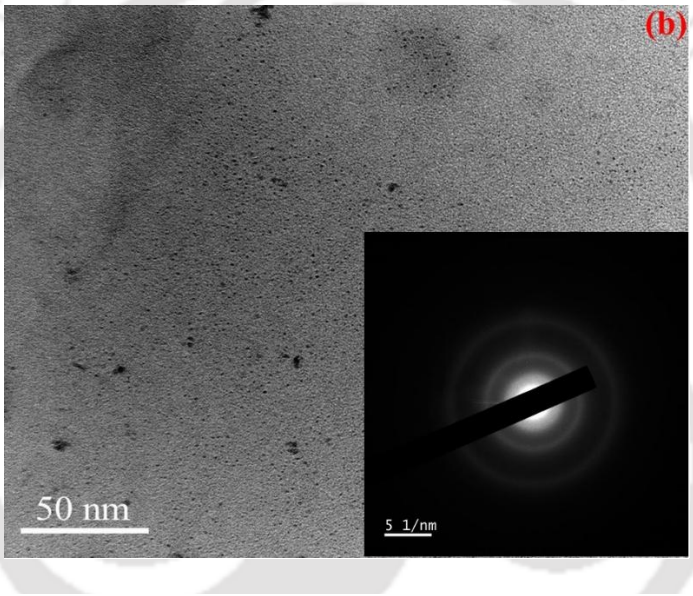

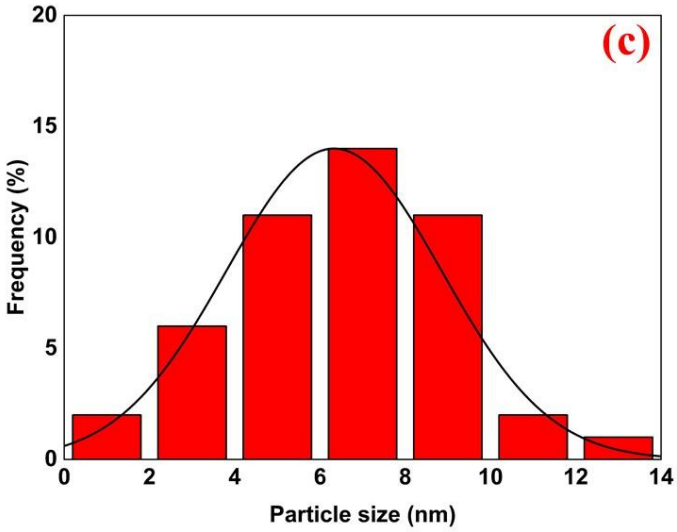

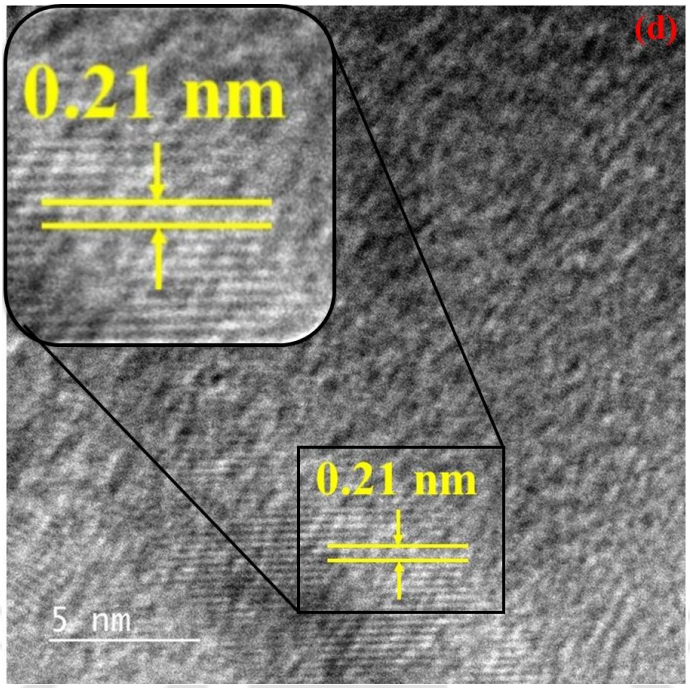

Figure 4.2.5 (a) FESEM image, (b) TEM image with insert SEAD pattern (c) size distribution histogram, and (d) HRTEM image and its corresponding lattice fringes of RH-QDs

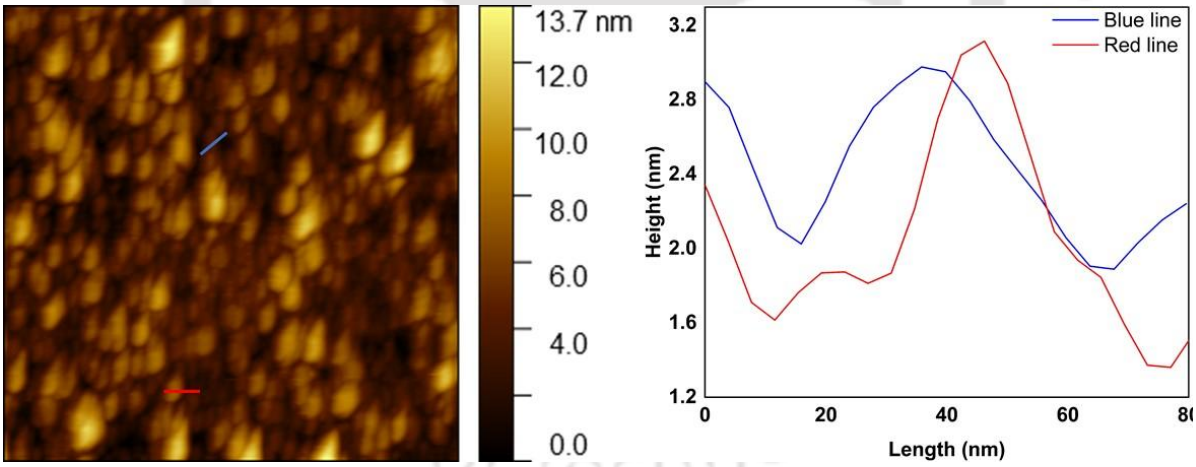

Figure 4.2.6 AFM image and corresponding height profile of RH-QDs

4.2.3.2 Analysis of coatings

The morphology of coatings on the carbon steel substrate was studied using FESEM micrographs. In the FESEM image of pure epoxy **(Figure 4.2.7a)**, a uniform surface with micropores was observed. After the addition of 0.1 and 0.5 wt% RH-QDs in epoxy, the pores or holes were not observed on the surface and resulted in a denser surface as shown in **Figure**

4.2.7(b-c). The uniform dispersion of RH-QDs in the epoxy matrix was responsible for the smooth surface and enhanced compactness of the coating. It indicates that the interfacial interaction between RH-QDs and epoxy is stronger and further, RH-QDs improved the compatibility between the matrix of epoxy and hardener.

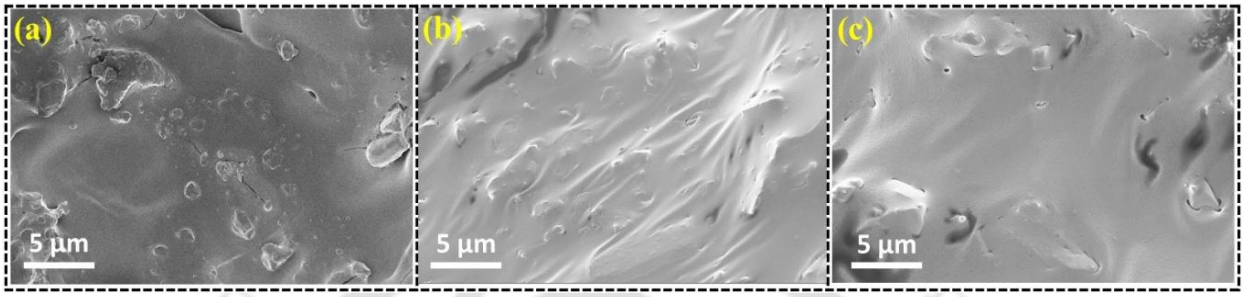

Figure 4.2.7 Morphology of the coating on the carbon steel substrate (a) epoxy, (b) 0.1 wt% RH-QD/epoxy, and (c) 0.5 wt% RH-QD/epoxy

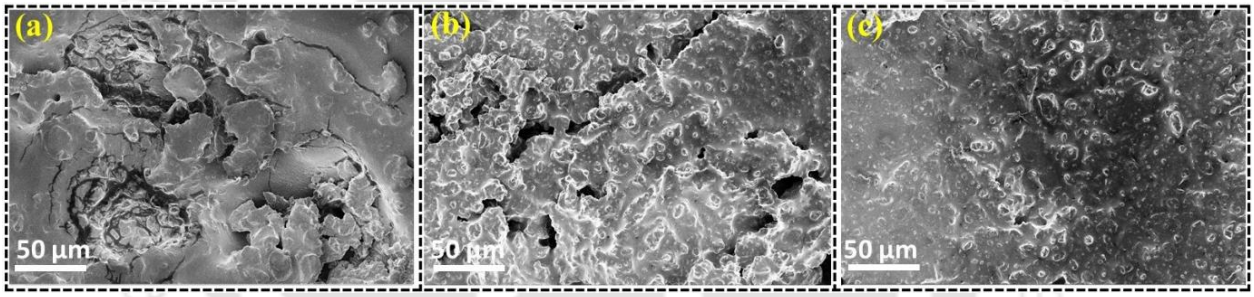

Figure 4.2.8 FESEM images of fracture surfaces (a) pure epoxy, (b) 0.1 wt% RH-QD/epoxy, and (c) 0.5 wt% RH-QD/epoxy

Further, FESEM micrograph of fracture surfaces are presented in **Figure 4.2.8 (a-c)**. The pure epoxy coating exhibited conspicuous voids and uneven fissures, as depicted in **Figure 4.2.8a**, resulting from the dehydration process that took place during the epoxy's curing phase (Qiu et al., 2017b; J. Wang et al., 2019). The fracture surface of the 0.1 wt% RHQD/epoxy coating exhibited multiple wrinkles and significant pores, which were caused by the accumulation of RHQD **(Figure 4.2.8b)**. However, when 0.5 wt% RHQD was added to the epoxy matrix, a smooth and flawless surface was achieved **(Figure 4.2.8c)**. This indicates that the well-distributed 0.5 wt% RHQD improved the overall strength and stability of the coating system.

Surface properties

The findings of the water contact angle on the prepared coatings are shown in **Figure 4.2.9.** The reported water contact angle is based on the average of three measurements made on each sample, and the error bar is determined by comparing the average reported data to the three measurements. The water contact angle of epoxy after 1-day immersion was 71.2 ± 1.1º and decrease to 62.02 ± 0.7º after 45 days of immersion in 3.5 wt% NaCl solution. The hydrophilic surface of the epoxy coating on the carbon steel substrate degrades when exposed to 3.5 wt% NaCl solution due to the hydrolytic breakdown of the epoxy coatings (Zhou et al., 2022d). The water contact angle of both 0.1 wt% RH-QD/epoxy and 0.5 wt% RH-QD/epoxy coatings is not significantly higher compared to pure epoxy coating. However, the values are slightly increased with respect to immersion time as evident from the **Figure 4.2.9**. As the surface becomes rougher and more hydrophobic when the immersion time increases, it appears that the epoxy matrix is damaged and the RH-QDs are in touch with the carbon steel surface.

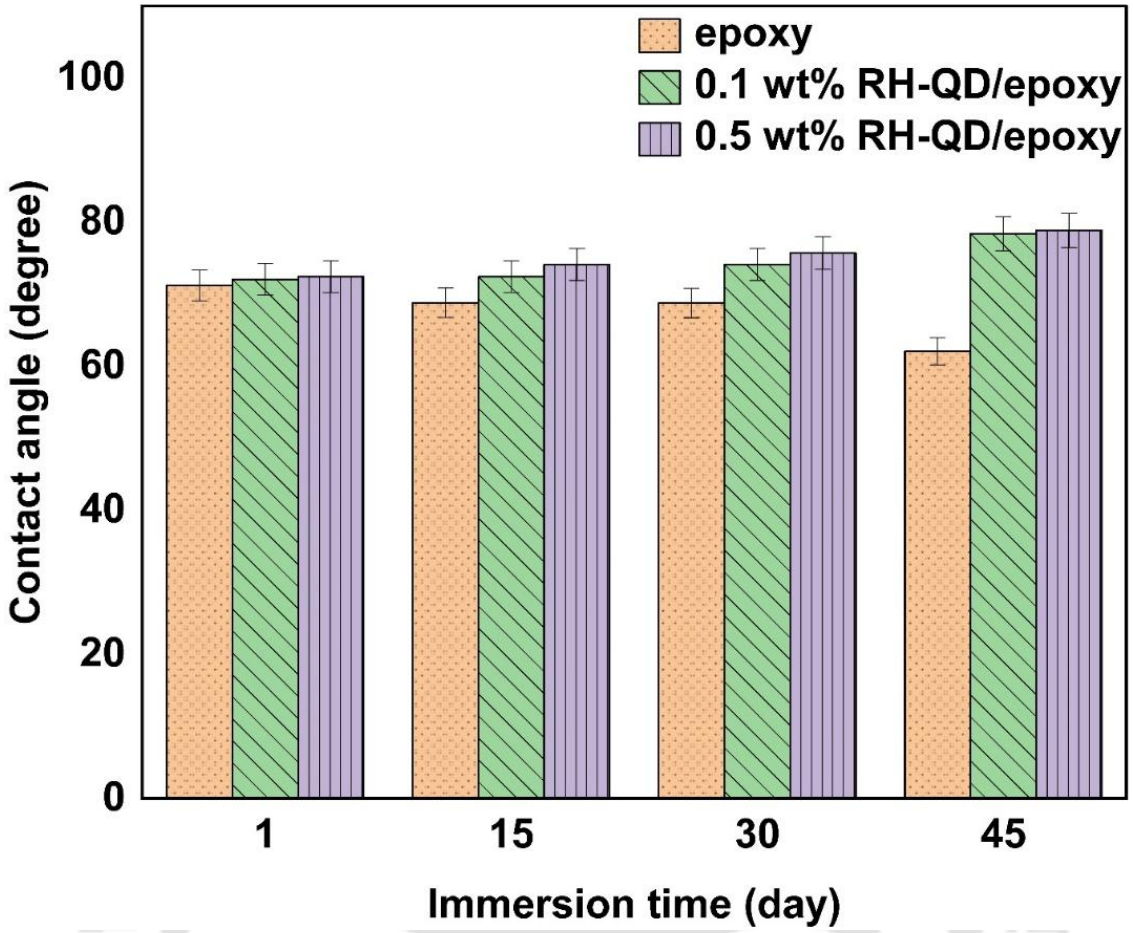

Figure 4.2.9 Contact angle of the coating on the carbon steel substrate (a) epoxy, (b) 0.1 wt% RH-QD/epoxy, and (c) 0.5 wt% RH-QD/epoxy

4.2.3.3 Coating Performance

Open circuit potential (OCP) measurement

Prior to perform the potentiodynamic polarization analysis (shown in **Figure 4.2.11**), the OCP experiments were conducted for epoxy, 0.1 wt% RH-QD/epoxy, and 0.5 wt% RH-QD/epoxy and presented in the **Figure 4.2.10**. The E_{corr} values for the epoxy, 0.1 wt% RH-QD/epoxy, and 0.5 wt% RH-QD/epoxy coating deviate from the OCP values due to changes occur on the coating surface during the cathodic scanning.

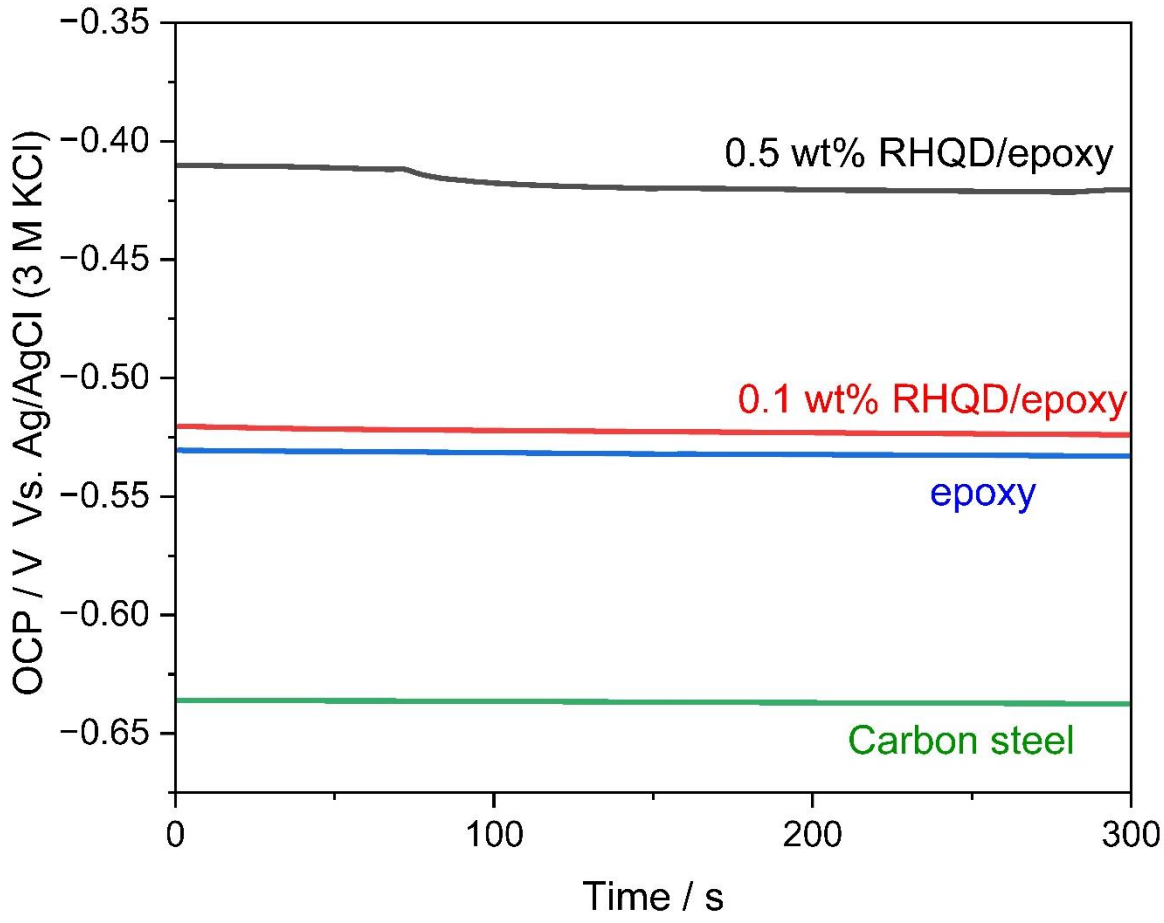

Figure 4.2.10 Open circuit potential for the pure epoxy, 0.1 wt% RH-QD/epoxy, and 0.5 wt% RH-QD/epoxy coatings in 3.5 wt% NaCl solution.

Potentiodynamic polarization

A potentiodynamic polarisation test was used to evaluate the anti-corrosion capabilities of carbon steel substrate with epoxy, 0.1 wt% RH-QDs/epoxy, and 0.5 wt% RH-QDs/epoxy coatings in 3.5 wt% NaCl solution (Lv et al., 2023; Rajitha et al., 2020; Talukdar et al., 2022a). The results obtained from these studies are presented in **Figure 4.2.11.** The values of corrosion current density (i_{corr}), corrosion potential (E_{corr}), cathodic Tafel slope (β_c) and anodic Tafel slope (β_a) which are extracted from these plots are reported in **Table 4.2.2.** Further, using the following Stern-Geary equation, the polarisation resistance (*Rp*), corrosion rate (CR), and coating protection efficiency (PE) were calculated(Kumar and Das, 2023a; Talukdar et al., 2023a).

$$R_p(\text{k}\Omega.\,\text{cm}^2) = \frac{\beta_a \beta_c}{2.303(\beta_a+\beta_c)i_{corr}} \qquad \textbf{(4.2.8)}$$

$$\text{PE}(\%) = \frac{i_{corr,o} - i_{corr,i}}{i_{corr.o}} \times 100 \qquad \textbf{(4.2.9)}$$

Where $i_{corr,o}$ and $i_{corr,i}$ represent corrosion current density (A/cm^2) of uncoated and coated carbon steel substrate respectively. The E_{corr} values of carbon steel coated with pure epoxy, 0.1 wt% RHQDs/epoxy, and 0.5 wt% RHQDs/epoxy coating shifted to a more positive potential with respect to uncoated carbon steel substrate. In comparison to the uncoated carbon steel, the differences in E_{corr} values for epoxy, 0.1 wt% RHQDs/epoxy, and 0.5 wt% RHQDs/epoxy coating are calculated to be 60, 89, and 110 mV, respectively. This significant positive shift illustrates the excellent anti-corrosion properties of the applied coatings, especially for the 0.5 wt% RHQDs/epoxy coating. The corrosion current density of 3.12 (µA/cm^2) was recorded for pure epoxy coating after exposure in 3.5 wt% NaCl. The addition of 0.1 and 0.5 wt% of RH-QDs to the epoxy matrix resulted in a significant decrease in the corrosion current density. It is evident that both the carbon steel dissolution (anodic) and oxygen reduction (cathodic) reaction rates are greatly hindered by 0.1 wt% RHQDs/epoxy and 0.5 wt% RHQDs/epoxy coating. Meanwhile, the 0.5 wt% RHQDs/epoxy coating exhibit a very high *Rp* value (14546.52 kΩ.cm^2), low corrosion rate (0.0002±0.00 mm/year) and excellent PE (99.90 %). This indicates that the very small amount of RHQDs plays a vital role to enhance the anti-corrosion characteristics of epoxy coating in the harsh sea environment.

Compare to pure epoxy coating, both the concentrations of RH-QDs (0.1 wt% and 0.5 wt%) show superior protection efficiency which indicates that RH-QDs are uniformly dispersed in the epoxy matrix without any significant agglomeration. The experiment was also performed with 1 wt% RHQD/epoxy However, the decrease in PE is observed due to the aggregation of RH-QDs in epoxy matrix (**Figure 4.2.12**). Electrochemical corrosion measurement of 1 wt% RH-QD/epoxy coating presented in the **Table 4.2.3**.

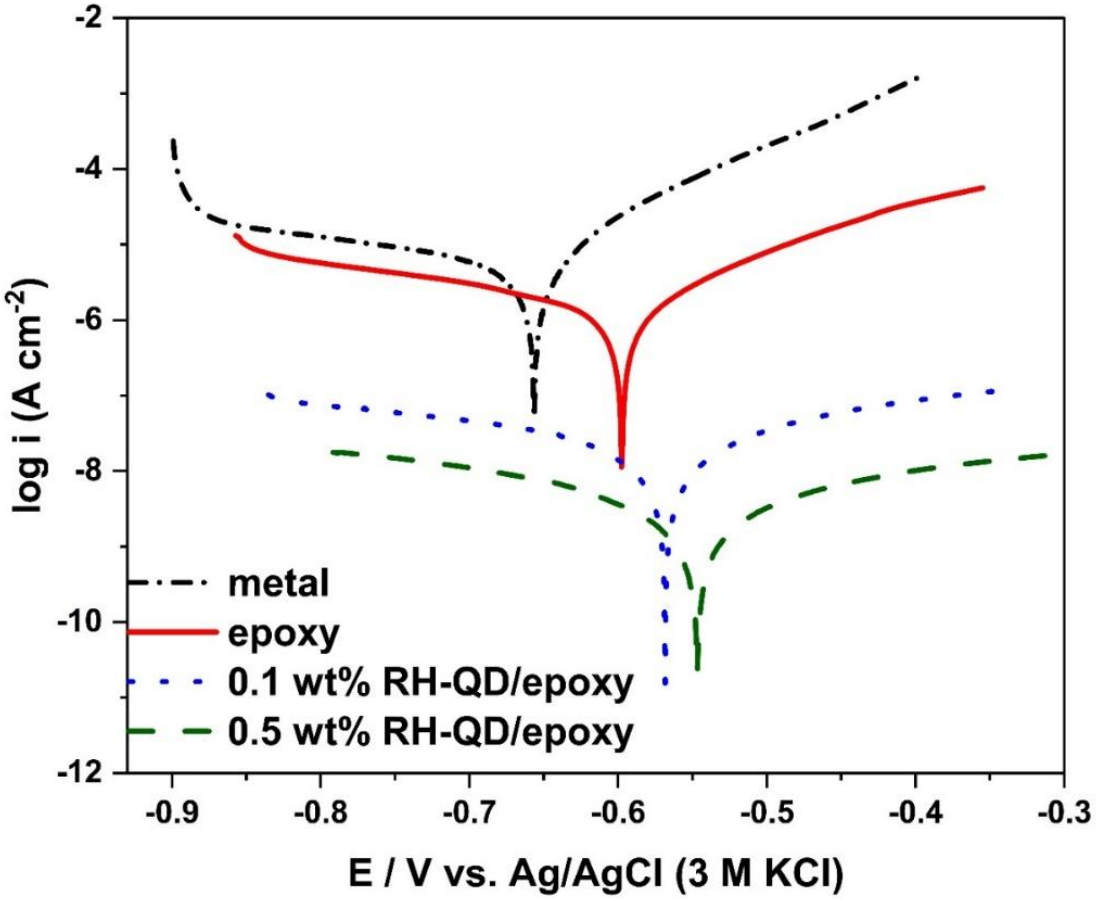

Figure 4.2.11 Potentiodyamic polarization curves of carbon steel (blank), epoxy, 0.1 wt% RH-QD/epoxy, and 0.5 wt% RH-QD/epoxy coatings in 3.5 wt% NaCl solution

Table 4.2.2 Electrochemical parameters of anticorrosive coatings

	E_{corr} (mV)	i_{corr} (μA/cm^2)	β_a (V/dec)	β_c (V/dec)	CR (mm/year)	R_p (KΩ.cm^2)	PE (%)
Carbon steel	-657±6.2	8.64±0.25	0.11±0.006	0.71±0.007	0.201±0.005	4.92±0.1	-
epoxy	-597±6.1	3.12±0.09	0.18±0.002	0.90±0.006	0.0720±0.003	21.17±0.4	63.8±0.15
0.1 wt% RHQD/epoxy	-568±4.8	0.16±0.006	0.82±0.006	0.56±0.009	0.003±0.00	900.96±18.1	98.1±0.49
0.5 wt% RHQD/epoxy	-547±5.0	0.01±0.001	0.65±0.003	0.54±0.004	0.0002±0.00	14546.52±36.4	99.9±0.54

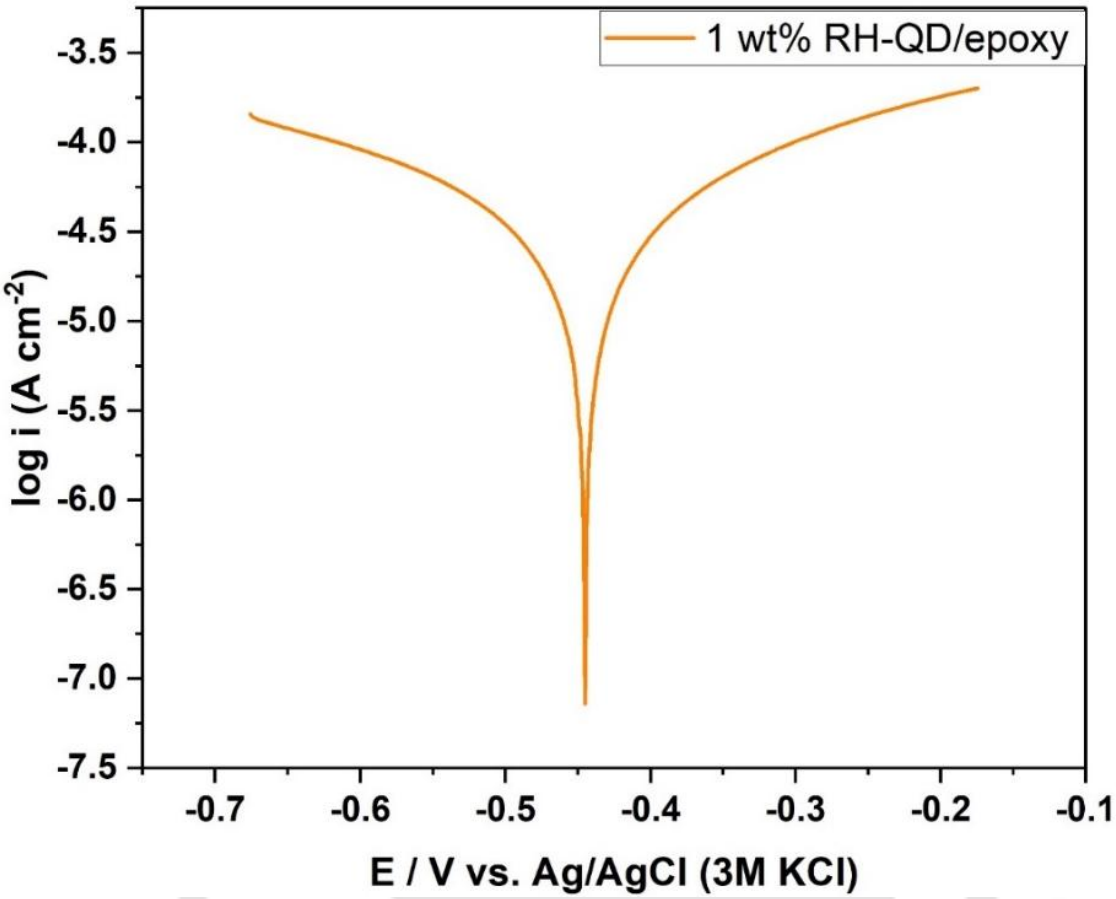

Figure 4.2.12 Polarization curve of 1 wt% RH-QD/epoxy coating in 3.5 wt% NaCl solution

Table 4.2.3 Electrochemical corrosion measurement of 1 wt% RH-QD/epoxy coating

	E_{corr} (mV)	i_{corr} (μA/cm^2)	β_a (V/dec)	β_c (V/dec)	CR (mm/year)	R_p (KΩ.cm^2)	PE (%)
1 wt% RHQD/epoxy	-445±7.12	0.59±0.004	2.14±0.01	1.11±0.008	0.013±0.004	530.16±5.83	93.07±1.03

EIS Analysis

EIS studies are employed to measure the coating's protection capacity against corrosion in 3.5 wt% NaCl solution. **Figure 4.2.13** shows the Nyquist plots of the epoxy, 0.1 wt% RH-QD/epoxy, and 0.5 wt% RH-QD/epoxy coatings following various intervals of soaking in the 3.5 wt% NaCl solution and the Bode plots are presented in **Figure 4.2.14.** The continuous solid

line in these diagrams represents the results of simulated impedance data from the electrical equivalent circuit (EEC). The dotted curve depicted in these figures represents the experimental data that were collected. Low-frequency impedance modulus ($|Z|_{0.01\ Hz}$) could be taken as an indicator to understand the impermeability of various coating. Wider capacitive arcs frequently indicate more effective protection of coating systems (Ye et al., 2021b). Initially, after 1 day of immersion in 3.5 wt% NaCl solution, the $|Z|_{0.01\ Hz}$ values of epoxy, 0.1 wt% RH-QD/epoxy, and 0.5 wt% RH-QD/epoxy coatings were 4.45×10^3, 1.31×10^7, and 1.53×10^8 ($\Omega\ cm^2$) respectively. It is clearly evident that the anti-corrosive property of RH-QDs is comparable to the QDs prepared from conventional chemical method. It is to be noted that when the concentration of RH-QDs in epoxy increases from 0.1 to 0.5 wt%, the $|Z|_{0.01\ Hz}$ values after 24 hours immersion in 3.5 wt% NaCl solution is also increasing from $\sim 10^7$ to 10^8 ($\Omega\ cm^2$). After 45 days of immersion, it was clear that the impedance values for epoxy and RH-QDs/epoxy coatings had significantly decreased. Nevertheless, during the whole immersion duration, the composite coating with a 0.5 wt% RH-QD/epoxy coating demonstrated the greatest impedance modulus. After 45 days of immersion in 3.5 wt% NaCl solution the $|Z|_{0.01\ Hz}$ values of 0.1 wt% RH-QD/epoxy, and 0.5 wt% RH-QD/epoxy coatings were noted as 2.62×10^5 and 9.12×10^5 ($\Omega\ cm^2$), respectively. The results show that the OCP value is significantly higher for RH-QDs/epoxy coatings as compared to pure epoxy coating even after 45 days of immersion. The breakpoint frequency (f_b), the frequency corresponds to the phase angle -45° in the Bode plot, is another parameter used to characterize the anti-corrosive performance(Chijia Wang et al., 2021; Yeganeh et al., 2019). Lower f_b value indicates the higher corrosion resistance. In this study, the f_b value is not observed for pure epoxy coating as the phase angle is greater than -45 ° in the high frequency region. It indicates that pure epoxy coating possesses lower corrosion resistance. Similar observations were reported for other coatings in the literature (Pourhashem et al., 2017; M. Zhang et al., 2022). However, the f_b value is lower for 0.5 wt% RH-QDs /epoxy

(158.48 Hz) compared to that of 0.1 wt% RH-QDs /epoxy (223.87 Hz) which is due to the higher corrosion resistance provided by the highly dispersed RH-QDs in the epoxy matrix. Although, f_b value is increasing with immersion time, still the value is lower for 0.5 wt% RH-QDs/epoxy even after 45 days of immersion.

To examine the anticorrosion properties of various coatings, the EEC modelling was employed and ZSimpWin software was used to estimate the EEC parameters. The EIS data was fitted with equivalent electrical circuit shown in **Figure 4.2.15**. The selected comparable circuit shows a best fit quality ($\chi^2 < 0.01$). In the model, R_s, Q_c, Q_{dl}, R_{pore} and R_{ct} represent solution resistance, capacitance, double layer capacitance, pore resistance and charge transfer resistance, respectively(Ye et al., 2021a). In place of an ideal capacitor, a constant phase element (CPE, Q) is proposed to provide better fitting results. The following equation describes the impedance of CPE (Devi et al., 2023a; Hazarika et al., 2023d; Zhou et al., 2022b).

$$Z = \frac{(j\omega)^{-n}}{Y_0} \qquad \textbf{(4.2.10)}$$

$$Q = Y_0(\omega_{max})^{n-1} \qquad \textbf{(4.2.11)}$$

Where ω_{max}, Y_0, and j denote for the angular frequency, CPE parameter, and imaginary root, respectively. The ω_{max} corresponds to the frequency associated with maximum Z_{imag}. When n = 1, the CPE is equivalent to ideal capacitor while n = 0 represents a resistor. The value of n deviates from 1 due to the heterogeneities of the electrode surface (Cheng et al., 2021b; N. R. Dhongde et al., 2023a). It can be clearly observed for all the coatings, the values of R_{po} / R_{ct} display a declining trend and Q_c / Q_{dl} shows an upward trend, indicating the decreased barrier capability of epoxy coating. After 1-day immersion of 0.1 wt% RH-QD/epoxy, and 0.5 wt% RH-QD/epoxy coatings, the values of R_{po} / R_{ct} were 1.33×10^7 / 1.29×10^8 and 2.83×10^7 / 2.86×10^8 (Ω cm^2), respectively as shown in **Figure 4.2.16(a-b).** The significant difference was not observed between the values of R_{po} and R_{ct} for 0.1 wt% RH-QD/epoxy, and 0.5 wt%

RH-QD/epoxy coatings after 15 to 45 days of immersion. **Figure 4.2.16(c-d)** show the Q_c and Q_{dl} trends w.r.t immersion time. After 1 day of immersion, the Q_c value for 0.1 wt% RH-QD/epoxy is higher than 0.5 wt% RH-QD/epoxy. However, overlapping trend was observed after 15 days of immersion for Q_c and Q_{dl} values. In previous studies (Ge et al., 2022; Liu et al., 2023; López-Campos et al., 2024; Shi et al., 2023; X. Yin et al., 2020; Zhou et al., 2022c), similar trends of Qc and Qdl were observed. Due to the higher interfacial interaction and, compatibility between RH-QDs and epoxy matrix, the protection performance of the epoxy coating is significantly improved by inhibiting the penetration of the corrosive fluids, according to the lower *Q* (Q_c, Q_{dl}) and higher *R* (R_{po}, R_{ct}) values.

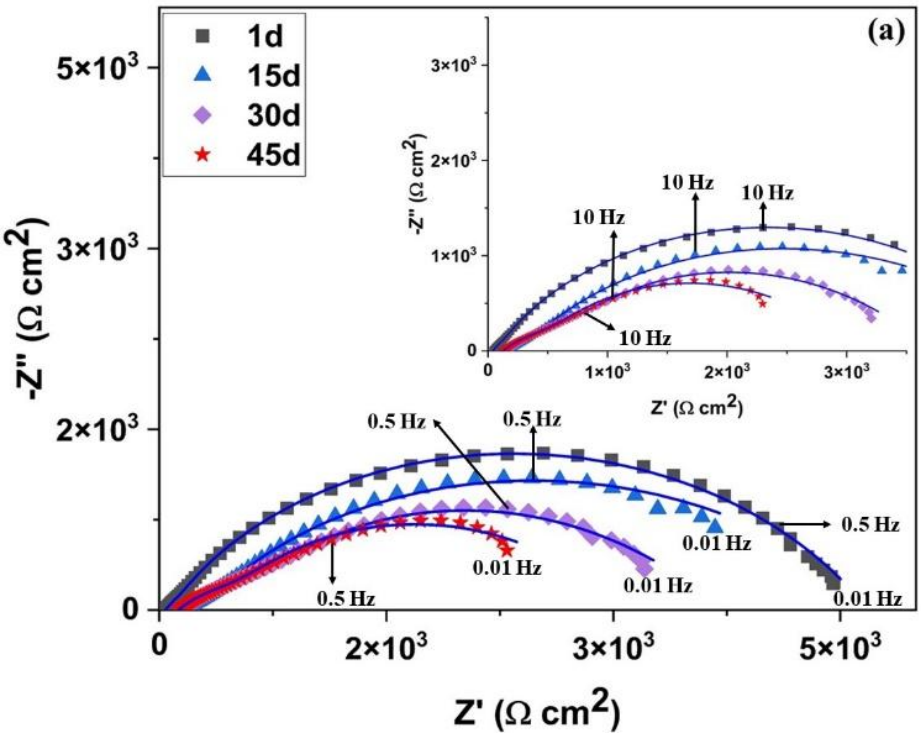

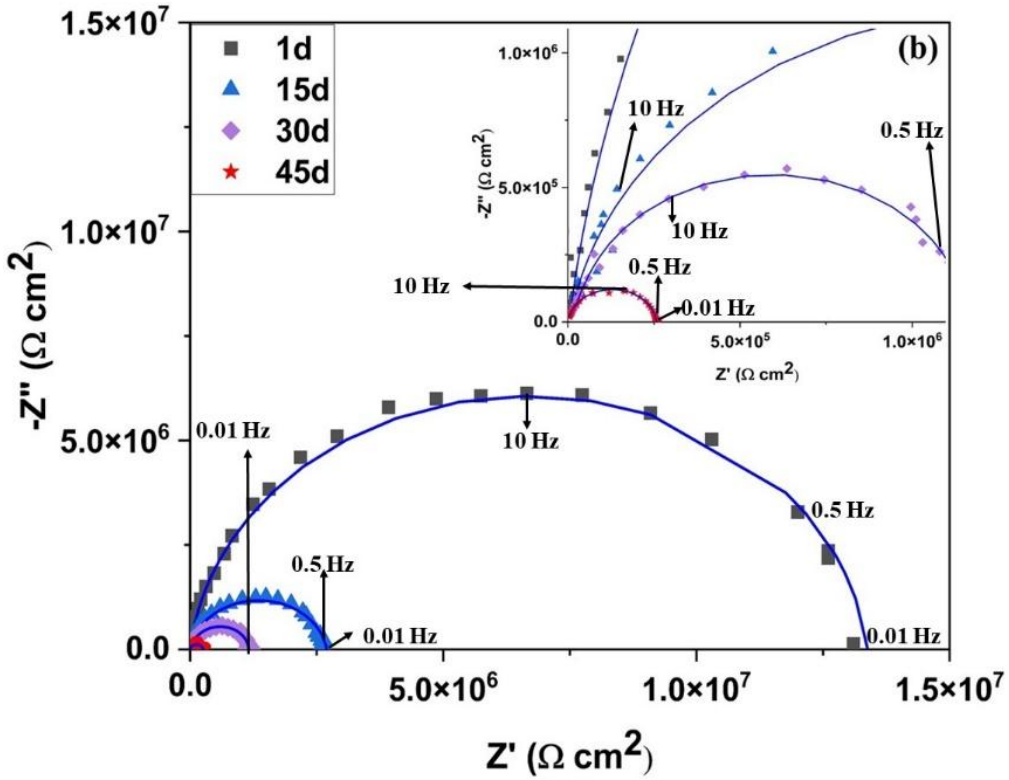

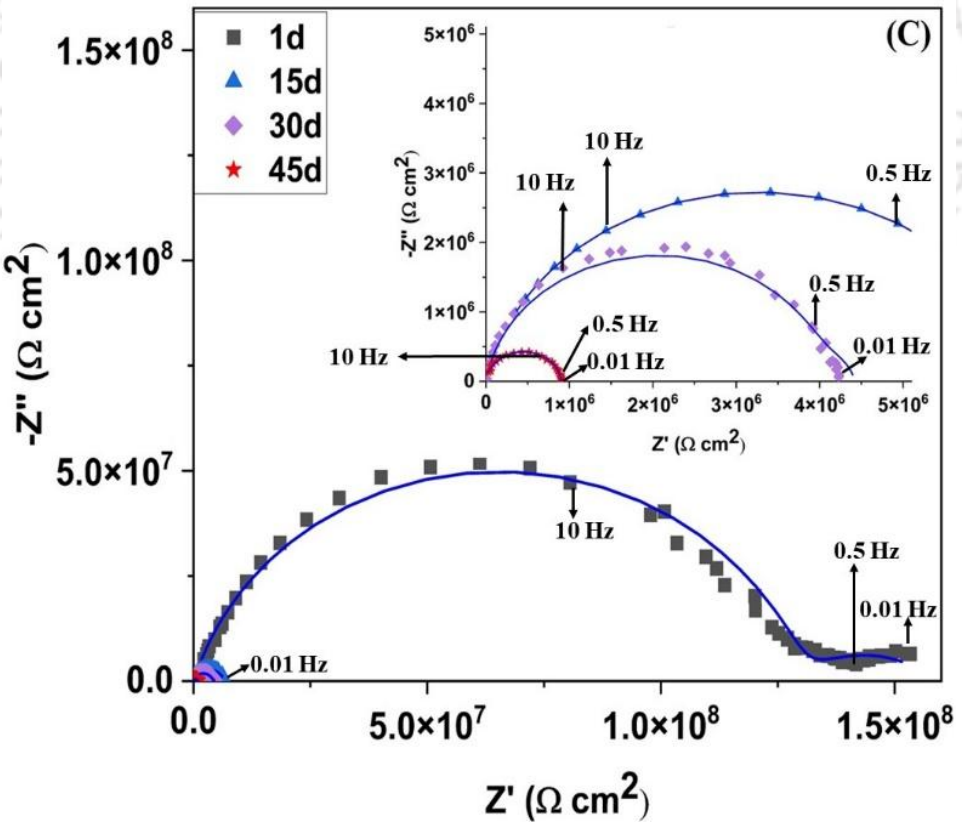

Figure 4.2.13 Nyquist plot of (a) epoxy, (b) 0.1 wt% RH-QD/epoxy, and (c) 0.5 wt% RH-QD/epoxy after immersion in 3.5 wt% NaCl solution for 1, 15, 30, and 45 days: The fitting and experimental data are represented by solid lines and marker points, respectively

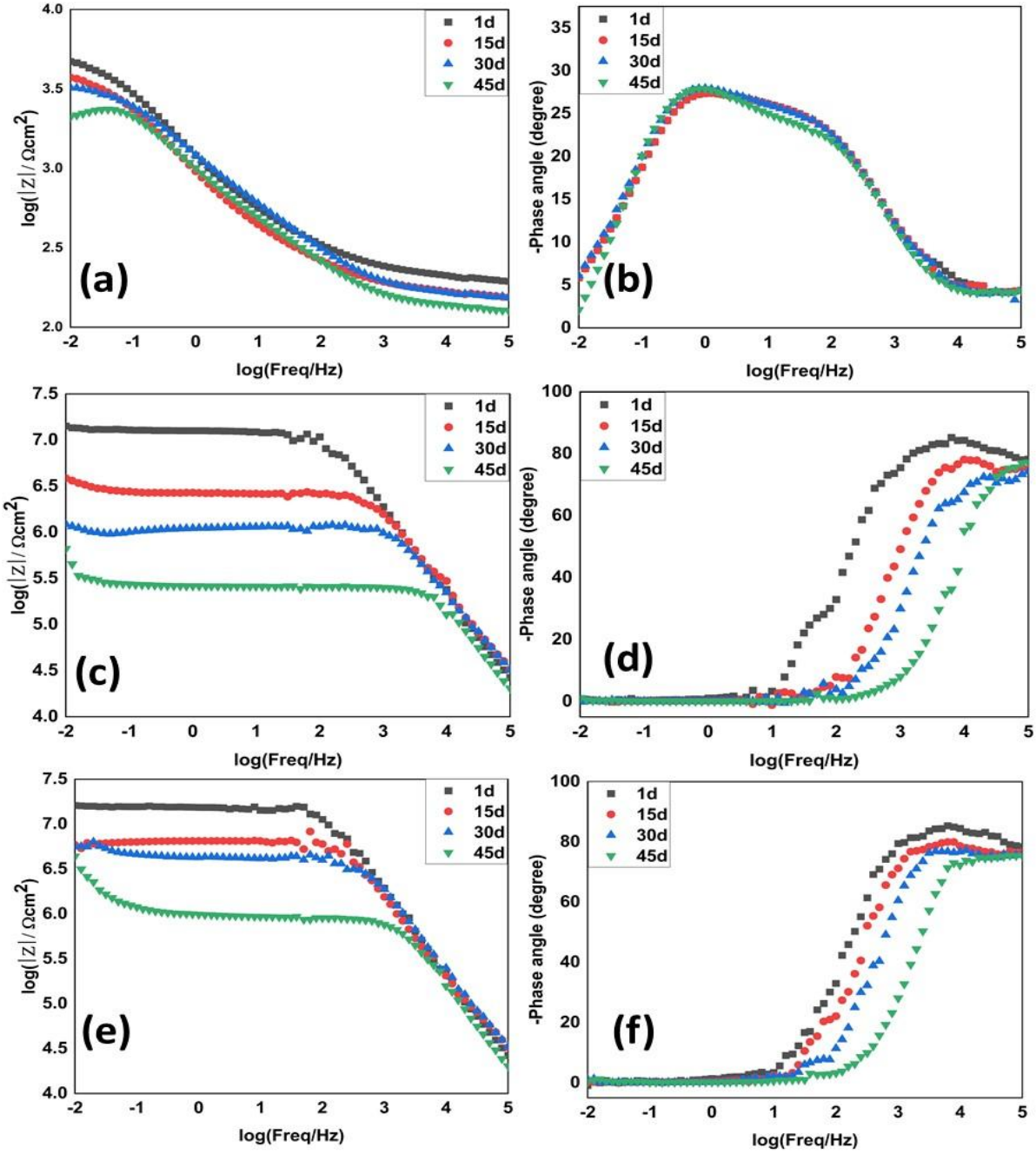

Figure 4.2.14 Bode plot and Phase plot of **(a-b)** epoxy, **(c-d)** 0.1 wt% RH-QD/epoxy, and **(e-f)** 0.5 wt% RH-QD/epoxy after immersion in 3.5 wt% NaCl solution for 1, 15, 30, and 45 day

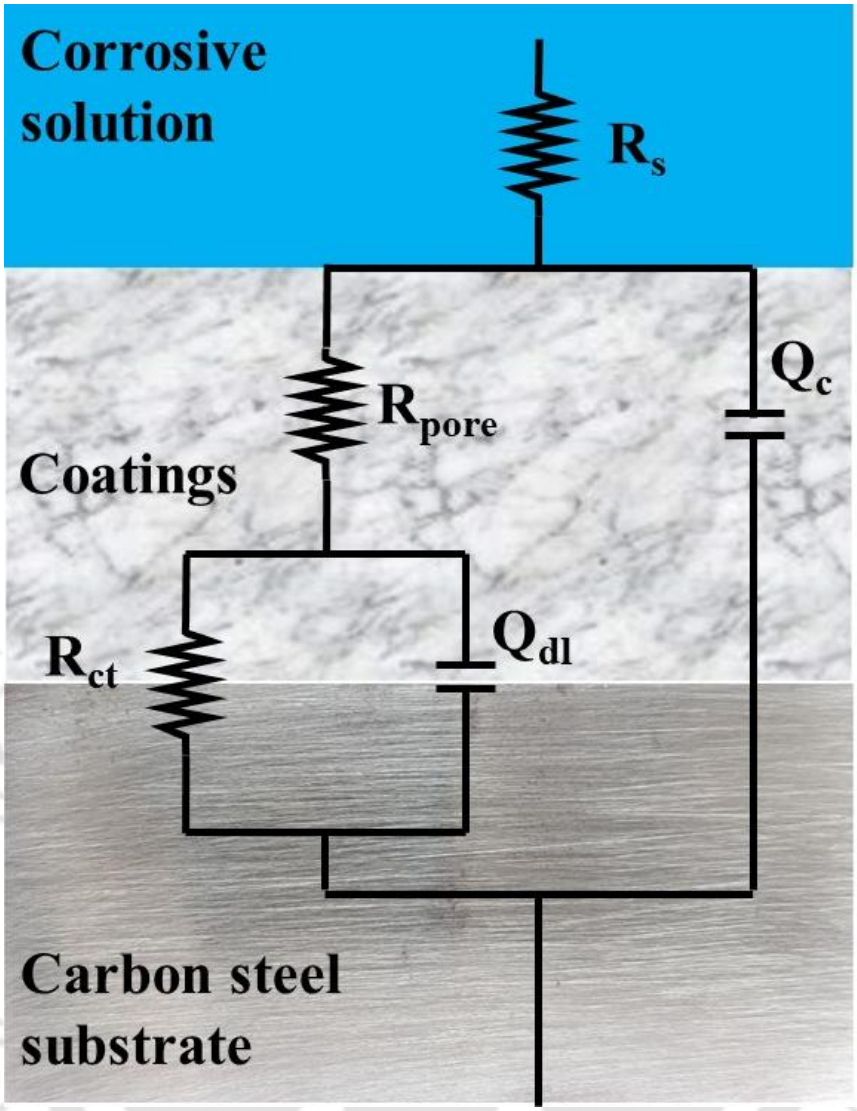

Figure 4.2.15 The equivalent electrical circuit employed to analysed the impedance data acquired for various coatings

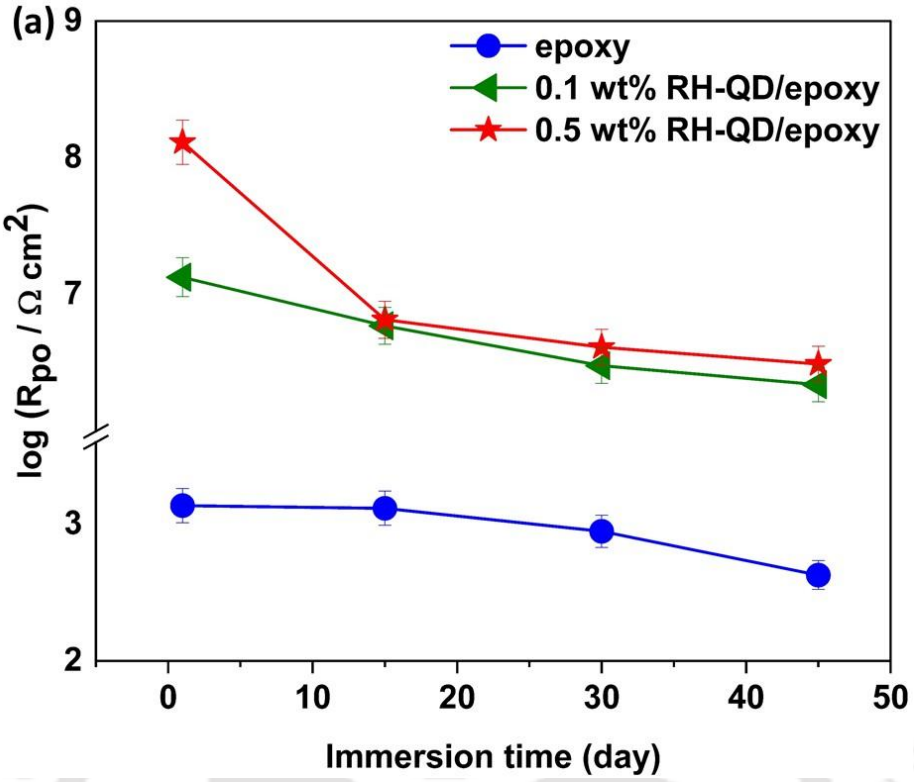

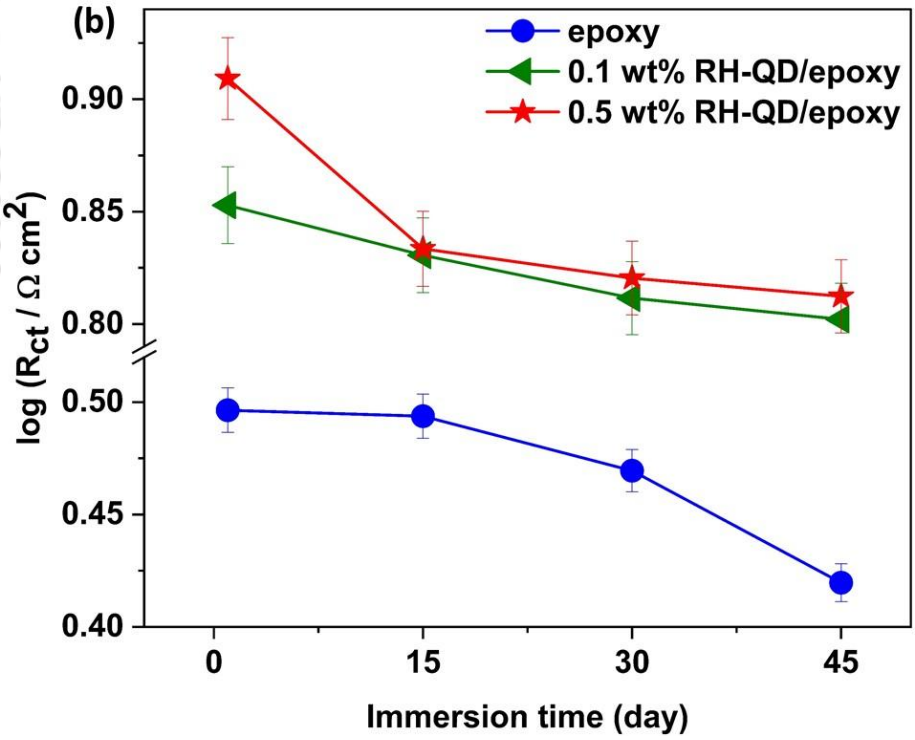

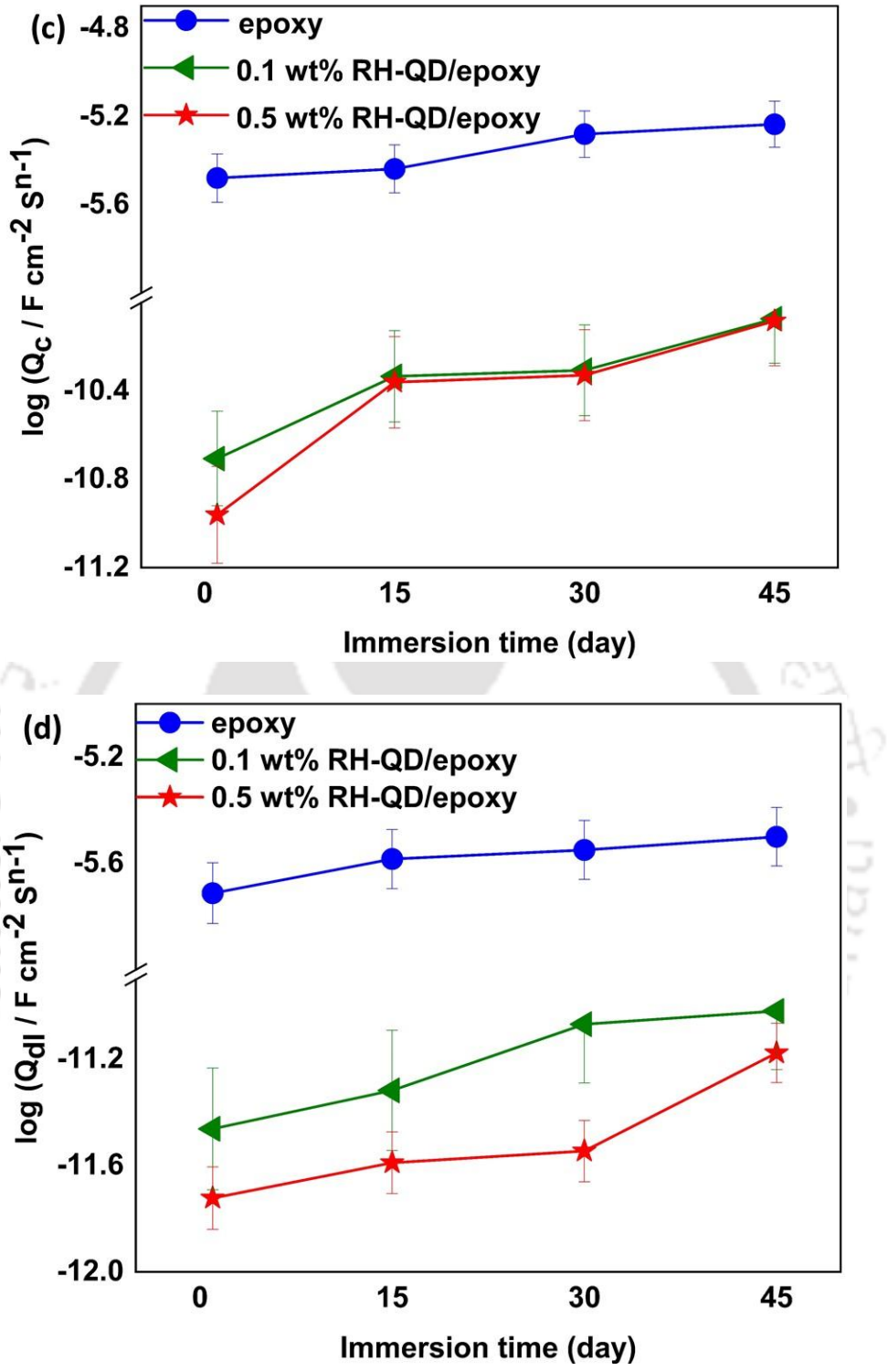

Figure 4.2.16 The values of (a) R_{po}, (b) R_{ct}, (c) Q_c, and (d) Q_{dl} obtained from the fitting results of epoxy, 0.1 wt% RH-QD/epoxy, and 0.5 wt% RH-QD/epoxy after immersion in 3.5 wt% NaCl solution

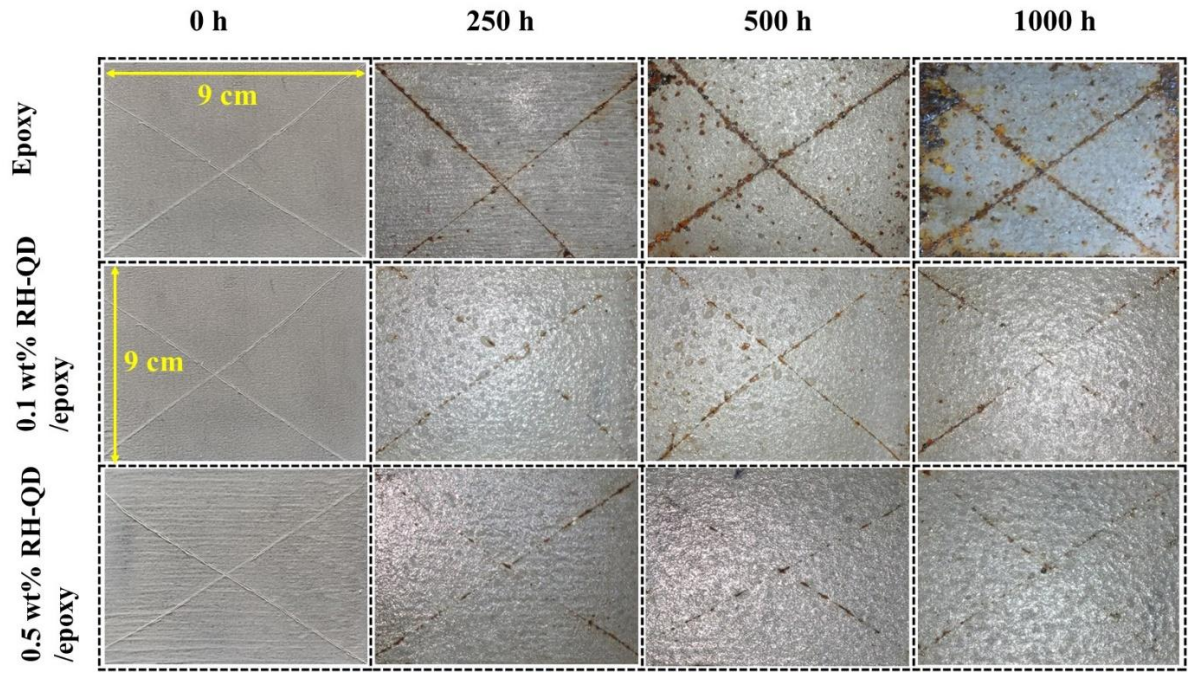

Figure 4.2.17 Photographs of salt spray analysis of carbon steel covered with epoxy, 0.1 wt% RH-QD/epoxy, and 0.5 wt% RH-QD/epoxy. And the dimension carbon steel plate is 9 × 9 × 5 cm^3

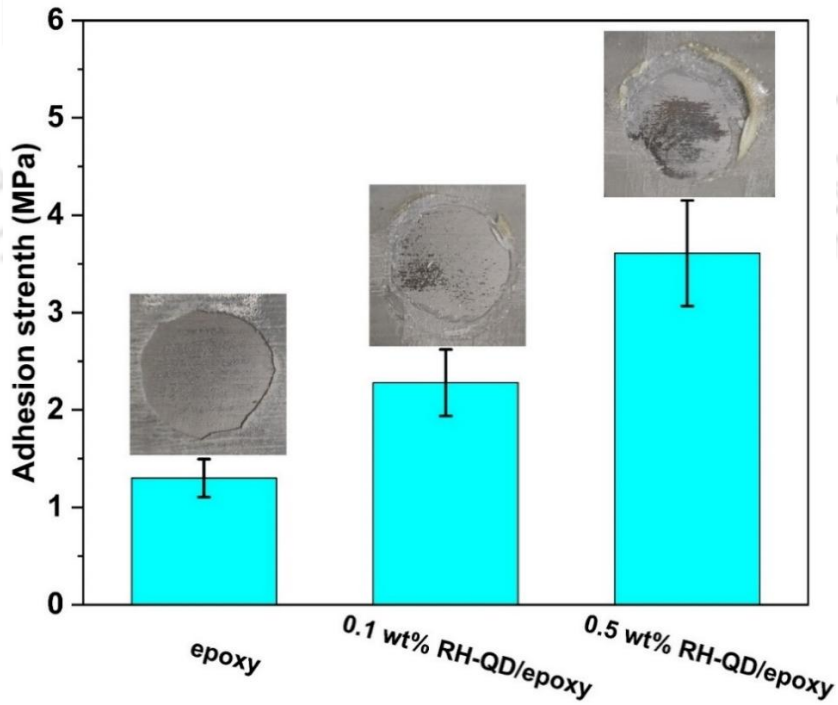

Figure 4.2.18 Adhesion strength of epoxy, 0.1 wt% RH-QD/epoxy, and 0.5 wt% RH-QD/epoxy on the carbon steel obtained from the pull-off test

Salt Spray test

Figure 4.2.17 depicts images taken from coated samples following salt spraying. As ocular investigation reveals, the epoxy coating shows unsatisfactory corrosion protection performance. The clear rust part was observed around the scratched surface of the epoxy coating after 500 h exposure in the salt spray chamber. 0.1 wt% RH-QDs/epoxy coating after 1000 h exposure shows a better corrosion protection performance compared to epoxy. The addition of 0.5 wt% RH-QDs to the epoxy matrix enhances the chemical interaction between coating and carbon steel and, eventually presented excellent anticorrosive properties after 1000 h (42 days) of exposure in salt spray environment. As previously observed by polarization and EIS results, the 0.5 wt% RH-QDs/epoxy coating shows higher anticorrosive properties compared to that of 0.1 wt% RH-QDs/epoxy coating.

Pull-off adhesion test

Figure 4.2.18 displays the coatings' pull-off adhesion strength on the carbon steel substrate. According to the pull-off adhesion test results, all the coatings eventually exhibit adhesive failure and are totally removed from the carbon steel substrate. The epoxy coating on carbon steel has the lowest adhesive strength (1.3 ± 0.5 MPa). The % increase of adhesion strength with respect to pure epoxy coating was found to be 42.22 and 63.88 % for 0.1 wt% RH-QDs/epoxy and 0.5 wt% RH-QDs/epoxy coating, respectively. It was observed that the adhesion strength is increasing with RH-QDs concentration in an epoxy matrix. It is likely due to the uniform dispersion of RH-QDs in the epoxy matrix. Also, the intact contact between the RH-QDs and the epoxy may restrict the free volume. The findings demonstrated that the RH-QDs significantly increased the adhesive strength and prevented the coating from detaching from the carbon steel surface. Polarization, EIS, and salt spray results revealed that the chemical interaction between 0.5 wt% RH-QDs/epoxy and carbon steel is higher and hence

exhibited higher corrosion protection performance. Still, tuning the composition of the RHQD/epoxy coatings further with suitable dopants/functionalizing agents and evaluating their anti-corrosive properties along with mechanical properties such as adhesion test (both wet and dry) degree of blistering and delamination etc. are necessary to employ this RHQD/epoxy coating in industrial applications.

4.2.3.6 Quantum chemical calculation

The experimental studies verified the existence of functional groups on RH-QDs. Furthermore, theoretical DFT calculations was employed to investigate the mechanism of RH-QDs interaction with epoxy and hardener mixture. The initial optimized structures as shown in **Figure 4.2.19(a)** were used to conjugate to the pair configuration of epoxy and hardener. The pair was optimized by using B3LYP level of density functional theory and by using 6-311G (d, p) basis set. It was seen from **Figure 4.2.19(a)** that both epoxy and hardener were interacting with each other via N and O atoms with H atoms. The corresponding N-H and O-H bond distances in Å are displayed in **Figure 4.2.19(a).** The complexes are primarily stabilised through van der Waals interaction, as showed by the minimal equilibrium distances of about 2.08 Å between these moieties. Further, the combined structure was redrawn in Gauss View 6 with RH-QDs and optimized using B3LYP level of theory with basis set 6-311G (d, p), and the same is shown in **Figure 4.2.19(b)**. From **Figure 4.2.19(b)**, short to medium range of interaction was observed between RH-QDs and the epoxy-hardener system. The minimum O-H distance was observed in the range of 2.57 Å - 3.18 Å. Whereas C-H bond was observed in the range between 2.86 Å to 3.75 Å. It implies that close and stronger interaction exists between RH-QDs and epoxy-hardener system leading to higher compactness. The minimum distance of nearest -H atom of the epoxy and hardener is about 2.57 Å, where it can be noted that the aromatic rings of the RH-QDs and H atoms interact via C-H-π interaction. Such alignment attributed to the π-π interaction of epoxy-hardener system with RH-QDs surface.

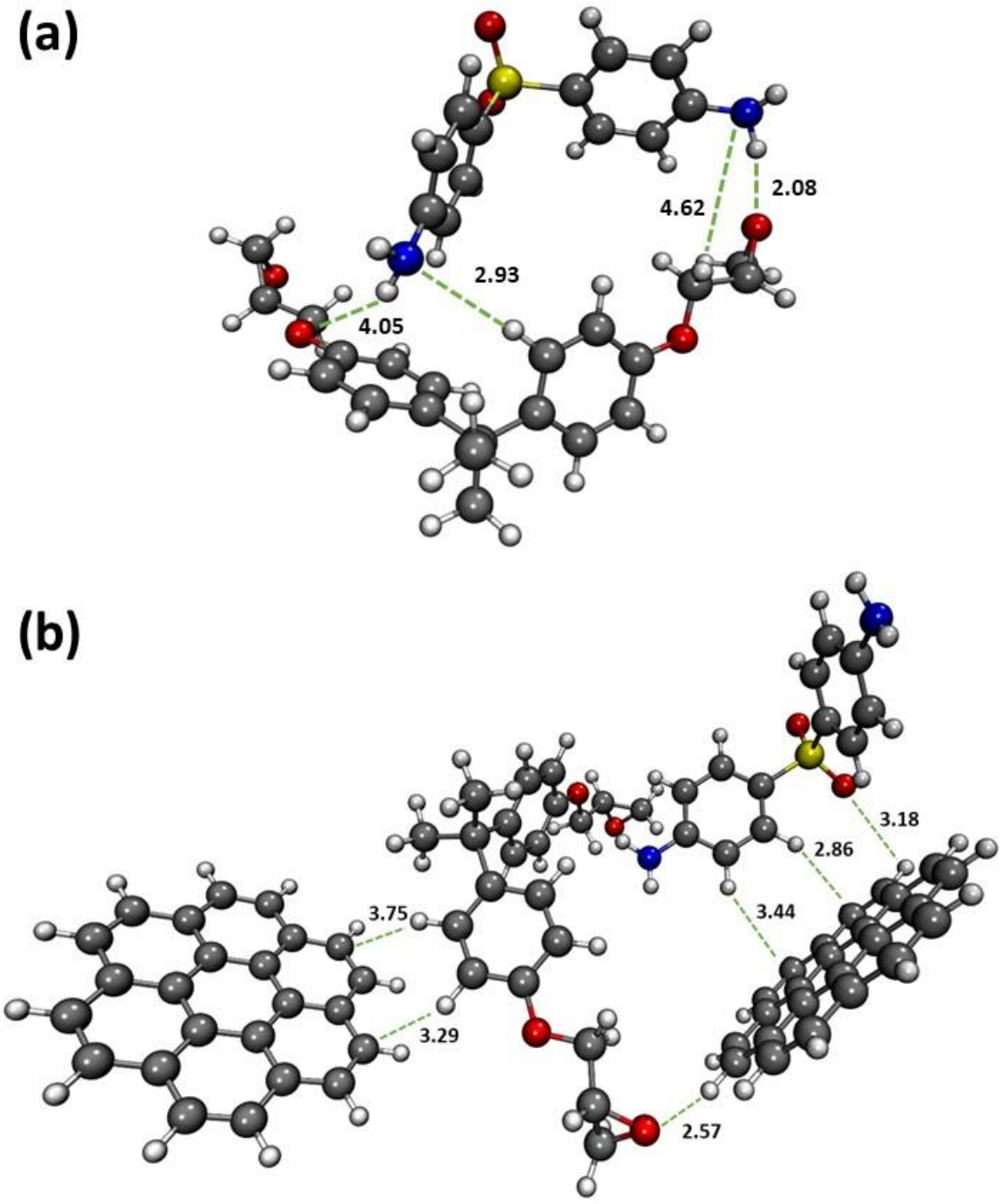

Figure 4.2.19 The optimized structure of (a) epoxy and hardener and (b) RH-DQs/epoxy-hardener

Distribution of HOMO-LUMO for this system shows that the frontier orbitals mostly expanded on the surface of RH-QDs. Therefore, the relative energy of each orbital determines the magnitude of the HOMO-LUMO energy gap *(ΔE_g)*, which aids in determining the electronic transport properties of molecules (Mishra et al., 2021). The *HOMO-LUMO* energy gap, on the

other hand, decreases when *HOMO* energy increases and *LUMO* energy decreases (He et al., 2021). The presence of soft materials is indicated by a small ΔE_g, whereas the presence of hard materials is indicated by a high ΔE_g. The HOMO-LUMO energy gap of the system was used to calculate the kinetic stability and reactivity of each component. *HOMO, LUMO* and *HOMO-LUMO* of epoxy, hardener, RH-QDs and conjugation of epoxy-hardener/ RH-QDs are shown in **Figure 4.2.20**. Higher E_{HOMO} values and a lower E_{LUMO} values indicate a high capacity for donating electrons to the metal's unoccupied d-orbitals and accepting electrons from the metal surface, meanwhile their energy gap reflects the reactivity of the inhibitor (Hsissou et al., 2020). The theoretical results of ΔE_g and quantum chemical descriptors including electronegativity (χ), chemical potential (μ), softness (σ), electrophilicity (ω) and chemical hardness (η) are reported in **Table 4.2.4**. As displayed in the table, ΔE_g was 0.148 eV and 0.142 eV for the pure RH-QDs and the RH-QDs-epoxy-hardener respectively. Compared to the energy gap of pure RH-QDs, the value of the ΔE_g decreases after the adsorption of epoxy-hardener over the surface of RH-QDs, demonstrated that it was more polarizable and reactive, and that it could interact with metallic surfaces quite strongly (Ogunyemi et al., 2020). The hardness value of the system RH-QDs-epoxy-hardener has decreased to 0.0710 eV, which indicates the easier adsorption of epoxy hardener mixer on the RH-QDs surface. Further the high value of chemical potential (0.1381 debye) of the system reveals that the adsorption can be done easily. Lower I and χ indicated a greater ability to donate electrons to the metal surface compared to its ability to receive electrons (Punathil Meethal et al., 2023c). Adsorption of inhibitor on metallic surface was further investigated by calculated ΔN value, the number of electrons transferred to the metallic surface with the help of equation 5.7. The ability of the molecules to transfer electrons to the empty d-orbitals of the metal surface is implied by the positive value of ΔN (33.041 eV) (Haque et al., 2020; Hsissou et al., 2019). In summary, the distribution of the *HOMO* and *LUMO* for this complex indicates that the frontier orbitals are

primarily expanded on the surface of the RH-QDs; thus, the attachment of the RH-QDs to the surface of the epoxy-hardener system is more likely. This is consistent with our experimental findings.

	HOMO	LUMO
epoxy	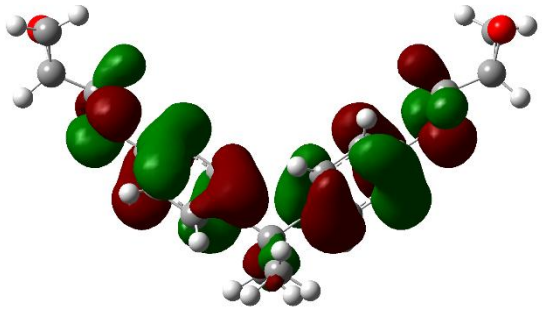	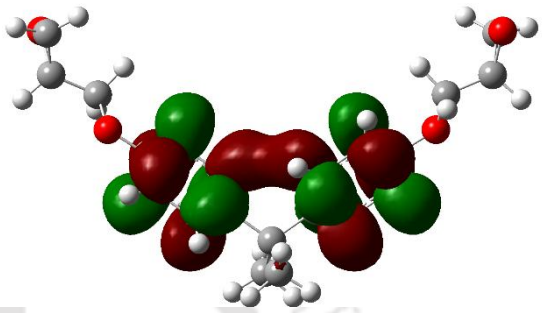
Hardener	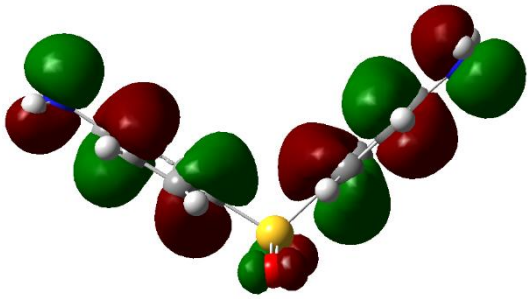	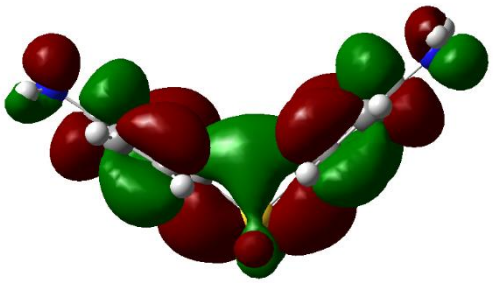
RH-QDs	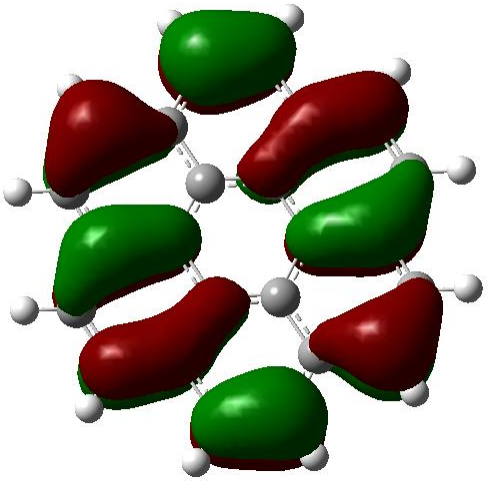	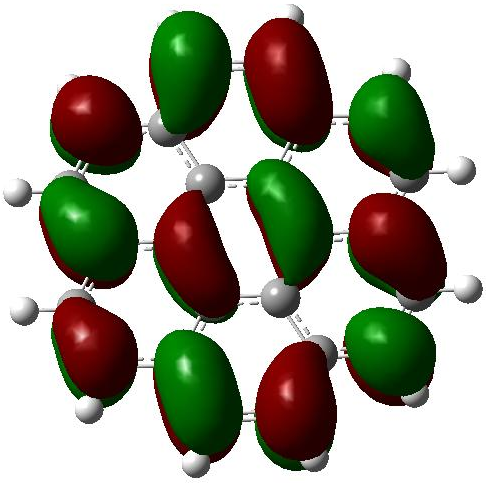

RH-QDs/epoxy-harder	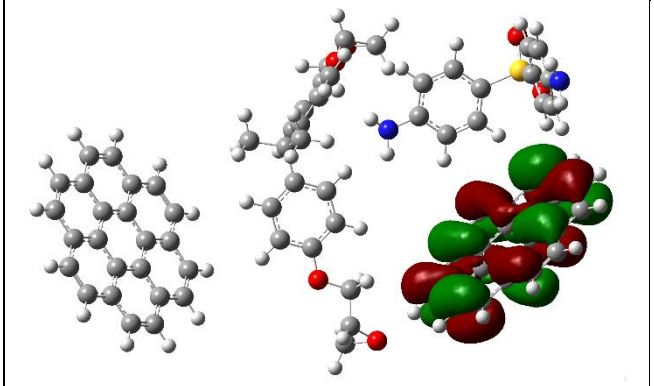	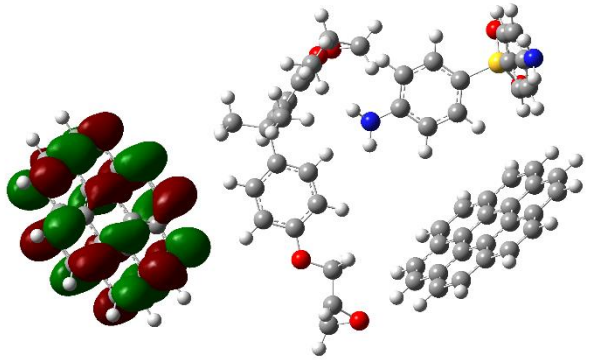

Figure 4.2.20 Distribution of HOMO and LUMO of epoxy, hardener, RH-QDs and conjugation of epoxy-hardener/RH-QDs

Table 4.2.4

Energy gap between HOMO (eV) and LUMO (eV) and quantum chemical parameters including chemical potential (μ) and chemical hardness (η), electronegativity (χ), softness (σ), and electrophilicity (ω) of the system

	ΔE_{LUMO} /eV	ΔE_{HOMO}/ eV	$\Delta E_{HOMO-LUMO}$/ eV	Hardness/ eV (η)	Chemical potential/debye (-μ)	electronegativity (χ)	Softness (σ)	electrophilicity (ω)
Epoxy	-0.0172	-0.2162	0.199	0.0995	0.1167	0.1167	10.0502	0.0684
Hardener	-0.0345	-0.2165	0.182	0.0910	0.1255	0.1255	10.9890	0.0865
RH-QDs	-0.0619	-0.2096	0.148	0.0738	0.1357	0.1357	13.5501	0.1247
RH-QDs-epoxy-hardener	-0.0671	-0.2091	0.142	0.0710	0.1381	0.1381	14.0845	0.1343

4.2.3.7 Possible Anti-corrosion mechanism

The schematic in **Figure 4.2.21** is provided to show how epoxy and RH-QDs/epoxy composite coatings interact with corrosive media. During the film production, fractures and micropores were created in the coating as observed in **Figure 4.2.8a**. Besides, the dissolved oxygen and other corrosive fluids, also contribute to typical epoxy coating defects (Wang et al., 2020; Xiao Wang et al., 2022). Corrosive fluids may easily penetrate the epoxy coating via these defects, reach the carbon steel substrate's surface and resulting in severe corrosion (Y. Zeng et al., 2022). The presence of inorganic or organic nanofillers in the epoxy matrix typically forms a solid barrier in the path of corrosive molecules traversing the epoxy. Thus, these molecules passing through the polymeric matrix are forced to take a more tortuous route, which slows the progression of the phenomenon (Wei et al., 2013; Weng et al., 2010). Besides, the number of defects is significantly lowered in the epoxy matrix in the presence of RHQDs as the coating structure becomes denser and more intact. This is evident from **Figure 4.2.8c**. Further, the corrosion product layer formed on the carbon steel surface becomes denser in the presence of RHQDs and hence offers higher protection against corrosion (Ding et al., 2022b) as depicted on **Figure 4.2.21.** The protection mechanism is attributed to the increased density of the coating, characterized by its reduced porosity, which effectively minimizes the ingress of corrosive species from the bulk solution to the underlying carbon steel surface.

The higher values of electronegativity (χ), softness (σ), and electrophilicity (ω) for RH-QDs-epoxy-hardener system were obtained via quantum chemical calculation reveals that the strong interaction exists between RH-QDs and epoxy matrix. This could eventually lead to restricting the generation of micropores and make the structure more intact. Hence, the introduction of RH-QDs effectively reinforces the barrier property of the epoxy coating. Additionally, the RH-QDs/epoxy coating has enhanced adhesion strength to the carbon steel substrate. In summary,

uniform dispersion and interaction ability of 0.5 wt% RH-QD with the epoxy coating and on the carbon steel surface makes a superior anticorrosive coating for carbon steel.

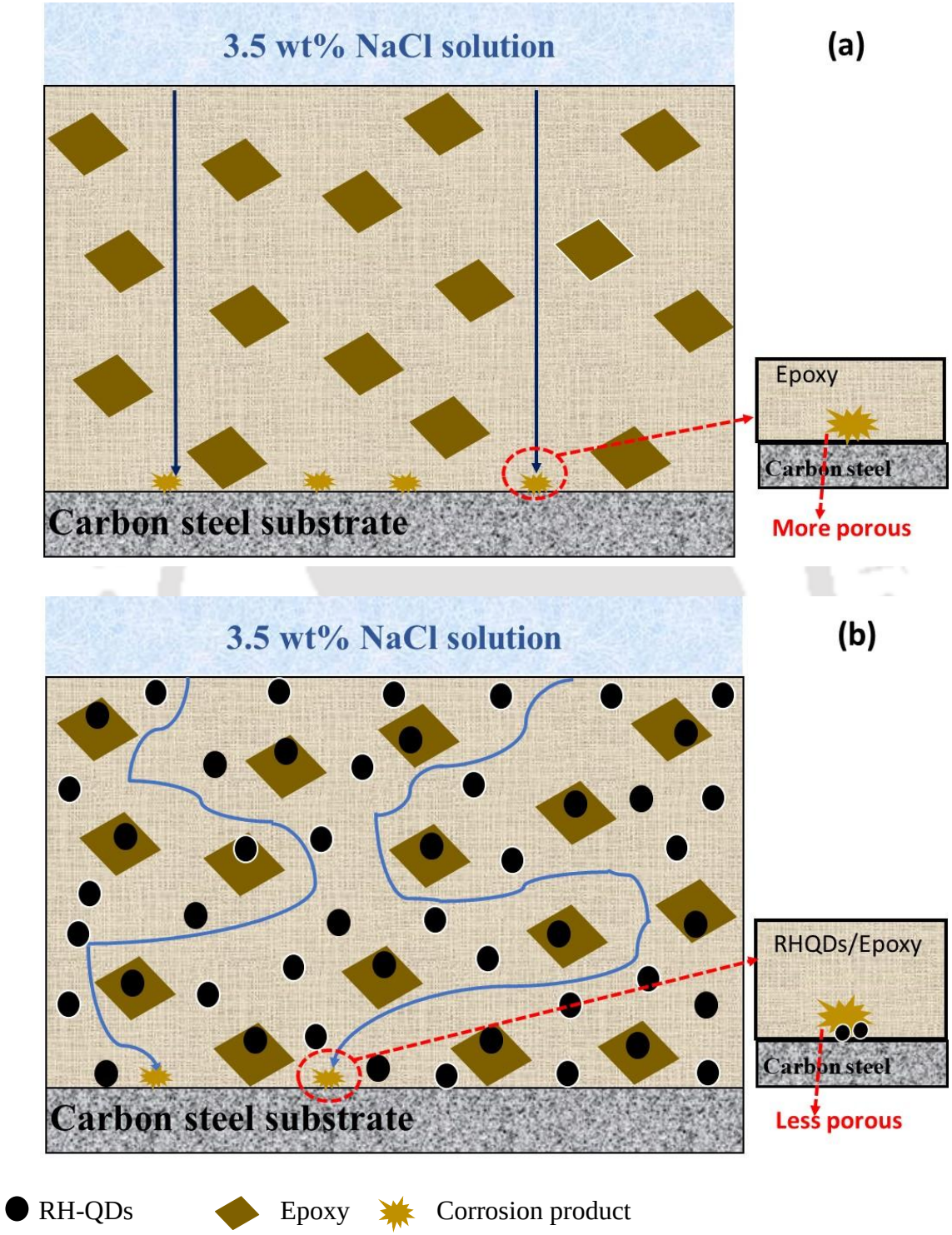

Figure 4.2.21 The suggested anti-corrosion mechanism for (a) pure epoxy and (b) RH-QDs/epoxy coatings on the carbon steel substrate

4.3 To investigate the corrosion inhibitory effects of azoles in alkaline medium for ruthenium chemical mechanical planarization applications: Electrochemical and theoretical analysis

4.3.1 Motivation

Azoles (Caldona et al., 2021; Zhou et al., 2020) and azole derivatives (J. Ji et al., 2022a; N. Zeng et al., 2022) are frequently used as corrosion inhibitors for metal CMP and post-CMP cleaning operations (Manivannan et al., 2014; Y. Wang et al., 2022). Especially for Ru CMP, Fu Luo and co-authors(Luo et al., 2023b) compared the corrosion inhibition performance of phytic acid and TAZ on the Ru surface in polishing slurry containing hydrogen peroxide (0.3 wt%), glycine (2 wt%), and isooctyl alcohol polyoxyethylene ether (3 ml/L), indicating that the inhibition performance of TAZ is better. Jenasree Hazarika et al. (Hazarika et al., 2023e) reported that with the addition of BTAH (5mM) in potassium iodate (0.2 M) based polishing slurry, the inhibition efficiency of 68.42 % was achieved for Ru at pH value of 9.

The adsorption mechanism between the azole-based corrosion inhibitors and Ru metal at the microscale level remains unexplained. Thus, to get insight on physicochemical interaction between azoles and Ru at the microscale level, molecular dynamics simulations along with quantum chemical calculations were employed in the present work. The present study aims to offer a preliminary comprehension of the potential impacts stemming from variations in molecular structure on their adsorption. Also, it provides valuable insights that could potentially be helpful in design and advancement of innovative organic inhibitor molecules, with the ultimate goal of protecting the Ru metal during the CMP process.

Thus, in this study, the inhibition efficiency of azole compounds which are commonly employed in CMP applications is investigated at pH 9 on Ru surface. Electrochemical experiments such as potentiodynamic polarization and electrochemical impedance spectroscopy (EIS) were

performed to understand the inhibition behaviour of inhibitors. Furthermore, the adsorption mechanism of IMD, TAZ, and BTAH on the Ru surface is explained via quantum chemical analysis and Monte Carlo simulations. The study shows the physicochemical interaction between azoles and Ru at the microscale level.

4.3.2 Experimental

4.3.2.1 Materials

Imidazole (HiMedia, India), 1, 2, 4-Traizole (Otto chemie Private Limited, India), and 1, 2, 3-Benzotriazole (Loba Chemicals Private Limited, India) chemicals were used without further purification. Potassium hydroxide (HiMedia, India) was used to adjust the pH value. The ruthenium metal (99.9% purity) was received from Tecnisco, Ltd and fabricated as per the requirements. All the electrolyte solutions were prepared using deionized (DI) water from Milli-Q Synthesis unit (Model: Elix 3, Millipore®, USA). The electrolyte solutions were prepared by introducing the stoichiometric quantity of inhibitor (IMD/TAZ/BTAH) into DI water. The electrolyte solution was subjected to magnetic stirring (Tarsons, India) for a duration of 1 min. in order to achieve appropriate dilution. A concentration of 0, 5, 10, and 15 (mM) was used to prepare the electrolyte solution of IMD, TAZ, and BTAH. The electrolyte solution is regarded as a blank electrolyte solution in the absence of an inhibitor at pH 9.

4.3.2.2 Surface characterization

The Ru samples underwent a comprehensive cleaning process involving polishing by use of emery sheets (600, 800, 1000, and 1200 grits) and abrasive alumina (1.0 and 0.3 μm) powder to eliminate any oxides or contaminants. After polishing, the sample was rinsed in Millipore water and subjected to ultrasonication for 2 minutes and then air dried. Subsequently, Ru samples were submerged in the desired solution for a predetermined period of time. Subsequently they were rinsed with deionized water, and then dried at room temperature

with nitrogen gas. Then, the contact angle was measured using goniometer (Holmarc Opto-Mechatronics, model: HO-IAD-CAM-01B) and the surface morphology was analyzed by field emission scanning electron microscope (FESEM) (Sigma 300, Zeiss, USA).

4.3.2.3 Electrochemical experiments

The electrochemical test was executed by employing three-electrode system using electrochemical workstation (Gamry Interface 1010E). Ru disk (99.9 % purity) 12 mm diameter sealed into Teflon tubes were used as the working electrode. A platinum wire and Ag/AgCl (3 M KCl) were used as counter electrode and reference electrode, respectively. The working electrode was polished using emery sheets in the following grit sizes: 320, 600, 1000 and 1200, and subsequently with 0.3 m and 1 m micro-polish alumina powder (Buehler, USA) before each run. The electrode was then extensively cleaned with DI water after being sonicated in ethanol. For each run, a fresh 100 ml electrolyte solution of IMD, TAZ, and BTAH was prepared with the concentration of 0, 5, 10, and 15 (mM). Prior to all electrochemical tests, the open circuit potential (OCP) was measured until it reached a stable state. The Potentiodynamic polarisation experiments were carried out at a scan rate of 1 mV/s from -250 to 250 mV w.r.t OCP. The electrochemical impedance spectroscopy (EIS) test was conducted at OCP in the frequency range of 10 kHz to 10 mHz and with sinusoidal perturbation of ±10 mV amplitude, ZSimpWin software was used to fit the acquired data with the appropriate electrical equivalent circuit.

4.3.2.4 Theoretical analysis

The initial structures of IMD, TAZ, and BTAH were generated and optimized using DMol^3 module-based DFT calculation in Biovia Material Studio (MS) software (Accelyrl company, USA) as shown in **Figure 4.3.1**.

IMD	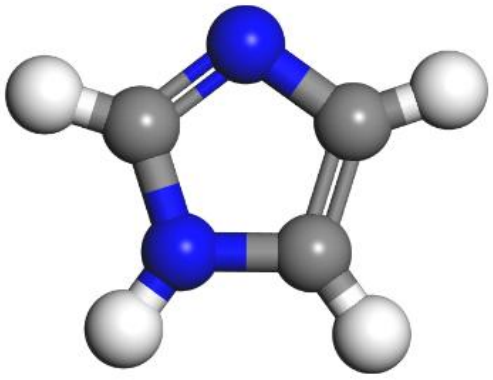
TAZ	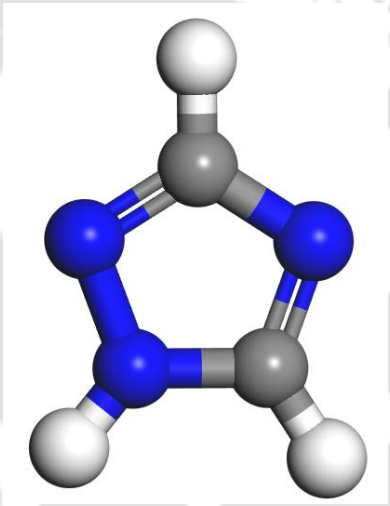
BTAH	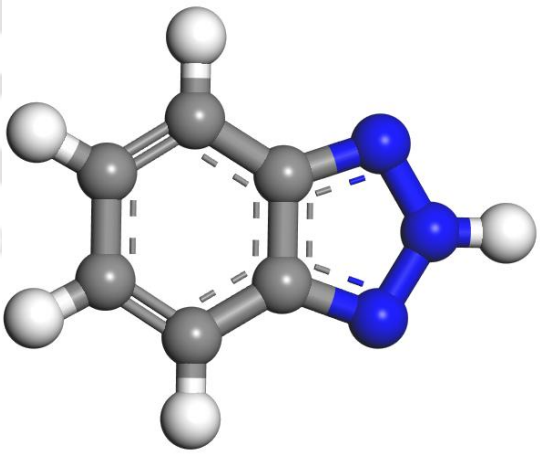
	

Figure 4.3.1 Optimized structure of IMD, TAZ, and BTAH molecules.

Atom legend: white = H, gray = C, and blue = N

The generalised gradient approximation (GGA) was used to perform DFT calculation using Becke-Lee-Yang-Parr (BLYP) with double numeric polarization (DNP) basis set including d as well as p orbital polarization functionals. All the DFT calculations were performed with the implicit COSMO solvent (Water) model. Compared to conventional DFT methods such as BLYP, this method is adapted adequately for calculating non-covalent interactions (Das et al., 2023b), making it appealing for the calculation of all three inhibitors and Ru (0 0 1) surface.

The chemical stability and reactivity of the system can be evaluated through the energy gap (ΔE) between HOMO (Highest Occupied Molecular Orbital) and LUMO (Lowest Unoccupied Molecular Orbital). The DFT was used to calculate the frontier molecular orbital, E_{HOMO} and E_{LUMO}. Besides the energy gap (ΔE), the quantum chemical parameters including ionization potential (*I*), electron affinity (*A*), electronegativity (χ), global hardness (η) were calculated using Eq. 6.2, Eq. 6.3, Eq. 6.4 and Eq. 6.5, respectively.

$$\Delta E = E_{LUMO} - E_{HOMO} \quad \textbf{(4.3.1)}$$

$$I = -E_{HOMO} \quad \textbf{(4.3.2)}$$

$$A = -E_{LUMO} \quad \textbf{(4.3.3)}$$

$$\chi = 0.5(I + A) \quad \textbf{(4.3.4)}$$

$$\eta = 0.5(I - A) \quad \textbf{(4.3.5)}$$

Further, global softness (σ) and absolute electrophilicity index (ω) can be calculated from the Eq. 6.6 and 6.7 respectively.

$$\sigma = \frac{1}{\eta} \quad \textbf{(4.3.6)}$$

$$\omega = \frac{\chi^2}{2\eta} \quad \textbf{(4.3.7)}$$

In addition, with the help of quantum chemical calculations, the number of electrons transferred between inhibitor and metal (ΔN) can be calculated as per the following equation

$$\Delta N = \frac{\phi_{Ru} - \chi_{Ru}}{2(\eta_{Ru} + \eta_{inhi})} \quad \textbf{(4.3.8)}$$

The η_{Ru} values of 0 (eV/mol) was chosen for the calculation of ΔN. The value ϕ_{Ru}, work function of Ru (001) was taken as 4.71 (eV)(Michaelson, 1977).

4.3.2.5 Adsorption energy calculation method

The adsorption energy calculations were performed with the help of an adsorption locator module in Biovia Material Studio (MS) (Accelyrl company, USA). A 12 layer optimal Ru surface (001) was chosen to simulate the system. Additionally, the system was simulated using a super cell (6×6) of Ru (0 0 1) and a vacuum slab with 15 Å along the C-axis in a simulation box with dimensions of 13.529 Å×13.529 Å×38 Å. Then, molecular dynamic simulations were conducted using cubic spline truncation method with a time step of 1 fs and a temperature of 298 K for 500 ps. The electrostatic forces and van der Waals forces were calculated using the atom-based summation method. A cut off distance of 12.5 Å was considered for this calculation. Finally, computational simulations were conducted to assess the adsorption energy associated with the inhibitor in the presence of the Ru metal. To accurately replicate the corrosion environment in the aqueous phase, ten water molecules along with the inhibitor molecule were considered in the simulations. The simulation methodology employs the universal force field in order to optimize the structural configuration of the complete corrosion system. Adsorption energy calculations were carried out to identify sites with low energy adsorption. The inhibitor molecule's orientation is adjusted to achieve the minimum free energy of adsorption. Consequently, the investigation of inhibitors' preferential adsorption characteristic can be studied (Heinz et al., 2009).The energy released by the corrosion inhibitor

molecule adsorbed on the metal surface is referred to as "adsorption energy," (Guo et al., 2020; Punathil Meethal et al., 2023b)and it is explained as

$$E_{ads} = E_{total} - \left(E_{surface+water} + E_{inhibitor+water}\right) + E_{water} \quad \textbf{(4.3.9)}$$

Where E_{total} is the overall energy of the whole investigated system containing Ru (0 0 1) with an inhibitor, $E_{surface+water}$ denoted the total energy total energy of Ru (0 0 1) surface and solution without the inhibitor, $E_{inhibitor+water}$ indicate the cumulative energy of both the inhibitor and the solution, and E_{water} is the total energy of the water.

4.3.3 Results and Discussion

4.3.3.1 Potentiodynamic polarization

According to Ru-H_2O Pourbaix diagram(Jiang et al., 2014b; Kim et al., 2009), the Ru dissolution at pH 9 occurs via the formation of various oxides and hydroxides such as are $Ru(OH)_3$, RuO_4^- and $RuO\ nH_2O$ as shown in the following reactions (Equation 10-13) (Zeng et al., 2012). If these oxides/hydroxides are unstable in the given solution of interest or porous in nature, it would not completely passivate the Ru surface and eventually resulted in dissolution.

Anodic reactions:

$$Ru + nOH^- = RuO_4^- + \left(\frac{n}{2}\right)H_2O + (n\text{-}1)e^- \quad \textbf{(4.3.10)}$$

$$Ru + nOH^- = Ru(OH)_3 + ne^- \quad \textbf{(4.3.11)}$$

$$Ru + nOH^- = RuO_2 \cdot \left(\frac{n}{2}\right)H_2O + ne^- \quad \textbf{(4.3.12)}$$

Cathodic reactions:

$$O_2 + 2H_2O + 4e^- = 4OH^- \quad \textbf{(4.3.13)}$$

Further, it is expected that the addition of inhibitors leads to the formation of passive film on Ru surface via adsorption. The adsorption could be either physisorption or chemisorption or combined physisorption and chemisorption. Besides, at pH 9, the inhibitors being studied undergo deprotonation and exist in ionic form as represented by the following reaction.

$$I = (I_1)^- + H^+ \qquad \textbf{(4.3.14)}$$

Where I represent neutral form of inhibitor molecules and $(I_1)^-$ represents the deprotonated form of the same.

The interaction of inhibitor (neutral molecules/deprotonated form) with the metal/metal oxides/metal hydroxides will result in the formation of Ru-inhibitor complex as per the following reactions.

$$Ru + n(I_1)^- \rightarrow Ru(I_1)_n + ne^- \qquad \textbf{(4.3.15)}$$

$$Ru^{X+} + X(I) \rightarrow Ru(I_1)_X + XH^+ \qquad \textbf{(4.3.16)}$$

$$nRu + n(I_1)^- + O_2 \rightarrow nRu\text{-}I_1 + (\frac{n}{2})H_2O + ne^- \qquad \textbf{(4.3.17)}$$

In general, azole-based compounds are a readily available class of corrosion inhibitors with remarkable efficacy against saline solutions, mineral acids, and alkaline environments, particularly for protecting copper, iron, and their alloys. Furthermore, the wide availability of azoles enhances their accessibility and cost-effectiveness(J. Ji et al., 2022b). However, it is crucial to acknowledge that certain azole-containing compounds may pose potential health risks to humans and animals. These risks can manifest as skin irritation, allergic reactions, or even endocrine disruption(Luo et al., 2023c). Therefore, implementing proper safety protocols

is paramount when handling these compounds, particularly in situations with high exposure potential.

The effect of inhibitors (IMD, TAZ, and BTAH) on these reactions at alkaline pH is investigated by Potentiodynamic polarization studies and the results obtained are displayed in **Figure 4.3.2**. The electrochemical corrosion characteristics, such as corrosion potential (E_{corr}), corrosion current density (i_{corr}), anodic Tafel anodic (βa), and cathodic Tafel slopes (βc) were extracted from these polarisation curves using the Gamry Echem Analyst software. The protection efficiency (PE) was calculated using the follow equation(N. R. Dhongde et al., 2023b; Kumar and Das, 2023b).

$$PE(\%) = \frac{i_{corr,o} - i_{corr,i}}{i_{corr.o}} \times 100 \qquad \textbf{(4.3.18)}$$

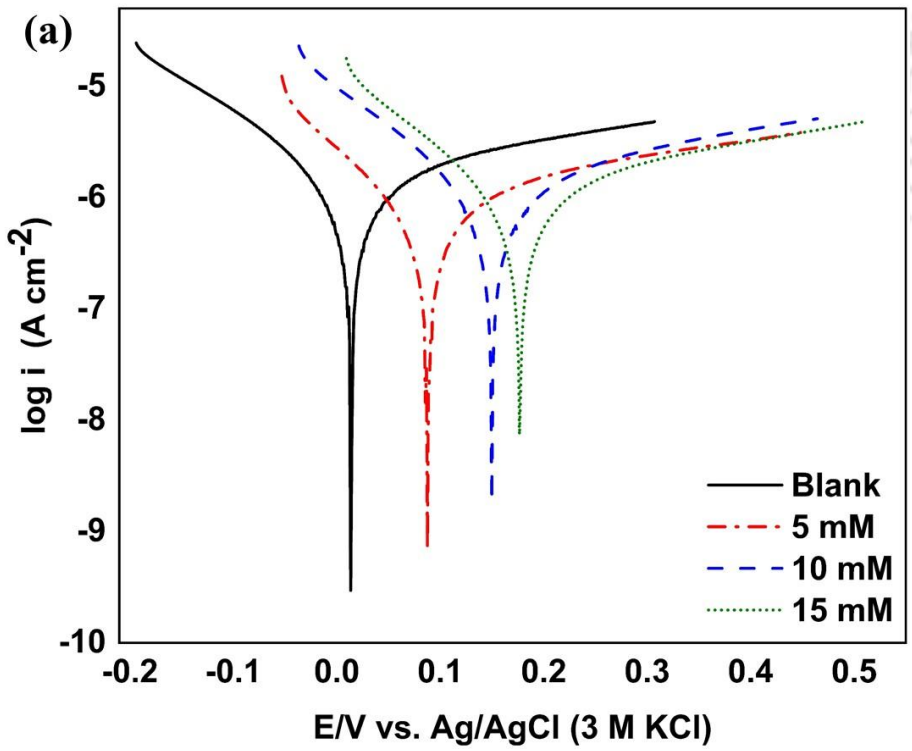

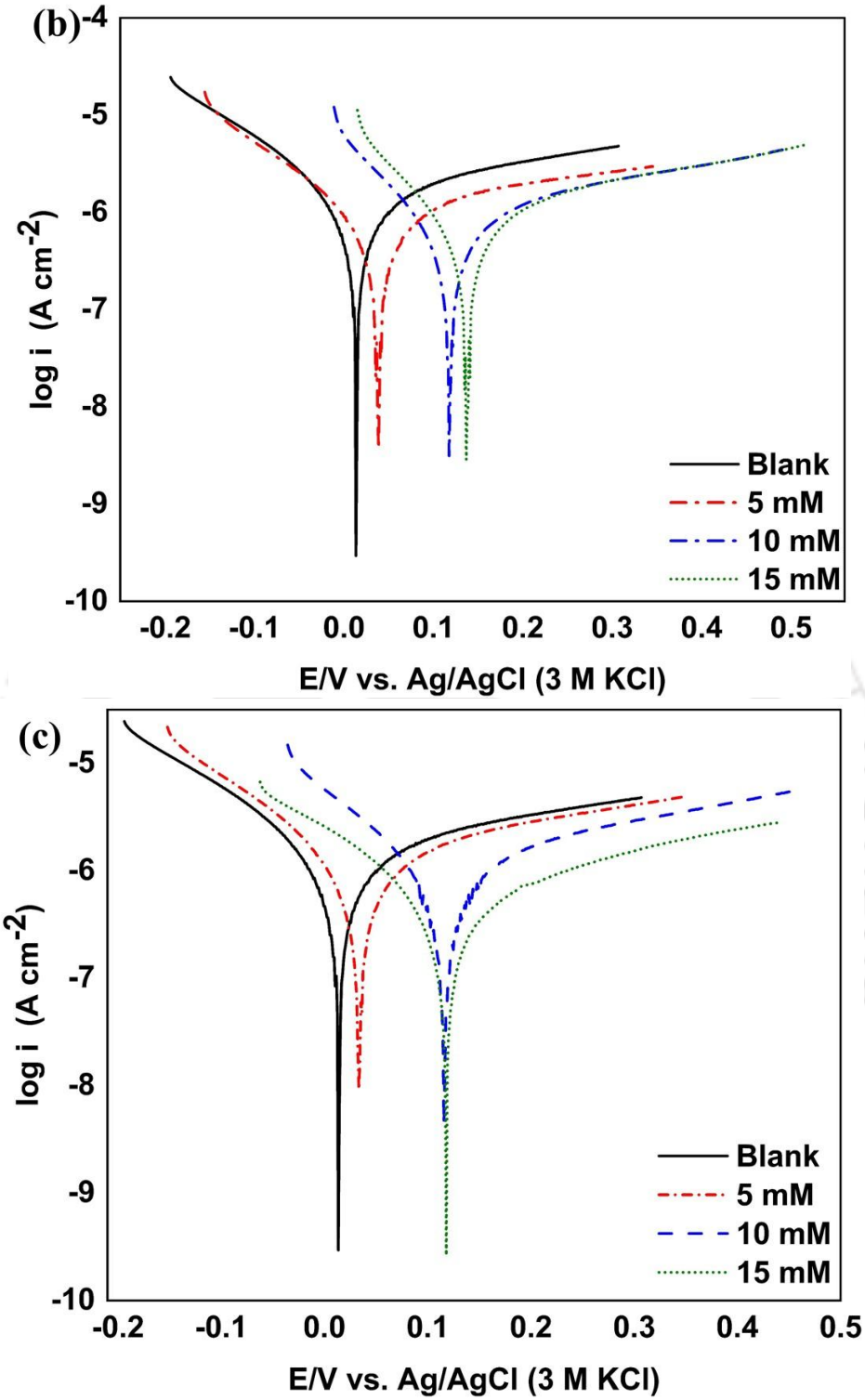

Figure 4.3.2 Potentiodynamic polarization curves of ruthenium in different concentrations of (a) IMD, (b) TAZ, and (c) BTAH

Here, $i_{corr,o}$ and $i_{corr,i}$ represent corrosion current density (A/cm^2) retrieved in the absence and presence of inhibitor respectively. Compared to the untreated Ru surface, the E_{corr} values for Ru treated with inhibitors (IMD, TAZ, and BTAH) shift in favour of positive potential. Besides, i_{corr} values for Ru treated surfaces are significantly lower than that of $i_{corr,o}$ and the value increases with increase in concentration for all the three inhibitors. The anodic polarisation curves are clearly moved to a lower current density with the addition and increasing concentration of IMD, TAZ, and BTAH(Devi et al., 2023b; Unnimaya et al., 2023). Time variance of the OCP of Ru exposed to with inhibitor and without inhibitor presented in **Figure 4.3.3**.

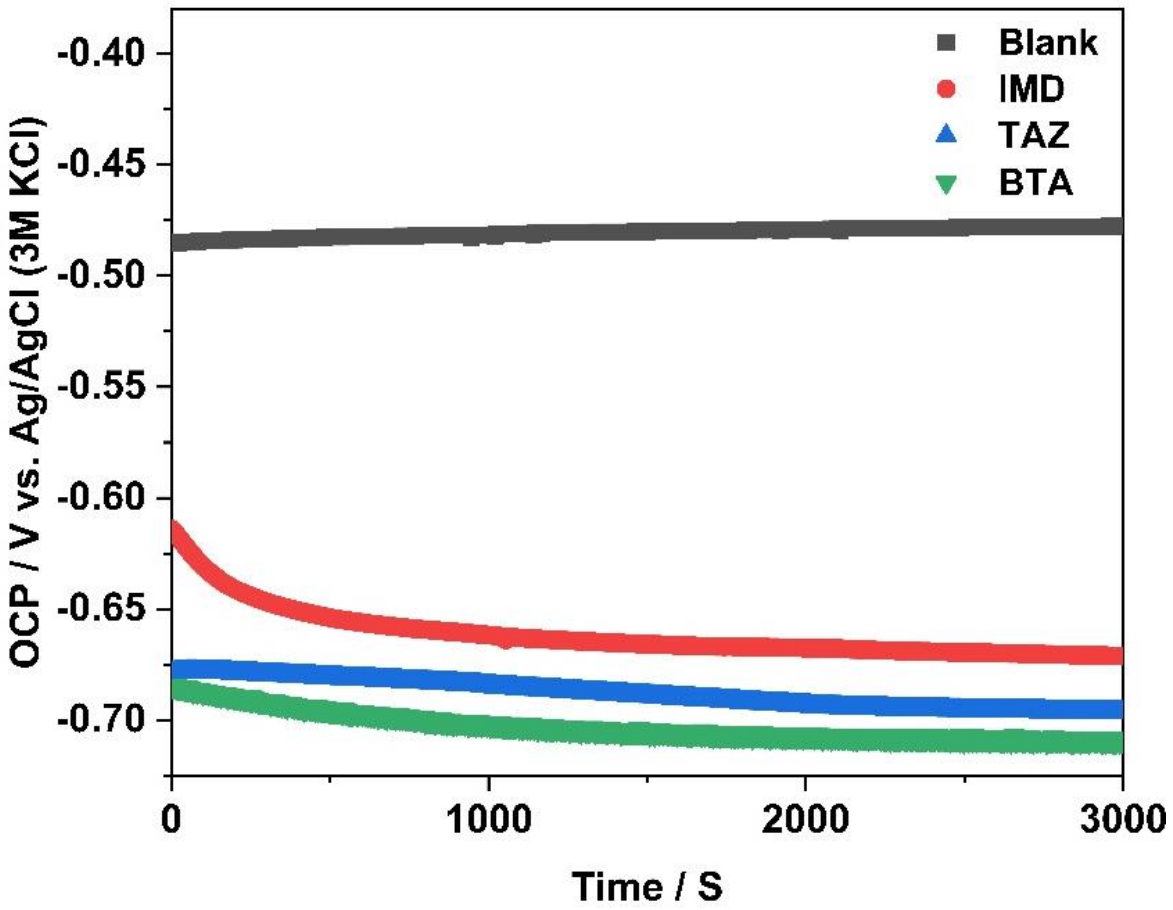

Figure 4.3.3 Time variance of the OCP of Ru exposed to with inhibitor and without inhibitor

Table 4.3.1 Electrochemical parameters obtained from polarisation curves of Ru in solution containing corrosion inhibitor

Inhibitors	Concentration (mM)	E_{corr} (mV)	i_{corr} (µA/cm^2)	βa (V/dec)	- βc (V/dec)	CR (mm/y)	PE (%)
Without	0	14.04 ± 0.185	2.15 ± 0.019	0.80 ± 0.008	0.20 ± 0.001	0.058±0.001	-
IMD	5	115.88 ± 2.433	0.62 ± 0.024	0.49 ± 0.196	0.17 ± 0.008	0.016±0.002	71.16 ± 0.156
	10	126.21 ± 2.536	0.51 ± 0.020	0.46 ± 0.020	0.17 ± 0.008	0.013±0.001	76.27 ± 0.221
	15	131.04 ± 1.323	0.26 ± 0.014	0.41 ± 0.018	0.12 ± 0.005	0.007±0.001	87.90 ± 0.316
TAZ	5	138.33 ± 2.642	0.55 ± 0.018	0.45 ± 0.007	0.18 ± 0.007	0.014±0.002	74.41 ± 0.141
	10	150.73 ± 2.125	0.22 ± 0.010	0.46 ± 0.016	0.17 ± 0.003	0.005±0.001	89.76 ± 0.376
	15	158.11 ± 2.845	0.19 ± 0.009	0.41 ± 0.013	0.11 ± 0.002	0.005±0.001	91.16 ± 0.446
BTAH	5	144.81 ± 3.909	0.49 ± 0.024	0.44 ± 0.017	0.18 ± 0.007	0.013±0.001	77.20 ± 0.355
	10	161.87 ± 3.720	0.17 ± 0.008	0.39 ± 0.016	0.15 ± 0.007	0.004±0.000	92.09 ± 0.165
	15	165.99 ± 2.157	0.15 ± 0.007	0.39 ± 0.008	0.10 ± 0.003	0.004±0.000	93.02 ± 0.446

The E_{corr} values increases from 14 mV to 131 mV, 158 mV, and 165 mV for IMD, TAZ, and BTAH respectively at 15 mM concentration. A significant shift in the E_{corr} value in the positive direction (> 85 mV) clearly indicates that the tested inhibitors mainly suppress the anodic reaction kinetics(Dhongde et al., 2024; Unnimaya et al., 2023). This significant positive shift in E_{corr} along with decrease in i_{corr} reveals the high inhibitory ability of the used inhibitors (V. Dhongde et al., 2023). It is to be noted that cathodic Tafel slope also changes with the addition of inhibitors and hence these inhibitors are mixed type with anodic predominant control(Javadian et al., 2013; W. Li et al., 2022b). Furthermore, the three groups have identical polarisation curves indicating that azole compounds have the similar corrosion prevention mechanism for Ru in alkaline conditions. The corrosion rate values of IMD, TAZ, and BTAH at a concentration of 15 mM were measured to be 0.007±0.001, 0.005±0.0010, and 004±0.000 (mm/y), respectively. The PE (%) evaluated from the i_{corr} values is reported in **Table 4.3.1.** The PE (%) of the BTAH inhibitor is higher compared to IMD and TAZ for any given concentration. Particularly, the electrolyte solution containing 15 (mM) BTAH showed the highest PE (93.02 ± 0.446 %) for Ru metal at pH 9, which indicate the superior adsorption of the BTAH on the Ru surface while TAZ and IMD showed PE of 91% and 87% respectively.

4.3.3.2 Adsorption isotherm model

Adsorption isotherms were inferred by fitting the surface coverage, which is estimated from the polarization curves, as a function of inhibitor concentration to understand the adsorption process of the examined IMD, TAZ, and BTAH molecules on the Ru/solution interface. Various adsorption isotherms, including Langmuir, Temkin, and Frumkin were considered. However, only the most suitable isotherm type is discussed here, while the remaining models are presented in **Figure 4.3.5 (**Temkin**) and Figure 4.3.6 (**Frumkin). The Langmuir isotherm, as computed in Eq. 6.19, was found to have the best fit in all the concentrations, with linear regression coefficients (R^2) being close to 1(W. Li et al., 2022a; Xu et al., 2020).

$$\frac{C_{inh}}{\theta} = \frac{1}{K_{ads}} + C_{inh} \qquad \textbf{(4.3.19)}$$

Herein, θ is the surface coverage which is estimated from Eq. 4.3.20, C_{inh} is the concentration of inhibitor, and K_{ads} is the equilibrium constant of the adsorption process.

$$\theta = 1 - \frac{i_{corr}o}{i_{corr}} \qquad \textbf{(4.3.20)}$$

Figure 4.3.4 shows the plots of C versus C/θ that yield straight lines with an intercept of $1/K_{ads}$. The standard adsorption free energy (ΔG_{ads}) can be calculated as follows(Sun et al., 2021a).

$$K_{ads} = \frac{1}{55.5} \exp\left(-\frac{\Delta G_{ads}}{RT}\right) \qquad \textbf{(4.3.21)}$$

Where *R* (kJ/mol) and *T* (K) denote the molar gas constant and the absolute temperature respectively. A high value of K_{ads} and a low value of ΔG_{ads} (kJ/mol) often point to a stronger potential for the inhibitor to be adsorbed on the metal surface, demonstrating a higher level of inhibitive ability. The order of K_{ads} of the inhibitors is BTAH > TAZ > IMD. The calculated ΔG_{ads} (kJ/mol) values of IMD, TAZ, and BTAH are -25.37, -25.74, and -26.05 (kJ/mol), respectively. These findings show that BTAH have higher adsorption affinity to the Ru surface, compared to that of TAZ and IMD. Furthermore, ΔG_{ads} (kJ/mol) value greater than -20 (kJ/mol) indicates physisorption, which is caused by electrostatic attraction between the inhibitor molecules and charged metal; whereas ΔG_{ads} (kJ/mol) value less than -40 (kJ/mol) indicates chemisorption, which is caused by sharing or transfer of electrons from inhibitor molecules to metal molecules.(W. Li et al., 2022c). The outcome from the present work demonstrates that adsorption is of mixed type (combined physisorption and chemisorption) with physisorption as the predominating mechanism as the values obtained are near to -20 (kJ/mol). However, the extent of chemisorption is higher for BTAH as the value is relatively far from -20 (kJ/mol).

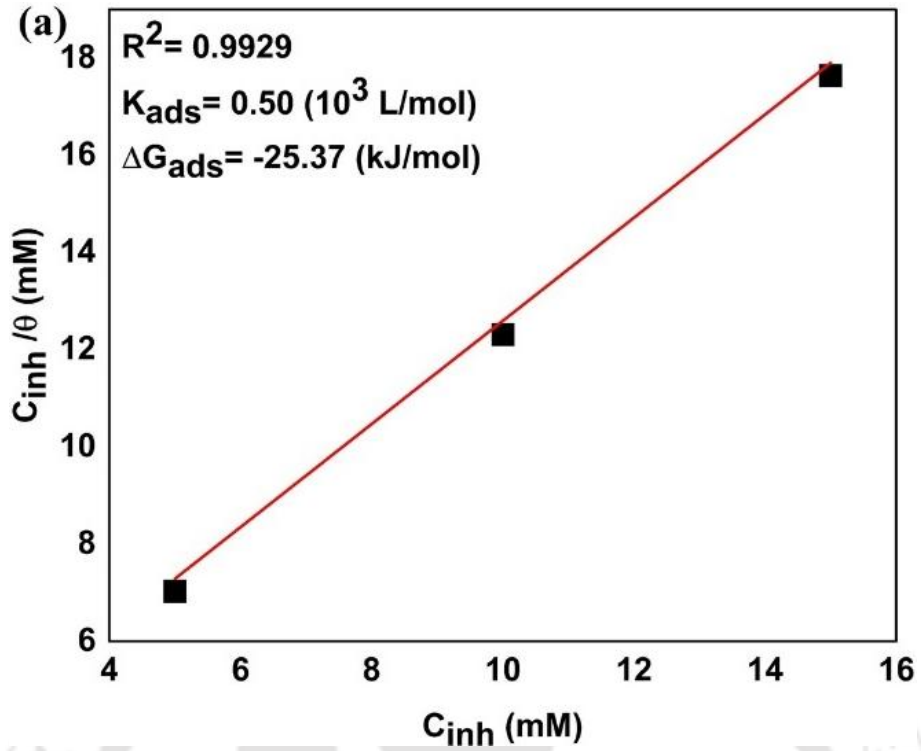

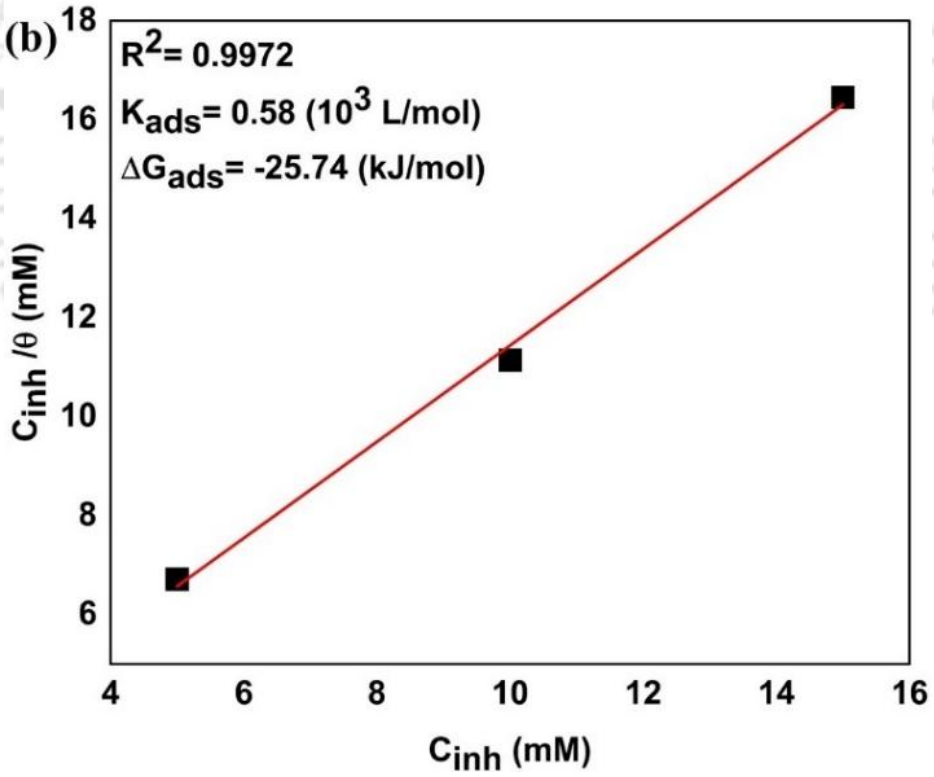

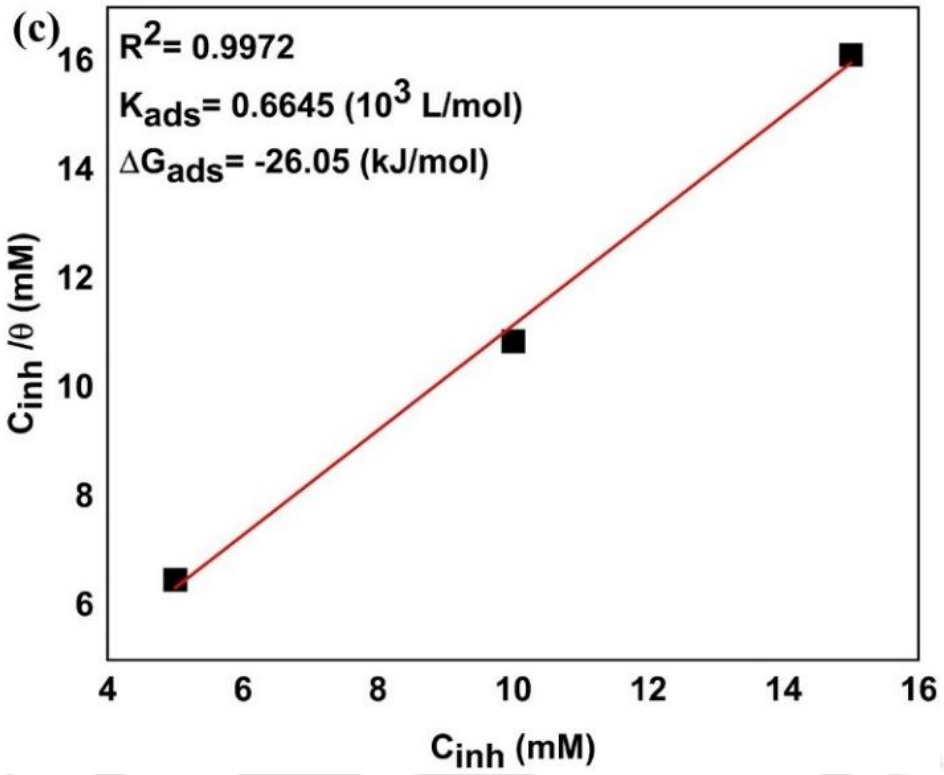

Figure 4.3.4 Langmuir adsorption isotherms of Ru in solution containing (a) IMD, (b) TAZ, and (c) BTAH

Temkin isotherm

$\theta = f^{-1} \ln(K_{ads}) + f^{-1} \ln(C_{inh})$ **(4.3.22)**

Frumkin isotherm

$\log [\theta/((1-\theta)C_{inh})] = \log(K_{ads}) + g\theta$ **(4.3.23)**

(a)

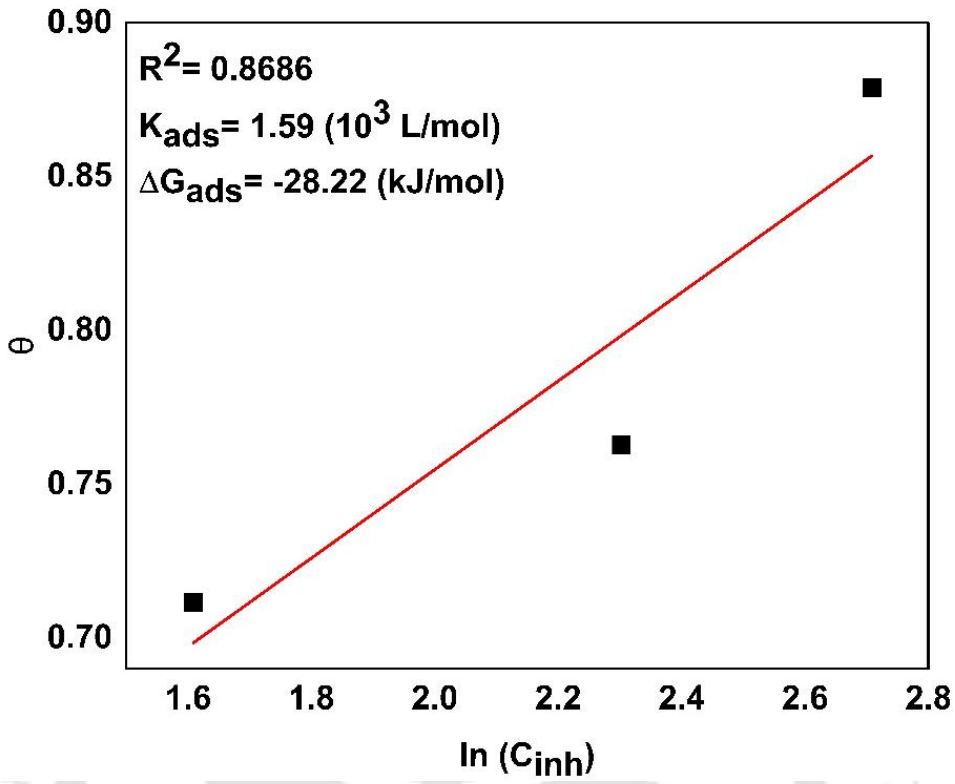

(b)

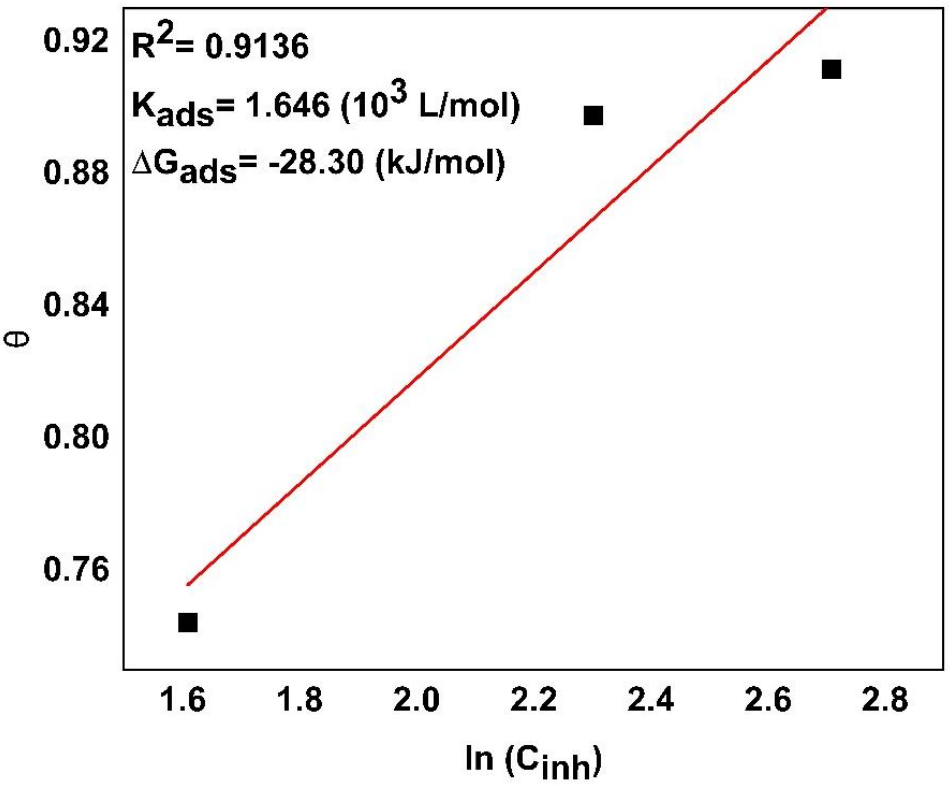

(c)

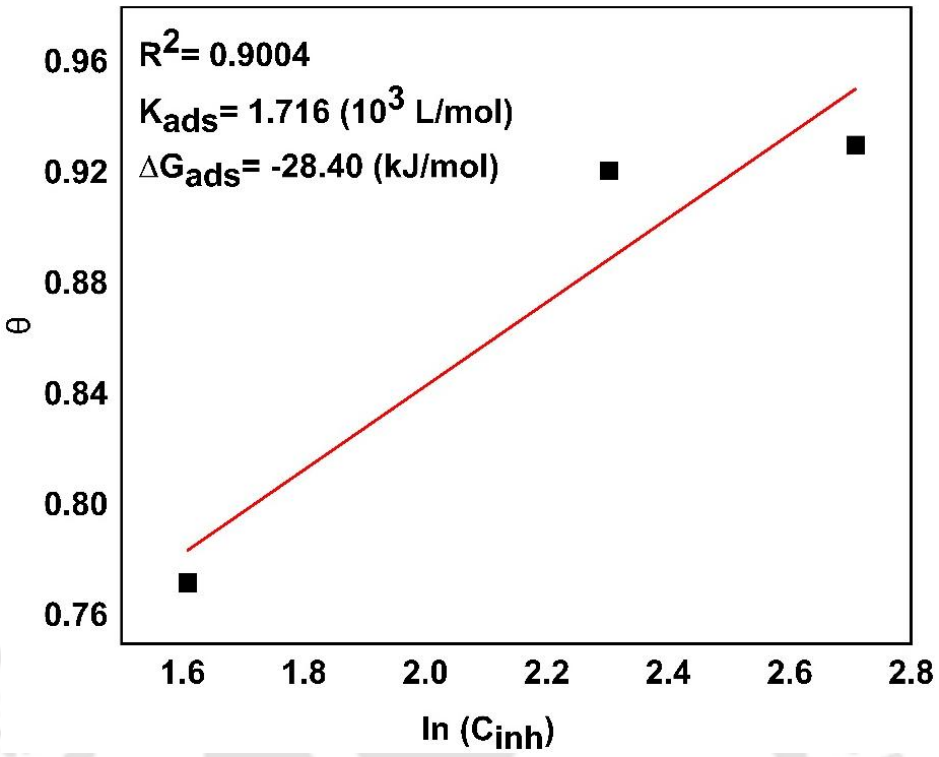

Figure 4.3.5 Temkin adsorption isotherms of Ru in solution containing (a) IMD, (b) TAZ, and (c) BTAH

(a)

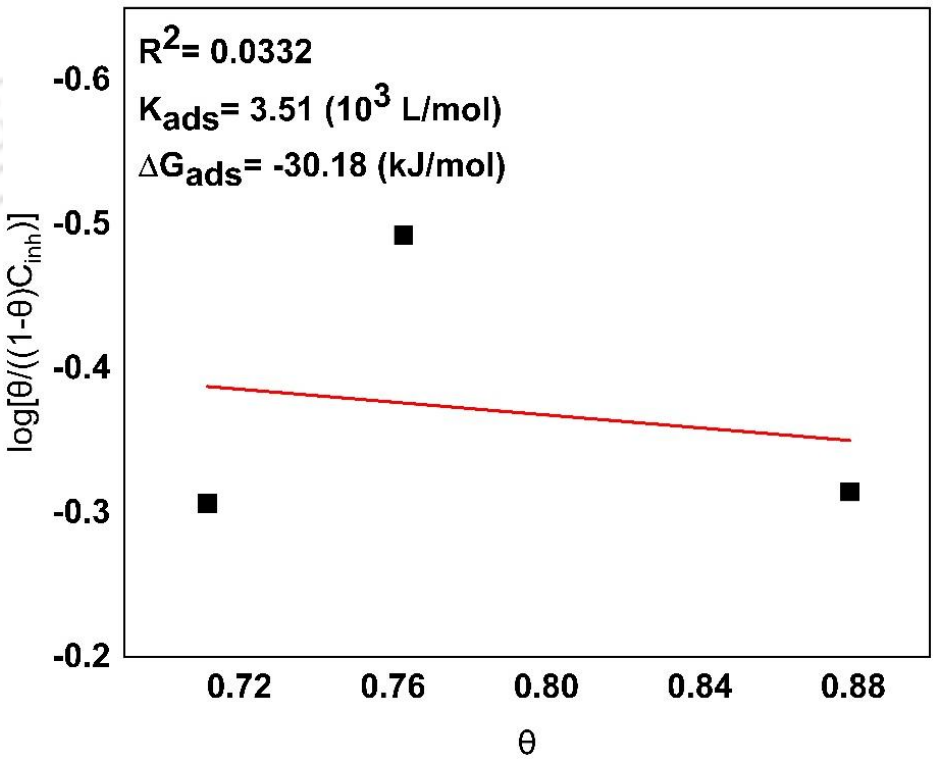

(b)

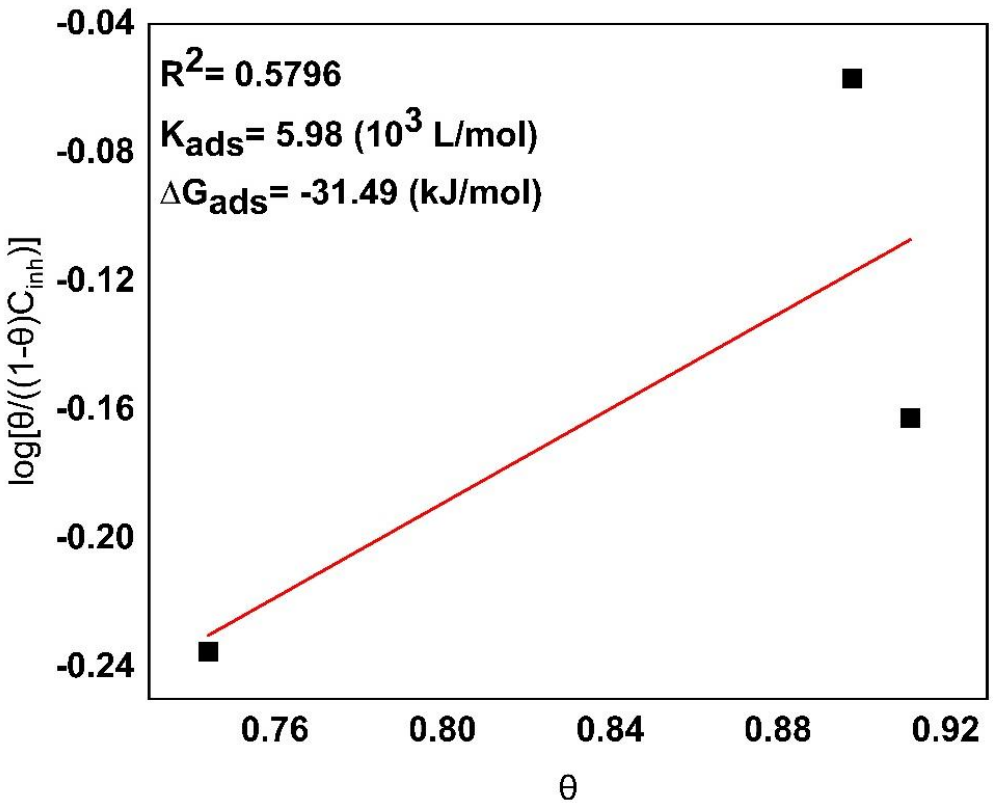

(c)

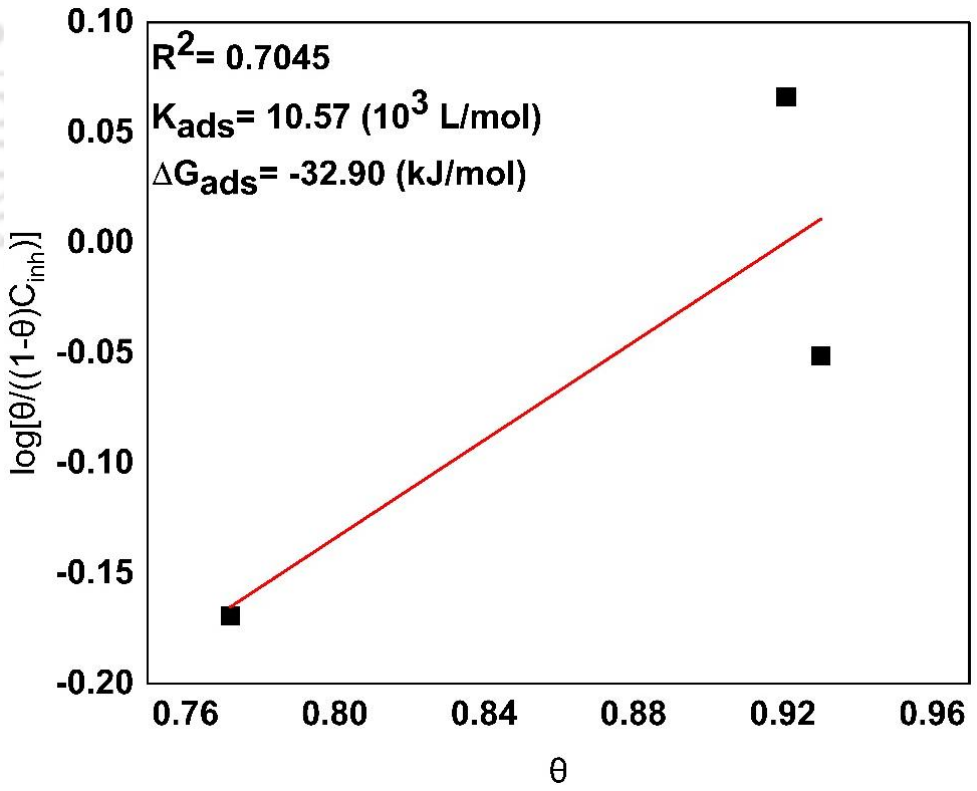

Figure 4.3.6 Fumkin adsorption isotherms of Ru in solution containing (a) IMD, (b) TAZ, and (c) BTAH

4.3.3.3 EIS Measurements

Electrochemical impedance spectroscopy (EIS) was further used to investigate the protective performance and electrochemical behaviours of IMD, TAZ, and BTAH inhibitors. The EIS measurements were conducted under steady-state OCP conditions. The Nyquist plots acquired for inhibitors-Ru at various concentrations are shown in **Figure 4.3.7**. The solid continuous curve in these figures illustrates the simulated EIS data from the electrical equivalent circuit (EEC) while the dotted curve indicates the experimental results that were recorded. In general, bigger capacitive diameters and arcs of the inhibitor system indicate superior inhibition effectiveness(Wang et al., 2023). For all three systems, capacitive arcs continue to increase with the increase in inhibitor concentration. The low-frequency impedance modulus ($|Z|_{0.01\ Hz}$) of IMD, TAZ, and BTAH at 15 mM was 116.02, 448.76, and 593.98 (kΩ cm^2), respectively while for blank, it was 9.72 kΩ cm^2.

The Nyquist plots are analysed with the appropriate EEC model as shown in **Figure 4.3.8.** In the circuit model, R_s represents the solution resistance. The Q_2 and R_2 correspond to double layer capacitance and charge transfer resistance at the metal-solution interface respectively; Q_1 and R_1 represent the capacitance and resistance associated with passive film formed by inhibitors on the Ru surface respectively. Two Maxwell elements (Q_1 and Q_2) along with solution resistance (R_s) were used to represent the Ru dissolution in the presence of inhibitors. The similar EEC circuit with Q_1 and Q_2 was also used in previous studies(W. Li et al., 2022d; Sun et al., 2021b; Wu et al., 2023). The constant phase element (CPE) is used instead of ideal capacitance (C) to account for non-ideal behaviour and its impedance is calculated as follows.

$$Z = \frac{(j\omega)^{-n}}{Y_0} \qquad \textbf{(4.3.24)}$$

$$C = Y_0(\omega_{max})^{n-1} \qquad \textbf{(4.3.25)}$$

Where ω_{max}, Y_0, and j denote the maximum angular frequency corresponds to the Z_{im}, CPE parameter, and imaginary root, respectively. When n = 1, the constant phase element (CPE) is treated as a pure capacitor while n = 0 is treated as a resistor(Adhikari et al., 2024; Mahanta et al., 2022). The non-ideal capacitance is characterized by 0<n<1 which arises due to the heterogeneities of the electrode surface (Talukdar et al., 2023b, 2022b). The polarization resistance (R_p) is calculated using the following equation.

$$Rp = R_1 + R_2 \qquad \textbf{(4.3.27)}$$

The inhibition efficiency (IE %) is estimated using the following equation.

$$IE\ (\%) = \frac{R_p - R_p o}{R_p} \times 100 \qquad \textbf{(4.3.28)}$$

Where R_p and R_po refer to the polarization resistance in the presence and absence of an inhibitor.

The EEC parameters obtained from the simulation are provided in **Table 4.3.2**. The selected comparable circuit shows a best fit quality. In general, Maxwell element (Q_1, R_1) is coupled i.e. when R_1 value increases, the value Q_1 tend to decrease or vice-versa. Here, an increase of both Q_1 and Q_2 values along with decrease in R_1 and R_2 values is observed as the concentration increases. It clearly indicates less corrosion, implying greater protection by the film-forming inhibitor molecules(Saleh et al., 2019). As shown in the **Table 4.3.2.** R_1 and R_2 values for the BTAH system are maximum compared to IMD and TAZ systems. About 99.02 % of PE was recorded for BTAH at 15 mM concentration, demonstrating that the Ru dissolution process is suppressed by the inhibitors' adsorption on the Ru surface. In addition, the adsorption layer becomes more denser with an increase in BTAH inhibitor concentration. However, PE of TAZ and IMD are also quite significant and hence, all the three inhibitors could be considered for protection of Ru metal from corrosion in CMP and post CMP applications.

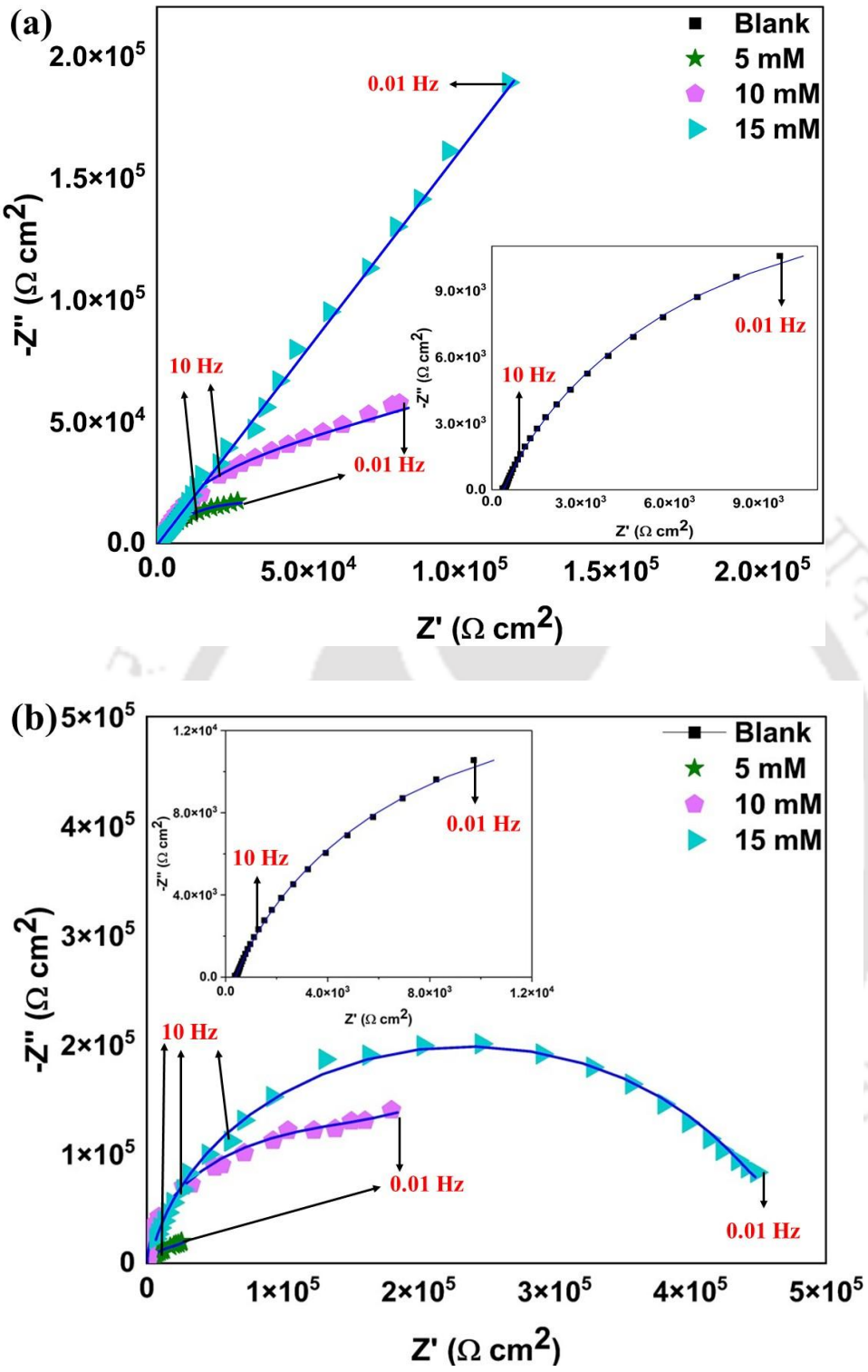

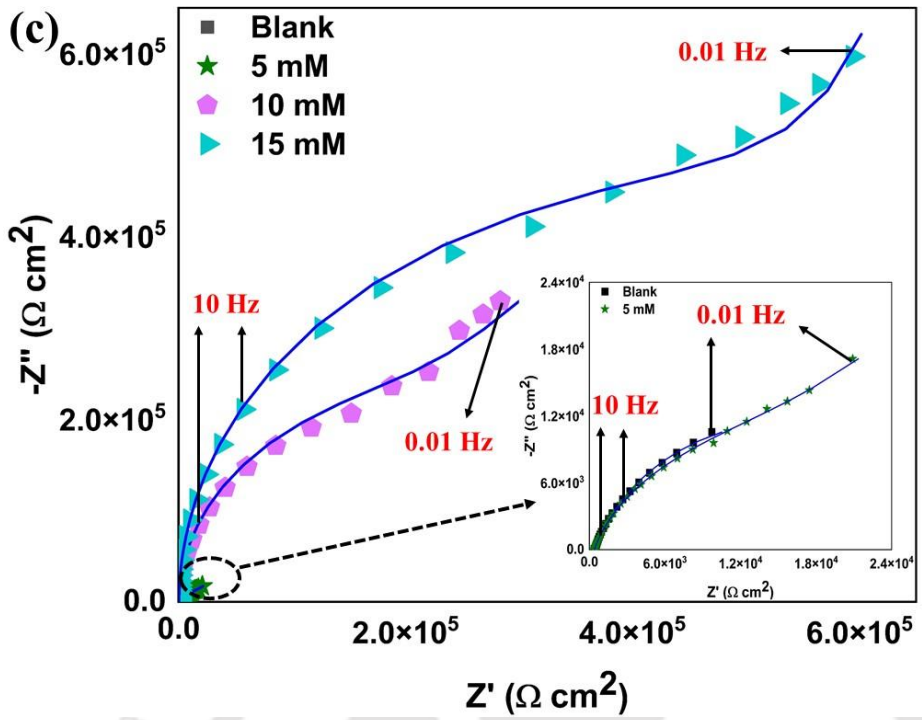

Figure 4.3.7 The Nyquist diagram of Ru with different concentrations of **(a)** IMD, **(b)** TAZ, and **(c)** BTAH; solid line and marker points represent the simulated and experimental data, respectively

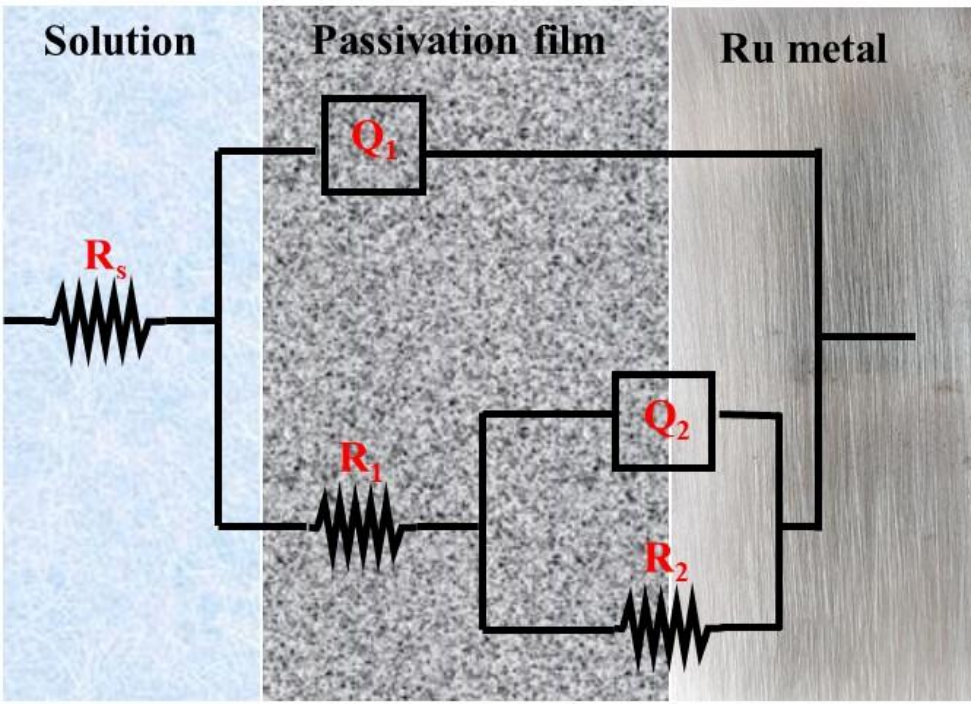

Figure 4.3.8 Electrical equivalent circuit proposed to simulate EIS data for Ru in alkaline solution containing inhibitors

Table 4.3.2 EEC fitting parameters of Nyquist plot of Ru with IMD, TAZ, and BTAH inhibitors

	Con. (mM)	**R_s ($k\Omega\ cm^2$)**	**Q-Yo 10^{-6} ($F\ cm^{-2}\ S^{n-1}$)**	**Q-n**	**Q_1 10^{-6} ($F\ cm^{-2}\ S^{n-1}$)**	**R_1 ($k\Omega\ cm^2$)**	**Q-Yo 10^{-6} ($F\ cm^{-2}\ S^{n-1}$)**	**Q-n**	**Q_2 10^{-6} ($F\ cm^{-2}\ S^{n-1}$)**	**R_2 ($k\Omega\ cm^2$)**	**R_p ($k\Omega\ cm^2$)**	**PE (%)**
Blank	0	0.10±0.001	0.11±0.004	0.75	0.01±0.000	3.51±0.126	90.53±2.444	0.81	15.13±0.287	90.12±3.613	93.63	-
IMD	5	0.13±0.006	9.99±0.429	0.71	0.54±0.019	5.00±0.160	102.4±3.072	0.79	12.29±0.356	320.11±3.233	325.11	71.20
	10	0.17±0.004	5.02±0.165	0.79	0.48±0.021	7.12±0.277	90.77±2.450	0.76	6.29±0.157	611.70±6.789	618.82	84.86
	15	0.22±0.010	2.85±0.094	0.73	0.12±0.010	9.04±0.343	9.84±0.167	0.91	3.28±0.101	1091.7±7.751	1100.74	91.49
TAZ	5	0.20±0.009	92.13±1.750	0.80	12.09±0.411	19.40±0.543	353.8±3.538	0.67	12.99±0.635	400.11± 6.841	419.51	77.68

	10	0.37±0.008	21.22±1.039	0.83	2.71±0.084	65.48±1.70	89.44±1.967	0.78	6.24±0.149	1001.3±7.109	1066.78	91.22
	15	0.40±0.004	11.44± 0.446	0.84	1.34±0.045	84.59±3.129	90.14±1.442	0.73	2.68±0.117	2101.01±6.513	2185.60	95.71
BTAH	5	0.23±0.005	38.79±1.590	0.96	26.42±0.618	102.55±3.076	102.4±1.638	0.84	21.25±0.85	611.11±6.172	713.66	86.88
	10	0.23±0.011	5.22±0.240	0.97	3.54±0.092	402.15±4.423	9.27±0.259	0.94	4.15±0.182	1909.98±9.740	2312.13	95.95
	15	0.31±0.012	3.85±0.188	0.97	2.69±0.078	712.34±4.986	7.14±0.128	0.92	2.33±0.102	8900.98±9.791	9613.32	99.02

4.3.3.4 Removal rate experiments at different temperature range

The CMP is conducted only at room temperature for the duration of 2-3 min. To gain insight into the physical and chemical behaviour of inhibitors at pH 9 on the Ru metal the experiments were conducted at various temperature (25°C to 55°C). The sample of Ru metal was submerged in a beaker containing 200 ml of a solution (blank/IMD/TAZ/BTAH) for a duration of 30 min. The Ru coupon was measured in terms of weight before and after being immersed in the solution, using an analytical balance (Sartorius, India) with a readability of 0.0001 g. Afterwards, the Ru metal coupon underwent a thorough washing process using deionized water and was subsequently dried at room temperature using nitrogen gas. In each case, a minimum of three experimental runs were conducted, and the average rate was recorded, accompanied by the standard deviation. The following equation used to calculate the removal rate (RR).

$$\text{Removal rate (RR)}\left(\frac{\text{nm}}{min}\right) = \frac{\text{Weight loss (gm)} \times 10^7}{\text{Density}\left(\frac{gm}{cm^3}\right) \times \text{Time}\,(min) \times \text{Surface area}(\text{cm}^2)} \quad \textbf{(4.3.29)}$$

Table 4.3.3 Effect of temperature on Ru metal in the presence and absence of inhibitor at pH 9

Temperature (K)	Inhibitor	RR (nm/min)
289	Blank	22±0.31
	IMD	19±0.26
	TAZ	18±0.32
	BTAH	14±0.18
313	Blank	34±0.37
	IMD	29±0.32
	TAZ	29±0.55

	BTAH	27±0.51
328	Blank	41±0.41
	IMD	39±0.11
	TAZ	33±0.33
	BTAH	30±0.31

Table 4.3.3 demonstrates the impact of temperature on the removal rate of Ru coupons, both with and without the presence of an inhibitor. The solution's pH was adjusted to 9 across all temperature fluctuations. The lowest RR was obtained for the BTAH inhibitor at all the temperate ranges compared to IMD and TAZ.

The activation energy (E_a) of Ru metal in the proposed solution (blank/IMD/TAZ/BTAH) was calculated using the Arrhenius equation as follow

$$log(\mathrm{RR}) = \log A - \frac{E_A}{2.303RT} \quad \textbf{(4.3.30)}$$

Where A stands for Arrhenius pre-exponential factor, T stands for absolute temperature, and R stands for universal gas constant (8.314 J/mol K). A straight line is interpolated whose intercept and slope is log A and $\frac{-E_A}{2.303R}$ respectively. The semi-logarithmic plot of log RR versus 1/T was plotted using Arrhenius equation, which is shown in **Figure 4.3.9**. Typically, an elevated E_a value signifies an increased energy barrier for the corrosion reaction, there by indicating enhanced efficacy of the inhibitor in impeding the reaction. The kinetic parameters of all the system were presented in the **Table 4.3.3**. The present study observed that the E_a values for the inhibited system were consistently higher than those for the uninhibited system across all concentrations of inhibitors. The maximum E_a (20.67 kJ/mol) value was observed for the BTAH system compare to blank, IMD, and TAZ.

Enthalpy and entropy of activation were calculated using transition state equation as follows

$$log\left(\frac{\mathrm{ER}}{\mathrm{T}}\right) = [log\left(\frac{\mathrm{R}}{\mathrm{Nh}}\right) + \frac{\Delta \mathrm{S_{act}}}{2.303\mathrm{R}}] - \frac{\Delta \mathrm{H_{act}}}{2.303\mathrm{RT}} \qquad \textbf{(4.3.31)}$$

Where, N is Avogadro's number (6.02252×10^{23} mol^{-1}), h stands for Plank's constant (6.626176×10^{-34} Js), ΔH_{act} is enthalpy of activation and ΔS_{act} stands for entropy of activation. Enthalpy and entropy were calculated by equating the intercept $[\log\left(\frac{R}{Nh}\right) + \frac{\Delta S_{act}}{2.303R}]$ and slope $[-\frac{\Delta H_{act}}{2.303R}]$ of the straight line as demonstrated in **Figure 4.3.10** and the are presented in the **Table 4.3.3**. The positive sign of enthalpy (ΔH_{act}) reflects the endothermic nature of the corrosion inhibition process. A negative value of (ΔS_{act}) indicates that the corrosion inhibition process is controlled by activation complex.

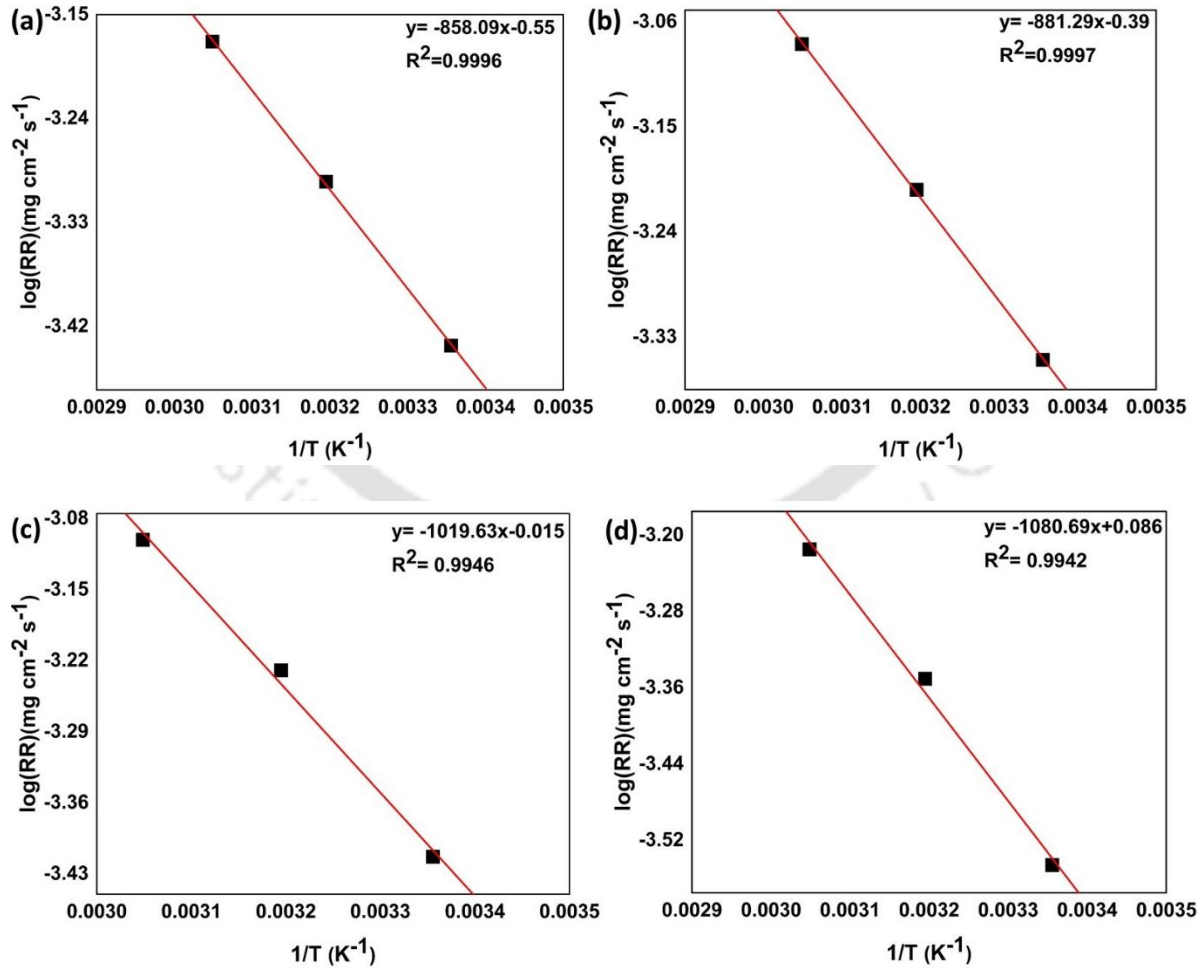

Figure 4.3.9 Arrhenius plot of Ru metal at pH 9 in the for (a) blank, (b) IMD, (c) TAZ, and (d) BTAH

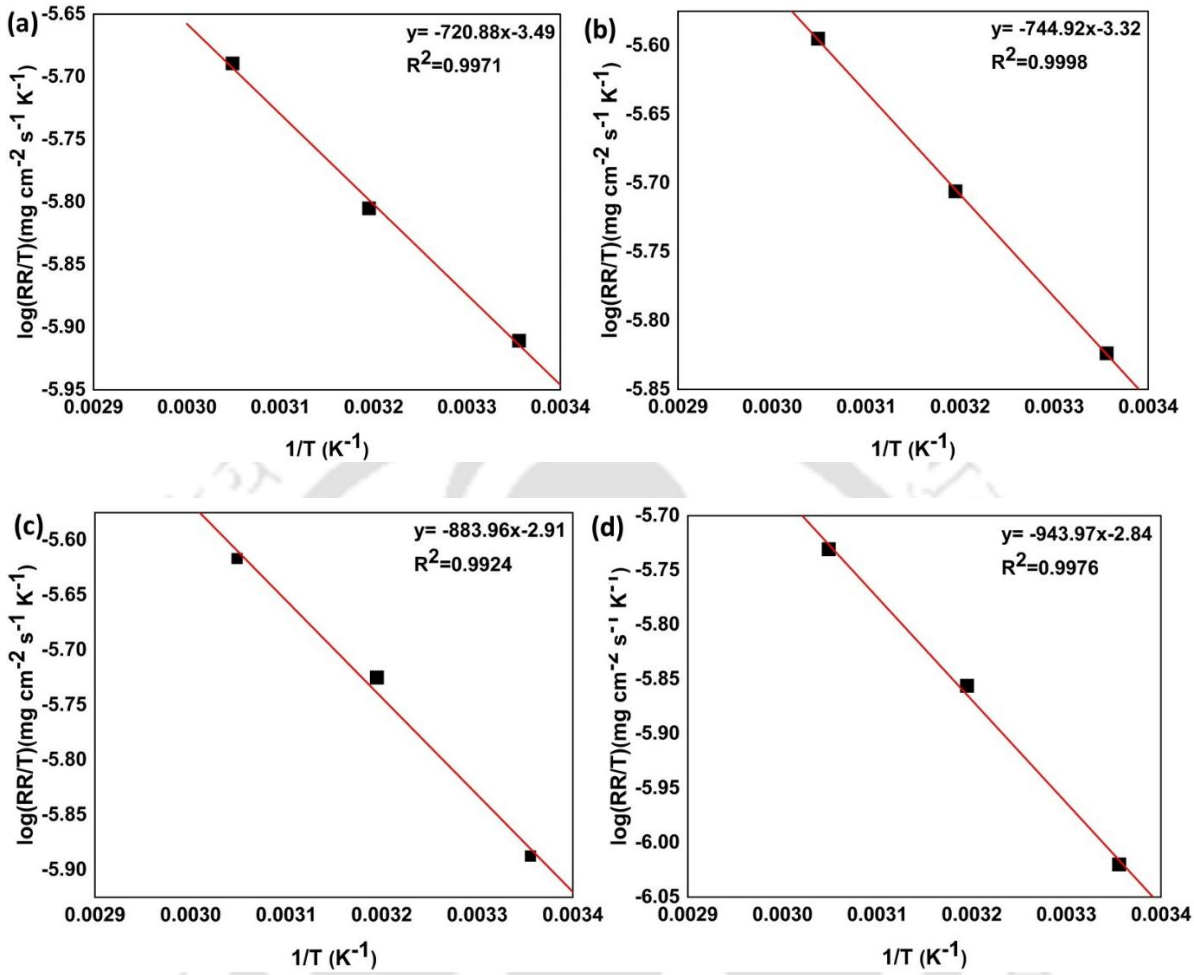

Figure 4.3.10 Plot of log (ER/T) vs. 1/T for Ru at pH 9 for (a) blank, (b) IMD, (c) TAZ, and (d) BTAH

Table 4.3.4 Kinetic parameters for blank, IMD, TAZ, and BTAH for Ru metal at 9 pH.

	E_a (kJ/mol)	**ΔH_{act}(kJ/mol)**	**ΔS_{act}(kJ/mol)**
Blank	16.42	13.80	-264.39
IMD	16.87	14.26	-261.14
TAZ	19.52	16.92	-253.36
BTAH	20.67	18.07	-251.95

4.3.3.5 Surface characterization

The confirmation of corrosion protection offered by IMD/TAZ/BTAH on the surface of Ru was validated through the utilization of contact angle measurements. The contact angle of Ru surface before and after treated with various inhibitors are shown in **Figure 4.3.11.** The contact angle of untreated Ru surface (in the absence of an inhibitor) yielded a value of 58º, confirms that the surface is hydrophilic in nature. Following exposure to solutions containing 15 mm of IMD/ TAZ/ BTAH, the contact angles observed on the Ru surface exhibited an increase to 86°, 94°, and 98°, respectively. The observed alteration in contact angle can be attributed to the creation of hydrophobic surface via the formation of film layer consisting of inhibitor molecules on the Ru surface. Nevertheless, the maximum contact angle is observed for BTAH treated Ru surface which is attributed to the adsorption of greater quantity of BTAH molecules on the Ru surface.

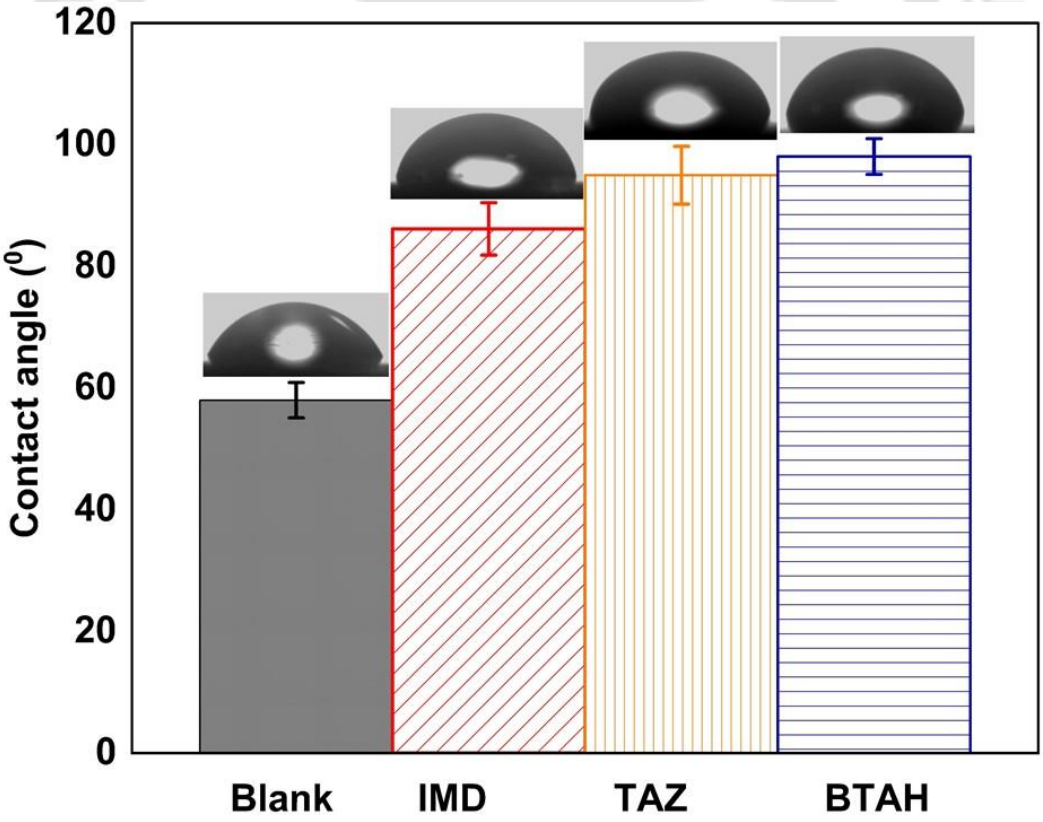

Figure 4.3.11 Contact angle of Ru surface treated with and without inhibitors at pH 9

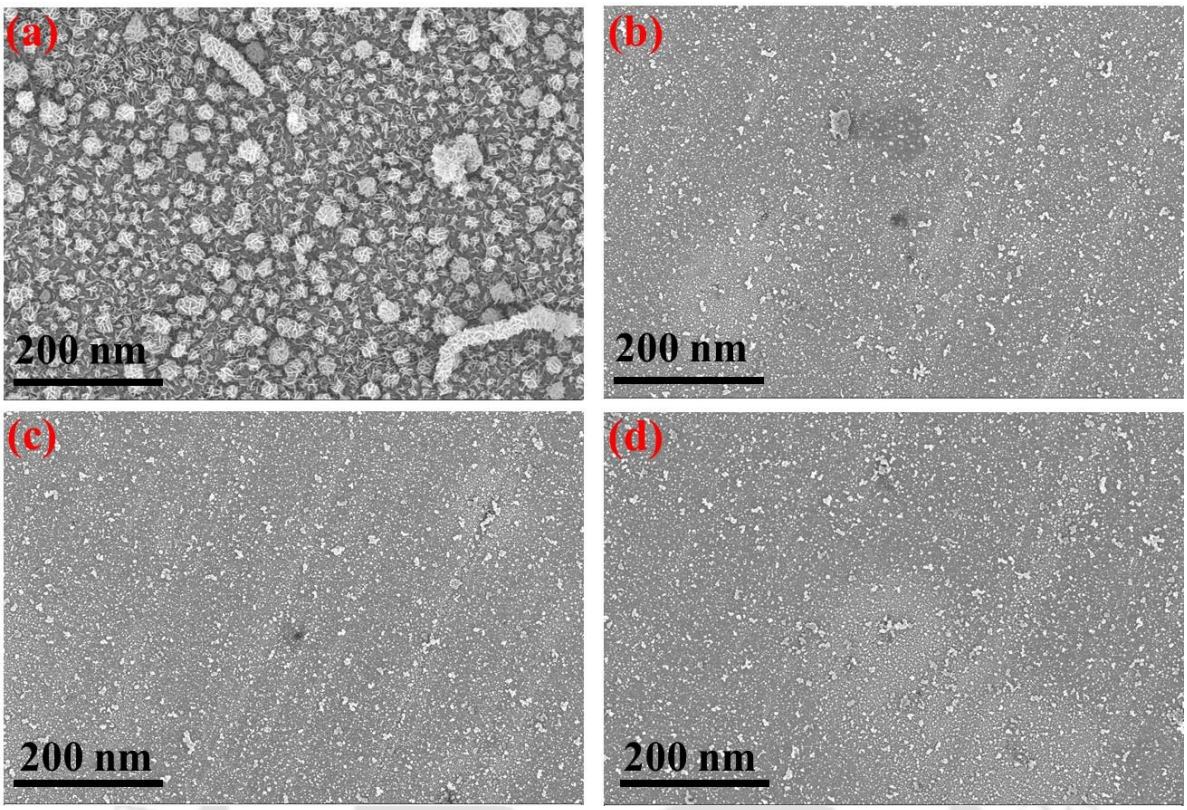

Figure 4.3.12 SEM image of Ru surface after immersion in (a) blank (b) IMD (c) TAZ, and (d) BTAH

In a similar manner, the surface of Ru material was subjected to FESEM analysis subsequent to immersion, both with and without the presence of inhibitor (IMD/TAZ/BTAH) at a concentration of 15 mM, as illustrated in **Figure 4.3.12**. Corrosion products were observed on the surface of Ru after immersion, as depicted in **Figure 4.3.12(a)**, in the absence of an inhibitor. The corrosion products are discontinuous in nature i.e. not completely covered the Ru surface to prevent it from dissolution. The surface micrographs shown in **Figure 4.3.12(b, c, and d)** did not exhibit any discernible pits, surface damage, or signs of corrosion product. Upon comparing the micrograph of Ru surface obtained from the blank solution, it becomes evident that the corrosion of Ru was significantly suppressed. This observation substantiates the existence of the inhibitor molecules on the Ru surface, manifesting a film layer that functions as a hindrance between the Ru sample and the alkaline solution.

4.3.3.6 Quantum chemical calculations

The ability of the inhibitor molecule to donate/accept electrons could be explained by an electron donation mechanism. Frontier molecular orbital analysis has been widely used in assessing the efficacy of inhibitors and explore the mechanisms behind their interactions with metal surfaces(Sim et al., 2018; C. Yu et al., 2016). Hence, the HOMO and LUMO energy levels were calculated for all the three inhibitors (IMD, TAZ, and BTAH) and are presented in **Figure 4.3.13.** Quantum chemical parameter, E_{HOMO} is associated with the molecule's electron donating ability i.e. when E_{HOMO} value is high, molecules donate electrons to other azole compounds that have unfilled molecular orbitals with lower energy levels(Zarrouk et al., 2012a). It is further indicating the stronger adsorption between inhibitor molecules and metal atom and hence, better inhibition efficiency. Low LUMO energy (E_{LUMO}), on the other hand, suggests that the molecules are more likely to receive electrons from the metal atoms and, results in a stronger inhibition efficiency. The characteristic value of chemical reactivity between molecules and metal atoms is represented by the gap between HOMO and LUMO, or E_{gap}. In general, the reduction of E_{gap} can enhance chemical reactivity, which will result in better inhibition efficiency(Fang and Li, 2002; Li et al., 2005).

Name	HOMO	LUMO
IMD	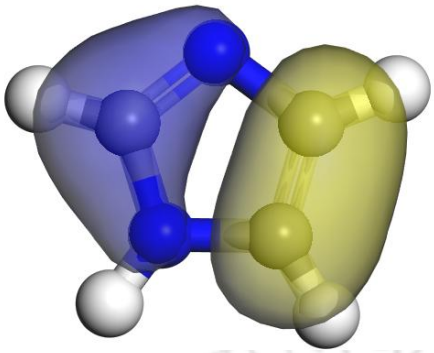	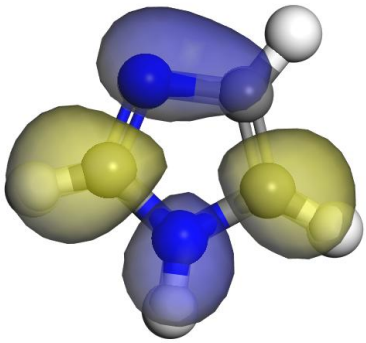
TAZ	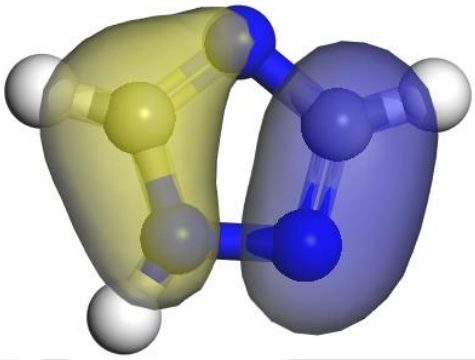	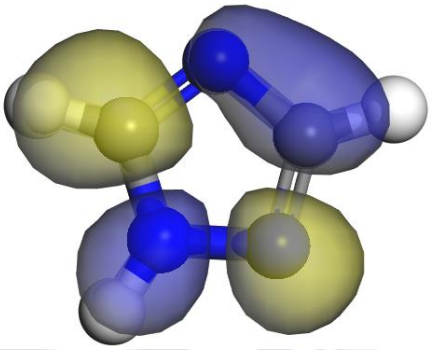
BTAH	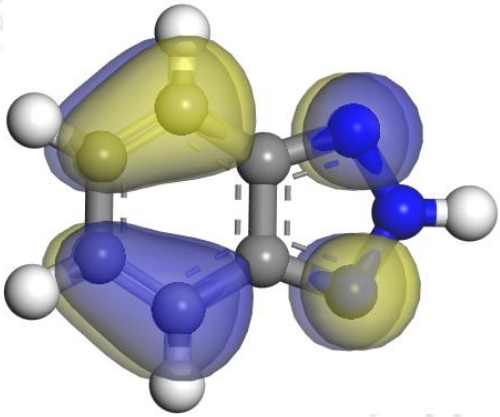	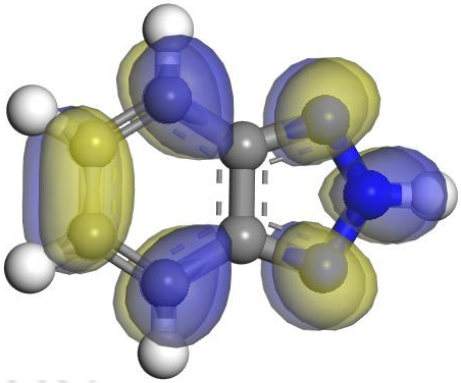

Figure 4.3.13 HUMO and LUMO molecular orbitals of IMD, TAZ, and BTAH molecules.

Atom legend: white = H, gray = C, and blue = N

The quantum chemical parameters are displayed in **Table 4.3.4**. The observed order of the HOMO values for the three inhibitors under investigation is as follows: IMD > BTAH > TAZ.

Hence, based solely on the HOMO and LUMO energy levels of the three inhibitor molecules under investigation, it is challenging to determine which inhibitor exhibits a greater adsorption capacity (Huang and Guo, 2020). The ordering of the ΔE values is as follows: TAZ > IMD> BTAH. This ordering suggests that BTAH exhibits a higher affinity for adsorption onto the Ru surface compared to IMD and TAZ. The difference in ΔE values between IMD (5.275 eV) and TAZ (5.644 eV) is minimal, indicating a lack of significant correlation with corrosion inhibition performance(Huang and Guo, 2020; Sun et al., 2021c). The order of η is TAZ < IMD < BTAH and the BTAH compound exhibits the highest global softness (σ) value (0.592 eV^{-1}) when compared to the IMD (0.379 eV^{-1}) and TAZ (0.354 eV^{-1}) compounds. These results clearly indicate the higher inhibitory effectiveness of BTAH (Yang et al., 2022; D. Yin et al., 2020b; Yin et al., 2021b). The electrophilicity index (ω) was also calculated and reported in **Table 4.3.5** for IMD, TAZ, and BTAH inhibitor. The ensuing inhibitory effectiveness of electron donation is related to the levels of ΔN. Lukovits (Lukovits et al., 2001) and co-workers reported that if the ΔN value is less than 3.6, the ability of the metal's surface to act as an electron donor causes the inhibition efficiency to increase. In this work, the three inhibitors (IMD, TAZ, and BTAH) present values of ΔN less than 3.6, implying that the Ru (0 0 1) surface is an acceptor and the inhibitor molecules are electron donors. The ΔN value of IMD, TAZ, and BTAH are 0.41, 0.22, and 0.28, respectively. The quantum chemical results indicate that all three inhibitors possess the ability to safeguard the Ru metal in an alkaline solution. However, this study clearly demonstrates that the trend observed for inhibition efficiency of inhibitors could not be merely understood from the quantum chemical descriptors. Similar observations are also reported in the literature(Huang and Guo, 2020; Khaled, 2008). The quantum chemical calculations and parameter of deprotonated IMD-, TAZ-, and BTA- is presented in the **Figure 4.3.14-4.3.16** and **Table 4.3.6**. The ΔN value for BTA- (deprotonated) is 0.146 is observed.

Table 4.3.5 Quantum chemical parameter of inhibitors

Quantum Chemical Parameters	**Components**		
Inhibitor	**IMD**	**TAZ**	**BTAH**
HOMO (eV)	-5.176	-6.288	-5.435
LUMO (eV)	0.099	-0.644	-2.059
ΔE_{gap} (eV)	5.275	5.644	3.376
Ionization potential (I) (eV)	5.176	6.288	5.435
Electron affinity (A) (eV)	-0.099	0.644	2.059
Electronegativity (χ) (eV)	2.538	3.466	3.747
Global hardness (η) (eV)	2.637	2.822	1.688
Global softness (σ) (eV^{-1})	0.379	0.354	0.592
electrophilicity index (ω) (eV)	1.221	2.128	4.158
ΔN	0.411	0.220	0.285

Based on the research conducted by Hohenberg and Kohn(Ju et al., 2008), it has been established that the overall energy of a system can be characterized as a distinct function of the charge density. This charge density encompasses the internal energy, potential energy, and kinetic energy components. The ground state energy corresponds to the overall energy function, exhibiting the lowest possible value within the given system(Zarrouk et al., 2012b). The recorded total energy values for the IMD, TAZ, and BTAH inhibitors were -226.26 Ha, -242.31 Ha, and -395.96 Ha, respectively. The BTAH inhibitor exhibits a lower total energy

compared to the IMD and TAZ inhibitors, indicating that the BTAH inhibitor possesses a higher inhibition efficiency.

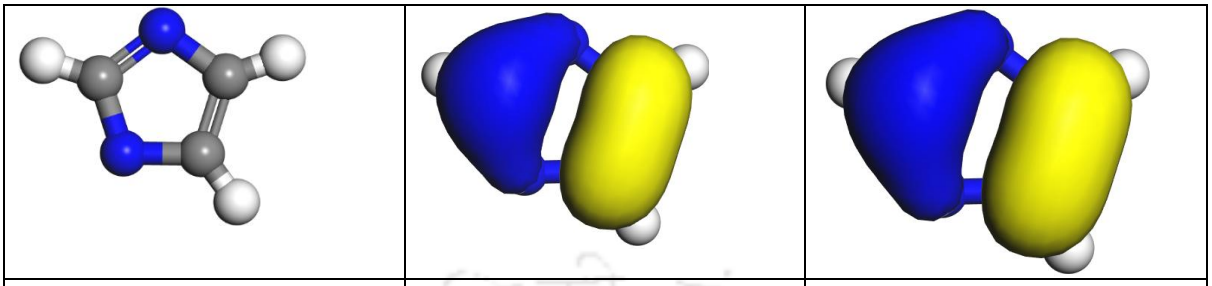

(a)	(b)	(c)

Figure 4.3.14 (a) Optimized structure of IMD- (b) HOMO and (c) LUMO of IMD-

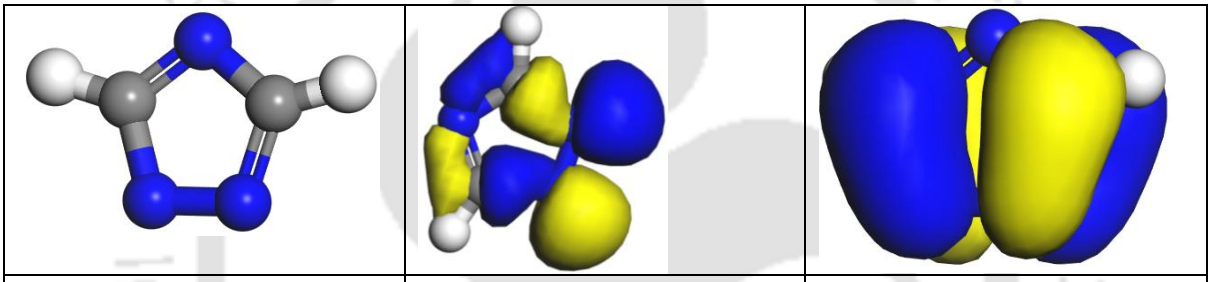

(a)	(b)	(c)

Figure 4.3.15 (a) Optimized structure of TAZ- (b) HOMO and (c) LUMO of TAZ-

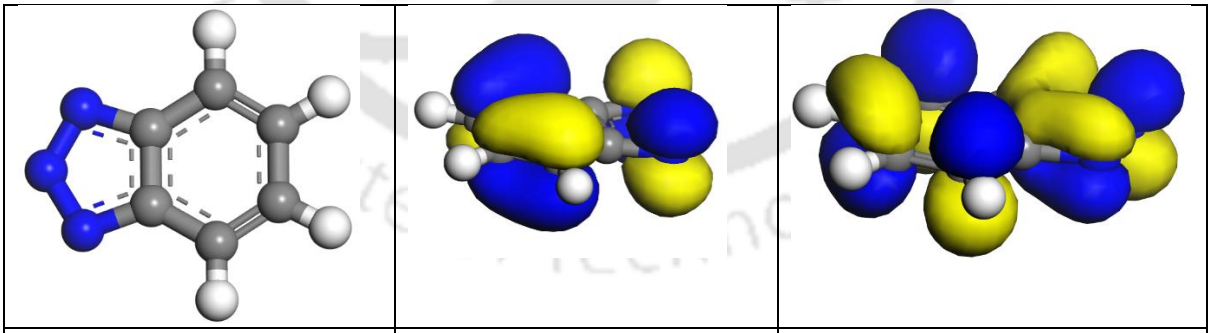

(a)	(b)	(c)

Figure 4.3.16 (a) Optimized structure of BTA- (b) HOMO and (c) LUMO of BTA-

Table 4.3.6 Quantum chemical parameter of inhibitors in deprotonated form

Quantum Chemical Parameters	**Components**		
Inhibitor	**IMD-**	**TAZ-**	**BTA-**
HOMO (eV)	-6.307	-6.799	-5.979
LUMO (eV)	-5.329	-6.156	-2.394
ΔE_{gap} (eV)	0.978	0.643	3.585
Ionization potential (I) (eV)	6.307	6.799	5.979
Electron affinity (A) (eV)	5.329	6.156	2.394
Electronegativity (χ) (eV)	5.818	6.477	4.186
Global hardness (η) (eV)	0.489	0.321	1.792
Global softness (σ) (eV^{-1})	2.044	3.110	0.557
electrophilicity index (ω) (eV)	34.610	65.25	4.888
ΔN	-1.132	-2.748	0.146

An analysis of the Mulliken population and HOMO population can yield potential adsorption centres for inhibitors(Hasanov et al., 2007; Kandemirli and Sagdinc, 2007). Atoms exhibiting the most pronounced Mulliken atomic negative charge are commonly regarded as possessing the greatest inclination to interact with the surface of the metal(Obot and Gasem, 2014). **Figure 4.3.17** and **Table 4.3.7** display the Mulliken charge density and Mulliken atomic charge of IMD, TAZ, and BTAH, respectively, as determined using the 3.5DNP basis set and GGA/BLYP theoretical approach. The IMD compound contains a pair of nitrogen atoms (N1,

N2) with negative charge while the TAZ contains three nitrogen atoms (N1, N2, N3) with negative charge. However, in the case of BTAH, in addition to nitrogen atoms (N13, N14) certain carbon atoms (C4, C5, C7, C8) also exhibit negative Mulliken negative charges. It reveals that BTAH molecule has more reactive sites for adsorption followed by TAZ and IMD. These atoms serve as reactive sites for adsorption, either electrophilic or nucleophilic in nature.

IMD	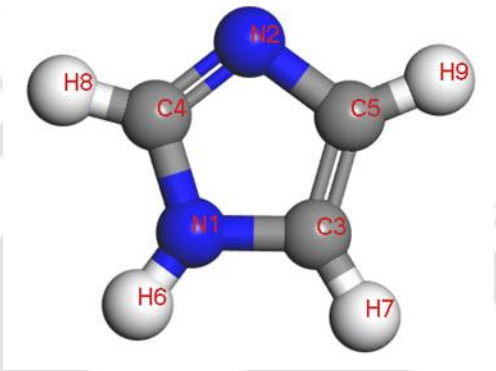
TAZ	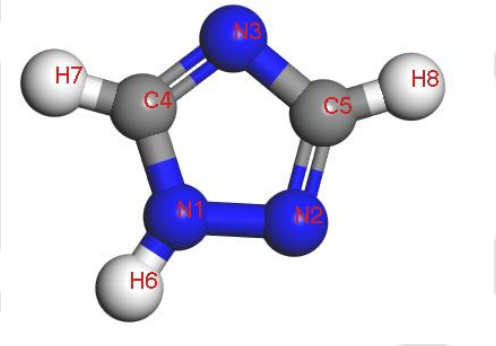
BTAH	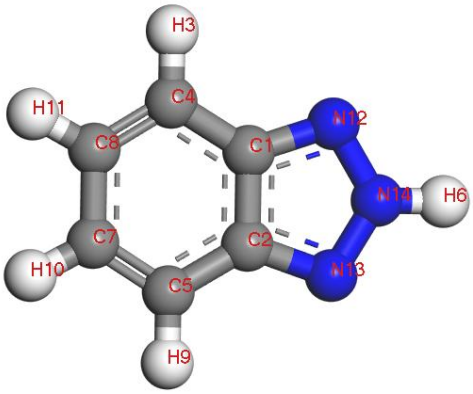

Figure 4.3.17 The Mulliken charge density of IMD, TAZ, and BTAH. [Atom legend: white = H; gray = C; blue = N]

Table 4.3.7 Calculated Mulliken atomic charge of heavy atoms of IMD, TAZ, and BTAH

IMD	Mulliken atomic charge	TAZ	Mulliken atomic charge	BTAH	Mulliken atomic charge
N1	-0.251	N1	-0.102	C1	0.207
N2	-0.458	N2	-0.312	C2	0.207
C3	0.07	N3	-0.443	H3	0.027
C4	0.219	C4	0.246	C4	-0.083
C5	0.062	C5	0.223	C5	-0.083
H6	0.196	H6	0.207	H6	0.214
H7	0.028	H7	0.05	C7	-0.022
H8	0.028	H8	0.031	C8	-0.022
H9	0.006			H9	0.027
				H10	0.026
				H11	0.026
				N12	-0.339
				N13	-0.339
				N14	0.056

4.3.3.7 Monte Carlo simulation of IMD, TAZ, and BTAH

	Side view	Top view
IMD	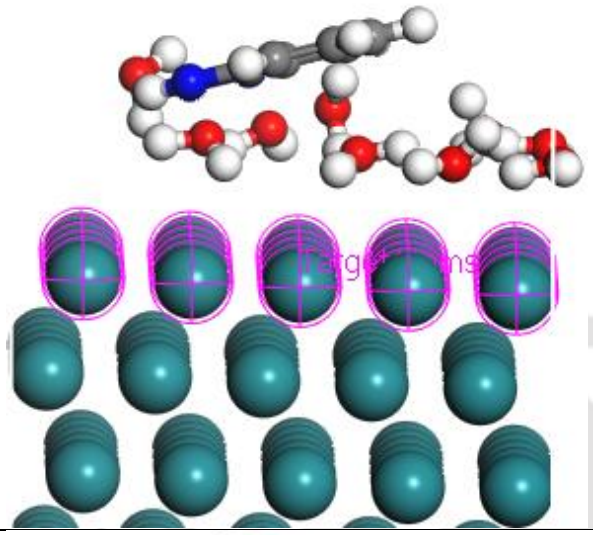	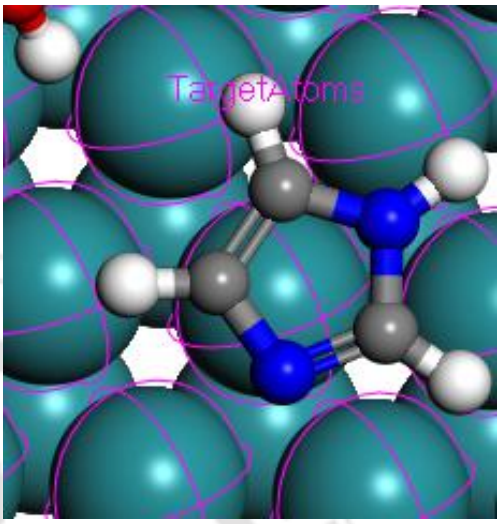
TAZ	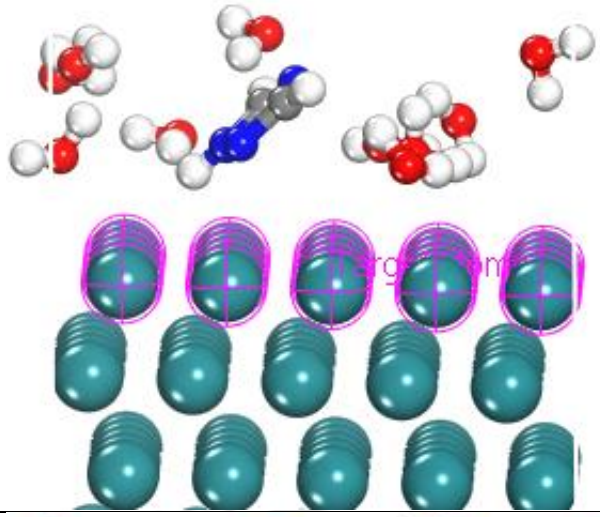	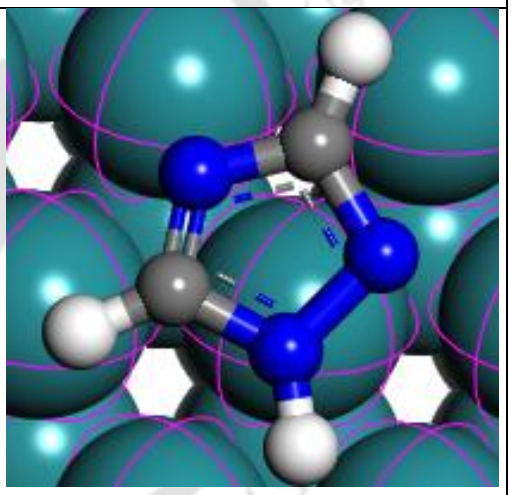
BTAH	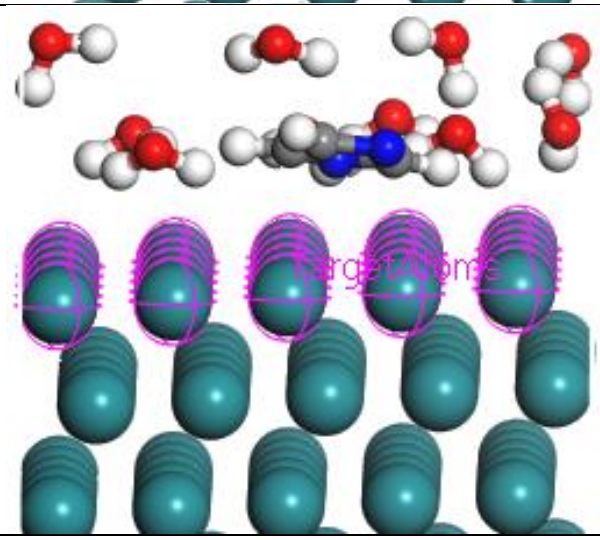	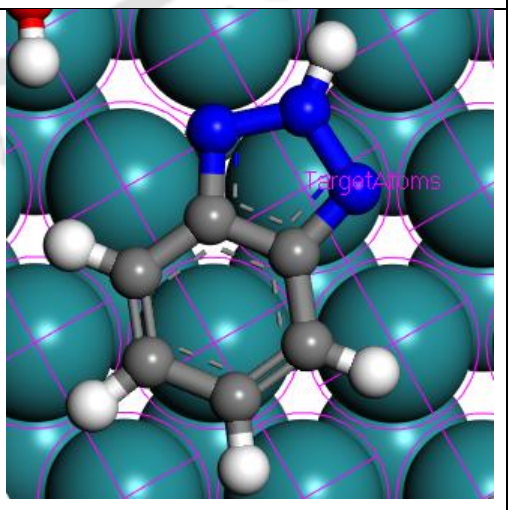

Figure 4.3.18 The adsorption model of IMD, TAZ, and BTAH on Ru (001) surface in aqueous phase

The equilibrium configurations of adsorbed IMD, TAZ, and BTAH on the Ru (0 0 1) surface in the aqueous phase are depicted in **Figure 4.3.18**. The side and top views representation of inhibitors interaction with Ru (0 0 1) surface shows a successful adsorption of all three inhibitors. The TAZ and IMD inhibitors make an angle of 40º and 10º to the Ru surface (**Figure 4.3.18**) whereas the flat, planar, and horizontal orientation was observed for the BTAH-Ru system. For superior corrosion prevention efficiency, it is typically preferred as it can cover a wider surface area of Ru surface and has higher binding energy(Haris et al., 2020b; Verma et al., 2018b). Similar findings have also been documented in the existing literature for BTAH and TAZ(D. Yin et al., 2020b; Yin et al., 2021b).

In order to estimate the lowest energy of the whole system, the adsorption energy calculation of inhibitor-Ru was carried out. The total energy, van der Waals energy, electrostatic energy, average total energy and intramolecular energy of IMD, TAZ, and BTAH on Ru surface (0 0 1) were shown in **Figure 4.3.19**. The three types of energy that make up the total are adsorption, rigid adsorption, and deformation energy. This comprises two elements: the energy linked to the sorbate binding to the surface in its initial conformation, known as rigid adsorption energy, and a secondary energy needed for the sorbate to adapt and unwind in the presence of the surface, referred to as deformation energy. The adsorption energy is the amount of energy released or needed when the adsorbate components adhere to the metal surface, without any adjustments to the arrangement. Deformation energy is the energy released when the adsorbed components of the adsorbate relax on the metal surface. The total energy comprises both the adsorption energy and the internal energy of the sorbate. In these circumstances, the energy of the substrate (metal surface) is regarded as zero(Guo et al., 2014; Qiang et al., 2016).

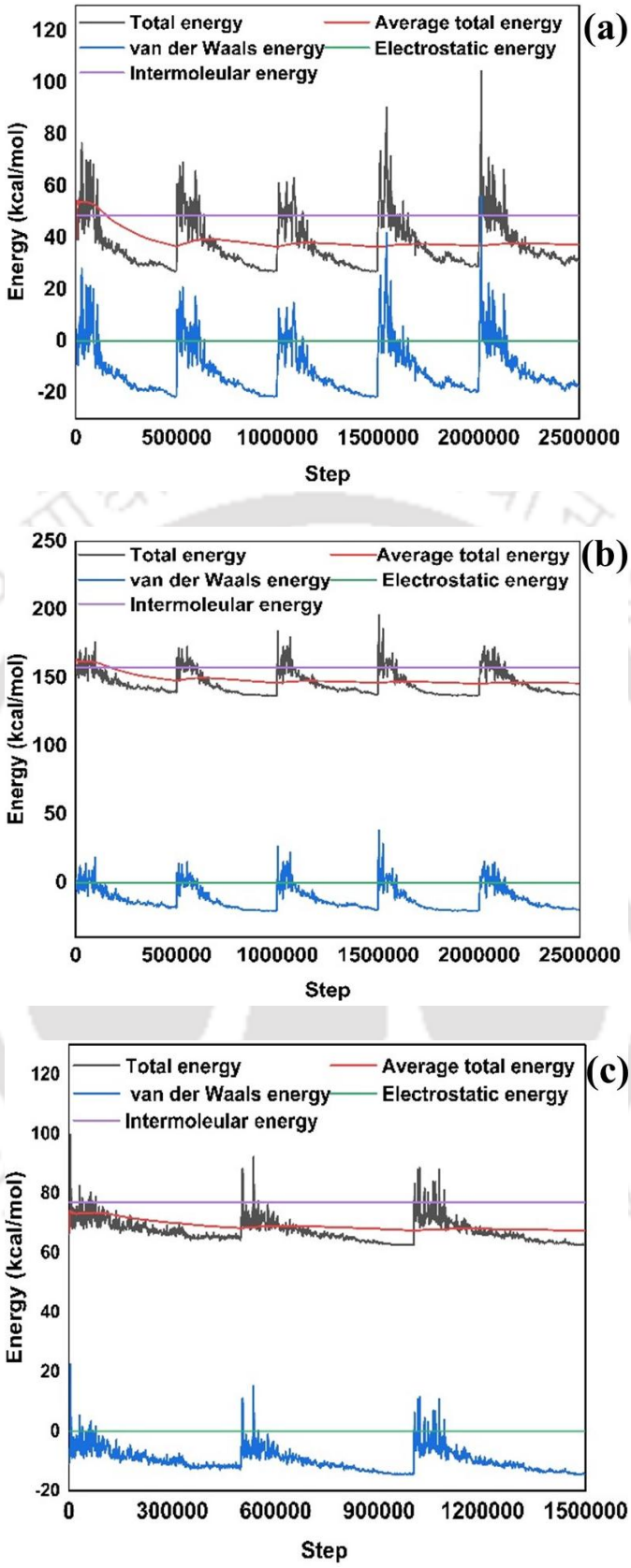

Figure 4.3.19 Total energy distribution of IMD, TAZ, and BTAH inhibitor on the Ru (001) surafce in aqueous phase (10 H_2O molecules)

Table 4.3.8 IMD, TAZ, and BTAH adsorption on Ru surface in liquid phase calculated by Mont Carlo simulation

Inhibitor	Total energy (kcal/mol)	Adsorption energy (kcal/mol)	Rigid adorption energy (kcal/mol)	Deformation energy (kcal/mol)	dE_{ad/dN_i} (kcal/mol)
IMD	16.5348	-31.9654	-18.9353	-13.0300	-14.6127
TAZ	39.4481	-39.6147	-16.6973	-22.9173	-24.4430
BTAH	116.4277	-41.3303	-14.8231	-26.5072	-26.1588

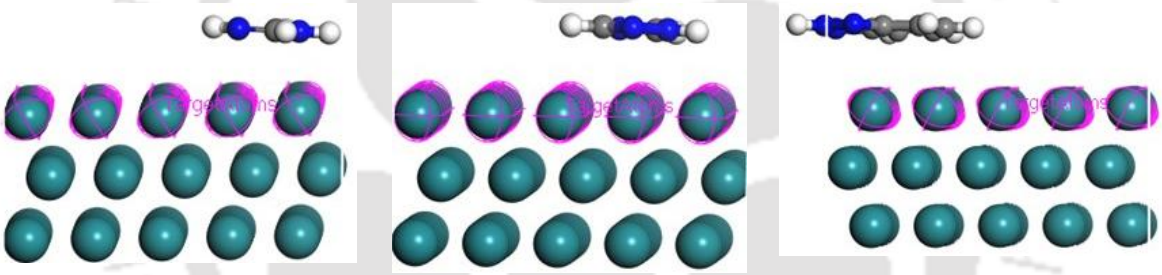

IMD **TAZ** **BTA**

Figure 4.3.20 The adsorption model of IMD, TAZ, and BTAH on Ru (001) surface in the gaseous phase

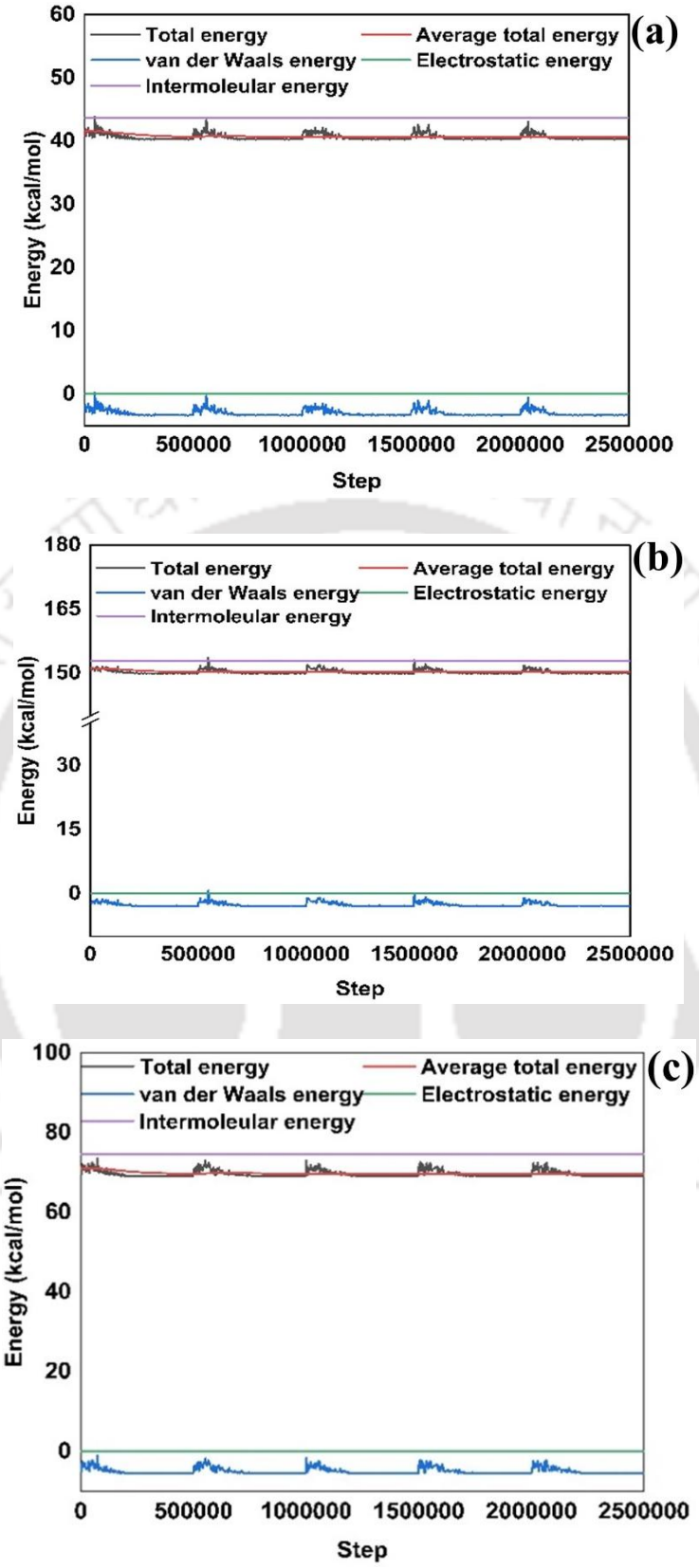

Figure 4.3.21 Total energy distribution of IMD, TAZ, and BTAH inhibitor on the Ru (001) surface in the gaseous phase

The dE_{ad}/d_{Ni} parameter represents the energy value that does not include any adsorbed component. These energy sources possess the ability to demonstrate the adsorption capacity for inhibition. **Table 4.3.8** displays the outputs and descriptors that were computed through the implementation of the Monte Carlo simulation. The manifestation of inhibitors' adsorption ability can be observed through these energy values. Furthermore, the simulation process demonstrates that inhibitors with the lowest adsorption energy exhibit the highest inhibition efficiency in accordance with theoretical principles (Haris et al., 2020b; Sun et al., 2021a). It can be observed that BTAH exhibits the lowest adsorption energy (-41.3303 kcal/mol) compared to IMD (-31.9654 kcal/mol) and TAZ (-39.6147 kcal/mol) when adsorbed on the Ru (0 0 1) surface. It is noteworthy to state that the adsorption energies of the inhibitors.

IMD, TAZ, and BTAH display negative values, which suggest that these inhibitors are efficiently adsorbed onto the Ru (0 0 1) metal surface. Therefore, it is likely that the inhibitor molecules under investigation have the ability to irreversibly adsorb onto the surface of Ru, thereby acting as a protective barrier against corrosion for the Ru surface. The phenomenon's observation is additionally bolstered by the aqueous phase's side view analysis that was conducted. The adsorption model and total energy distribution IMD, TAZ, and BTAH on Ru (001) surface in the gaseous phase is performed and depicted in the **Figure 4.3.20**. In addition, results obtained from the Monte Carlo simulation for the adsorption of IMD, TAZ, and BTA on Ru (001) surface in the gaseous phase **(Figure 4.3.21)** is presented in the **Table 4.3.9**.

Table 4.3.9 IMD, TAZ, and BTAH adsorption on Ru surface in gaseous calculated by Mont Carlo simulation

Gaseous phase					
Inhibitor	**Total energy (kcal/mol)**	**Adsorption energy (kcal/mol)**	**Rigid adsorption energy (kcal/mol)**	**Deformation energy (kcal/mol)**	dE_{ad/dN_i} **(kcal/mol)**
IMD	32.2851	-11.3325	-3.1705	-8.1620	-11.3325
TAZ	129.8902	-22.9853	-1.3593	-21.6259	-22.9853
BTAH	51.1258	-23.5427	-4.9991	-18.543	-23.5427

The adsorption densities of IMD, TAZ, and BTAH on the Ru surface were determined through the utilization of the Monte Carlo method. **Figure 4.3.12** illustrates the adsorption density of IMD, TAZ, and BTAH on the Ru surface in an aqueous phase. The comparative analysis reveals that the adsorption densities of BTAH and TAZ are higher than IMD, indicating that BTAH and TAZ exhibits a greater propensity for the formation of a compact passivation film on the Ru surface. Hence, it is probable that the investigated molecules exhibit stable adsorption on the surface, thereby impeding the corrosion of the Ru surface. It can be concluded that BTAH exhibits a superior inhibitory effect compared to TAZ and IMD.

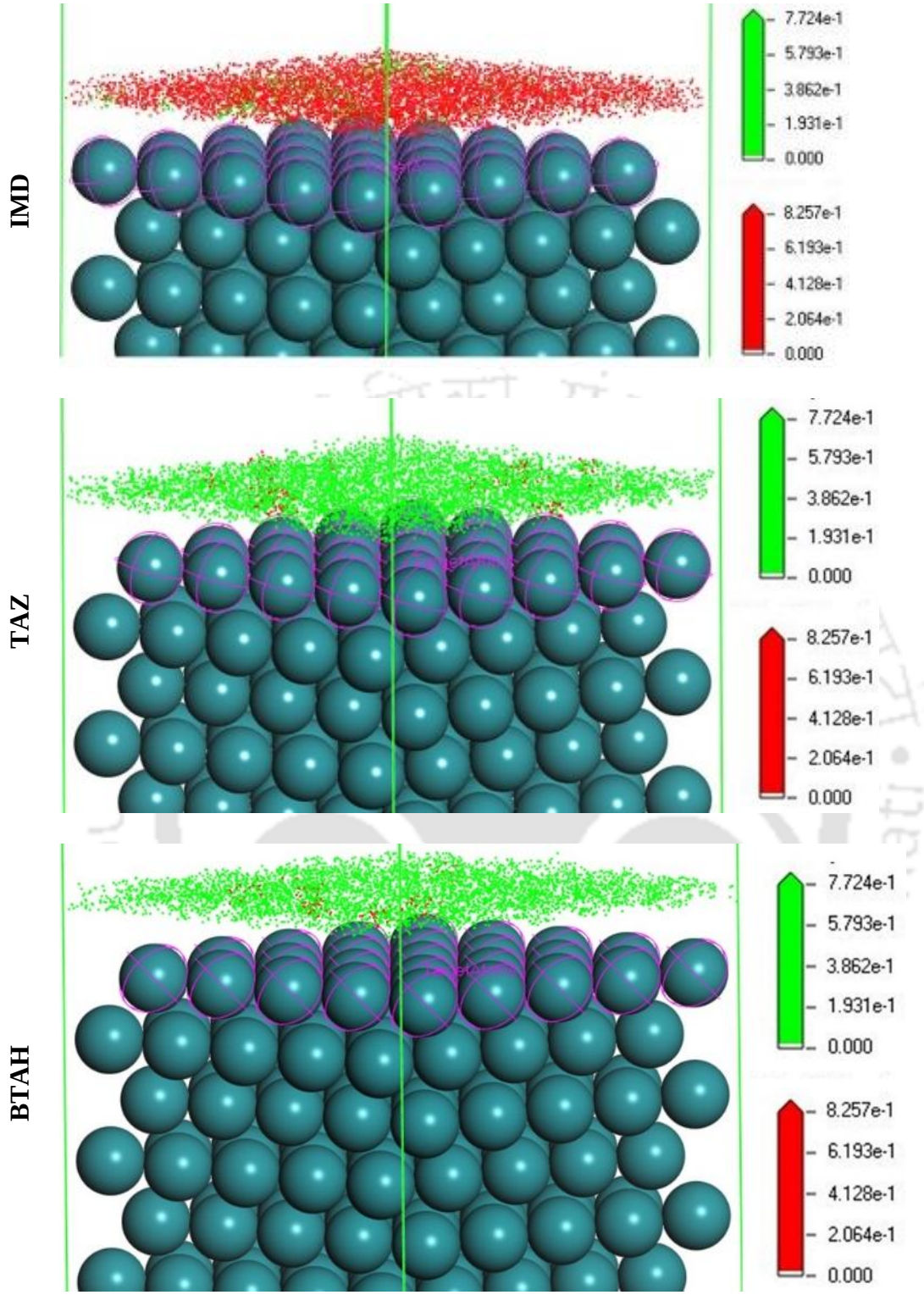

Figure 4.3.22 The adsorption density of IMD, TAZ, and BTAH inhibitor on the Ru (001) surafce in aqueous phase

4.3.3.8 The suggested corrosion inhibition mechanism for Ru in alkaline solution

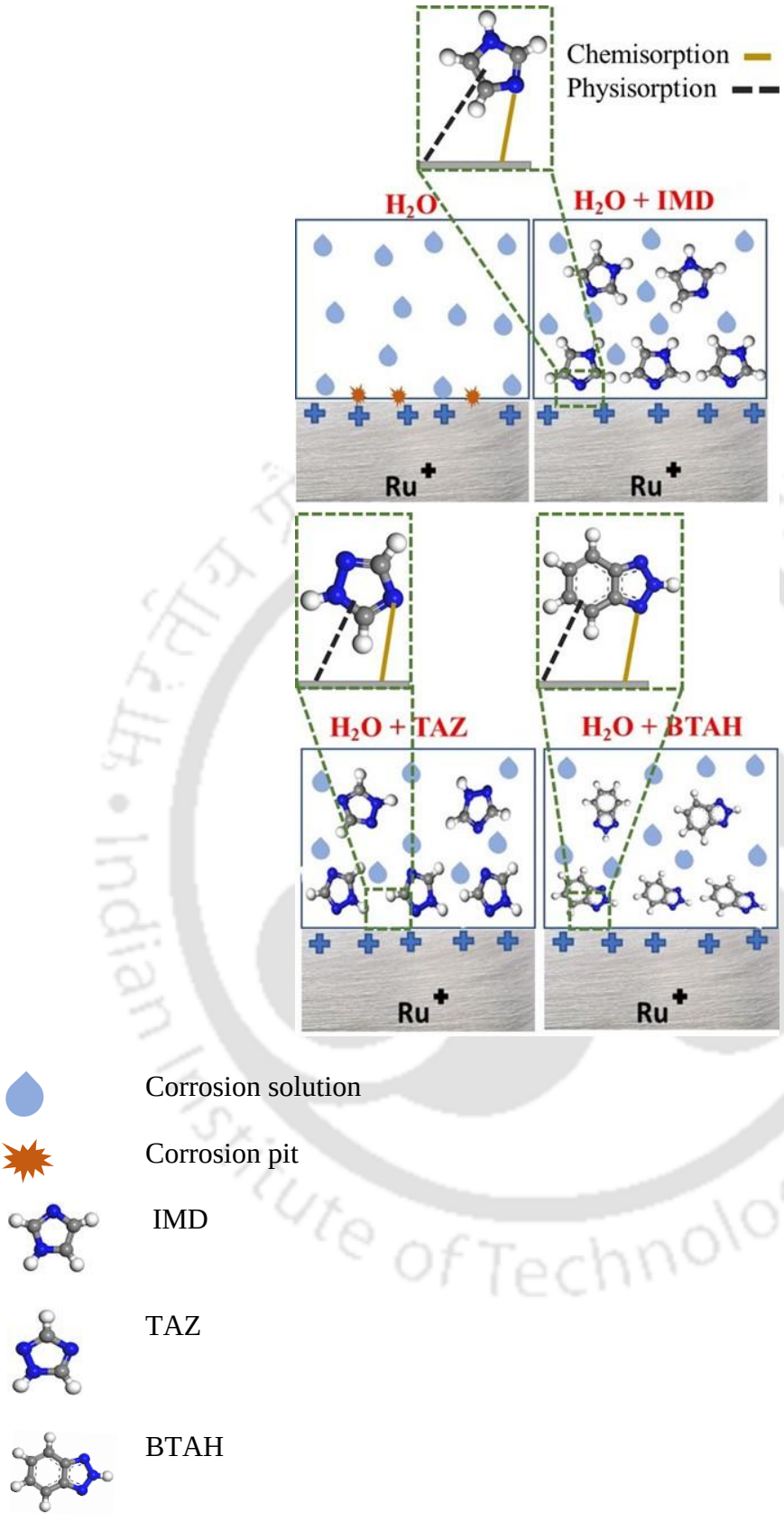

Figure 4.3.23 The possible schematic diagram for corrosion inhibition mechanism with and without inhibitor

Figure 4.3.23 illustrates a possible schematic diagram depicting the corrosion inhibition mechanism, both with and without the presence of an inhibitor. When a corrosive solution comes into direct contact with the surface of Ru without the presence of any inhibitor in the corrosive solution, Ru exhibits a swift reaction with hydroxide ions (OH-) leading to the formation of various oxides such as Ru trioxide (RuO_3) and Ru dioxide dihydrate ($RuO_2 \cdot 2H_2O$). Therefore, the presence of corrosion pits can be observed on the surface of the Ru metal, as depicted in **Figure 4.3.12**. It is to be noted that in alkaline solution, inhibitor molecules mostly exist in anionic form especially BTAH and IMD as their pKa values <9. Further, polarization measurements confirmed that the Ru metal exhibits positive potential in alkaline solution for all the three inhibitors. In the presence of an inhibitor, the negatively charged inhibitor (IMD/TAZ/BTAH) undergoes physical adsorption onto the positively charged Ru surface, resulting in the formation of a Ru-inhibitor complex and the subsequent development of a stable passivating film. The monolayer adsorbs inhibitor functions as a protective barrier between the surface of the Ru metal and the corrosive solution, effectively inhibiting both the anodic and cathodic reactions. Furthermore, the better adsorption of BTAH may be attributed to the presence of conjugated pi-electron cloud in benzene moiety fused with the five-membered heterocyclic ring. The performance of IMD and TAZ may be compared with the presence of heteroatom (N) in the molecular scaffold. Along with physisorption, weak chemisorption of inhibitors molecules also occurs on the metal surface as evident from the adsorption isotherm analysis and ΔN value estimated from quantum chemical calculations for all three inhibitors (<3.6). Among the three inhibitors being investigated, BTAH offers higher protection efficiency followed by TAZ and IMD. It is mainly attributed to the higher number of actives sites available on BTAH molecules compared to the TAZ and IMD as revealed by Mulliken charge density analysis and the favourable orientation of BTAH molecules (the flat planar and horizontal) during adsorption as observed in Monte Carlo simulations.

CHAPTER 5

SUMMARY AND CONCLUSION

5.1 SUMMARY OF THE PRESENT WORK

In recent decades, corrosion has become a subject of extensive research in both industries and academia due to its significant effects on the economy, material resources, and human lives. Carbon steel is the most frequently used material in the oil and gas industry. However, it is prone to corrosion when exposed to corrosive substances like acids, chlorides, or sulphides. Thus, in order to manage and avert metal corrosion, various corrosion-control strategies are available, such as material selection, cathodic protection, coatings, and corrosion inhibitors. The advantages and disadvantages of various corrosion-control strategies are presented in the introduction section (chapter 1.4) of the present thesis. In the present study employs coatings and corrosion inhibitor strategies to protect metal in corrosive environments.

Carbon steel is a highly significant and valuable material that finds extensive use in various applications such as pipelines, shipping, biomedical implants, rail transportation, and infrastructure construction. This is primarily due to its exceptional processability, high tensile strength, ability to be recycled, and low cost. Nevertheless, chemical compounds such as water, oxygen, and halides have the potential to cause corrosion in them under various conditions. In the present study (objective 1 and 2), epoxy-based coating with alkyl imidazolium ionic liquids with GO and carbon-based fillers were used to protect the carbon steel substrate in a 3.5 wt% NaCl solution.

Ruthenium (Ru) is highly sought after as a barrier material in the microelectronics fabrication industry. Chemical mechanical planarization (CMP) is an essential process that effectively smooths metal surfaces at both the local and global scales using a chemical slurry containing different additives. Safeguarding the barrier metal in the CMP process against corrosion is

considered a crucial element. Therefore, in the present study (objective 3), azole-based inhibitors are employed to protect the Ru metal in CMP applications.

One of the best methods for protecting carbon steel in a corrosive environment is an epoxy-based anticorrosive coating. However, the long-term anti-corrosion performance of epoxy-based coating is unsatisfactory. Hence, it necessary to introduced an appropriate filler in the epoxy matrix to increase the reinforcement of the epoxy matrix. This thesis examines two alternative fillers for use in anticorrosive coating applications, which are outlined as objectives 1 and 2, respectively. The fillers consist of (i) graphene oxide functionalized with ionic liquid (FGO) and (ii) carbon quantum dots derived from rice husk (RHQDs).

Specifically, in objective 1 of the present study, due to its high productivity and satisfactory reaction safety, most studies have focused on the conventional Hummers' technique for the synthesis of GO. However, the oxidation procedure adopted in these synthesis methods leads to the release of toxic gases such as NO_2 and N_2O_4 with an additional challenge in removing the remaining Na^+ and NO_3^- ions from the liquid waste created during the GO synthesis and purification operations (Chen et al., 2013b). So, in the present study, improved Hummers' method was opted over conventional Hummer's method of GO synthesis, as in this technique, Marcano et al. (Marcano et al., 2010b) improvised the process by eliminating $NaNO_3$, increasing the quantity of $KMnO_4$, and carrying out the reaction with H_2SO_4 and H_3PO_4 in a ratio of 9:1 (by volume) making the process environment friendly. The reaction yield was successfully increased by this improvement, and the generation of harmful gases were decreased with ease in control of reaction temperature (Marcano et al., 2010b).

The alkyl imidazolium ionic liquids with GO as a filler have very limited literature for carbon steel corrosion in saline water. Thus, 1 butyl – 3 methylimidazolium acetate ionic liquid, which is prominent IL among other ILs was employed, as it has greater solubility and electrochemical

window (Cabaço et al., 2012b; Shiflett et al., 2010). Bogolistyn and co-workers (Bogolitsyn et al., 2009b) reported the physiochemical properties of 1 butyl – 3 methylimidazolium acetate ionic liquid. The primary objective 1 of the thesis is to investigate the anticorrosive properties of FGO/epoxy coating in 3.5 wt% NaCl solution.

Similarly, in the second objective, rice husk is rich in carbon, green, abundant, and easily available. Thus, it could be an ideal precursor for the synthesis of QDs. The QDs have been synthesised from various precursors including RH. Aayushi Kundu et. al. (Kundu et al., 2022b) prepared quantum dots from rice husk and employed in dual-mode nanosensors that can identify metal ions and fluoroquinolones. The potential of rice husk derive QDs is also being explored for Fe^{3+} sensing and cadmium adsorption(W. Wang et al., 2018b; Zainal Abidin et al., 2020b). Although carbon quantum dots derived from rice husk have been explored for various applications such as supercapacitors, sensors etc., their effectiveness as anti-corrosive coatings have not been evaluated. Also, to the best of author's knowledge, the anti-corrosive properties of epoxy coating with biomass-derived carbon quantum dots as filler have not been reported in the literature yet. Hence, the primary objective 2 of the present study is to assess the corrosion-resistant characteristics of carbon quantum dots obtained from rice husk in the harsh corrosive environment.

Various characterization techniques were employed to analysed the purity of synthesised fillers (FGO and RHQDs) such as FTIR, Raman spectroscopy, XPS, XRD, TGA, BET, FESEM, and TEM. The anticorrosive behaviours of fillers (FGO and RHQDs) in 3.5 wt % NaCl solution was analysed using electrochemical techniques such as potentiodynamic polarization and electrochemical impedance spectroscopy (EIS). In addition, salt spray, and pull-off adhesion tests is also used to analysed the anticorrosive behaviours of fillers (FGO and RHQDs).

In microelectronic chip fabrication, one of the critical steps is metal layer planarization, which is achieved by the chemical mechanical planarization (CMP) process. It relies on the synergistic interaction of chemical and mechanical actions to achieve high flatness on wafer surfaces. A chemical slurry containing various additives is required to achieve surface planarization. Protecting the concave area of the wafer's surface from corrosion while removing the convex portion selectively is a crucial component of metal interconnect polishing. Thus, inhibitors play a vital role in achieving the same in CMP applications. The addition of corrosion inhibitors to the slurry is preferred due to their low cost, high inhibition efficiency, ease of use, and developed technology.

The field of theoretical chemistry has seen rapid advancements in recent years, significantly enhancing research on inhibition effectiveness. While these principles are being applied with increasing sophistication today, their roots in corrosion studies and surface chemistry date back several decades. Quantum chemistry computations are extensively employed to examine the chemical reactivity characteristics and adsorption mechanism of inhibitors. This approach can also be used to study reaction mechanisms at the molecular level and their associated electronic structure level. Calculations based on DFT are performed to investigate the predictive properties. Da Yin et al. (Yin et al., 2021) employed DFT and Monte Carlo simulation methods to evaluate the inhibition effect of BTAH and M-BTAH (5 - Methyl (1 H) benzotriazole) on copper at the molecular level. Da Yin and co-workers (Yin et al., 2020) proposed that the adsorption mechanism of BTAH and 1,2,4-triazole inhibitors on the cobalt surface using DFT and Monte Carlo simulation. However, the adsorption mechanism between the azole-based corrosion inhibitors and Ru metal at the microscale level remains unexplained. Thus, the primary objective 3 of this thesis is to get insight on physicochemical interaction between azoles and Ru at the microscale level.

The first objective of the present work is presented in three parts. Initially, an ionic liquid (1 butyl - 3 methylimidazolium acetate) functionalized graphene oxide (synthesised via the improved Hummers' method) material is prepared. After that, the FGO material is used as a filler in the epoxy matrix to enhance the corrosion protection ability. Finally, the anticorrosion behaviour of the FGO/epoxy coating is analysed using electrochemical experiments and surface characterization. The outcomes of objectives 1 shows that the IL is successfully grafted on the GO (synthesised via improved Hummers' method) and is used to enhance the anticorrosive properties of the epoxy resin coating on the CS substrate. The GO sheets with and without IL functionalization are characterized using various measurements and results confirm the attachment of IL on GO sheets via covalent bonding. The morphology of epoxy/FGO coating shows that uniform dispersion of FGO in the epoxy matrix and TGA results illustrated the desirable thermal stability of epoxy/FGO coating. Additionally, the contact angle measurements of epoxy/FGO coating show higher hydrophobicity even after 30 days of immersion in 3.5 wt% NaCl solution. The corrosion performance of epoxy coatings without and with GO/FGO on CS electrodes was measured by potentiodynamic polarisation and EIS in 3.5 wt% NaCl solution. It is observed from **Figure 4.1.9** and **Table 4.1.4** that the E_{corr} values for carbon steel coated with epoxy, epoxy/GO, and epoxy/FGO coating shifts towards positive potential as compared to the blank CS substrate. Further, a substantial drop in the anodic current density regime is observed for the coated CS substrates in the order epoxy<epoxy/GO<epoxy/FGO. The epoxy/FGO coating exhibits satisfactory corrosion resistance performance with extremely high polarization resistance (2520 kΩ.cm^2), low CR (0.002 mm/year), and high corrosion protection efficiency of 99.90%. The EIS results suggested that the composite coating containing FGO had the greatest impedance modulus throughout the immersion duration. For epoxy/FGO coatings **(Figure 4.1.10e-f)**, the $|Z|_{0.01Hz}$ values were much higher compared to epoxy coating and epoxy/GO coating. It indicates that

the effect of IL modification on the GO strengthening corrosion resistance. Additionally, the epoxy/FGO coating displayed the greatest $|Z|_{0.01Hz}$ value, after 1 and, 10 days immersion the $|Z|_{0.01Hz}$ value was 5.5×10^7 (Ω cm^2) and 1.09×10^7 (Ω cm^2) respectively. Even after 45 days of immersion in 3.5 wt.% NaCl solution the $|Z|_{0.01Hz}$ value dropped to 2.21×10^6 (Ω cm^2). The epoxy/FGO composite coating's higher R_{pore} / R_{ct} and lower Q_c / Q_{dl} values indicate that the right quantity of ILGO, evenly distributed throughout the coating, excellently prevents the entry of corrosive media and greatly boosts barrier the performance. Finally, due to better adhesion strength, the epoxy/FGO coating shows the excellent corrosion protection performance even after 500 h salts spray exposure **(Figure 4.1.12)**.

In the second objective of this thesis, carbon quantum dots (derived from rice husk) material is used as a filler to enhance the anticorrosive properties of the epoxy coating in a 3.5 wt% NaCl solution. The anticorrosive behaviour of RHQDs/epoxy coating analysed via surface characterization, electrochemical experiments and quantum chemical calculates. The outcomes of objective 2 suggested that the biomass-derived carbon quantum dots (RH-QDs) were synthesised using the hydrothermal method. The synthesized RH-QDs are incorporated into the epoxy matrix at different loadings (0.1 and 0.5 wt%) and their anti-corrosive properties are evaluated through electrochemical impedance spectroscopy, potentiodynamic polarization and salt spray test results. The E_{corr} values of carbon steel coated with pure epoxy, 0.1 wt% RHQDs/epoxy, and 0.5 wt% RHQDs/epoxy coating shifted to a more positive potential with respect to uncoated carbon steel substrate **(Figure 4.2.12)**. This significant positive shift illustrates the excellent anti-corrosion properties of the applied coatings, especially for the 0.5 wt% RHQDs/epoxy coating. It is evident that both the carbon steel dissolution (anodic) and oxygen reduction (cathodic) reaction rates are greatly hindered by 0.1 wt% RHQDs/epoxy and 0.5 wt% RHQDs/epoxy coating. Meanwhile, the 0.5 wt% RHQDs/epoxy coating exhibit a very high Rp value (14546.52 $k\Omega.cm^2$) and excellent protection efficiency (99.90 %) (Table 4.2.2).

This indicates that the very small amount of RHQDs plays a vital role to enhance the anti-corrosion characteristics of epoxy coating in the harsh sea environment. The EIS results shows, after 1 day of immersion in 3.5 wt% NaCl solution, the $|Z|_{0.01\ Hz}$ values of epoxy, 0.1 wt% RH-QD/epoxy, and 0.5 wt% RH-QD/epoxy coatings were 4.45 × 10^3, 1.31 ×10^7, and 1.53 × 10^8 (Ω cm^2) respectively **(Figure 4.2.13)**. Additionally, due to the higher interfacial interaction and, compatibility between RH-QDs and epoxy matrix, the protection performance of the epoxy coating is significantly improved by inhibiting the penetration of the corrosive fluids, according to the lower Q (Q_c, Q_{dl}) and higher R (R_{po}, R_{ct}) values. The addition of 0.5 wt% RH-QDs to the epoxy matrix enhances the chemical interaction between coating and carbon steel and, eventually presented excellent anticorrosive properties after 1000 h (42 days) of exposure in salt spray environment **(Figure 4.2.17).** Furthermore, it was observed that the adhesion strength of the epoxy coating on carbon steel increased significantly to a value of 3.61 ± 0.50 MPa when incorporating 0.5 wt% RH-QDs **(Figure 4.2.18)**. The enhanced anti-corrosive and mechanical properties are mainly attributed to the more intact structure of coating which is achieved through uniform dispersion of RH-QDs in the epoxy matrix and the strong interaction between RH-QDs and epoxy-hardener. Finally, the distribution of the HOMO and LUMO for this complex indicates that the frontier orbitals are primarily expanded on the surface of the RH-QDs; thus, the attachment of the RH-QDs to the surface of the epoxy-hardener system is more likely. This is consistent with our experimental findings.

The FGO/epoxy and RHQDs/epoxy coatings are proficient to enhance the anticorrosive properties of the epoxy coating. Comparatively, the polarization resistance (R_p) for the FGO/epoxy and RHQDs/epoxy are 2520 and 14546 (KΩ.cm^2), respectively **(Figure 4.1.11. and 4.2.2).** Hence, the potentiodynamic polarization results (Figure A1) suggested that the anticorrosive properties of the RHQDs/epoxy coating are higher than the FGO/epoxy coating in 3.5 wt% NaCl solution.

The third objective is to investigate the corrosion inhibitory effects of azoles in alkaline medium for ruthenium chemical mechanical planarization applications. The corrosion inhibition of the azole-based inhibitors is analysed via electrochemical and theoretical calculations. Therefore, potentiodynamic polarization and EIS measurements were performed with and without inhibitor (IMD/TAZ/BTAH). The E_{corr} values increases from 14 mV to 131 mV, 158 mV, and 165 mV for IMD, TAZ, and BTAH respectively at 15 mM concentration **(Table 4.3.1).** A significant shift in the E_{corr} value in the positive direction (> 85 mV) clearly indicates that the tested inhibitors mainly suppress the anodic reaction kinetics. It is to be noted that cathodic Tafel slope also changes with the addition of inhibitors and hence these inhibitors are mixed type with anodic predominant control. The protection efficiency (%) of the BTAH inhibitor is higher compared to IMD and TAZ for any given concentration. Particularly, the electrolyte solution containing 15 (mM) BTAH showed the highest PE (93.02 ± 0.44 %) for Ru metal at pH 9, which indicate the superior adsorption of the BTAH on the Ru surface. The calculated ΔG_{ads} (kJ/mol) values of IMD, TAZ, and BTAH are -25.37, -25.74, and -26.05 (kJ/mol), respectively **(Figure 4.3.4).** The outcomes from isotherms study demonstrates that adsorption is of mixed type (combined physisorption and chemisorption) with physisorption as the predominating mechanism as the values obtained are near to -20 (kJ/mol). The low-frequency impedance modulus ($|Z|_{0.01\ Hz}$) of IMD, TAZ, and BTAH at 15 mM was 116.02, 448.76, and 593.98 (kΩ cm^2), respectively while for blank, it was 9.72 kΩ cm^2. The EEC results shows the 99.02 % of protection efficiency was for BTAH at 15 mM concentration, demonstrating that the Ru dissolution process is suppressed by the inhibitors' adsorption on the Ru surface. The contact angle **(Figure 4.3.11)** and FESEM **(Figure 4.3.12)** results provide evidence supporting the occurrence of a barrier formation between the inhibitor and the Ru surface. This barrier formation is attributed to the adsorption of the inhibitor onto the surface of Ru. The molecular dynamics simulations along with quantum chemical calculations were

employed in the present work. Our findings further demonstrated that the Monte Carlo simulation is better in explaining the experimental trend compared to the quantum chemical descriptors. However, Quantum chemical calculations showed that the BTAH provides higher inhibition efficiency as evidence from the ΔN value **(Table 4.3.4).** The trend obtained for inhibition efficiency (i.e. BTAH>TAZ>IMD) is not explained by quantum chemical descriptors. The Mulliken charge density and molecular dynamic simulation further confirms that the BTAH offers higher production efficiency. This is attributed to the higher number of active cites (C4, C5, C7, C8), planner/horizontal orientation of the BTAH molecule adsorption on the Ru surface and lower adsorption energy. Further, the experimental trend is well explained by the molecular dynamic simulation via adsorption energy calculation, However, the results of this article will provide valuable insights for choosing an appropriate corrosion inhibitor in the CMP process of Ru metal. The Monte Carlo simulation results shows the TAZ and IMD inhibitors make an angle of 40º and 10º to the Ru surface (Figure 4.3.18) whereas the flat, planar, and horizontal orientation was observed for the BTAH-Ru system. For superior corrosion prevention efficiency, it is typically preferred as it can cover a wider surface area of Ru surface and has higher binding energy. **Table 4.3.8** displays the outputs and descriptors that were computed through the implementation of the Monte Carlo simulation. The manifestation of inhibitors' adsorption ability can be observed through these energy values. Furthermore, the simulation process demonstrates that inhibitors with the lowest adsorption energy exhibit the highest inhibition efficiency in accordance with theoretical principles. It can be observed that BTAH exhibits the lowest adsorption energy (-41.3303 kcal/mol) compared to IMD (-31.9654 kcal/mol) and TAZ (-39.6147 kcal/mol) when adsorbed on the Ru (0 0 1) surface **(Table 4.3.6)**. Therefore, it is likely that the inhibitor molecules under investigation have the ability to irreversibly adsorb onto the surface of Ru, thereby acting as a protective barrier against corrosion for the Ru surface.

5.2 CONCLUSION

The major conclusions that can be extracted from the thesis are presented objectively, as follows:

In the conclusion of objective 1, the IL was successfully grafted on the GO nanosheet and is used to enhance the anticorrosive properties of the epoxy resin coating on the carbon steel substrate. The GO sheets with and without IL functionalization are characterized using various measurements. TGA and BET studies confirm the attachment of IL on GO sheets via covalent bonding. The morphology of epoxy/FGO coating shows that uniform dispersion of FGO in the epoxy matrix and TGA results illustrated the desirable thermal stability of epoxy/FGO coating. Additionally, the contact angle measurements of epoxy/FGO coating show higher hydrophobicity even after 30 days of immersion in 3.5 wt% NaCl solution. The corrosion performance of epoxy coatings without and with GO and FGO on CS electrodes was measured by potentiodynamic polarisation and EIS in 3.5 wt% NaCl solution. Composite coating with of FGO exhibited the lowest i_{corr} (0.10 µA/cm^2) and highest $|Z|_{0.01Hz}$ values (5.50 × 10^7 Ω cm^2) after 24 h soaking in 3.5 wt% NaCl solution compared to the epoxy and epoxy/GO coating. Furthermore, the Q_{ct} and Q_{pore} values of epoxy/FGO coating are not significantly varied during 45 days immersion in NaCl solution (3.5 wt%). Due to better adhesion strength, the epoxy/FGO coating shows the excellent corrosion protection performance even after 500 h salts spray exposure. The simple and environmentally friendly technology is suggested to prepare IL-based GO/nanomaterial composite which shows superior anti-corrosive properties.

In conclusion of objective 2, biomass derived carbon quantum dots (RH-QDs) were synthesized using hydrothermal method. The aforementioned technique is characterized by its lack of potential harm, cost-effectiveness, and eco-friendly nature, rendering it suitable for extensive industrial application. Further, the RH-QDs are incorporated into the epoxy matrix

at different loadings (0.1 and 0.5 wt%) and their anti-corrosive properties are evaluated through electrochemical impedance spectroscopy, potentiodynamic polarization and salt spray test results. The results demonstrated that the epoxy coating containing 0.5 wt% RH-QDs exhibited the highest anti-corrosion performance. Furthermore, it was observed that the adhesion strength of the epoxy coating on carbon steel increased significantly to a value of 3.61 ± 0.50 MPa when incorporating 0.5 wt% RH-QDs. The enhanced anti-corrosive and mechanical properties are mainly attributed to the more intact structure of coating which is achieved through uniform dispersion of RH-QDs in the epoxy matrix and the strong interaction between RH-QDs and epoxy-hardener. Quantum chemical descriptors estimated through molecular simulations have also provided corroborating evidence for the same. Thus, this present study reveals that QDs derived from biomass, specifically rice husk, exhibit significant promise in enhancing the anti-corrosive characteristics and longevity of epoxy coatings within challenging marine environments.

In the conclusion of objective 3, a range of comprehensive and systematic approaches were utilised to examine the inhibitory capacity and mechanism of azole-based inhibitors in safeguarding Ru throughout the CMP process. The potentiodynamic polarization results demonstrate that all three azole inhibitors exhibit significant corrosion suppression effects on Ru at a pH of 9 and exhibit mixed-type behaviour, as evidenced by the change in E_{corr} falling within the range of ±85 mV. As the azole inhibitor adsorb on the Ru surface via a combined physisorption (predominant) and chemisorption (weak) mechanism, as confirmed ΔG_{ads} (kJ/mol) value obtained from the Langmuir isotherm. The PE (%) values for IMD, TAZ, and BTAH at a concentration of 15 mM were determined to be 91.49 %, 95.71%, and 99.02 %, respectively. The contact angle and FESEM results provide evidence supporting the occurrence of a barrier formation between the inhibitor and the Ru surface. This barrier formation is attributed to the adsorption of the inhibitor onto the surface of Ru. Quantum chemical

calculations showed that the BTAH provides higher inhibition efficiency as evidence from the ΔN value. However, the trend obtained for inhibition efficiency (i.e. BTAH>TAZ>IMD) could not be explained by quantum chemical descriptors. Mulliken charge density and molecular dynamic simulation further confirms that the BTAH offers higher production efficiency. This is attributed to the higher number of active cites (N13, N14, C4, C5, C7, C8), planner/horizontal orientation of the BTAH molecule on the Ru surface during adsorption process and significantly lower adsorption energy. Further, the experimental trend is well explained by the molecular dynamic simulation studies via adsorption energy calculation. The key findings from this work helps to understand the physicochemical interaction between azole (IMD, TAZ, and BTAH) and Ru metal at the microscale level. In addition, this work establishes a framework for designing effective Ru CMP slurries with suitable corrosion inhibitors to control Ru dissolution rate as being studied here. Further, as all the three azole inhibitors offer good protection efficiency, it can be considered in future studies on controlling galvanic corrosion of Ru with other metals which is also of interest in the semiconductor industries.

5.3 SUGGESIONS FOR FUTURE WORK

- Investigate the potential of FGO/epoxy and RH-QDs/epoxy coatings to resist fouling and ice formation. The hydrophobic and nanoscale features of FGO and RH-QDs can reduce ice adhesion and biofilm growth, making them suitable for marine and cold-climate applications.
- Study the effects of functionalized RH-QDs on the properties of epoxy composites. Improved dispersion and interfacial bonding through RH-QD modification can enhance mechanical, thermal, and electrical performance, addressing challenges observed in the current work.
- Explore the anticorrosion performance of FGO/epoxy and RH-QDs/epoxy coatings in H_2S, CO_2, and acidic conditions across various temperatures. Understanding their behavior in corrosive and high-temperature environments is critical for industrial applications like pipelines and storage tanks.
- Employing the various carbon-based materials such as modified MXene, Metal–Organic Frameworks, and nanotubes for the anticorrosive applications.
- The adsorption mechanism of inhibitors in the presence of other additives at molecular level using molecular dynamics simulation.

References:

Abbas, A., Mariana, L.T., Phan, A.N., 2018. Biomass-waste derived graphene quantum dots and their applications. Carbon N Y 140, 77–99. https://doi.org/10.1016/j.carbon.2018.08.016

Abbas, A., Tabish, T.A., Bull, S.J., Lim, T.M., Phan, A.N., 2020. High yield synthesis of graphene quantum dots from biomass waste as a highly selective probe for Fe3+ sensing. Sci Rep 10, 21262. https://doi.org/10.1038/s41598-020-78070-2

Adhikari, S., Dhongde, N.R., Talukdar, M.K., Khan, S., Rajaraman, P.V., 2024. Investigation of Carbon Steels (API 5L X52 and API 5L X60) Dissolution CO2–H2S Solutions in the Presence of Acetic Acid: Mechanistic Reaction Pathway and Kinetics. Arab J Sci Eng. https://doi.org/10.1007/s13369-024-08812-1

Al-Gaashani, R., Najjar, A., Zakaria, Y., Mansour, S., Atieh, M.A., 2019. XPS and structural studies of high quality graphene oxide and reduced graphene oxide prepared by different chemical oxidation methods. Ceram Int 45, 14439–14448. https://doi.org/10.1016/j.ceramint.2019.04.165

Aljeaban, N.A., Goni, L.K.M.O., Alharbi, B.G., Jafar Mazumder, M.A., Ali, S.A., Chen, T., Quraishi, M.A., Al-Muallem, H.A., 2020. Polymers Decorated with Functional Motifs for Mitigation of Steel Corrosion: An Overview. Int J Polym Sci 2020, 1–23. https://doi.org/10.1155/2020/9512680

Alum, M., Eze, T., 2020. The New Faces of Corrosion and Damage Detection in Oil and Gas Facilities: A Brief of What has Worked So Far and How it Can Work for You, in: Day 1 Tue, August 11, 2020. SPE. https://doi.org/10.2118/203745-MS

Ashwathareddy, A., Rao, S., Shree Subramaniyam, S., Gopala Krishna, P., Monnppa Rama, K., Kodange, S., 2024. Corrosion mitigation of mild steel in acidic medium using liquid crystals: A comprehensive review. Inorg Chem Commun 169, 113071. https://doi.org/10.1016/j.inoche.2024.113071

Astuti, E.S., Sonief, A.A., Sarosa, M., Ngafwan, N., Wardana, I.N.G., 2022. Synthesis, characterization and energy gap of silica quantum dots from rice husk. Bioresour Technol Rep 20, 101263. https://doi.org/10.1016/j.biteb.2022.101263

Bartley, J., Huynh, N., Bottle, S.E., Flitt, H., Notoya, T., Schweinsberg, D.P., 2003. Computer simulation of the corrosion inhibition of copper in acidic solution by alkyl esters of 5-carboxybenzotriazole. Corros Sci 45, 81–96. https://doi.org/10.1016/S0010-938X(02)00051-3

Becke, A.D., 1988. Density-functional exchange-energy approximation with correct asymptotic behavior. Phys Rev A (Coll Park) 38, 3098–3100. https://doi.org/10.1103/PhysRevA.38.3098

Bhandari, K., Roy Maulik, S., Bhattacharyya, A.R., 2020. Synthesis and Characterization of Microcrystalline Cellulose from Rice Husk. Journal of The Institution of Engineers (India): Series E 101, 99–108. https://doi.org/10.1007/s40034-020-00160-7

Bogolitsyn, K.G., Skrebets, T.E., Makhova, T.A., 2009a. Physicochemical properties of 1-butyl-3-methylimidazolium acetate. Russ J Gen Chem 79, 125–128. https://doi.org/10.1134/S1070363209010198

Bogolitsyn, K.G., Skrebets, T.E., Makhova, T.A., 2009b. Physicochemical properties of 1-butyl-3-methylimidazolium acetate. Russ J Gen Chem 79, 125–128. https://doi.org/10.1134/S1070363209010198

Boughoues, Y., Benamira, M., Messaadia, L., Ribouh, N., 2020. Adsorption and corrosion inhibition performance of some environmental friendly organic inhibitors for mild steel in HCl solution via experimental and theoretical study. Colloids Surf A Physicochem Eng Asp 593, 124610. https://doi.org/10.1016/j.colsurfa.2020.124610

Bouibed, A., Doufnoune, R., 2019. Synthesis and characterization of hybrid materials based on graphene oxide and silica nanoparticles and their effect on the corrosion protection properties of epoxy resin coatings. J Adhes Sci Technol 33, 834–860. https://doi.org/10.1080/01694243.2019.1571660

Cabaço, M.I., Besnard, M., Danten, Y., Coutinho, J.A.P., 2012a. Carbon Dioxide in 1-Butyl-3-methylimidazolium Acetate. I. Unusual Solubility Investigated by Raman Spectroscopy and DFT Calculations. J Phys Chem A 116, 1605–1620. https://doi.org/10.1021/jp211211n

Cabaço, M.I., Besnard, M., Danten, Y., Coutinho, J.A.P., 2012b. Carbon Dioxide in 1-Butyl-3-methylimidazolium Acetate. I. Unusual Solubility Investigated by Raman Spectroscopy and DFT Calculations. J Phys Chem A 116, 1605–1620. https://doi.org/10.1021/jp211211n

Caldona, E.B., Zhang, M., Liang, G., Hollis, T.K., Webster, C.E., Smith, D.W., Wipf, D.O., 2021. Corrosion inhibition of mild steel in acidic medium by simple azole-based aromatic compounds. Journal of Electroanalytical Chemistry 880, 114858. https://doi.org/10.1016/j.jelechem.2020.114858

Cao, Z., Tang, Y., Cang, H., Xu, J., Lu, G., Jing, W., 2014. Novel benzimidazole derivatives as corrosion inhibitors of mild steel in the acidic media. Part II: Theoretical studies. Corros Sci 83, 292–298. https://doi.org/10.1016/j.corsci.2014.02.025

Chen, J., Li, B., Zeng, X., Li, Z., Wen, Y., Hu, Q., Yang, Q., Zhou, M., Yang, B., 2023. Study on the Influence of Accelerated Aging on the Properties of an RTV Anti-Pollution Flashover Coating. Polymers (Basel) 15, 751. https://doi.org/10.3390/polym15030751

Chen, J., Yao, B., Li, C., Shi, G., 2013a. An improved Hummers method for eco-friendly synthesis of graphene oxide. Carbon N Y 64, 225–229. https://doi.org/10.1016/j.carbon.2013.07.055

Chen, J., Yao, B., Li, C., Shi, G., 2013b. An improved Hummers method for eco-friendly synthesis of graphene oxide. Carbon N Y 64, 225–229. https://doi.org/10.1016/j.carbon.2013.07.055

Chen, X., Qu, Z., Liu, Z., Ren, G., 2022. Mechanism of Oxidization of Graphite to Graphene Oxide by the Hummers Method. ACS Omega 7, 23503–23510. https://doi.org/10.1021/acsomega.2c01963

Cheng, J., Wang, T., Pan, J., Lu, X., 2016. Corrosion Investigations of Ruthenium in Potassium Periodate Solutions Relevant for Chemical Mechanical Polishing. J Electron Mater 45, 4067–4075. https://doi.org/10.1007/s11664-016-4579-1

Cheng, M., Li, F., Wang, Z., Li, C., Sun, S., Hu, S., 2021a. New valve-free organosilica nanocontainer for active anticorrosion of polymer coatings. Compos B Eng 224, 109185. https://doi.org/10.1016/j.compositesb.2021.109185

Cheng, M., Li, F., Wang, Z., Li, C., Sun, S., Hu, S., 2021b. New valve-free organosilica nanocontainer for active anticorrosion of polymer coatings. Compos B Eng 224, 109185. https://doi.org/10.1016/j.compositesb.2021.109185

Chieng, S., Kuan, S.H., 2022. Harnessing bioenergy and high value–added products from rice residues: a review. Biomass Convers Biorefin 12, 3547–3571. https://doi.org/10.1007/s13399-020-00891-y

Clover, D., Kinsella, B., Pejcic, B., De Marco, R., 2005a. The influence of microstructure on the corrosion rate of various carbon steels. J Appl Electrochem 35, 139–149. https://doi.org/10.1007/s10800-004-6207-7

Clover, D., Kinsella, B., Pejcic, B., De Marco, R., 2005b. The influence of microstructure on the corrosion rate of various carbon steels. J Appl Electrochem 35, 139–149. https://doi.org/10.1007/s10800-004-6207-7

Cui, J., Bao, Y., Sun, Y., Wang, H., LI, J., 2023. Critical factors on corrosion protective waterborne coatings containing functionalized graphene oxide: A review. Compos Part A Appl Sci Manuf 174, 107729. https://doi.org/10.1016/j.compositesa.2023.107729

da S. Medeiros, F., Cury, C.S.R., de Vasconcelos, C.K.B., Silva, G.G., 2022. Reduced graphene oxide as an adhesion enhancer of fusion-bonded epoxy coatings. Prog Org Coat 171, 107057. https://doi.org/10.1016/j.porgcoat.2022.107057

Dagdag, O., Berisha, A., Safi, Z., Dagdag, S., Berrani, M., Jodeh, S., Verma, C., Ebenso, E.E., Wazzan, N., El Harfi, A., 2020. Highly durable macromolecular epoxy resin as anticorrosive coating material for carbon steel in 3% NaCl: Computational supported experimental studies. J Appl Polym Sci 137. https://doi.org/10.1002/app.49003

Das, N.K., Mishra, D.K., Naik, P.K., Dehury, P., Bose, S., Banerjee, T., 2023a. Dihydrolevoglycosenone as a novel bio-based nanofluid for thermal energy storage: Physiochemical and quantum chemical insights. J Energy Storage 59, 106365. https://doi.org/10.1016/j.est.2022.106365

Das, N.K., Mishra, D.K., Naik, P.K., Dehury, P., Bose, S., Banerjee, T., 2023b. Dihydrolevoglycosenone as a novel bio-based nanofluid for thermal energy storage: Physiochemical and quantum chemical insights. J Energy Storage 59, 106365. https://doi.org/10.1016/j.est.2022.106365

Das, P., Mandal, B., Gumma, S., 2020a. Engineering of structural and surface functional characteristics of graphite oxide nanosheets by controlling oxidation temperature. Appl Surf Sci 504, 144444. https://doi.org/10.1016/j.apsusc.2019.144444

Das, P., Mandal, B., Gumma, S., 2020b. Engineering of structural and surface functional characteristics of graphite oxide nanosheets by controlling oxidation temperature. Appl Surf Sci 504, 144444. https://doi.org/10.1016/j.apsusc.2019.144444

Devi, Y.G., Adhikari, S., Pulikkal, A.K., Rajaraman, P.V., 2023a. Impacts of pyridinium gemini surfactants on corrosion inhibition of carbon steel. Surfaces and Interfaces 103796. https://doi.org/10.1016/j.surfin.2023.103796

Devi, Y.G., Adhikari, S., Pulikkal, A.K., Rajaraman, P.V., 2023b. Impacts of pyridinium gemini surfactants on corrosion inhibition of carbon steel. Surfaces and Interfaces 103796. https://doi.org/10.1016/j.surfin.2023.103796

Deyab, M.A., Mele, G., 2020. Stainless steel bipolar plate coated with polyaniline/Zn-Porphyrin composites coatings for proton exchange membrane fuel cell. Sci Rep 10, 3277. https://doi.org/10.1038/s41598-020-60288-9

Dhongde, N.R., Baranwal, P.K., Rajaraman, P.V., 2023a. Functionalization of graphene oxide with an ionic liquid (1-butyl-3-methylimidazolium acetate): Preparation of epoxy-based coating on carbon steel for anticorrosive applications. J Appl Polym Sci. https://doi.org/10.1002/app.54026

Dhongde, N.R., Baranwal, P.K., Rajaraman, P.V., 2023b. Functionalization of graphene oxide with an ionic liquid (1-butyl-3-methylimidazolium acetate): Preparation of epoxy-based coating on carbon steel for anticorrosive applications. J Appl Polym Sci 140. https://doi.org/10.1002/app.54026

Dhongde, N.R., Das, N.K., Banerjee, T., Rajaraman, P.V., 2024. Synthesis of carbon quantum dots from rice husk for anti-corrosive coating applications: Experimental and theoretical investigations. Ind Crops Prod 212, 118329. https://doi.org/10.1016/j.indcrop.2024.118329

Dhongde, V., Velpandian, M., Haider, M.A., Basu, S., 2023. A $Sr_2CoNbO_{6-\delta}$@$Sm_{0.2}Ce_{0.8}O_{2-\delta}$ nanofiber composite as cathode accelerates oxygen reduction reaction for IT-SOFC. ECS Trans 111, 2271–2276. https://doi.org/10.1149/11106.2271ecst

Ding, J., Zhao, H., Yu, H., 2022a. Structure and performance insights in carbon dots-functionalized MXene-epoxy ultrathin anticorrosion coatings. Chemical Engineering Journal 430, 132838. https://doi.org/10.1016/j.cej.2021.132838

Ding, J., Zhao, H., Yu, H., 2022b. Structure and performance insights in carbon dots-functionalized MXene-epoxy ultrathin anticorrosion coatings. Chemical Engineering Journal 430, 132838. https://doi.org/10.1016/j.cej.2021.132838

Ding, Z., Li, F., Wen, J., Wang, X., Sun, R., 2018. Gram-scale synthesis of single-crystalline graphene quantum dots derived from lignin biomass. Green Chemistry 20, 1383–1390. https://doi.org/10.1039/C7GC03218H

Dong, Y., Cheng, Y., Xu, G., Cheng, H., Huang, K., Duan, J., Mo, D., Zeng, J., Bai, J., Sun, Y., Liu, J., Yao, H., 2019. Selectively Enhanced Ion Transport in Graphene Oxide Membrane/PET Conical Nanopore System. ACS Appl Mater Interfaces 11, 14960–14969. https://doi.org/10.1021/acsami.9b01071

Du, Y., Wang, C., Zhou, J., Zhang, W., Ji, J., Han, L., Li, Y., 2017. Effect of Guanidinium Ions on Ruthenium CMP in H_2O_2-Based Slurry. ECS Journal of Solid State Science and Technology 6, P521–P525. https://doi.org/10.1149/2.0131708jss

Dwivedi, D., Lepková, K., Becker, T., 2017a. Carbon steel corrosion: a review of key surface properties and characterization methods. RSC Adv 7, 4580–4610. https://doi.org/10.1039/C6RA25094G

Dwivedi, D., Lepková, K., Becker, T., 2017b. Carbon steel corrosion: a review of key surface properties and characterization methods. RSC Adv 7, 4580–4610. https://doi.org/10.1039/C6RA25094G

Esmaily, M., Svensson, J.E., Fajardo, S., Birbilis, N., Frankel, G.S., Virtanen, S., Arrabal, R., Thomas, S., Johansson, L.G., 2017. Fundamentals and advances in magnesium alloy corrosion. Prog Mater Sci 89, 92–193. https://doi.org/10.1016/j.pmatsci.2017.04.011

Fallah, Z., Zare, E.N., Khan, M.A., Iftekhar, S., Ghomi, M., Sharifi, E., Tajbakhsh, M., Nikfarjam, N., Makvandi, P., Lichtfouse, E., Sillanpaa, M., Varma, R.S., 2021. Ionic liquid-based antimicrobial materials for water treatment, air filtration, food packaging and anticorrosion coatings. Adv Colloid Interface Sci 294, 102454. https://doi.org/10.1016/j.cis.2021.102454

Fang, J., Li, J., 2002. Quantum chemistry study on the relationship between molecular structure and corrosion inhibition efficiency of amides. Journal of Molecular Structure: THEOCHEM 593, 179–185. https://doi.org/10.1016/S0166-1280(02)00316-0

Ferraa, N., Ouakki, M., El Harmouchi, H., Cherkaoui, M., Bennani Ziatni, M., 2023. Investigation of the inhibition behavior of an octacalcium phosphate as a green corrosion inhibitor against carbon steel in 3 % NaCl medium. Inorg Chem Commun 157, 111343. https://doi.org/10.1016/j.inoche.2023.111343

Fu, Y., Singh, D.J., 2018. Applicability of the Strongly Constrained and Appropriately Normed Density Functional to Transition-Metal Magnetism. Phys Rev Lett 121, 207201. https://doi.org/10.1103/PhysRevLett.121.207201

Gajalakshmi, D., Tamilmani, V., 2020. Tuning pyrrole oligomers for optoelectronic and anti-corrosion applications: a DFT/TDDFT study. Theor Chem Acc 139, 175. https://doi.org/10.1007/s00214-020-02690-0

Ge, Y., Cheng, J., Xue, L., Zhang, B., Zhang, P., Cui, X., Hong, S., Wu, Y., Zhang, X., Liang, X., 2022. Durability and corrosion behaviors of superhydrophobic amorphous coatings: a contrastive investigation. RSC Adv 12, 32813–32824. https://doi.org/10.1039/D2RA06073F

Ghali, E., Dietzel, W., Kainer, K.-U., 2004. General and Localized Corrosion of Magnesium Alloys: A Critical Review. J Mater Eng Perform 13, 7–23. https://doi.org/10.1361/10599490417533

Gong, P., Wang, J., Hou, K., Yang, Z., Wang, Z., Liu, Z., Han, X., Yang, S., 2017. Small but strong: The influence of fluorine atoms on formation and performance of graphene quantum dots using a gradient F-sacrifice strategy. Carbon N Y 112, 63–71. https://doi.org/10.1016/j.carbon.2016.10.091

Grimme, S., 2005. Accurate Calculation of the Heats of Formation for Large Main Group Compounds with Spin-Component Scaled MP2 Methods. J Phys Chem A 109, 3067–3077. https://doi.org/10.1021/jp050036j

Guo, L., Tan, B., Li, W., Li, Q., Zheng, X., Obot, I.B., 2021. Banana leaves water extracts as inhibitor for X70 steel corrosion in HCl medium. J Mol Liq 327, 114828. https://doi.org/10.1016/j.molliq.2020.114828

Guo, L., Tan, J., Kaya, S., Leng, S., Li, Q., Zhang, F., 2020. Multidimensional insights into the corrosion inhibition of 3,3-dithiodipropionic acid on Q235 steel in H2SO4 medium: A combined experimental and in silico investigation. J Colloid Interface Sci 570, 116–124. https://doi.org/10.1016/j.jcis.2020.03.001

Guo, L., Zhu, S., Zhang, S., He, Q., Li, W., 2014. Theoretical studies of three triazole derivatives as corrosion inhibitors for mild steel in acidic medium. Corros Sci 87, 366–375. https://doi.org/10.1016/j.corsci.2014.06.040

Han, J., Brown, B.N., Nešić, S., 2010. Investigation of the Galvanic Mechanism for Localized Carbon Dioxide Corrosion Propagation Using the Artificial Pit Technique. CORROSION 66, 095003-095003–12. https://doi.org/10.5006/1.3490308

Haque, J., Srivastava, V., Quraishi, M.A., Singh Chauhan, D., Lgaz, H., Chung, I.-M., 2020. Polar group substituted imidazolium zwitterions as eco-friendly corrosion inhibitors for mild steel in acid solution. Corros Sci 172, 108665. https://doi.org/10.1016/j.corsci.2020.108665

Haris, N.I.N., Sobri, S., Yusof, Y.A., Kassim, N.K., 2020a. An Overview of Molecular Dynamic Simulation for Corrosion Inhibition of Ferrous Metals. Metals (Basel) 11, 46. https://doi.org/10.3390/met11010046

Haris, N.I.N., Sobri, S., Yusof, Y.A., Kassim, N.K., 2020b. An Overview of Molecular Dynamic Simulation for Corrosion Inhibition of Ferrous Metals. Metals (Basel) 11, 46. https://doi.org/10.3390/met11010046

Hasanov, R., Sadıkoğlu, M., Bilgiç, S., 2007. Electrochemical and quantum chemical studies of some Schiff bases on the corrosion of steel in H2SO4 solution. Appl Surf Sci 253, 3913–3921. https://doi.org/10.1016/j.apsusc.2006.08.025

Hazarika, J., Talukdar, A., Rajaraman, P.V., 2023a. Effect of Potassium Iodate-Based Slurry for Polishing of Ruthenium (Ru) as Advanced Interconnects. J Electron Mater 52, 6551–6565. https://doi.org/10.1007/s11664-023-10585-6

Hazarika, J., Talukdar, A., Rajaraman, P.V., 2023b. Effect of oxalic acid (complexing agent) on anodic dissolution of Cobalt in hydrogen peroxide solutions: mechanism and kinetic analysis by electrochemical impedance spectroscopy. Journal of Solid State Electrochemistry 27, 895–909. https://doi.org/10.1007/s10008-023-05379-z

Hazarika, J., Talukdar, A., Rajaraman, P.V., 2023c. Effect of oxalic acid (complexing agent) on anodic dissolution of Cobalt in hydrogen peroxide solutions: mechanism and kinetic analysis by electrochemical impedance spectroscopy. Journal of Solid State Electrochemistry 27, 895–909. https://doi.org/10.1007/s10008-023-05379-z

Hazarika, J., Talukdar, A., Rajaraman, P.V., 2023d. Effect of Potassium Iodate-Based Slurry for Polishing of Ruthenium (Ru) as Advanced Interconnects. J Electron Mater 52, 6551–6565. https://doi.org/10.1007/s11664-023-10585-6

He, Y., Guo, Y., Yan, F., Yu, T., Liu, L., Zhang, X., Zheng, T., 2021. Density functional theory study of adsorption of ionic liquids on graphene oxide surface. Chem Eng Sci 245, 116946. https://doi.org/10.1016/j.ces.2021.116946

Heinz, H., Farmer, B.L., Pandey, R.B., Slocik, J.M., Patnaik, S.S., Pachter, R., Naik, R.R., 2009. Nature of Molecular Interactions of Peptides with Gold, Palladium, and Pd−Au Bimetal Surfaces in Aqueous Solution. J Am Chem Soc 131, 9704–9714. https://doi.org/10.1021/ja900531f

Hsissou, R., Abbout, S., Seghiri, R., Rehioui, M., Berisha, A., Erramli, H., Assouag, M., Elharfi, A., 2020. Evaluation of corrosion inhibition performance of phosphorus polymer for carbon steel in [1 M]

HCl: Computational studies (DFT, MC and MD simulations). Journal of Materials Research and Technology 9, 2691–2703. https://doi.org/10.1016/j.jmrt.2020.01.002

Hsissou, R., Dagdag, O., Abbout, S., Benhiba, F., Berradi, M., El Bouchti, M., Berisha, A., Hajjaji, N., Elharfi, A., 2019. Novel derivative epoxy resin TGETET as a corrosion inhibition of E24 carbon steel in 1.0 M HCl solution. Experimental and computational (DFT and MD simulations) methods. J Mol Liq 284, 182–192. https://doi.org/10.1016/j.molliq.2019.03.180

Huang, H., Guo, X., 2020. The relationship between the inhibition performances of three benzo derivatives and their structures on the corrosion of copper in 3.5 wt.% NaCl solution. Colloids Surf A Physicochem Eng Asp 598, 124809. https://doi.org/10.1016/j.colsurfa.2020.124809

Huang, T.-C., Yeh, T.-C., Huang, H.-Y., Ji, W.-F., Chou, Y.-C., Hung, W.-I., Yeh, J.-M., Tsai, M.-H., 2011. Electrochemical studies on aniline-pentamer-based electroactive polyimide coating: Corrosion protection and electrochromic properties. Electrochim Acta 56, 10151–10158. https://doi.org/10.1016/j.electacta.2011.08.114

Javadian, S., Yousefi, A., Neshati, J., 2013. Synergistic effect of mixed cationic and anionic surfactants on the corrosion inhibitor behavior of mild steel in 3.5% NaCl. Appl Surf Sci 285, 674–681. https://doi.org/10.1016/j.apsusc.2013.08.109

Ji, J., Tan, B., Zhang, S., Ma, T., Guo, L., Li, W., Yan, M., Wang, F., Du, H., Wang, X., 2022a. Investigation on the control effect of benzotriazole and two derivatives on cobalt pitting corrosion in chemical mechanical polishing process: A combination of experiments and theoretical simulations. J Mol Liq 367, 120487. https://doi.org/10.1016/j.molliq.2022.120487

Ji, J., Tan, B., Zhang, S., Ma, T., Guo, L., Li, W., Yan, M., Wang, F., Du, H., Wang, X., 2022b. Investigation on the control effect of benzotriazole and two derivatives on cobalt pitting corrosion in chemical mechanical polishing process: A combination of experiments and theoretical simulations. J Mol Liq 367, 120487. https://doi.org/10.1016/j.molliq.2022.120487

Ji, X., Seif, A., Duan, J., Rashidi, A., Zhou, Z., Pourhashem, S., Mirzaee, M., Zhai, X., Zhao, X., Hou, B., 2022a. Experimental and DFT studies on corrosion protection performance of epoxy/graphene quantum dots@TiO2 nanotubes coatings. Constr Build Mater 322, 126501. https://doi.org/10.1016/j.conbuildmat.2022.126501

Ji, X., Wang, W., Zhao, X., Wang, L., Ma, F., Wang, Y., Duan, J., Hou, B., 2022b. Poly(dimethyl siloxane) anti-corrosion coating with wide pH-responsive and self-healing performance based on core−shell nanofiber containers. J Mater Sci Technol 101, 128–145. https://doi.org/10.1016/j.jmst.2021.06.014

Jiang, F., Zhao, W., Wu, Yangmin, Wu, Yinghao, Liu, G., Dong, J., Zhou, K., 2019. A polyethyleneimine-grafted graphene oxide hybrid nanomaterial: Synthesis and anti-corrosion applications. Appl Surf Sci 479, 963–973. https://doi.org/10.1016/j.apsusc.2019.02.193

Jiang, L., He, Y., Li, Y., Luo, J., 2014a. Effect of ionic strength on ruthenium CMP in H2O2-based slurries. Appl Surf Sci 317, 332–337. https://doi.org/10.1016/j.apsusc.2014.08.063

Jiang, L., He, Y., Li, Y., Luo, J., 2014b. Effect of ionic strength on ruthenium CMP in H2O2-based slurries. Appl Surf Sci 317, 332–337. https://doi.org/10.1016/j.apsusc.2014.08.063

Jing, S., Zhao, Y., Sun, R.-C., Zhong, L., Peng, X., 2019. Facile and High-Yield Synthesis of Carbon Quantum Dots from Biomass-Derived Carbons at Mild Condition. ACS Sustain Chem Eng 7, 7833–7843. https://doi.org/10.1021/acssuschemeng.9b00027

John, S., Joseph, A., 2013. Quantum chemical and electrochemical studies on the corrosion inhibition of aluminium in 1 N HNO_3 using 1,2,4-triazine. Materials and Corrosion 64, 625–632. https://doi.org/10.1002/maco.201206782

Ju, H., Kai, Z.-P., Li, Y., 2008. Aminic nitrogen-bearing polydentate Schiff base compounds as corrosion inhibitors for iron in acidic media: A quantum chemical calculation. Corros Sci 50, 865–871. https://doi.org/10.1016/j.corsci.2007.10.009

Kandemirli, F., Sagdinc, S., 2007. Theoretical study of corrosion inhibition of amides and thiosemicarbazones. Corros Sci 49, 2118–2130. https://doi.org/10.1016/j.corsci.2006.10.026

Kaur, G., Kumar, H., 2022. Unravelling the Interactions Prevailing in Mixed Micellar System of Surface-Active Ionic Liquid and Cationic Surfactant. ECS Trans 107, 5249–5262. https://doi.org/10.1149/10701.5249ecst

Keshmiri, N., Najmi, P., Ramezanzadeh, M., Ramezanzadeh, B., Bahlakeh, G., 2022. Ultrastable Porous Covalent Organic Framework Assembled Carbon Nanotube as a Novel Nanocontainer for Anti-Corrosion Coatings: Experimental and Computational Studies. ACS Appl Mater Interfaces 14, 19958–19974. https://doi.org/10.1021/acsami.1c24185

Khaled, K.F., 2008. Molecular simulation, quantum chemical calculations and electrochemical studies for inhibition of mild steel by triazoles. Electrochim Acta 53, 3484–3492. https://doi.org/10.1016/j.electacta.2007.12.030

Kim, I.-K., Cho, B.-G., Park, J.-G., Park, J.-Y., Park, H.-S., 2009. Effect of pH in Ru Slurry with Sodium Periodate on Ru CMP. J Electrochem Soc 156, H188. https://doi.org/10.1149/1.3058594

Kokalj, A., 2021. On the alleged importance of the molecular electron-donating ability and the HOMO–LUMO gap in corrosion inhibition studies. Corros Sci 180, 109016. https://doi.org/10.1016/j.corsci.2020.109016

Kokalj, A., 2012. On the HSAB based estimate of charge transfer between adsorbates and metal surfaces. Chem Phys 393, 1–12. https://doi.org/10.1016/j.chemphys.2011.10.021

Kudin, K.N., Ozbas, B., Schniepp, H.C., Prud'homme, R.K., Aksay, I.A., Car, R., 2008. Raman Spectra of Graphite Oxide and Functionalized Graphene Sheets. Nano Lett 8, 36–41. https://doi.org/10.1021/nl071822y

Kumar, A., Das, C., 2023a. A novel eco-friendly inhibitor of chayote fruit extract for mild steel corrosion in 1 M HCl: Electrochemical, weight loss studies, and the effect of temperature. Sustain Chem Pharm 36, 101261. https://doi.org/10.1016/j.scp.2023.101261

Kumar, A., Das, C., 2023b. A novel eco-friendly inhibitor of chayote fruit extract for mild steel corrosion in 1 M HCl: Electrochemical, weight loss studies, and the effect of temperature. Sustain Chem Pharm 36, 101261. https://doi.org/10.1016/j.scp.2023.101261

Kumar, D., Jain, V., Rai, B., 2018a. Unravelling the mechanisms of corrosion inhibition of iron by henna extract: A density functional theory study. Corros Sci 142, 102–109. https://doi.org/10.1016/j.corsci.2018.07.011

Kumar, D., Jain, V., Rai, B., 2018b. Unravelling the mechanisms of corrosion inhibition of iron by henna extract: A density functional theory study. Corros Sci 142, 102–109. https://doi.org/10.1016/j.corsci.2018.07.011

Kumar, D., K, V.M., Jain, V., Rai, B., 2024. Accelerating corrosion inhibitor discovery through computational routes: a case of naphthalene 1-thiocarboxamide. Npj Mater Degrad 8, 5. https://doi.org/10.1038/s41529-023-00421-x

Kundu, A., Maity, B., Basu, S., 2022a. Rice Husk-Derived Carbon Quantum Dots-Based Dual-Mode Nanoprobe for Selective and Sensitive Detection of Fe^{3+} and Fluoroquinolones. ACS Biomater Sci Eng 8, 4764–4776. https://doi.org/10.1021/acsbiomaterials.2c00798

Kundu, A., Maity, B., Basu, S., 2022b. Rice Husk-Derived Carbon Quantum Dots-Based Dual-Mode Nanoprobe for Selective and Sensitive Detection of Fe^{3+} and Fluoroquinolones. ACS Biomater Sci Eng 8, 4764–4776. https://doi.org/10.1021/acsbiomaterials.2c00798

Lee, J., Ray, R., Lemieux, E., Falster, A., Little, B., 2004. An Evaluation of Carbon Steel Corrosion under Stagnant Seawater Conditions. Biofouling 20, 237–247. https://doi.org/10.1080/08927010400013274

Lee, K., Sun, S., Lee, G., Yoon, G., Kim, D., Hwang, J., Jeong, H., Song, T., Paik, U., 2021. Galvanic corrosion inhibition from aspect of bonding orbital theory in Cu/Ru barrier CMP. Sci Rep 11, 21214. https://doi.org/10.1038/s41598-021-00689-6

Li, G., Xu, Q., Singh, R., Zhang, W., Marques, C., Xie, Y., Zhang, B., Kumar, S., 2022. Graphene Oxide/Multiwalled Carbon Nanotubes Assisted Serial Quadruple Tapered Structure-Based LSPR Sensor for Glucose Detection. IEEE Sens J 22, 16904–16911. https://doi.org/10.1109/JSEN.2022.3193455

Li, H., Gao, C., Tang, L., Wang, C., Chen, Q., Zheng, Q., Yang, S., Sheng, S., Zan, X., 2020. Lysozyme (Lys), Tannic Acid (TA), and Graphene Oxide (GO) Thin Coating for Antibacterial and Enhanced Osteogenesis. ACS Appl Bio Mater 3, 673–684. https://doi.org/10.1021/acsabm.9b01017

Li, W., Ma, T., Tan, B., Zhang, S., Yan, M., Ji, J., Wang, F., Du, H., Wang, X., 2022a. The effect of structural properties of benzo derivative on the inhibition performance for copper corrosion in alkaline medium: Experimental and theoretical investigations. Colloids Surf A Physicochem Eng Asp 649, 129531. https://doi.org/10.1016/j.colsurfa.2022.129531

Li, W., Ma, T., Tan, B., Zhang, S., Yan, M., Ji, J., Wang, F., Du, H., Wang, X., 2022b. The effect of structural properties of benzo derivative on the inhibition performance for copper corrosion in alkaline medium: Experimental and theoretical investigations. Colloids Surf A Physicochem Eng Asp 649, 129531. https://doi.org/10.1016/j.colsurfa.2022.129531

Li, W., Tan, B., Zhang, S., Gao, B., Ma, B., Guo, L., Du, H., Wang, F., Wang, X., 2023. Application of an optimized alkaline cleaning solution for inhibitor removal during the post-CMP process: Performance evaluation and mechanism analysis. J Mol Liq 369, 120892. https://doi.org/10.1016/j.molliq.2022.120892

Li, W., Tan, B., Zhang, S., Guo, L., Ji, J., Yan, M., Wang, R., 2022c. Insights into triazole derivatives as potential corrosion inhibitors in CMP process: Experimental evaluation and theoretical analysis. Appl Surf Sci 602, 154165. https://doi.org/10.1016/j.apsusc.2022.154165

Li, W., Tan, B., Zhang, S., Guo, L., Ji, J., Yan, M., Wang, R., 2022d. Insights into triazole derivatives as potential corrosion inhibitors in CMP process: Experimental evaluation and theoretical analysis. Appl Surf Sci 602, 154165. https://doi.org/10.1016/j.apsusc.2022.154165

Li, Y., Zhao, P., Liang, Q., Hou, B., 2005. Berberine as a natural source inhibitor for mild steel in 1M H2SO4. Appl Surf Sci 252, 1245–1253. https://doi.org/10.1016/j.apsusc.2005.02.094

Liang, Z., Zeng, L., Cao, X., Wang, Q., Wang, X., Sun, R., 2014. Sustainable carbon quantum dots from forestry and agricultural biomass with amplified photoluminescence by simple NH $_4$ OH passivation. J. Mater. Chem. C 2, 9760–9766. https://doi.org/10.1039/C4TC01714E

Liu, C., Qiu, S., Du, P., Zhao, H., Wang, L., 2018a. An ionic liquid–graphene oxide hybrid nanomaterial: synthesis and anticorrosive applications. Nanoscale 10, 8115–8124. https://doi.org/10.1039/C8NR01890A

Liu, C., Qiu, S., Du, P., Zhao, H., Wang, L., 2018b. An ionic liquid–graphene oxide hybrid nanomaterial: synthesis and anticorrosive applications. Nanoscale 10, 8115–8124. https://doi.org/10.1039/C8NR01890A

Liu, S., Zhang, X., Rao, J., Yu, L., Lu, W., Zhou, H., Chen, S., Zhang, Y., Liu, X., 2023. Ni-Co hydrotalcite modified diatom to achieve corrosion inhibition and Cl− adsorption for long-term corrosion protection of steel. Corros Sci 225, 111589. https://doi.org/10.1016/j.corsci.2023.111589

Liu, W., Ning, C., Sang, R., Hou, Q., Ni, Y., 2021. Lignin-derived graphene quantum dots from phosphous acid-assisted hydrothermal pretreatment and their application in photocatalysis. Ind Crops Prod 171, 113963. https://doi.org/10.1016/j.indcrop.2021.113963

Liu, Z., Wang, Q., Huang, X., Qian, X., 2022. Surface Functionalization of Graphene Oxide with Hyperbranched Polyamide-Amine and Microcrystalline Cellulose for Efficient Adsorption of Heavy Metal Ions. ACS Omega 7, 10944–10954. https://doi.org/10.1021/acsomega.1c06647

López, D.A., Pérez, T., Simison, S.N., 2003. The influence of microstructure and chemical composition of carbon and low alloy steels in CO2 corrosion. A state-of-the-art appraisal. Mater Des 24, 561–575. https://doi.org/10.1016/S0261-3069(03)00158-4

López-Campos, J.E.D., Mojica-Gómez, J., Maciel-Cerda, A., Castaño, V.M., Hernández-Padrón, G., 2024. Hybrid epoxy-SiO2/GO nanosheets anti-corrosive coating for aeronautic aluminum Al6061-T5. J Coat Technol Res 21, 559–574. https://doi.org/10.1007/s11998-023-00838-8

Lukovits, I., Kálmán, E., Zucchi, F., 2001. Corrosion Inhibitors—Correlation between Electronic Structure and Efficiency. CORROSION 57, 3–8. https://doi.org/10.5006/1.3290328

Luo, F., Niu, X., Yan, H., Zhang, Y., Qu, M., Zhu, Y., Hou, Z., 2023a. Synergistic effect of 1,2,4-triazole and phytic acid as inhibitors on copper film CMP for ruthenium - based copper interconnected and the surface action mechanism analysis. Mater Sci Semicond Process 156, 107276. https://doi.org/10.1016/j.mssp.2022.107276

Luo, F., Niu, X., Yan, H., Zhang, Y., Qu, M., Zhu, Y., Hou, Z., 2023b. Synergistic effect of 1,2,4-triazole and phytic acid as inhibitors on copper film CMP for ruthenium - based copper interconnected and the surface action mechanism analysis. Mater Sci Semicond Process 156, 107276. https://doi.org/10.1016/j.mssp.2022.107276

Luo, F., Niu, X., Yan, H., Zhang, Y., Qu, M., Zhu, Y., Hou, Z., 2023c. Synergistic effect of 1,2,4-triazole and phytic acid as inhibitors on copper film CMP for ruthenium - based copper interconnected

and the surface action mechanism analysis. Mater Sci Semicond Process 156, 107276. https://doi.org/10.1016/j.mssp.2022.107276

Lv, Y., Zhao, W., Qiang, Y., Zhao, J., 2023. Constructing the interface of g-C3N4/epoxy composites using carbon quantum dots to achieve self-repairing, early corrosion monitoring and superior anticorrosion performance. Corros Sci 225, 111601. https://doi.org/10.1016/j.corsci.2023.111601

Lvovich, V.F., Smiechowski, M.F., 2006. Impedance characterization of industrial lubricants. Electrochim Acta 51, 1487–1496. https://doi.org/10.1016/j.electacta.2005.02.135

Ma, H., Guan, L., Chen, M., Zhang, Y., Wu, Y., Liu, Z., Wang, D., Wang, F., Li, X., 2023. Synthesis and enhancement of carbon quantum dots from Mopan persimmons for Fe3+ sensing and anti-counterfeiting applications. Chemical Engineering Journal 453, 139906. https://doi.org/10.1016/j.cej.2022.139906

Ma, H., He, J., Li, Z., Dong, L., Guo, S., Zhu, X., Li, D., Zang, L., Shi, L., Ba, T., 2022. Lignin-derived carbon quantum dots/Ni-MOL heterojunction from red phosphorus-assisted ball milling pretreatment and their application in photocatalysis: An insight from experiment and DFT calculation. Ind Crops Prod 189, 115829. https://doi.org/10.1016/j.indcrop.2022.115829

Ma, T., Tan, B., Xu, Y., Yin, D., Liu, G., Zeng, N., Song, G., Kao, Z., Liu, Y., 2020. Corrosion control of copper wiring by barrier CMP slurry containing azole inhibitor: Combination of simulation and experiment. Colloids Surf A Physicochem Eng Asp 599, 124872. https://doi.org/10.1016/j.colsurfa.2020.124872

Ma, Y., Li, Y., Wang, F., 2009a. Corrosion of low carbon steel in atmospheric environments of different chloride content. Corros Sci 51, 997–1006. https://doi.org/10.1016/j.corsci.2009.02.009

Ma, Y., Li, Y., Wang, F., 2009b. Corrosion of low carbon steel in atmospheric environments of different chloride content. Corros Sci 51, 997–1006. https://doi.org/10.1016/j.corsci.2009.02.009

Ma, Y., Li, Y., Wang, F., 2009c. Corrosion of low carbon steel in atmospheric environments of different chloride content. Corros Sci 51, 997–1006. https://doi.org/10.1016/j.corsci.2009.02.009

Madkour, L.H., Kaya, S., Obot, I.B., 2018. Computational, Monte Carlo simulation and experimental studies of some arylazotriazoles (AATR) and their copper complexes in corrosion inhibition process. J Mol Liq 260, 351–374. https://doi.org/10.1016/j.molliq.2018.01.055

Mahanta, J., Basak, M., Parmar, P.R., Saha, D.R., Mandal, T.K., Bandyopadhyay, D., 2022. Enhanced Hydrogen Production during Electro-Oxidation of Ethanol using Plasmonic Gold Nanoparticles. Energy Technology 10. https://doi.org/10.1002/ente.202200134

Mamand, D.M., Anwer, T.M.K., Qadr, H.M., 2023. Electronic structure and quantum chemical analysis of the corrosion inhibition efficiency of quinoxalines. Journal of the Indian Chemical Society 100, 101018. https://doi.org/10.1016/j.jics.2023.101018

Manivannan, R., Cho, B.-J., Hailin, X., Ramanathan, S., Park, J.-G., 2014. Characterization of non-amine-based post-copper chemical mechanical planarization cleaning solution. Microelectron Eng 122, 33–39. https://doi.org/10.1016/j.mee.2014.02.034

Marcano, D.C., Kosynkin, D. V., Berlin, J.M., Sinitskii, A., Sun, Z., Slesarev, A., Alemany, L.B., Lu, W., Tour, J.M., 2010a. Improved Synthesis of Graphene Oxide. ACS Nano 4, 4806–4814. https://doi.org/10.1021/nn1006368

Marcano, D.C., Kosynkin, D. v., Berlin, J.M., Sinitskii, A., Sun, Z., Slesarev, A., Alemany, L.B., Lu, W., Tour, J.M., 2010b. Improved Synthesis of Graphene Oxide. ACS Nano 4, 4806–4814. https://doi.org/10.1021/nn1006368

Mestry, S., Mhaske, S.T., 2019a. Synthesis of epoxy resins using phosphorus-based precursors for flame-retardant coating. J Coat Technol Res 16, 807–818. https://doi.org/10.1007/s11998-018-00157-3

Mestry, S., Mhaske, S.T., 2019b. Synthesis of epoxy resins using phosphorus-based precursors for flame-retardant coating. J Coat Technol Res 16, 807–818. https://doi.org/10.1007/s11998-018-00157-3

Michaelson, H.B., 1977. The work function of the elements and its periodicity. J Appl Phys 48, 4729–4733. https://doi.org/10.1063/1.323539

Mishra, D.K., Gopakumar, G., Pugazhenthi, G., Siva Brahmmananda Rao, C.V., Nagarajan, S., Banerjee, T., 2021. Molecular and Spectroscopic Insights into a Metal Salt-Based Deep Eutectic Solvent: A Combined Quantum Theory of Atoms in Molecules, Noncovalent Interaction, and Density Functional Theory Study. J Phys Chem A 125, 9680–9690. https://doi.org/10.1021/acs.jpca.1c07809

Muthayya, S., Sugimoto, J.D., Montgomery, S., Maberly, G.F., 2014. An overview of global rice production, supply, trade, and consumption. Ann N Y Acad Sci 1324, 7–14. https://doi.org/10.1111/nyas.12540

Obot, I.B., Gasem, Z.M., 2014. Theoretical evaluation of corrosion inhibition performance of some pyrazine derivatives. Corros Sci 83, 359–366. https://doi.org/10.1016/j.corsci.2014.03.008

Ogunyemi, B.T., Latona, D.F., Adejoro, I.A., 2020. Molecular modeling and quantitative structure–property relationships (QSPRs) of purine derivatives as corrosion inhibitor in acid medium. Sci Afr 8, e00336. https://doi.org/10.1016/j.sciaf.2020.e00336

Oyeneyin, O.E., Ojo, N.D., Ipinloju, N., James, A.C., Agbaffa, E.B., 2022. Investigation of Corrosion Inhibition Potentials of Some Aminopyridine Schiff Bases Using Density Functional Theory and Monte Carlo Simulation. Chemistry Africa 5, 319–332. https://doi.org/10.1007/s42250-021-00304-1

Peethala, B.C., Roy, D., Babu, S. V., 2011. Controlling the Galvanic Corrosion of Copper during Chemical Mechanical Planarization of Ruthenium Barrier Films. Electrochemical and Solid-State Letters 14, H306. https://doi.org/10.1149/1.3589308

Pham, T.A., Kumar, N.A., Jeong, Y.T., 2010. Covalent functionalization of graphene oxide with polyglycerol and their use as templates for anchoring magnetic nanoparticles. Synth Met 160, 2028–2036. https://doi.org/10.1016/j.synthmet.2010.07.034

Pourhashem, S., Vaezi, M.R., Rashidi, A., Bagherzadeh, M.R., 2017. Distinctive roles of silane coupling agents on the corrosion inhibition performance of graphene oxide in epoxy coatings. Prog Org Coat 111, 47–56. https://doi.org/10.1016/j.porgcoat.2017.05.008

Prasad, A.R., Kunyankandy, A., Joseph, A., 2020. Corrosion Inhibition in Oil and Gas Industry, in: Corrosion Inhibitors in the Oil and Gas Industry. Wiley, pp. 135–150. https://doi.org/10.1002/9783527822140.ch5

Punathil Meethal, R., Jalalzai, P., Muskan, Kumar, S., Peter, J., Klipp, A., Kim, T.-G., Park, J.-G., 2023a. Benzethonium chloride as a tungsten corrosion inhibitor in neutral and alkaline media for the post-chemical mechanical planarization application. J Colloid Interface Sci 643, 465–479. https://doi.org/10.1016/j.jcis.2023.04.012

Punathil Meethal, R., Jalalzai, P., Muskan, Kumar, S., Peter, J., Klipp, A., Kim, T.-G., Park, J.-G., 2023b. Benzethonium chloride as a tungsten corrosion inhibitor in neutral and alkaline media for the post-chemical mechanical planarization application. J Colloid Interface Sci 643, 465–479. https://doi.org/10.1016/j.jcis.2023.04.012

Punathil Meethal, R., Jalalzai, P., Muskan, Kumar, S., Peter, J., Klipp, A., Kim, T.-G., Park, J.-G., 2023c. Benzethonium chloride as a tungsten corrosion inhibitor in neutral and alkaline media for the post-chemical mechanical planarization application. J Colloid Interface Sci 643, 465–479. https://doi.org/10.1016/j.jcis.2023.04.012

Qadr, H.M., Mamand, D.M., 2021. Molecular Structure and Density Functional Theory Investigation Corrosion Inhibitors of Some Oxadiazoles. J Bio Tribocorros 7, 140. https://doi.org/10.1007/s40735-021-00566-9

Qiang, Y., Guo, L., Zhang, S., Li, W., Yu, S., Tan, J., 2016. Synergistic effect of tartaric acid with 2,6-diaminopyridine on the corrosion inhibition of mild steel in 0.5 M HCl. Sci Rep 6, 33305. https://doi.org/10.1038/srep33305

Qiu, S., Li, W., Zheng, W., Zhao, H., Wang, L., 2017a. Synergistic Effect of Polypyrrole-Intercalated Graphene for Enhanced Corrosion Protection of Aqueous Coating in 3.5% NaCl Solution. ACS Appl Mater Interfaces 9, 34294–34304. https://doi.org/10.1021/acsami.7b08325

Qiu, S., Li, W., Zheng, W., Zhao, H., Wang, L., 2017b. Synergistic Effect of Polypyrrole-Intercalated Graphene for Enhanced Corrosion Protection of Aqueous Coating in 3.5% NaCl Solution. ACS Appl Mater Interfaces 9, 34294–34304. https://doi.org/10.1021/acsami.7b08325

Qiu, Y., Wang, F., Ma, X., Yin, F., Li, D., Li, J., 2023. Carbon quantum dots derived from cassava stems via acid/alkali-assisted hydrothermal carbonization: formation, mechanism and application in drug release. Ind Crops Prod 204, 117243. https://doi.org/10.1016/j.indcrop.2023.117243

Rajitha, K., Mohana, K.N.S., Mohanan, A., Madhusudhana, A.M., 2020. Evaluation of anti-corrosion performance of modified gelatin-graphene oxide nanocomposite dispersed in epoxy coating on mild steel in saline media. Colloids Surf A Physicochem Eng Asp 587, 124341. https://doi.org/10.1016/j.colsurfa.2019.124341

Ramezanzadeh, B., Mohamadzadeh Moghadam, M.H., Shohani, N., Mahdavian, M., 2017. Effects of highly crystalline and conductive polyaniline/graphene oxide composites on the corrosion protection performance of a zinc-rich epoxy coating. Chemical Engineering Journal 320, 363–375. https://doi.org/10.1016/j.cej.2017.03.061

Ramezanzadeh, B., Niroumandrad, S., Ahmadi, A., Mahdavian, M., Moghadam, M.H.M., 2016. Enhancement of barrier and corrosion protection performance of an epoxy coating through wet transfer of amino functionalized graphene oxide. Corros Sci 103, 283–304. https://doi.org/10.1016/j.corsci.2015.11.033

Rao, S., Upadhyay, J., Polychronopoulou, K., Umer, R., Das, R., 2018. Reduced Graphene Oxide: Effect of Reduction on Electrical Conductivity. Journal of Composites Science 2, 25. https://doi.org/10.3390/jcs2020025

Ravula, S., Baker, S.N., Kamath, G., Baker, G.A., 2015. Ionic liquid-assisted exfoliation and dispersion: stripping graphene and its two-dimensional layered inorganic counterparts of their inhibitions. Nanoscale 7, 4338–4353. https://doi.org/10.1039/C4NR01524J

Ropalekar, A.A., Ghadge, R.R., Anekar, N., 2023. A review on functionalization methods of graphene oxide for enhancement in mechanical properties of epoxy composites. Mater Today Proc. https://doi.org/10.1016/j.matpr.2023.09.098

Ryu, H.-Y., Teugels, L., Devriendt, K., Struyf, H., Kim, T.-G., Park, J.-G., 2021. Effects of H_2O_2 and pH on the Chemical Mechanical Planarization of Molybdenum. ECS Journal of Solid State Science and Technology 10, 094001. https://doi.org/10.1149/2162-8777/ac26d3

Sagi, K. V., Teugels, L.G., van der Veen, M.H., Struyf, H., Babu, S. V., 2017. Chemical Mechanical Polishing and Planarization of Mn-Based Barrier/Ru Liner Films in Cu Interconnects for Advanced Metallization Nodes. ECS Journal of Solid State Science and Technology 6, P259–P264. https://doi.org/10.1149/2.0161705jss

Saha, S.Kr., Banerjee, P., 2015. A theoretical approach to understand the inhibition mechanism of steel corrosion with two aminobenzonitrile inhibitors. RSC Adv 5, 71120–71130. https://doi.org/10.1039/C5RA15173B

Saleh, M.M., Mahmoud, M.G., Abd El-Lateef, H.M., 2019. Comparative study of synergistic inhibition of mild steel and pure iron by 1-hexadecylpyridinium chloride and bromide ions. Corros Sci 154, 70–79. https://doi.org/10.1016/j.corsci.2019.03.048

Sastri, V.S., Perumareddi, J.R., 1997. Molecular Orbital Theoretical Studies of Some Organic Corrosion Inhibitors. Corrosion 53.

Saxena, A.P., Deepa, M., Joshi, A.G., Bhandari, S., Srivastava, A.K., 2011a. Poly(3,4-ethylenedioxythiophene)-Ionic Liquid Functionalized Graphene/Reduced Graphene Oxide Nanostructures: Improved Conduction and Electrochromism. ACS Appl Mater Interfaces 3, 1115–1126. https://doi.org/10.1021/am101255a

Saxena, A.P., Deepa, M., Joshi, A.G., Bhandari, S., Srivastava, A.K., 2011b. Poly(3,4-ethylenedioxythiophene)-Ionic Liquid Functionalized Graphene/Reduced Graphene Oxide Nanostructures: Improved Conduction and Electrochromism. ACS Appl Mater Interfaces 3, 1115–1126. https://doi.org/10.1021/am101255a

Schäfer, A., Horn, H., Ahlrichs, R., 1992. Fully optimized contracted Gaussian basis sets for atoms Li to Kr. J Chem Phys 97, 2571–2577. https://doi.org/10.1063/1.463096

Schriver, M., Regan, W., Gannett, W.J., Zaniewski, A.M., Crommie, M.F., Zettl, A., 2013. Graphene as a Long-Term Metal Oxidation Barrier: Worse Than Nothing. ACS Nano 7, 5763–5768. https://doi.org/10.1021/nn4014356

Shahini, M.H., Mousavi, M., Masoud Arabi, A., Mahdavian, M., Ramezanzadeh, B., 2021. Ce-oxide quantum dots decorated graphene oxide (CeO-QDs-GO) nano-platforms synthesis and application in epoxy matrix for efficient anti-corrosion ability. Journal of Industrial and Engineering Chemistry 101, 51–65. https://doi.org/10.1016/j.jiec.2021.06.024

Shen, L., He, S., Xie, W., Miao, L., Liu, J., Zhou, H., Li, B., Qiang, Y., 2022. Corrosion protection of PPy-Ti3C2-modifed epoxy zinc-rich coatings in dilute NaCl solution. Prog Org Coat 172, 107148. https://doi.org/10.1016/j.porgcoat.2022.107148

Shen, L., Li, Y., Zhao, W., Wang, K., Ci, X., Wu, Y., Liu, G., Liu, C., Fang, Z., 2020. Tuning F-doped degree of rGO: Restraining corrosion-promotion activity of EP/rGO nanocomposite coating. J Mater Sci Technol 44, 121–132. https://doi.org/10.1016/j.jmst.2019.09.043

Shen, L., Zhao, W., Miao, L., 2021a. Designed a novel EP + GO/ZRC + GO coating with bilayered structure for enhancing corrosion resistance of steel substrate. J Hazard Mater 403, 123670. https://doi.org/10.1016/j.jhazmat.2020.123670

Shen, L., Zhao, W., Wang, K., Xu, J., 2021b. GO-Ti3C2 two-dimensional heterojunction nanomaterial for anticorrosion enhancement of epoxy zinc-rich coatings. J Hazard Mater 417, 126048. https://doi.org/10.1016/j.jhazmat.2021.126048

Sheng, X., Cai, W., Zhong, L., Xie, D., Zhang, X., 2016. Synthesis of Functionalized Graphene/Polyaniline Nanocomposites with Effective Synergistic Reinforcement on Anticorrosion. Ind Eng Chem Res 55, 8576–8585. https://doi.org/10.1021/acs.iecr.6b01975

Shi, N., Li, H., Li, X., Luo, H., Jin, J., Wang, J., Li, S., 2023. ZIF-8 and benzimidazole co-modified h-BN for enhancing anti-corrosion performance of epoxy coatings. Prog Org Coat 183, 107808. https://doi.org/10.1016/j.porgcoat.2023.107808

Shiflett, M.B., Drew, D.W., Cantini, R.A., Yokozeki, A., 2010. Carbon Dioxide Capture Using Ionic Liquid 1-Butyl-3-methylimidazolium Acetate. Energy & Fuels 24, 5781–5789. https://doi.org/10.1021/ef100868a

Shiflett, M.B., Yokozeki, A., 2010. Chemical Absorption of Sulfur Dioxide in Room-Temperature Ionic Liquids. Ind Eng Chem Res 49, 1370–1377. https://doi.org/10.1021/ie901254f

Sim, S., Andou, Y., Bashid, H.A.A., Lim, H., Altarawneh, M., Jiang, Z., Eksiler, K., Iikubo, S., 2018. Development of Organo-Dispersible Graphene Oxide via Pseudo-Surface Modification for Thermally Conductive Green Polymer Composites. ACS Omega 3, 18124–18131. https://doi.org/10.1021/acsomega.8b02478

Singh, A., Ansari, K.R., Haque, J., Dohare, P., Lgaz, H., Salghi, R., Quraishi, M.A., 2018. Effect of electron donating functional groups on corrosion inhibition of mild steel in hydrochloric acid: Experimental and quantum chemical study. J Taiwan Inst Chem Eng 82, 233–251. https://doi.org/10.1016/j.jtice.2017.09.021

Singh, P., Rani, N., Kumar, S., Kumar, P., Mohan, B., Pallavi, Bhankar, V., Kataria, N., Kumar, R., Kumar, K., 2023. Assessing the biomass-based carbon dots and their composites for photocatalytic treatment of wastewater. J Clean Prod 413, 137474. https://doi.org/10.1016/j.jclepro.2023.137474

Singh, S.K., Savoy, A.W., 2020. Ionic liquids synthesis and applications: An overview. J Mol Liq 297, 112038. https://doi.org/10.1016/j.molliq.2019.112038

Solovyeva, V.A., Almuhammadi, K.H., Badeghaish, W.O., 2023. Current Downhole Corrosion Control Solutions and Trends in the Oil and Gas Industry: A Review. Materials 16, 1795. https://doi.org/10.3390/ma16051795

Sørensen, P.A., Kiil, S., Dam-Johansen, K., Weinell, C.E., 2009a. Anticorrosive coatings: a review. J Coat Technol Res 6, 135–176. https://doi.org/10.1007/s11998-008-9144-2

Sørensen, P.A., Kiil, S., Dam-Johansen, K., Weinell, C.E., 2009b. Anticorrosive coatings: a review. J Coat Technol Res 6, 135–176. https://doi.org/10.1007/s11998-008-9144-2

Srinivasan, R., Fasmin, F., 2021. An Introduction to Electrochemical Impedance Spectroscopy. CRC Press, First edition. | Boca Raton : CRC Press, 2021. https://doi.org/10.1201/9781003127932

Stankovich, S., Dikin, D.A., Piner, R.D., Kohlhaas, K.A., Kleinhammes, A., Jia, Y., Wu, Y., Nguyen, S.T., Ruoff, R.S., 2007. Synthesis of graphene-based nanosheets via chemical reduction of exfoliated graphite oxide. Carbon N Y 45, 1558–1565. https://doi.org/10.1016/j.carbon.2007.02.034

Sujatha, H.S., Lavanya, M., 2023. An insight to HOMO LUMO aspects in corrosion applications. Canadian Metallurgical Quarterly 62, 761–772. https://doi.org/10.1080/00084433.2022.2140398

Sun, X., Ma, T., Yin, D., Tan, B., Yang, F., Liu, M., Gao, P., Zhang, S., Wang, Y., He, Y., 2021a. Adsorption Mechanism of Potassium Oleate on Cobalt Surface Based on Cobalt Interconnection CMP: A Combined Experimental and DFT Investigation. ECS Journal of Solid State Science and Technology 10, 024003. https://doi.org/10.1149/2162-8777/abe1d8

Sun, X., Ma, T., Yin, D., Tan, B., Yang, F., Liu, M., Gao, P., Zhang, S., Wang, Y., He, Y., 2021b. Adsorption Mechanism of Potassium Oleate on Cobalt Surface Based on Cobalt Interconnection CMP: A Combined Experimental and DFT Investigation. ECS Journal of Solid State Science and Technology 10, 024003. https://doi.org/10.1149/2162-8777/abe1d8

Sun, X., Ma, T., Yin, D., Tan, B., Yang, F., Liu, M., Gao, P., Zhang, S., Wang, Y., He, Y., 2021c. Adsorption Mechanism of Potassium Oleate on Cobalt Surface Based on Cobalt Interconnection CMP: A Combined Experimental and DFT Investigation. ECS Journal of Solid State Science and Technology 10, 024003. https://doi.org/10.1149/2162-8777/abe1d8

Sun, X., Xie, J., Zhang, J., Sang, M., Li, Y., Lyu, P., Chen, D., Zhou, H., 2022. Hydrophobic Al2O3/SiO2/PDMS Composite Coatings for Anti-corrosion Application of 304 Stainless-Steel. J Inorg Organomet Polym Mater 32, 4237–4249. https://doi.org/10.1007/s10904-022-02423-9

Surekha, G., Krishnaiah, K.V., Ravi, N., Padma Suvarna, R., 2020. FTIR, Raman and XRD analysis of graphene oxide films prepared by modified Hummers method. J Phys Conf Ser 1495, 012012. https://doi.org/10.1088/1742-6596/1495/1/012012

Talukdar, A., Baranwal, P.K., Rajaraman, P.V., 2022a. Kinetics and mechanistic reaction pathway of carbon steel dissolution in simulated CO_2–H_2S medium in the presence of formic acid. Corrosion Reviews 40, 159–172. https://doi.org/10.1515/corrrev-2021-0062

Talukdar, A., Baranwal, P.K., Rajaraman, P.V., 2022b. Kinetics and mechanistic reaction pathway of carbon steel dissolution in simulated CO_2–H_2S medium in the presence of formic acid. Corrosion Reviews 40, 159–172. https://doi.org/10.1515/corrrev-2021-0062

Talukdar, A., Baranwal, P.K., Talukdar, M.K., Rajaraman, P.V., 2023a. Synergistic Effect of H2S and Acetic Acid on CO2 Corrosion of Carbon Steel at Elevated Temperature. JOM 75, 3757–3770. https://doi.org/10.1007/s11837-023-05952-x

Talukdar, A., Baranwal, P.K., Talukdar, M.K., Rajaraman, P.V., 2023b. Synergistic Effect of H2S and Acetic Acid on CO2 Corrosion of Carbon Steel at Elevated Temperature. JOM 75, 3757–3770. https://doi.org/10.1007/s11837-023-05952-x

Talukdar, A., Rajaraman, P.V., 2020. Investigation of Acetic Acid Effect on Carbon Steel Corrosion in CO_2–H_2S Medium: Mechanistic Reaction Pathway and Kinetics. ACS Omega 5, 11378–11388. https://doi.org/10.1021/acsomega.0c00387

Tan, X.-Q., Mo, W., Mohamed, A.R., Ong, W.-J., 2024. Synergizing Aspen plus and life cycle assessment of nascent photocatalytic dry methane reforming over thermocatalytic and biomass gasification toward syngas generation. J Clean Prod 436, 140270. https://doi.org/10.1016/j.jclepro.2023.140270

Tang, J., Liu, Y., Wang, C., Niu, X., Tan, B., Gao, B., 2018. Application of surfactant for facilitating benzotriazole removal and inhibiting copper corrosion during post-CMP cleaning. Microelectron Eng 202, 1–8. https://doi.org/10.1016/j.mee.2018.09.005

Udunwa, D.I., Onukwuli, O.D., Anadebe, V.C., 2022. Synthesis and evaluation of 1-butyl-3-methylimidazolium chloride based ionic liquid for acid corrosion inhibition of aluminum alloy: Empirical, DFT/MD-simulation and RSM modeling. J Mol Liq 364, 120019. https://doi.org/10.1016/j.molliq.2022.120019

Unnimaya, Shetty, P., Kumari, P., Kagatikar, S., 2023. Glutathione as green corrosion inhibitor for 6061Al-SiC(p) composite in HCl medium: electrochemical and theoretical investigation. Journal of Solid State Electrochemistry 27, 255–270. https://doi.org/10.1007/s10008-022-05315-7

Verma, C., Lgaz, H., Verma, D.K., Ebenso, E.E., Bahadur, I., Quraishi, M.A., 2018a. Molecular dynamics and Monte Carlo simulations as powerful tools for study of interfacial adsorption behavior of corrosion inhibitors in aqueous phase: A review. J Mol Liq 260, 99–120. https://doi.org/10.1016/j.molliq.2018.03.045

Verma, C., Lgaz, H., Verma, D.K., Ebenso, E.E., Bahadur, I., Quraishi, M.A., 2018b. Molecular dynamics and Monte Carlo simulations as powerful tools for study of interfacial adsorption behavior of corrosion inhibitors in aqueous phase: A review. J Mol Liq 260, 99–120. https://doi.org/10.1016/j.molliq.2018.03.045

Victoria, S.N., Sharma, P.P., Suni, I.I., Ramanathan, S., 2010. Potassium Bromate as an Oxidizing Agent in a Titania-Based Ru CMP Slurry. Electrochemical and Solid-State Letters 13, H385. https://doi.org/10.1149/1.3481948

Vinod, S., Tiwary, C.S., Samanta, A., Ozden, S., Narayanan, T.N., Vajtai, R., Agarwal, V., Singh, A.K., John, G., Ajayan, P.M., 2018. Graphene Oxide Epoxy (GO-xy): GO as Epoxy Adhesive by Interfacial Reaction of Functionalities. Adv Mater Interfaces 5. https://doi.org/10.1002/admi.201700657

Wang, Chijia, Liu, S., Li, M., Wang, Z., Luo, H., Fan, W., Liu, Z., Liu, F., Wang, H., 2021. Novel Environmentally Friendly Waterborne Epoxy Coating with Long-Term Antiscaling and Anticorrosion Properties. Langmuir 37, 9439–9450. https://doi.org/10.1021/acs.langmuir.1c01124

Wang, Chenwei, Wang, Chao, Li, H., Zhou, J., Zhang, X., Tian, Y., Xu, C., 2021. Effect of UV Radiation on Oxidation for Ru CMP. ECS Journal of Solid State Science and Technology 10, 034007. https://doi.org/10.1149/2162-8777/abe97b

Wang, G., Li, W., Wang, X., Fan, S., Yang, H., 2023. Experimental and theoretical investigations of three Mannich-base imidazoline quaternary ammonium salts as efficient inhibitors for Q235 steel in sulfuric acid. Appl Surf Sci 638, 157946. https://doi.org/10.1016/j.apsusc.2023.157946

Wang, J., Du, P., Zhao, H., Pu, J., Yu, C., 2019. Novel nitrogen doped carbon dots enhancing the anticorrosive performance of waterborne epoxy coatings. Nanoscale Adv 1, 3443–3451. https://doi.org/10.1039/C9NA00155G

Wang, J., Liu, B., Liu, C.T., Liu, Y., 2018. Strengthening mechanism in a high-strength carbon-containing powder metallurgical high entropy alloy. Intermetallics (Barking) 102, 58–64. https://doi.org/10.1016/j.intermet.2018.07.016

Wang, J., Wang, S., 2019. Preparation, modification and environmental application of biochar: A review. J Clean Prod 227, 1002–1022. https://doi.org/10.1016/j.jclepro.2019.04.282

Wang, S., Hu, Z., Shi, J., Chen, G., Zhang, Q., Weng, Z., Wu, K., Lu, M., 2019a. Green synthesis of graphene with the assistance of modified lignin and its application in anticorrosive waterborne epoxy coatings. Appl Surf Sci 484, 759–770. https://doi.org/10.1016/j.apsusc.2019.03.229

Wang, S., Hu, Z., Shi, J., Chen, G., Zhang, Q., Weng, Z., Wu, K., Lu, M., 2019b. Green synthesis of graphene with the assistance of modified lignin and its application in anticorrosive waterborne epoxy coatings. Appl Surf Sci 484, 759–770. https://doi.org/10.1016/j.apsusc.2019.03.229

Wang, W., Wang, Z., Liu, J., Peng, Y., Yu, X., Wang, Weixing, Zhang, Z., Sun, L., 2018a. One-Pot Facile Synthesis of Graphene Quantum Dots from Rice Husks for Fe $^{3+}$ Sensing. Ind Eng Chem Res 57, 9144–9150. https://doi.org/10.1021/acs.iecr.8b00913

Wang, W., Wang, Z., Liu, J., Peng, Y., Yu, X., Wang, Weixing, Zhang, Z., Sun, L., 2018b. One-Pot Facile Synthesis of Graphene Quantum Dots from Rice Husks for Fe $^{3+}$ Sensing. Ind Eng Chem Res 57, 9144–9150. https://doi.org/10.1021/acs.iecr.8b00913

Wang, X., Fan, W., Zhang, M., Shang, Y., Wang, Y., Liu, D., Guo, H., Dai, F., Sun, D., 2019. Ligand controlled structure of cadmium(II) metal-organic frameworks for fluorescence sensing of Fe3+ ion and nitroaromatic compounds. Chinese Chemical Letters 30, 801–805. https://doi.org/10.1016/j.cclet.2018.12.009

Wang, Xiao, Li, C., Zhang, M., Lin, D., Yuan, S., Xu, F., Zhou, Y., Wang, C., Zhu, Y., Wang, H., 2022. A novel waterborne epoxy coating with anti-corrosion performance under harsh oxygen environment. Chemical Engineering Journal 430, 133156. https://doi.org/10.1016/j.cej.2021.133156

Wang, X., Li, Y., Li, C., Zhang, X., Lin, D., Xu, F., Zhu, Y., Wang, H., Gong, J., Wang, T., 2020. Highly orientated graphene/epoxy coating with exceptional anti-corrosion performance for harsh oxygen environments. Corros Sci 176, 109049. https://doi.org/10.1016/j.corsci.2020.109049

Wang, Xintong, Yang, J., Chen, X., Ding, W., 2022. Synergism of 2-mercaptobenzimidazole and oleic imidazoline on corrosion inhibition of carbon steel in CO2 -saturated brine solutions. J Mol Liq 368, 120645. https://doi.org/10.1016/j.molliq.2022.120645

Wang, Y., Zhang, S., Tan, B., Li, W., Ji, J., Yan, M., Cui, Z., 2022. Effect of Corrosion Inhibitor BTA on Silica Particles and their Adsorption on Copper Surface in Copper Interconnection CMP. ECS Journal of Solid State Science and Technology 11, 044002. https://doi.org/10.1149/2162-8777/ac627c

Wang, Z., Huang, B., Dai, Y., Liu, Y., Zhang, X., Qin, X., Wang, J., Zheng, Z., Cheng, H., 2012. Crystal facets controlled synthesis of graphene@TiO $_2$ nanocomposites by a one-pot hydrothermal process. CrystEngComm 14, 1687–1692. https://doi.org/10.1039/C1CE06193C

Wang, Z., Yu, J., Zhang, X., Li, N., Liu, B., Li, Yanyan, Wang, Y., Wang, W., Li, Yezhou, Zhang, L., Dissanayake, S., Suib, S.L., Sun, L., 2016. Large-Scale and Controllable Synthesis of Graphene Quantum Dots from Rice Husk Biomass: A Comprehensive Utilization Strategy. ACS Appl Mater Interfaces 8, 1434–1439. https://doi.org/10.1021/acsami.5b10660

Wei, H., Ding, D., Wei, S., Guo, Z., 2013. Anticorrosive conductive polyurethane multiwalled carbon nanotube nanocomposites. J Mater Chem A Mater 1, 10805. https://doi.org/10.1039/c3ta11966a

Weng, C.-J., Huang, J.-Y., Huang, K.-Y., Jhuo, Y.-S., Tsai, M.-H., Yeh, J.-M., 2010. Advanced anticorrosive coatings prepared from electroactive polyimide–TiO2 hybrid nanocomposite materials. Electrochim Acta 55, 8430–8438. https://doi.org/10.1016/j.electacta.2010.07.063

Wongso, V., Sambudi, N.S., Sufian, S., Isnaeni, 2021. The effect of hydrothermal conditions on photoluminescence properties of rice husk-derived silica-carbon quantum dots for methylene blue degradation. Biomass Convers Biorefin 11, 2641–2654. https://doi.org/10.1007/s13399-020-00662-9

Wu, P., Zhang, B., Wang, Y., Xie, M., Liu, S., Liu, M., Xian, W., Cui, D., Zhang, K., 2023. Effect of synergetic inhibition of nonionic surfactant and benzotriazone for molybdenum in chemical mechanical polishing. Colloids Surf A Physicochem Eng Asp 664, 131164. https://doi.org/10.1016/j.colsurfa.2023.131164

Wu, Q., Zhou, W., Liu, Q., Zhou, P., Chen, T., Lu, Y., Qiao, Q., Yang, S., 2016. Solution-Processable Ionic Liquid as an Independent or Modifying Electron Transport Layer for High-Efficiency Perovskite Solar Cells. ACS Appl Mater Interfaces 8, 34464–34473. https://doi.org/10.1021/acsami.6b12683

Wu, Y., Zhao, W., Qiang, Y., Chen, Z., Wang, L., Gao, X., Fang, Z., 2020a. π-π interaction between fluorinated reduced graphene oxide and acridizinium ionic liquid: Synthesis and anti-corrosion application. Carbon N Y 159, 292–302. https://doi.org/10.1016/j.carbon.2019.12.047

Wu, Y., Zhao, W., Qiang, Y., Chen, Z., Wang, L., Gao, X., Fang, Z., 2020b. π-π interaction between fluorinated reduced graphene oxide and acridizinium ionic liquid: Synthesis and anti-corrosion application. Carbon N Y 159, 292–302. https://doi.org/10.1016/j.carbon.2019.12.047

Xu, Y., Ma, T., Liu, Y., Tan, B., Zhang, S., Wang, Y., Song, G., 2022. Effect of ethylenediamine on CMP performance of ruthenium in H $_2$ O $_2$ -based slurries. RSC Adv 12, 228–240. https://doi.org/10.1039/D1RA08243D

Xu, Y., Tan, B., Hu, L., Liu, Y., 2020. Synergetic Effect of 5-Methyl-1H-Benzotriazole and Sodium Dodecyl Benzene Sulfonate on CMP Performance of Ruthenium Barrier Layer in KIO $_4$ -Based Slurry. ECS Journal of Solid State Science and Technology 9, 104005. https://doi.org/10.1149/2162-8777/abbea0

Yadav, K., Bisen, J.C., Victoria, S.N., Manivannan, R., 2017. Sodium hypochlorite as an oxidizing agent in silica based ruthenium chemical mechanical planarization slurry. Microelectron Eng 180, 96–100. https://doi.org/10.1016/j.mee.2017.06.006

Yan, D., Liu, Jialiang, Zhang, Z., Wang, Y., Zhang, M., Song, D., Zhang, T., Liu, Jingyuan, He, F., Wang, J., 2021. Dual-functional graphene oxide-based nanomaterial for enhancing the passive and active corrosion protection of epoxy coating. Compos B Eng 222, 109075. https://doi.org/10.1016/j.compositesb.2021.109075

Yang, L., Yin, D., Tan, B., Zhang, W., Han, T., Zhao, P., Wang, T., Liu, Y., 2022. Composite complex agent based on organic amine alkali for BTA removal in post CMP cleaning of copper interconnection. Journal of Electroanalytical Chemistry 910, 116187. https://doi.org/10.1016/j.jelechem.2022.116187

Yang, X., Hou, S., Chu, T., Han, J., Li, R., Guo, Y., Gong, Y., Li, H., Wan, Z., 2021. Preparation of magnesium, nitrogen-codoped carbon quantum dots from lignin with bright green fluorescence and sensitive pH response. Ind Crops Prod 167, 113507. https://doi.org/10.1016/j.indcrop.2021.113507

Ye, Y., Chen, H., Zou, Y., Zhao, H., 2021a. Study on self-healing and corrosion resistance behaviors of functionalized carbon dot-intercalated graphene-based waterborne epoxy coating. J Mater Sci Technol 67, 226–236. https://doi.org/10.1016/j.jmst.2020.06.023

Ye, Y., Chen, H., Zou, Y., Zhao, H., 2021b. Study on self-healing and corrosion resistance behaviors of functionalized carbon dot-intercalated graphene-based waterborne epoxy coating. J Mater Sci Technol 67, 226–236. https://doi.org/10.1016/j.jmst.2020.06.023

Yeganeh, M., Omidi, M., Rabizadeh, T., 2019. Anti-corrosion behavior of epoxy composite coatings containing molybdate-loaded mesoporous silica. Prog Org Coat 126, 18–27. https://doi.org/10.1016/j.porgcoat.2018.10.016

Yin, D., Yang, L., Niu, X., Ma, Y., Liu, M., Sun, X., Gao, B., Tan, B., 2020a. Theoretical and electrochemical analysis on inhibition effect of benzotriazole and 1,2,4-triazole on cobalt surface. Colloids Surf A Physicochem Eng Asp 591, 124516. https://doi.org/10.1016/j.colsurfa.2020.124516

Yin, D., Yang, L., Niu, X., Ma, Y., Liu, M., Sun, X., Gao, B., Tan, B., 2020b. Theoretical and electrochemical analysis on inhibition effect of benzotriazole and 1,2,4-triazole on cobalt surface. Colloids Surf A Physicochem Eng Asp 591, 124516. https://doi.org/10.1016/j.colsurfa.2020.124516

Yin, D., Yang, L., Tan, B., Ma, T., Zhang, S., Wang, Y., Guo, L., Gao, B., He, Y., 2021a. Theoretical and electrochemical analysis on inhibition effects of benzotriazole derivatives (un- and methyl) on copper surface. J Mol Struct 1243, 130871. https://doi.org/10.1016/j.molstruc.2021.130871

Yin, D., Yang, L., Tan, B., Ma, T., Zhang, S., Wang, Y., Guo, L., Gao, B., He, Y., 2021b. Theoretical and electrochemical analysis on inhibition effects of benzotriazole derivatives (un- and methyl) on copper surface. J Mol Struct 1243, 130871. https://doi.org/10.1016/j.molstruc.2021.130871

Yin, X., Mu, P., Wang, Q., Li, J., 2020. Superhydrophobic ZIF-8-Based Dual-Layer Coating for Enhanced Corrosion Protection of Mg Alloy. ACS Appl Mater Interfaces 12, 35453–35463. https://doi.org/10.1021/acsami.0c09497

Yin, Z.F., Feng, Y.R., Zhao, W.Z., Bai, Z.Q., Lin, G.F., 2009. Effect of temperature on CO_2 corrosion of carbon steel. Surface and Interface Analysis 41, 517–523. https://doi.org/10.1002/sia.3057

Yu, C., Wu, S., Huang, Z., Zhao, Y., Zeng, Z., Xue, W., 2016. Water/ethanol complexation induced solubility variation of hexaquocobalt(II) bis (p-toluenesulfonate) and hexaquonickel(II) bis (p-toluenesulfonate). J Mol Liq 224, 139–145. https://doi.org/10.1016/j.molliq.2016.09.094

Yu, H., Zhang, B., Bulin, C., Li, R., Xing, R., 2016. High-efficient Synthesis of Graphene Oxide Based on Improved Hummers Method. Sci Rep 6, 36143. https://doi.org/10.1038/srep36143

Zaaba, N.I., Foo, K.L., Hashim, U., Tan, S.J., Liu, W.-W., Voon, C.H., 2017. Synthesis of Graphene Oxide using Modified Hummers Method: Solvent Influence. Procedia Eng 184, 469–477. https://doi.org/10.1016/j.proeng.2017.04.118

Zainal Abidin, N.H., Wongso, V., Hui, K.C., Cho, K., Sambudi, N.S., Ang, W.L., Saad, B., 2020a. The effect of functionalization on rice-husks derived carbon quantum dots properties and cadmium removal. Journal of Water Process Engineering 38, 101634. https://doi.org/10.1016/j.jwpe.2020.101634

Zainal Abidin, N.H., Wongso, V., Hui, K.C., Cho, K., Sambudi, N.S., Ang, W.L., Saad, B., 2020b. The effect of functionalization on rice-husks derived carbon quantum dots properties and cadmium removal. Journal of Water Process Engineering 38, 101634. https://doi.org/10.1016/j.jwpe.2020.101634

Zambare, R., Song, X., Bhuvana, S., Antony Prince, J.S., Nemade, P., 2017. Ultrafast Dye Removal Using Ionic Liquid–Graphene Oxide Sponge. ACS Sustain Chem Eng 5, 6026–6035. https://doi.org/10.1021/acssuschemeng.7b00867

Zambare, R.S., Song, X., Bhuvana, S., Tang, C.Y., Prince, J.S.A., Nemade, P.R., 2022a. Ionic Liquid-Reduced Graphene Oxide Membrane with Enhanced Stability for Water Purification. ACS Appl Mater Interfaces 14, 43339–43353. https://doi.org/10.1021/acsami.2c12488

Zambare, R.S., Song, X., Bhuvana, S., Tang, C.Y., Prince, J.S.A., Nemade, P.R., 2022b. Ionic Liquid-Reduced Graphene Oxide Membrane with Enhanced Stability for Water Purification. ACS Appl Mater Interfaces 14, 43339–43353. https://doi.org/10.1021/acsami.2c12488

Zarrouk, A., Zarrok, H., Salghi, R., Hammouti, B., Al-Deyab, S.S., Touzani, R., Bouachrine, M., Warad, I., Hadda, T.B., 2012a. A Theoretical Investigation on the Corrosion Inhibition of Copper by Quinoxaline Derivatives in Nitric Acid Solution. Int J Electrochem Sci 7, 6353–6364. https://doi.org/10.1016/S1452-3981(23)19486-7

Zarrouk, A., Zarrok, H., Salghi, R., Hammouti, B., Al-Deyab, S.S., Touzani, R., Bouachrine, M., Warad, I., Hadda, T.B., 2012b. A Theoretical Investigation on the Corrosion Inhibition of Copper by Quinoxaline Derivatives in Nitric Acid Solution. Int J Electrochem Sci 7, 6353–6364. https://doi.org/10.1016/S1452-3981(23)19486-7

Zeng, N., Wang, C., Luo, C., Zhao, H., Liu, Y., Wang, W., Ma, T., 2022. An optimized passivation mechanism at the copper film recess for achieving efficient planarization of copper chemical mechanical polishing. Mater Sci Semicond Process 139, 106321. https://doi.org/10.1016/j.mssp.2021.106321

Zeng, X., Wang, J.-X., Lu, H.-S., Chen, F., Zhang, X.-M., Qu, X.-P., 2012. Improved Removal Selectivity of Ruthenium and Copper by Glycine in Potassium Periodate (KIO_4)-Based Slurry. J Electrochem Soc 159, C525–C529. https://doi.org/10.1149/2.055211jes

Zeng, Y., Kang, L., Wu, Y., Wan, S., Liao, B., Li, N., Guo, X., 2022. Melamine modified carbon dots as high effective corrosion inhibitor for Q235 carbon steel in neutral 3.5 wt% NaCl solution. J Mol Liq 349, 118108. https://doi.org/10.1016/j.molliq.2021.118108

Zhang, C., Dai, X., Wang, Y., Sun, G., Li, P., Qu, L., Sui, Y., Dou, Y., 2019. Preparation and Corrosion Resistance of ETEO Modified Graphene Oxide/Epoxy Resin Coating. Coatings 9, 46. https://doi.org/10.3390/coatings9010046

Zhang, Cheng, Ling, Y., Zhang, X., Liang, M., Zou, H., 2022. Ultra-thin carbon fiber reinforced carbon nanotubes modified epoxy composites with superior mechanical and electrical properties for the aerospace field. Compos Part A Appl Sci Manuf 163, 107197. https://doi.org/10.1016/j.compositesa.2022.107197

Zhang, Chenyang, Li, W., Liu, C., Zhang, Chunfeng, Cao, L., Kong, D., Wang, W., Chen, S., 2022a. Effect of covalent organic framework modified graphene oxide on anticorrosion and self-healing properties of epoxy resin coatings. J Colloid Interface Sci 608, 1025–1039. https://doi.org/10.1016/j.jcis.2021.10.024

Zhang, Chenyang, Li, W., Liu, C., Zhang, Chunfeng, Cao, L., Kong, D., Wang, W., Chen, S., 2022b. Effect of covalent organic framework modified graphene oxide on anticorrosion and self-healing properties of epoxy resin coatings. J Colloid Interface Sci 608, 1025–1039. https://doi.org/10.1016/j.jcis.2021.10.024

Zhang, M., Xu, F., Lin, D., Peng, J., Zhu, Y., Wang, H., 2022. A smart anti-corrosion coating based on triple functional fillers. Chemical Engineering Journal 446, 137078. https://doi.org/10.1016/j.cej.2022.137078

Zhang, X., Li, K., Li, H., Lu, J., Fu, Q., Chu, Y., 2014. Graphene nanosheets synthesis via chemical reduction of graphene oxide using sodium acetate trihydrate solution. Synth Met 193, 132–138. https://doi.org/10.1016/j.synthmet.2014.04.007

Zhang, X., Pan, G., Hu, L., Wang, H., Wang, C., 2020. Effects of nitrilotriacetic acid and corrosion inhibitor on cobalt barrier chemical–mechanical polishing: Experimental and density functional theory analysis. Colloids Surf A Physicochem Eng Asp 605, 125392. https://doi.org/10.1016/j.colsurfa.2020.125392

Zhao, Z., Guo, L., Feng, L., Lu, H., Xu, Y., Wang, J., Xiang, B., Zou, X., 2019. Polydopamine functionalized graphene oxide nanocomposites reinforced the corrosion protection and adhesion properties of waterborne polyurethane coatings. Eur Polym J 120, 109249. https://doi.org/10.1016/j.eurpolymj.2019.109249

Zhou, J., Niu, X., Cui, Y., Wang, Z., Wang, J., Wang, R., 2020. Study on the film forming mechanism, corrosion inhibition effect and synergistic action of two different inhibitors on copper surface chemical mechanical polishing for GLSI. Appl Surf Sci 505, 144507. https://doi.org/10.1016/j.apsusc.2019.144507

Zhou, Z., Pourhashem, S., Wang, Z., Duan, J., Zhang, R., Hou, B., 2022a. Distinctive roles of graphene oxide, ZnO quantum dots, and their nanohybrids in anti-corrosion and anti-fouling performance of waterborne epoxy coatings. Chemical Engineering Journal 439, 135765. https://doi.org/10.1016/j.cej.2022.135765

Zhou, Z., Pourhashem, S., Wang, Z., Duan, J., Zhang, R., Hou, B., 2022b. Distinctive roles of graphene oxide, ZnO quantum dots, and their nanohybrids in anti-corrosion and anti-fouling performance

of waterborne epoxy coatings. Chemical Engineering Journal 439, 135765. https://doi.org/10.1016/j.cej.2022.135765

Zhou, Z., Pourhashem, S., Wang, Z., Duan, J., Zhang, R., Hou, B., 2022c. Distinctive roles of graphene oxide, ZnO quantum dots, and their nanohybrids in anti-corrosion and anti-fouling performance of waterborne epoxy coatings. Chemical Engineering Journal 439, 135765. https://doi.org/10.1016/j.cej.2022.135765

Zhou, Z., Seif, A., Pourhashem, S., Duan, J., Rashidi, A., Mirzaee, M., Silvestrelli, P.L., Hou, B., 2023a. Anti-corrosion and anti-fouling properties of ball-like GQDs hybrided MOFs functionalized with silane in waterborne epoxy-polydimethylsiloxane coatings: Experimental and theoretical studies. Appl Mater Today 30, 101704. https://doi.org/10.1016/j.apmt.2022.101704

Zhou, Z., Seif, A., Pourhashem, S., Duan, J., Rashidi, A., Mirzaee, M., Silvestrelli, P.L., Hou, B., 2023b. Anti-corrosion and anti-fouling properties of ball-like GQDs hybrided MOFs functionalized with silane in waterborne epoxy-polydimethylsiloxane coatings: Experimental and theoretical studies. Appl Mater Today 30, 101704. https://doi.org/10.1016/j.apmt.2022.101704

Zhou, Z., Seif, A., Pourhashem, S., Silvestrelli, P.L., Ambrosetti, A., Mirzaee, M., Duan, J., Rashidi, A., Hou, B., 2022d. Experimental and Theoretical Studies toward Superior Anti-corrosive Nanocomposite Coatings of Aminosilane Wrapped Layer-by-Layer Graphene Oxide@MXene/Waterborne Epoxy. ACS Appl Mater Interfaces 14, 51275–51290. https://doi.org/10.1021/acsami.2c14145

Appendix:

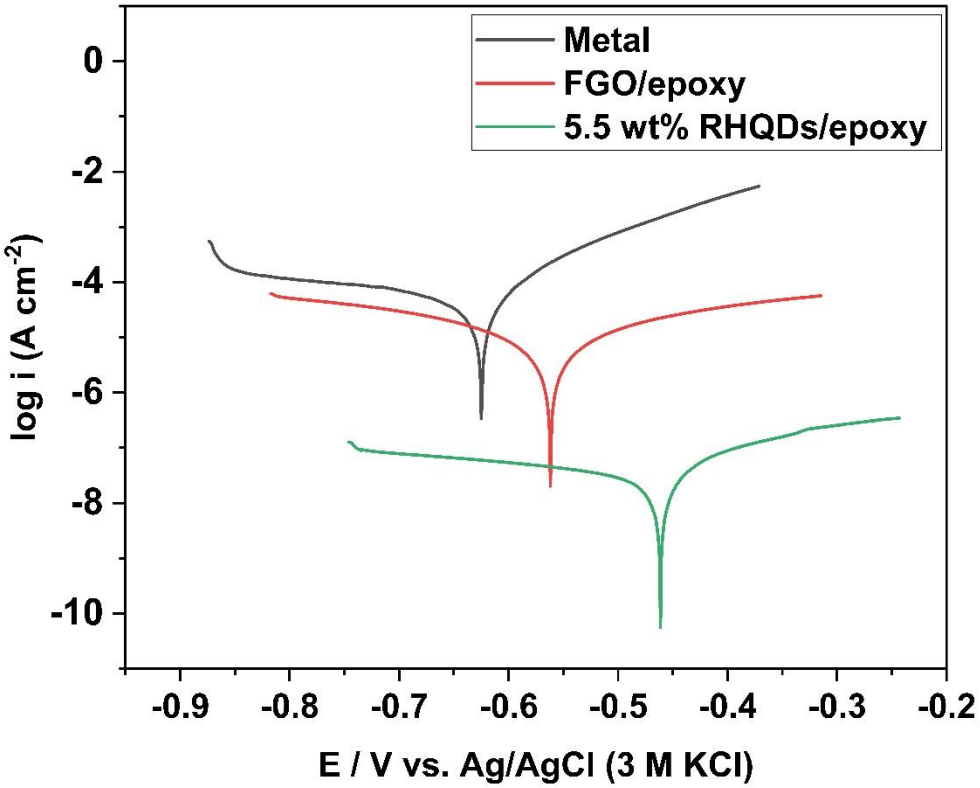

Figure A1 Potentiodynamic polarization curve of FGO/epoxy and RH-QDs/epoxy coating

RESEACH OUTPUT FROM THE THESIS

Journal publications

1. Nikhil Rahul Dhongde, Prince Kumar Baranawal, Prasanna Venkatesh Rajaraman, Functionalization of graphene oxide with an ionic liquid (1 butyl - 3 methylimidazolium acetate): Preparation of epoxy-based coating on carbon steel for anticorrosive applications. ***Journal of Applied Polymer Science, Wiley***. 10.1002/app.54959, 141, 7, (2023).

2. Nikhil Rahul Dhongde, Nipu Kumar Das, Prasanna Venkatesh Rajaraman, Synthesis of carbon quantum dots from rice husk for anti-corrosive coating applications: Experimental and theoretical investigations. ***Industrial Crops and Products, Elsevier***. 212 (2024): 118329.

3. Nikhil Rahul Dhongde, Nipu Kumar Das, Jenasree Hazarika, Jin-Goo Park, Tamal Banerjee, Prasanna Venkatesh Rajaraman, Azoles as corrosion inhibitors in alkaline medium for Ruthenium chemical mechanical planarization applications: Electrochemical and Theoretical analysis***. Journal of Molecular Structure, Elsevier.*** 1320 (2025): 139651.

Journal publications other work

Sayani Adhikari, **Nikhil Rahul Dhongde**, Prasanna Venkatesh Rajaramn, Investigation of corrosion behavior of carbon steel API 5L X52/X60 in CO_2-H_2S system in the presence of acetic acid at elevated temperature. ***Arabian Journal for Science and engineering***. 49.6 (2024): 8363-8381.

Nikhil Rahul Dhongde, Sayani Adhikari, Prasanna Venkatesh Rajaraman, Anticorrosion properties of ionic liquid functionalized graphene oxide epoxy composite coating on the carbon steel for CCUS environment. *(Revision submitted)*

Conference presentation

1. Nikhil Rahul Dhongde, Prince Kumar Baranawal, Prasanna Venkatesh Rajaraman, "Anti-corrosive behavior of epoxy composite coating on carbon steel with different mixing ratios" *International Conference on Corrosion and Coatings, Jamshedpur, India* (7-8 December, 2022)

2. Nikhil Rahul Dhongde, Prasanna Venkatesh Rajaraman, "Anticorrosion properties of ionic liquid (Triethylsulfonium bis-trifluoromethylsulfonyl-imide) functionalized graphene oxide-based epoxy coating on the steel in high-pressure CO2" *3rd International Conference on New Frontiers in Chemical, Energy and Environmental Engineering (INCEEE - 2023), NIT Warangal, India.* 24-25 November, 2023. ***(Best Oral Presentation: Technical session)***

Workshops attended

1. Applied statistical Modeling and Data Analytics for Petroleum Engineering and Related Application held at Indian Institute of Technology Guwahati, Assam, India from, and sponsored by ***SPE IIT Guwahati student chapter***. **(22-24 November 2022)**

2. Karyashaala event on Quantum chemical calculations and molecular dynamics simulations held at Indian Institute of Technology Guwahati, Assam, India, and sponsored by ***SERB, India***. **(4-10 January 2024)**